UNIVERSITY OF MONTENEGRO
FACULTY OF CIVIL ENGINEERING

MSc Šemso Kalač

EXPERIMENTAL AND THEORETICAL RESEARCH OF THE PLANAR ALUMINIUM LATTICE STRUCTURE JOINTS

DOCTORAL DISSERTATION

Podgorica, 2025.

UNIVERZITET CRNE GORE
GRAĐEVINSKI FAKULTET

Mr Šemso Kalač

EKSPERIMENTALNO I TEORIJSKO ISPITIVANJE RAVANSKIH VEZA ALUMINIJUMSKIH REŠETKASTIH KONSTRUKCIJA

DOKTORSKA DISERTACIJA

Podgorica, 2025.

PODACI O DOKTORANDU, MENTORU I ČLANOVIMA KOMISIJE

Doktorand	Mr Šemso Kalač
Datum rođenja:	30.09.1991. god.
Naziv završenog studijskog programa i godina završetka:	Poslijediplomske magistarske studije Građevinskog fakulteta Univerziteta Crne Gore 2017
Mentor:	Prof. dr Duško Lučić, redovni profesor Građevinskog fakulteta Univerziteta Crne Gore
Članovi komisije za odbranu doktorske disertacije:	Prof. dr Radomir Zejak, redovni profesor Građevinskog fakulteta Univerziteta Crne Gore Prof. dr Duško Lučić, redovni profesor Građevinskog fakulteta Univerziteta Crne Gore Prof. dr Biljana Šćepanović, redovni profesor Građevinskog fakulteta Univerziteta Crne Gore Prof. dr Srđa Aleksić, redovni profesor Građevinskog fakulteta Univerziteta Crne Gore Prof. dr Milivoje Rogač, vanredni profesor Građevinskog fakulteta Univerziteta Crne Gore
Datum odbrane doktorske disertacije:	

ZAHVALNOST

Želim da izrazim svoju iskrenu zahvalnost mom mentor i prijetelju, prof. dr Dušku Lučiću, na kontinuiranoj podršci, stručnom vodstvu i savjetima koji su mi bili dragocjeni tokom izrade ove disertacije. Njegova posvećenost i razumijevanje značajno su doprinijeli kvalitetu ovog rada.

Od srca se zahvaljujem svojim roditeljima i porodici, koji su bili moj najveći oslonac i podrška u svim fazama istraživanja i pisanja.

Posebnu zahvalnost dugujem Laboratoriji Građevinskog fakulteta Univerziteta Crne Gore, kao i kolegama Draganu Ćaliću i Zoranu Aleksiću, na pomoći i saradnji tokom eksperimentalnih ispitivanja.

Takođe, izražavam zahvalnost prof. dr Martinu Mensingeru i dr. Christini Radlbeck na podršci i mentorstvu tokom istraživačkog boravka na Tehničkom univerzitetu u Minhenu, koji je za mene predstavljao značajno profesionalno i lično iskustvo.

Zahvaljujem se i prof. dr Biljani Šćepanović na reviziji aplikacije za istraživački grant, čiji je doprinos bio od velikog značaja za realizaciju istraživanja.

Na kraju, zahvalnost dugujem kompanijama Remid Vis, Eurotehnika Zagreb i Šekom Kalač Š. doo na podršci i finansijskoj pomoći u pripremi uzoraka za eksperimentalna ispitivanja.

Sažetak

Uvod

Aluminijumske konstrukcije sve više pronalaze primjenu u savremenom građevinarstvu zahvaljujući svojoj maloj težini, otpornosti na koroziju i estetskim karakteristikama. Međutim, jedno od ključnih ograničenja njihove šire primjene jeste nedovoljno poznavanje ponašanja zavarenih spojeva, naročito u zoni uticaja toplote (ZUT), gdje dolazi do značajnog smanjenja mehaničkih svojstava usled termičkog uticaja zavarivanja.

Cilj istraživanja

Cilj ovog doktorskog istraživanja je definisanje jasnih smjernica i preporuka koje omogućuju pouzdanu, efikasnu i racionalnu interpretaciju nosivosti ravanskih veza elemenata aluminijumske rešetkaste konstrukcije.

Upotpunjavanje svjetske baze podatka rezultatima eksperimentalnog istraživanja kao osnov za dalje analize.

Hipoteze:

Nosivost zavarenih ravanskih veza u aluminijumskim rešetkastim konstrukcijama može se preciznije definisati redefinisanjem izraza za nosivost zavarenih veza u čeličnim konstrukcijama (EN 1993 1-8). Navedena hipoteza potvrđena kroz definisanje analitičkog izraza za nosivost X-čvora aluminijumske rešetke.

Metodologija

Istraživanje je sprovedeno u saradnji sa Građevinskim fakultetom Univerziteta Crne Gore i Tehničkim univerzitetom u Minhenu. Uključena su eksperimentalna ispitivanja zavarenih uzoraka od legure EN AW-6082-T6, mjerenje tvrdoće metodom po Vickersu, kao i digitalna korelacija slike (DIC) za praćenje raspodjele deformacija. Paralelno su razvijeni numerički modeli pomoću softvera ANSYS koji su validirani eksperimentalnim podacima.

Eksperimentalna istraživanja

Eksperimentalni dio istraživanja realizovan je u dvije faze: prvo u Laboratoriji za ispitivanje materijala na Građevinskom fakultetu Univerziteta Crne Gore, a zatim na Tehničkom univerzitetu u Minhenu. Odrađene su dvije grupe ispitivanja, ispitivanja mehaničkih svojstava materijala u osnovnom materijalu i ZUT-u i ispitivanja zavarenih veza aluminjumskih rešetkastih nosača (izolovanih i veza kao integralnog dijela nosača). Uzorci su izrađeni od legure EN AW-6082-T6, koja je poznata po dobroj zavarljivosti i visokim mehaničkim osobinama. Prije zavarivanja odrađena je priprema površina kako bi se uklonio oksidni sloj, a proces zavarivanja je izveden TIG metodom korišćenjem dodatnog materijala ER 5356. Testiranja su uključivala mjerenje tvrdoće duž ZUT-a, kao i ispitivanja zatezne čvrstoće pomoću univerzalne mašine za ispitivanje. Poseban fokus stavljen je na lokalizaciju deformacija i mehanizme loma koji se javljaju u zoni oko zavara.

Za potrebe ispitivanja mehaničkih osobina uzoraka, pripremljeni su standardizovani ispitni uzorci (dog-bone uzorci) u skladu sa EN ISO 6892-1:2019. Ispitivanja zatezne čvrstoće sprovedena su na univerzalnoj mašini za ispitivanje čvrstoće (Instron, kapaciteta 100 kN). Primijenjena je optička metoda digitalne korelacije slike (DIC) za analizu polja deformacija u realnom vremenu. Na osnovu dobijenih rezultata zabilježena je jasno izražena lokalizacija deformacija u ZUT-u, što ukazuje na termičku degradaciju mikrostrukture materijala. Svi eksperimentalni podaci su statistički obrađeni. Rezultati mjerenja tvrdoće pokazuju da ZUT obuhvata širinu od 20 do 30 mm u zavisnosti od debljine elementa i korišćene metode zavarivanja.

Uzorci korišćeni za eksperimentalna ispitivanja su pripremljeni od šupljih profila kvadratnog (SHS) i kružnog (CHS) poprečnog presjeka. Proces rezanja je izveden na tračnoj testeri uz hlađenje emulzijom kako bi se minimiziralo unošenje toplote i očuvala mikrostruktura legure EN AW-6082 T6. Zavarivanje je sprovedeno TIG postupkom, pri čemu su zavarivači koristili propisane parametre pod nadzorom sertifikovanog inženjera zavarivanja. Svi spojevi su pripremljeni sa posebnim osvrtom na pripremu površina.

U okviru ovog eksperimentalnog istraživanja ukupno je ispitano i šest rešetkastih nosača izrađenih od aluminijumske legure EN AW-6082-T6. Rešetkasti nosači imali su visinu od 600 mm i raspon od 3000 mm. Svi ispitani nosači posjedovali su identične pojaseve izvedene od profila SHS 100×5 (slika 1). Radi sprovođenja parametarske

analize variran je oblik i dimenzija dijagonala. Tri nosača konstruisana su korišćenjem kružnih šupljih profila (CHS) prečnika 40, 50 i 60 mm, dok su preostala tri nosača imala dijagonale izvedene od SHS profila širine 40, 50 i 60 mm. Čvorovi su izvedeni centrično, bez ekscentriciteta (e = 0), uz prisustvo zazora čija je veličina zavisila od dimenzija dijagonale. Dijagonale su spajane sa pojasevima pod uglom θi = 45°. U skladu s tim, koeficijent β se kretao u intervalu od 0,4 (za SHS40 i CHS40) do 0,6 (za SHS60 i CHS60), pri čemu β predstavlja odnos širine ili prečnika dijagonale prema širini pojasa. Svi čvorovi ispunjavali su zahtjeve definisane standardom EN 1993-1-8 [3], te su izvedeni u centričnoj konfiguraciji sa zazorom.

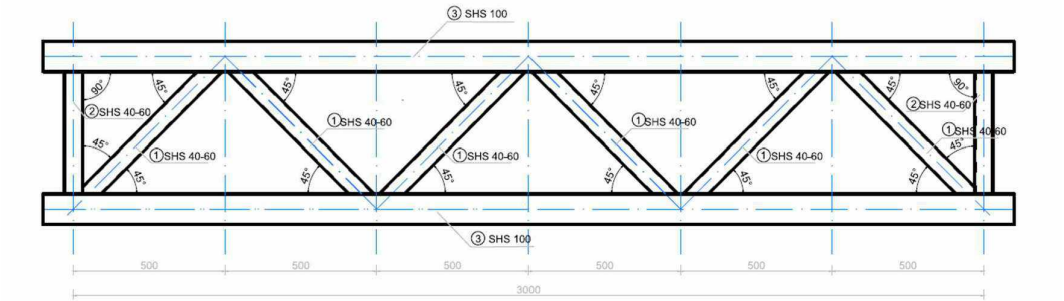

Slika 1. Geometrija aluminijumskog rešetkastog nosača.

Rešetkasti nosači označeni su u skladu sa poprečnim presjekom dijagonala od kojih su izrađeni. Na taj način, uzorci su klasifikovani kao SHS40, SHS50, SHS60, te CHS40, CHS50 i CHS60.

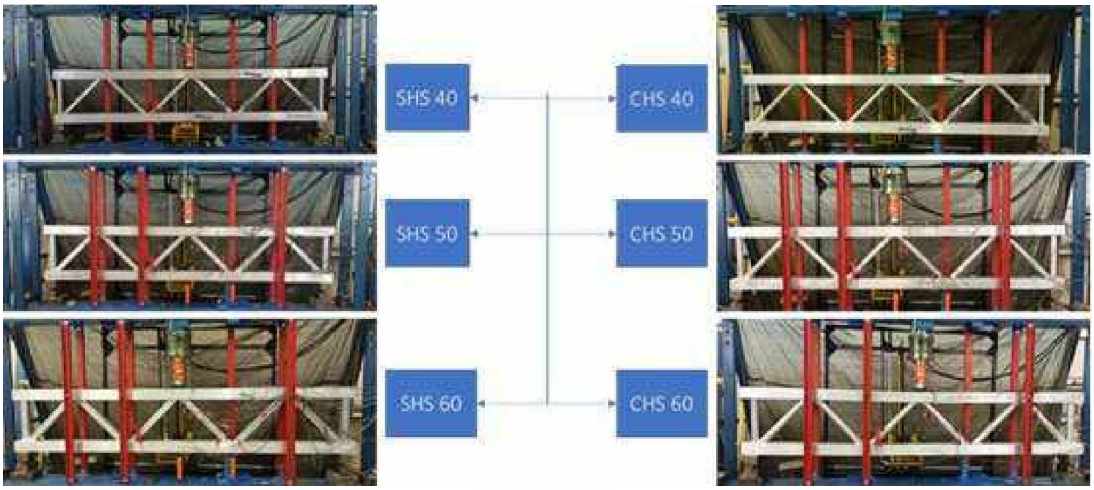

Slika 2. Označavanje rešetkastih nosača.

Čvorovi su označeni na osnovu tipologije spoja, položaja unutar rešetkastog nosača, kao i pravca djelovanja aksijalne sile u pojasu. K-čvorovi u zategnutom pojasu označeni su kao KTL (pozicionirani lijevo) i KTR (pozicionirani desno), dok su K-čvorovi u pritisnutom pojasu označeni oznakom KC. Položaji označenih X-čvorova i K-čvorova prikazani su na slici 3.

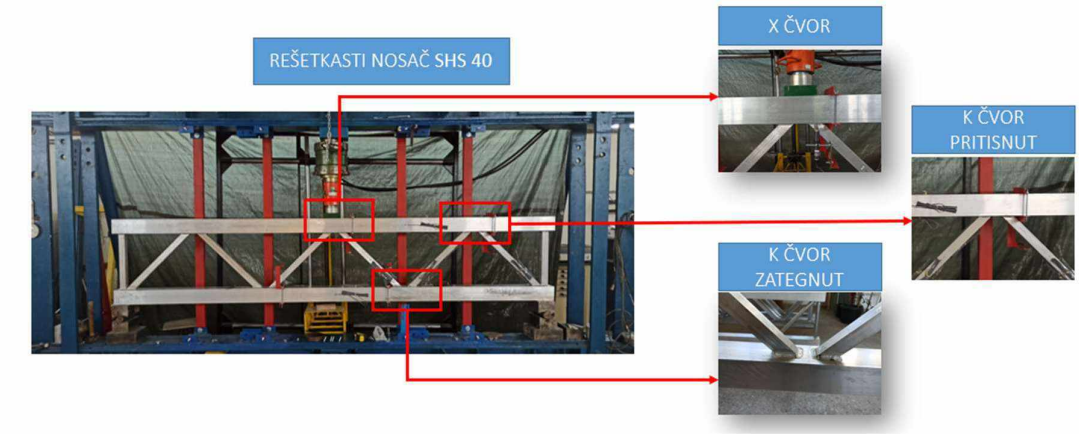

Slika 3. Označavanje čvorova unutar rešetkastog nosača.

Rešetkasti nosač [51], prikazan na slici 4, zglobno je oslonjen (I, II) u ramu za ispitivanje (III) i izložen aksijalnog koncentrisanoj sili (IV) nanešenoj u sredini raspona. Pomjeranja Y-čvorova (I, II) bila su spriječena. U slučaju izvijanja, bočna pomjeranja pritisnutog pojasa rešetkastog nosača spriječena su na svakih 500 mm pomoću zavrtnjeva povezanih sa UPE profilima (V). Ćelija za mjerenje sile (A), montirana na čeličnoj ploči dimenzija 120×30×100 mm, registrovala je opterećenje koje je dolazilo od hidraulične prese (IV) iznad. Ugibomjeri su korišćeni za mjerenje lokalnih deformacija na površinama pojaseva. Konkretno, ugibomjeri postavljeni na zategnuti pojas (C, E) mjerili su lokalne deformacije u KTL- i KTR-čvorovima, dok je ugibomjer postavljen na pritisnuti pojas (D) mjerio lokalnu deformaciju u KC-čvoru. Ugibomjer postavljen na ram, za ispitivanje

(F, G) služili su za mjerenje ukupnog ugiba nosača. Dodatno, ugibomjer A mjerio je lokalnu deformaciju X-čvora.

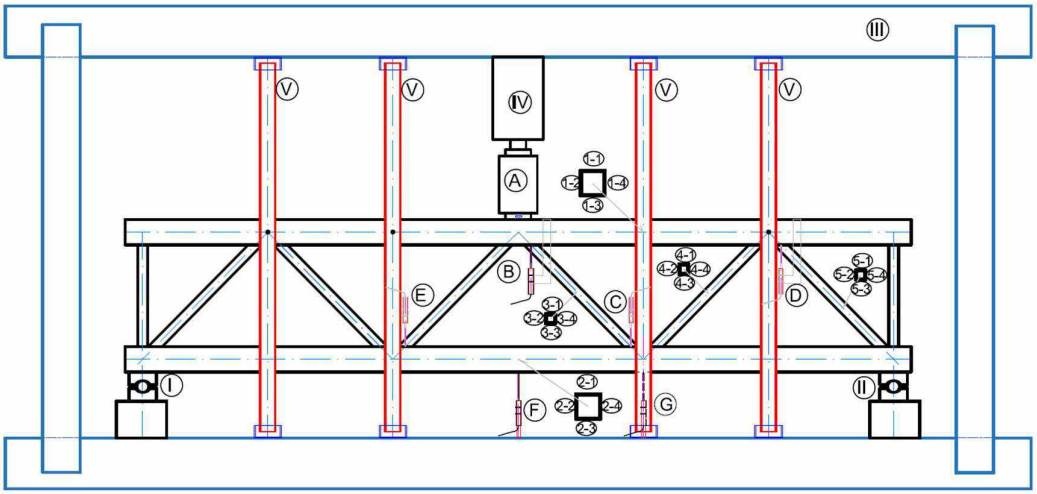

Slika 4: Shematski prikaz eksperimentalnog ispitivanja.

U okviru ovog eksperimentalnog istraživanja ispitano je i dvanaest izolovanih X-čvorova (slika 5), izrađenih od aluminijumske legure EN AW-6082 T6. Dužina pojasa iznosila je 600 mm, dok je dužina dijagonale bila 300 mm. Svi ispitani X-čvorovi imali su identične pojaseve, izvedene od SHS 100×5 profila. Radi sprovođenja parametarske analize varirani su oblik i dimenzije dijagonala. Šest čvorova je konstruisano korišćenjem kružnih šupljih profila (CHS) prečnika 40, 50 i 60 mm, pri čemu je svaka dimenzija dijagonale ponovljena dva puta. Preostalih šest čvorova izvedeno je sa dijagonalama iz SHS profila širine 40, 50 i 60 mm. Čvorovi su bili izvedeni centrično, bez ekscentriciteta ($e = 0$). Dijagonale su povezane sa pojasevima pod uglom $\theta i = 90°$. Shodno tome, koeficijent β se kretao od 0,4 (za SHS40 i CHS40) do 0,6 (za SHS60 i CHS60), pri čemu β predstavlja odnos širine ili prečnika dijagonale prema širini pojasa. Svi čvorovi su ispunjavali zahtjeve standarda EN 1993-1-8 [3] i bili su izvedeni u centričnoj konfiguraciji.

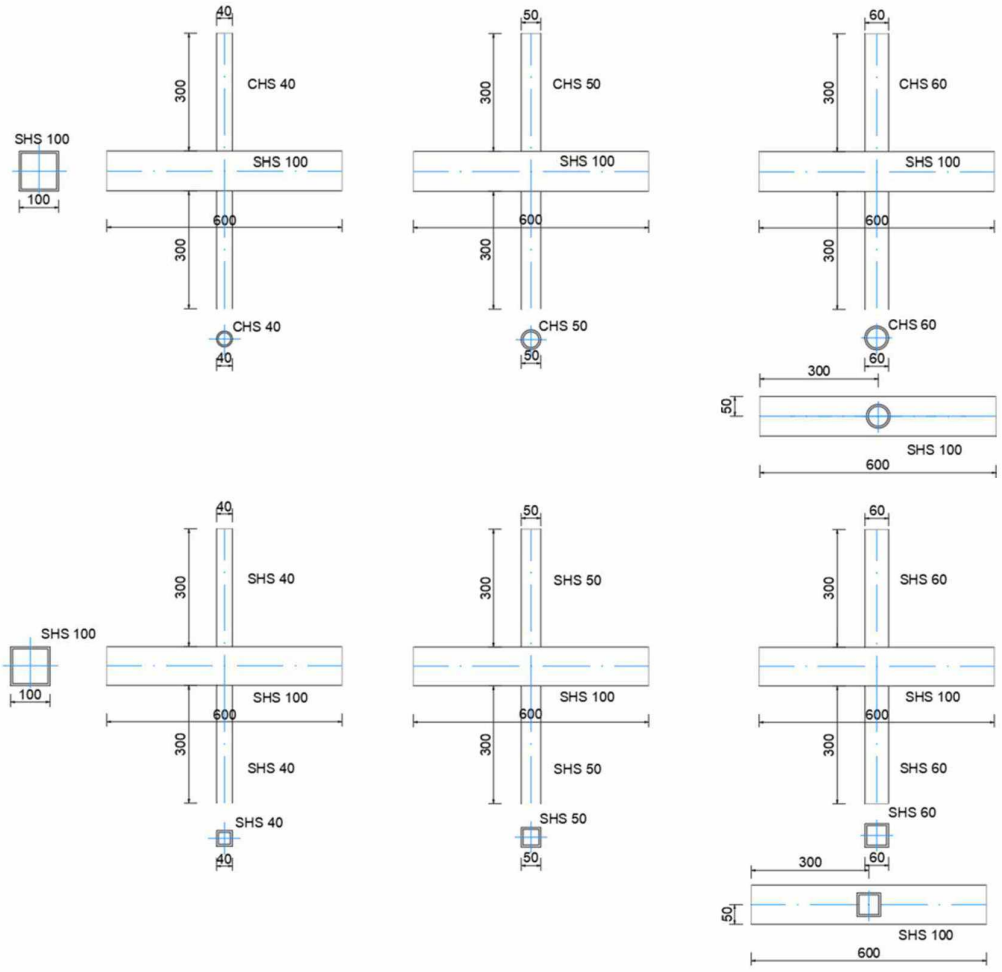

Slika 5: Uzorci izolovanih X čvorova.

X-čvorovi su označeni na osnovu poprečnog presjeka dijagonala od kojih su izrađeni. Prema tome, uzorci su označeni kao: X SHS 40-1, X SHS 40-2, X SHS 50-1, X SHS 50-2, X SHS 60-1, X SHS 60-2, X CHS 40-1, X CHS 40-2, X CHS 50-1, X CHS 50-2, X CHS 60-1 i X CHS 60-2, slika 5.

Slika 6. Označavanje uzoraka.

X-čvor, prikazan na slici 7, bio je instaliran u ispitnom ramu (I) i izložen koncentrisanoj aksijalnoj sili (II), nanešenoj na vrhu štapa ispune. Ćelija za mjerenje sile (III), postavljena na vrhu ispune i registrovala je opterećenje koje je dolazilo od hidraulične prese (II) iznad. Ugibomjeri su korišćeni za mjerenje lokalnih pomjeranja na površinama pojasa (1, 2). Nakon pozicioniranja uzorka u ispitnom ramu, primijenjeno je početno predopterećenje od 0,5 kN, kako bi se omogućilo optimalno naleganje uzorka. Zatim je opterećenje povećavano inkrementalno, brzinom od 1 kN/min, pomoću hidraulične prese, dok su uređaji za akviziciju podataka kontinuirano bilježili rezultate, sve do pojave plastifikacije X-čvora, definisane kao povećanje deformacija čvora bez daljeg rasta opterećenja. Maksimalna deformacija čvora registrovana je u zoni kontakta između pritisnute ispune i pojasa.

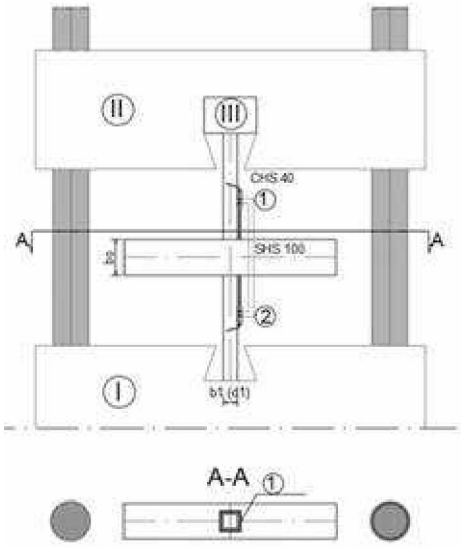

Slika 7. Shema eksperimentalnog ispitivanja.

Eksperimentalna ispitivanja kako materijala tako i zavarenih čvorova su pokazala da dolazi do značajnog smanjenja napona na granici tečenja u ZUT-u, pri čemu je zabilježeno i do 50% smanjenja u odnosu na osnovni materijal. Tvrdoća mjerena Vickers metodom potvrđuje ove nalaze, jer su minimalne vrijednosti tvrdoće locirane upravo u neposrednoj blizini zavara. Deformacione slike dobijene metodom DIC ukazuju na izraženu lokalizaciju deformacija u ZUT-u, što potvrđuje hipotezu da je upravo ta zona najosjetljivija na plastične deformacije i lom.

Numerička analiza

Numerički modeli [51] su precizno simulirali ponašanje zavarenih čvorova i razvijeni su u računarskom paketu ANSYS korišćenjem metode konačnih elemenata (MKE). Modeli su obuhvatili trodimenzionalno modelovanje zavarenih spojeva sa preciznim definisanjem materijalnih osobina, uključujući smanjenje čvrstoće u ZUT-u.

Zbog simetrije, modelovan je samo jedan kvadrant uzorka. Oslonac na liniji C–C modelovan je kao oslonac sa spriječenim pomjeranjima u Y i X pravcu, dok je oslonac na liniji B–B modelovan kao oslonac sa spriječenim pomjeranjem u X pravcu, što je prikazano na slici 8.

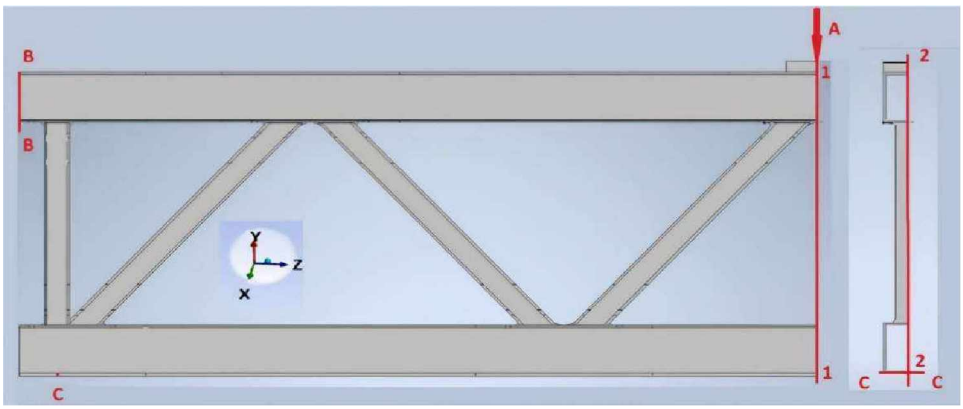

Slika 8. Granični uslovi i uslovi simetrije.

U ANSYS modelu [51] posebno su modelovane zone uticaja toplote (ZUT) sa efektima omekšavanja. Kod pojasa, ZUT 1 je definisana kao oblast preklapanja sa dijagonalom, koja se prostire 20 mm sa obje strane dijagonale duž konture poprečnog presjeka pojasa.

Kod dijagonale, ZUT 1 je predstavljala zonu dužine 20 mm od mjesta kontakta sa pojasom. ZUT 2 je definisana kao dodatna zona širine 10 mm, koja se nadovezuje na ZUT 1 i prostire se u oba elementa – i u pojas i u dijagonalu. Za opis ponašanja materijala u zonama ZUT 1 i ZUT 2 korišćeni su multilinearni dijagrami. Položaji ZUT zona prikazani su na slici 9. Za modelovanje interakcija između zavara i zona uticaja toplote, kao i između HAZ zona i osnovnog materijala, korišćeni su *bonded* kontakti.

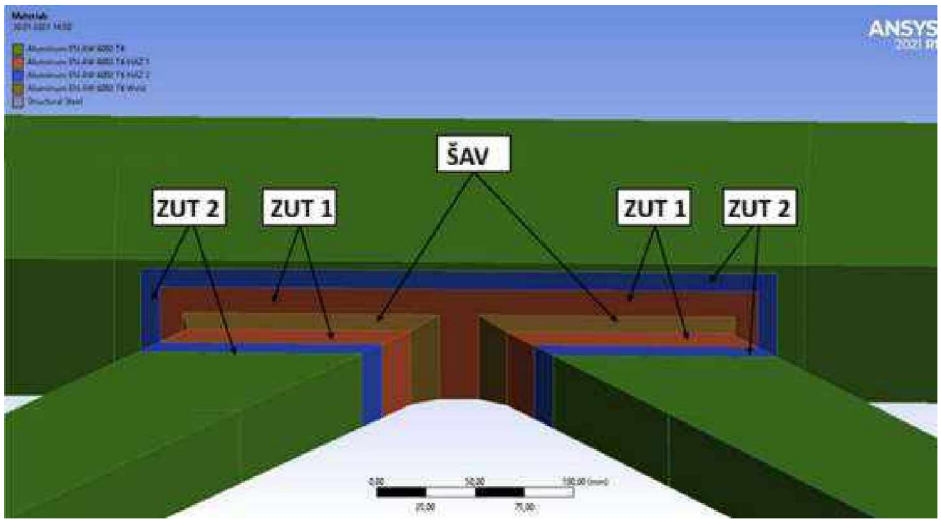

Slika 9. Materijalne zone.

U numeričkoj analizi [51] korišćeni su solid konačni elementi tipa HEX20 sa redukovanom integracijom. Ovi elementi karakterišu se sa 20 čvorova, pri čemu svaki čvor ima tri stepena slobode, a elementi se mogu orijentisati u bilo kojem pravcu. Za modelovanje ZUT 1 i ŠAV zone primijenjena su tri sloja, dok su za ZUT 2 zonu korišćena dva sloja elemenata. ŠAV zone su predstavljene pomoću TET10 elemenata, koji imaju 10 čvorova, svaki sa tri stepena slobode, i mogu biti orijentisani u bilo kojem pravcu.

Širina konačnih elemenata u ZUT 1 i ŠAV zonama iznosila je 2 mm, u ZUT 2 zoni 5 mm, u osnovnom materijalu u blizini ZUT zona 10 mm, dok je u ostatku rešetkastog nosača širina konačnih elemenata bila 20 mm, što je prikazano na slici 10. Zazor između dijagonale i pojasa modelovan je na način da se prenos sile ostvaruje isključivo preko zavara.

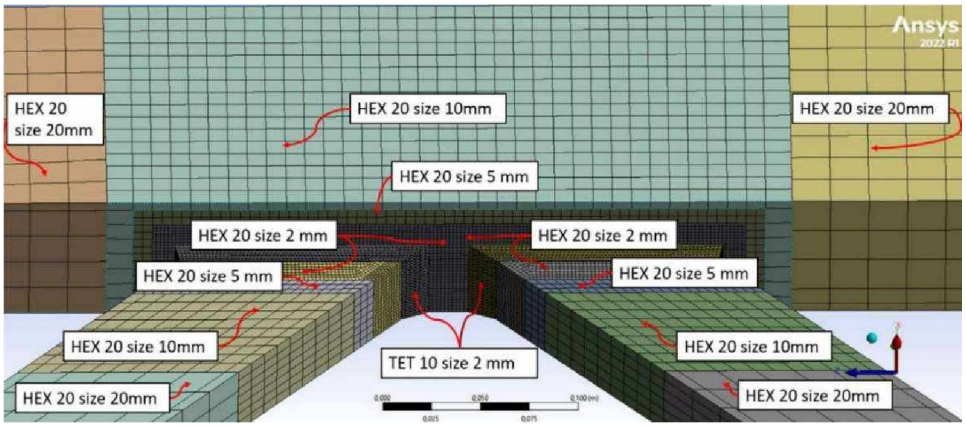

Slika 10. Konačni elementi SHS K čvora.

Analizom rezultata, identifikovana su kritična područja koncentracije napona i deformacija. Dobijeni rezultati su upoređeni sa eksperimentalnim mjerenjima radi validacije modela. Analiza je pokazala visok stepen slaganja, čime su modeli potvrđeni kao pouzdani za dalje parametarske studije.

Analitički model

Analitičko istraživanje u okviru ove disertacije bilo je usmjereno na razvoj pouzdanih izraza za proračun nosivosti zavarenih spojeva u aluminijumskim rešetkastim nosačima. Imajući u vidu da standard EN 1999-1-1 ne pruža dovoljno jasne smjernice za projektovanje zavarenih spojeva kod aluminijuma, korišćeni su izrazi iz EN 1993-1-8 razvijeni za čelične konstrukcije, uz njihovu prilagodbu specifičnostima aluminijumskih legura i ponašanju materijala u zoni uticaja toplote (ZUT).

Poseban fokus stavljen je na spojeve sa kvadratnim šupljim profilima (SHS), gdje je dominantan mehanizam otkazivanja plastifikacija lica pojasa. Za razvoj izraza korišćena je energetska metoda u kombinaciji sa metodom plastičnih linija tečenja (yield line method), kojom je identifikovano formiranje plastičnih mehanizama unutar spoja. Na osnovu toga definisana je funkcija unutrašnjeg rada i eksternog rada, a uslov ravnoteže korišćen za izvođenje izraza za nosivost.

Da bi se obuhvatio efekat degradacije materijala u ZUT-u, uvedeni su redukcioni koeficijenti definisani u EN 1999-1-1 koji koriguju granične vrijednosti čvrstoće u analitičkim izrazima.

Rezultati pokazuju da predloženi analitički modeli omogućavaju precizno predviđanje nosivosti zavarenih čvorova, uz odstupanja manjim od ±10% u odnosu na eksperimentalne rezultate. Ovo potvrđuje njihovu pouzdanost i pogodnost za praktičnu

primjenu, kao i za buduće unapređenje Eurokoda 9 u dijelu koji se odnosi na zavarene čvorove u aluminijumskim rešetkastim konstrukcijama.

Uporedna analiza prema Eurokod standardima

Standard EN 1999-1-1 trenutno ne nudi potpune metode za proračun zavarenih čvorova u aluminijumskim konstrukcijama kada su u pitanju efekti ZUT-a. U praksi se i dalje često koristi standard EN 1993-1-8 razvijen za čelične konstrukcije. U ovom istraživanju, izvršena je adaptacija postojećih izraza iz EN 1993-1-8 na osnovu eksperimentalnih korekcija. Novi izrazi su kalibrisani na osnovu stvarnih podataka i preporučuju se kao dopuna postojećim normama.

Zaključak

Istraživanje je potvrdilo da zavarivanje značajno utiče na smanjenje mehaničkih svojstava aluminijumskih legura, naročito u ZUT-u. Na osnovu eksperimentalnih ispitivanja, numeričke analize i analitičkog proračuna, predloženi su novi analitički izrazi za proračun zavarenih čvorova u skladu sa standardom EN 1999-1-1. Disertacija doprinosi razvoju naučnih saznanja o ponašanju zavarenih čvorova i ima praktičnu primjenu u projektovanju laganih aluminijumskih konstrukcija u građevinarstvu, energetici, transportu i industriji.

Preporuke za buduća istraživanja

Buduća istraživanja treba da se fokusiraju na ponašanje spojeva pod zamorom, kao i na primjenu naprednih tehnika zavarivanja poput trenjem-uslovljenog zavarivanja (FSW) koje pokazuje manji uticaj na degradaciju mehaničkih osobina. Takođe, potrebno je proširiti istraživanja na druge tipove legura i varijante geometrije čvorova, uključujući prostorne čvorove i čvorove sa ekscentricitetom.

Značaj i doprinos disertacije

Ova disertacija daje značajan doprinos razumijevanju ponašanja zavarenih aluminijumskih čvorova kroz razvoj numeričkih modela i analitičkih izraza za proračun nosivosti koji su verifikovani rezultatima eksperimentalnog ispitivanja realnih konstrukcija. Novi izrazi za proračun nosivosti uzimaju u obzir degradaciju materijala u ZUT-u, čime se postiže veća sigurnost i tačnost u projektovanju. Rezultati ovog rada mogu se direktno primijeniti za projektovanje aluminijumskih rešetkastih konstrukcija.

Naučna oblast: Građevinarstvo

Uža naučna oblast: Konstrukcije

Abstract

The growing demand for lightweight, corrosion-resistant, and sustainable construction materials has led to the increased use of aluminum alloys in civil engineering. Among the structural applications, aluminum truss systems offer significant advantages in terms of reduced self-weight, durability, and simplified installation processes. However, the adoption of aluminum structures in construction sector remains limited due to a lack of comprehensive understanding of welded joint behavior—particularly in the heat-affected zone (HAZ), where significant material degradation occurs as a result of welding.

This doctoral research aims to systematically investigate the mechanical performance of welded planar joints in aluminum truss structures, with a focus on quantifying the strength reduction within the HAZ and developing reliable predictive models. The study integrates experimental, numerical, and analytical approaches to assess the structural behavior of welded joints composed of square (SHS) and circular (CHS) hollow section profiles. Particular attention is given to evaluating joint configurations commonly encountered in lattice girders, such as X and K joints.

The experimental component of this research was conducted in collaboration with the Faculty of Civil Engineering at the University of Montenegro and the Chair of Metal Structures at the Technical University of Munich. It involved the fabrication, instrumentation, and testing of full-scale welded aluminum truss specimens using EN AW-6082 T6 alloy. Mechanical characterization included tensile testing, Vickers hardness testing, and Digital Image Correlation (DIC) to capture localized strain distributions and identify plastification in the HAZ. In parallel, finite element models were developed using ANSYS software to simulate joint behavior under realistic loading conditions. These models were calibrated and validated using the experimental data.

Analytically, the research builds on and extends existing steel-based design provisions found in EN 1993-1-8, adapting them to the context of aluminum welded joints by incorporating reduction factors for the HAZ, modified yield-line models, and deformation-based limit states. The study examines chord face plastification failure mechanisms, and correlates them with geometric parameters including the brace-to-chord width ratio (β) and thickness-to-width ratio.

The results demonstrate that conventional design approaches underestimate the effects of welding in aluminum structures and may lead to unconservative predictions if HAZ softening is not accounted for. Experimental findings show up to 50% reduction in yield strength within the HAZ compared to the base material, consistent with previous studies yet quantitatively refined through extensive testing. Numerical simulations and analytical models presented herein provide improved predictive accuracy and design reliability.

This research contributes to the body of knowledge by proposing practical design recommendations and validated analytical expressions tailored to welded aluminum joints. These findings support the enhancement of Eurocode 9 (EN 1999-1-1) and promote safer, more efficient utilization of aluminum in structural engineering. The work is particularly relevant for applications involving long-span roofs, transport infrastructure, offshore platforms, and prefabricated systems in corrosive or hard-to-access environments. Ultimately, the study offers a pathway for integrating aluminum more confidently into modern load-bearing structural systems.

Scientific area: Civil Engineering
Specific scientific area: Structures

Table of Contents

1 Introduction

1.1 Background and motivation for this research

Aluminum structures [1] are used in modern construction due to their low weight, corrosion resistance, and aesthetic qualities. They are particularly important in the construction of lightweight truss structures, where they enable a reduction in the overall mass of the building and an increase in load-bearing capacity, while simultaneously offering material savings and reduced maintenance costs. However, one of the major challenges in designing and constructing aluminum structures is the reliable assessment of the mechanical behavior of welded joints, especially in the heat-affected zone (HAZ).

Welding is one of the methods commonly used for joining aluminum structural elements, but it simultaneously causes local changes in microstructure and mechanical properties due to heat input. These changes can significantly reduce the load-bearing capacity of the joints and affect the overall stability of the structure.

The objective of this research is to thoroughly investigate the mechanical behavior of welded planar joints in aluminum truss structures through experimental, numerical, and analytical methods. The expected results will contribute to a better understanding of the impact of welding on the load-bearing capacity of joints, which can have direct implications for improving European standards for the design of aluminum structures.

Furthermore, there is a significant need for the development of reliable calculation methods that will enable more efficient use of aluminum in construction. The use of numerical models based on the finite element method provides the opportunity for more accurate assessment of joint capacity and optimization of their shape and dimensions. Experimental testing is necessary to verify the numerical models and ensure their applicability in real-world conditions.

This research will also contribute to the development of a practical guidelines for the implementation of Eurocode EN 1999-1-1, specifically in the section related to the design of welded joints in aluminum truss structures. This will enable designers and engineers to perform more reliable and efficient design of aluminum structures. In this way, the work will provide a broader scientific and practical contribution, improving the safety and economic viability of aluminum structures.

1.2 Significance of the research on welded aluminum joints

Welded joints in aluminum structures are critical elements in the transfer of loads and the overall stability of the structures. Their mechanical properties directly affect the safety and reliability of structures used in various engineering fields, including construction, transportation, energy, and aerospace industries. Research into welded aluminum joints is particularly significant due to their sensitivity to thermal changes during welding, which leads to alterations in the microstructure and mechanical properties of the material.

One of the major challenges in welded aluminum joints is the softening of the material in the heat-affected zone (HAZ), which can cause a significant reduction in the load-bearing capacity of the structure. Understanding the behavior of these joints under load is crucial for optimizing welded aluminum structures and developing relevant standards that will make them more competitive in the market.

Further research in this area contributes to the development of more accurate numerical models based on the finite element method (FEM), which enable the prediction of welded joint behavior under real conditions. Experimental testing is essential for validating these models and developing reliable design recommendations. The results of this research could have applications in improving Eurocodes and national standards for the design of aluminum structures.

Moreover, the significance of this research extends to the economic aspect. Improved efficiency of welded joints could lead to reduced material costs, increased durability of structures, and lower maintenance requirements. This is especially important in areas where structures are subjected to high loads and extreme conditions, such as bridges, platforms, long-span structures in inaccessible locations, and constructions exposed to aggressive environments.

Ultimately, research into welded aluminum joints enables advancements in the safety, durability, and sustainability of modern structures. The development of new methods to improve the performance of these joints contributes to the broader acceptance of aluminum as a construction material in the modern engineering.

1.3 Objective of the research

The objective of this research is to define clear guidelines and recommendations that enable a reliable, efficient, and rational interpretation of the load-bearing capacity of planar joints in aluminum truss structures.

This objective was achieved through a detailed analysis of the mechanical behavior of welded aluminum joints in truss structures using experimental, numerical, and analytical methods. The focus of the research is on understanding the impact of welding on the reduction of load-bearing capacity in the heat-affected zone (HAZ) and the optimization of design methods for a more reliable application of aluminum as a construction material in civil engineering.

The main aspects of this research include:

- Experimental testing of welded aluminum joints to determine changes in mechanical properties, particularly in the HAZ.
- Development of numerical models based on the finite element method (FEM) for analyzing the stress-strain state of welded joints.
- Validation of numerical models through experimental results and the development of improved methods for predicting the behavior of welded joints.
- Formulation of design recommendations for welded aluminum planar joints in accordance with existing codes and standards, with the potential for enhancing Eurocode 9 (EN 1999).

The results of this research will contribute to a better understanding of the behavior of aluminum alloys during and after welding, optimizing and increasing the safety and efficiency of aluminum structures. The ultimate goal is to improve engineering practices in the design and execution of aluminum truss structures through reliable experimental and numerical methods.

1.4 Hypothesis

The load-bearing capacity of welded planar joints in aluminum truss structures can be more precisely defined by redefining the expressions for the load-bearing capacity of welded joints in steel structures defined in the EN 1993-1-8.

1.5 Methods and research plan

The research methodology encompassed the application of analytical, numerical, and experimental methods (Fig. 1), which included:

- Collection and systematization of available literature and data on previous research in this field.
- Field research through practical experience at the Institute for Civil Engineering d.o.o., focusing on the most common aluminum joints in practice and the use of aluminum structures in Montenegro.
- Numerical modeling of joints using the ANSYS software package, applying the finite element method.
- Experimental testing of truss joints of aluminum structures in the laboratory of the Faculty of Civil Engineering, University of Montenegro, and at Chair of Metal Structures at the Technical University of Munich.
- Statistical data processing.
- Analytical modeling of joints according to the Eurocode for joints in steel truss structures.
- Analysis of the results obtained from the experiments, numerical method results, and the analytical model according to the Eurocode.
- Synthesis of the obtained results and conclusions in the form of guidelines for the design of joints in aluminum truss structures.

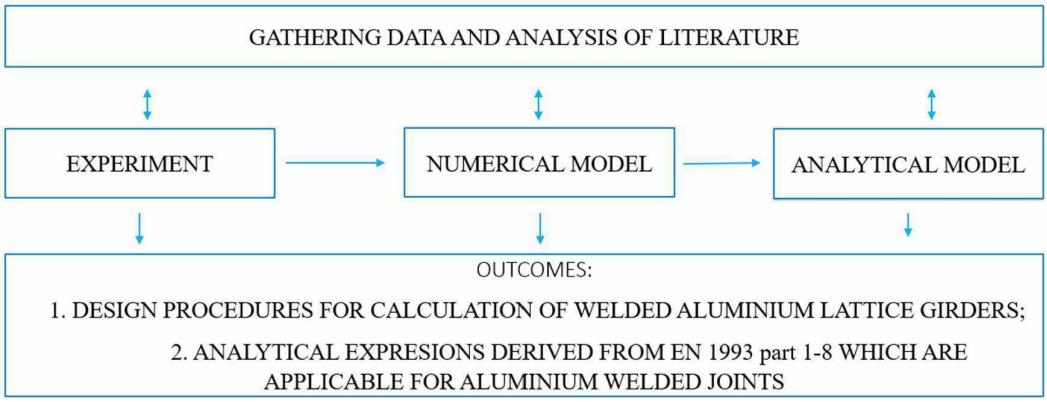

Fig.1: Research plan

2 General information on aluminum structures

Pure aluminum [2], as a material, does not possess strong mechanical properties; however, when combined with other metals as alloying elements (Zn, Mg, Si, and Cu), it can achieve mechanical properties comparable to steel, while being approximately 2.5 times lighter than steel. The volumetric mass of aluminum alloys ranges from 2600 to 2800 kg/m^3.

Aluminum and its alloys, due to their physical and mechanical characteristics, have significant applications in all areas of industry: food processing, electrical industry for the production of power cables and overhead lines, automotive and aerospace industries, and, of course, in construction as a building material.

Aluminum alloys can achieve a tensile strength of up to 500 MPa (7000 series) , making them comparable to high-quality steel. Additionally, aluminum alloys are known for their exceptional resistance to corrosion. The recycling of aluminum is a simple and cost-effective process, which makes it an environmental frendly material in the construction industry (EN 1999-1-1:2019, Eurocode 9: Design of Aluminum Structures - Part 1-1: General Rules).

Aluminum and its alloys also demonstrate remarkable resistance to brittle fracture at low temperatures [3]. The tensile strength of aluminum alloys does not depend on the duration of exposure to low temperatures, nor is it reduced when the temperature increases again. The increase in tensile strength of aluminum alloys at low temperatures is negligible up to -50°C but rises significantly at temperatures below -100°C [3].

Aluminum structures are 70% lighter compared to a reference steel structure and 90% lighter than reinforced concrete structures. This weight saving is possible and depends on the ratio of permanent and variable loads. The greater the ratio of permanent to variable load, the greater the weight savings [2]. High-span structures with a large permanent-to-variable-load ratio are the main candidates for the rational (cost-effective) use of aluminum as a structural material [2].

As a metal, aluminum has good corrosion resistance compared to steel. A prime example of its corrosion resistance is the roofing of the dome of St. Jacob's Church in Rome, which represents one of the first uses of aluminum in construction. The thickness of the

aluminum sheets on the roof is 1.25 mm, and after more than 110 years, the thickness of the sheet has decreased by only 0.13 mm. The primary reason for aluminum's good resistance to corrosion is the layer of aluminum oxide that always forms on the surface of the element exposed to atmospheric conditions [2].

As the first major structural project in civil engineering to utilize aluminum as the primary construction material, the Arvida Aluminum Bridge, completed in 1950 in Saguenay, Québec, marked a significant milestone in the field. This groundbreaking achievement marked a significant departure from traditional steel-based structures, showcasing aluminum's potential in large-scale infrastructure projects. Spanning 153.6 meters over the Saguenay River, the bridge features a 91.5-meter parabolic arch, which demonstrated the material's capabilities in long-span applications. The use of aluminum, specifically the Alcan 26S-T alloy, resulted in a bridge that weighed only 163 t — approximately half the mass of a comparable steel bridge—thus reducing the overall dead load and improving seismic performance. This innovative project highlighted the advantages of aluminum, leading the way for its broader adoption in civil engineering applications globally [4].

Fig. 2: Arvida Bridge

Due to its softness, complex shapes can be produced in the manufacturing process without complex technology through casting or extrusion. This allows fast production of wide range of profiles in various sizes, which is advantageous for designers when selecting the appropriate profile during the design process [2].

In construction, aluminum alloys are used for [1]:

- Roof structures for medium and large spans;
- Facade constructions;
- Structures in aggressive environments;
- Structures with moving parts (pontoon bridges, movable bridges);
- Structures for storage and transport of materials that aggressively affect steel (tanks, pipelines...);
- Structures located in hard-to-reach areas that are difficult to maintain (lighthouses, overhead power lines...);
- Structures in areas with extremely low temperatures;
- Prefabricated and demountable structures for various purposes;
- Existing structures where an increase in variable load is anticipated.

2.1 Disadvantages of aluminum construction applications

Although construction [5] with aluminum alloys as structural material offers numerous advantages, its application in engineering practice faces several challenges, particularly in terms of experience in design and execution. While aluminum alloys can achieve tensile strengths comparable to steel, their elastic modulus is significantly lower, and this limitation cannot be corrected. The elastic modulus of aluminum alloys ranges from 69 GPa to 72 GPa, which may affect the design of structures that require high bending and stress forces. However, through intelligent design, optimizing the material's strength in tension and compression, and limiting exposure to bending, it is possible to design structures with structural integrity comparable to those made of steel. The use of hollow profiles, such as tubular and box profiles, reduces exposure to bending and torsional deformation, while maintaining the dominant influence of first-order effects from tension and compression.

Another challenge is the development of weakened zones during welding, particularly in the heat-affected zones (HAZ) in many aluminum alloys. These zones can reduce the load-bearing capacity of the structure by up to 50%. However, alloys in the O temper

(annealed state) and T4 temper (solution-annealed, naturally aged) do not exhibit these weaknesses, making them more suitable for certain applications [6].

Corrosion of aluminum [2] and its alloys is also possible. Atmospheric corrosion can occur due to the action of rain or condensation, forming an electrolyte in a very thin layer on the metal surface, which may lead to the breakdown of the aluminum oxide passive layer. However, this process is typically short time, as there is usually enough oxygen to reactivate the oxidation process and restore the passive oxide layer. The most common form of atmospheric corrosion is pitting corrosion, which typically occurs in industrial and coastal areas.

Galvanic (contact) corrosion [2] occurs when aluminum comes into contact with a metal that has a different electrochemical potential. In the presence of an electrolyte, a galvanic current is generated, leading to the degradation of the electrochemically negative material. This type of corrosion often occurs when aluminum comes into contact with steel, and such joints must be specially treated. To reduce galvanic corrosion, it is recommended to carefully select materials whose contact will not lead to corrosion, apply protective coatings, and use materials such as zinc, cadmium, and magnesium in aggressive environments.

2.2 Aluminum alloys

Aluminum alloys are classified into two main groups: wrought alloys and cast alloys [7]. Wrought alloys are mechanically processed to achieve the desired shape, while cast alloys are melted and poured into molds that define their shape. Additionally, alloys can be further categorized based on their primary alloying element. In construction, the most commonly used alloys are those containing alloying elements such as copper (Cu), manganese (Mn), silicon (Si), magnesium (Mg), and zinc (Zn).

Aluminum alloys [7] can also be classified into heat-treatable and non-heat-treatable categories. Heat-treatable alloys include compositions such as Al-Mg-Si and Al-Zn-Mg, while non-heat-treatable alloys are typically those containing manganese and magnesium [7].

Given the wide variety of aluminum alloys, a standardized nomenclature system is essential. In the European Union, the EN 573-1 [8] regulation provides this system,

consisting of four parts. The system uses a four-digit numerical code with the prefix EN AW (Aluminum Wrought). "EN" refers to the European standard, "A" indicates aluminum, and "W" stands for wrought. The first digit in the code identifies the dominant alloying element, while the remaining digits provide further details about the alloy's properties.

Table 1. presents the cast and wrought alloys based on their alloying elements and their corresponding designations according to the EN 573-1 standard [8]. Wrought alloys are shown in bold letters, while cast alloys are displayed in italics [8].

Tab.1: Composition of Aluminum Alloys by Alloying Elements [8].

	Mn	Mg	Si	Zn	Cu
Mn	AlMn 3xxx				
Mg	AlMgMn 5xxx	AlMg 5xxx	AlMgSi 6xxxx		
Si		AlSiMg 6xxx	AlSi 4xxx		AlSi/Cu 4xxx
Zn		AlZnMg AlZnMgCu 7xxx			
Cu		AlCuMg 2xxx			AlCu 2xxx

According to EN 573-1 [8], wrought aluminum alloys are grouped into the following series, designated "EN AW," where the first digit denotes the principal alloying element:

- EN AW 1xxx – Aluminum (Al)
- EN AW 2xxx – Copper (Cu)
- EN AW 3xxx – Manganese (Mn)
- EN AW 4xxx – Silicon (Si)
- EN AW 5xxx – Magnesium (Mg)

- EN AW 6xxx – Magnesium and silicon
- EN AW 7xxx – Zinc (Zn)
- EN AW 8xxx – Other elements

Alloys in the EN AW 6xxx series contain magnesium and silicon in proportions that form the Mg_2Si phase. They combine good corrosion resistance, weldability, and machinability, although their ultimate strength is lower than that of the 2xxx and 7xxx series. Consequently, they are widely employed as structural materials in construction [7, 8].

According to EN 1999-1-1 [6], aluminum alloys are further classified into three durability categories—A, B, and C—based on their expected service life. Assigning the correct durability category is essential for specifying appropriate protective measures for the structure. In cases where multiple alloys of differing durability categories are used in the same structure, the alloy with the lowest durability classification determines the required protection level.

It is also necessary to distinguish alloy designations by their temper or condition; see Table 2 for details [6].

Tab.2: Temper (Condition) Designations for Aluminum Alloys [6].

Designation	Meaning
F	*As-fabricated* – No deliberate thermal or mechanical treatment performed after initial fabrication.
O	*Annealed* – Heat-treated to achieve the lowest strength, maximum ductility, and optimum dimensional accuracy.
H	*Strain-hardened* (cold-worked) – Strengthened by plastic deformation at ambient temperature.
T	*Heat-treated* – Subjected to thermal processes (sometimes combined with cold working) to develop a stable temper through artificial or natural aging.

W	*Solution-heat-treated* – Solution annealed and quenched to produce a supersaturated solid solution, typically followed by natural aging to reach temper stability.

In the annealed condition (O), three sub-designations—O1, O2, and O3—are defined, corresponding to increasing degrees of annealing and ductility [10]. Strain-hardened tempers (H) carry one to three numerical digits after the "H" symbol (e.g., H1, H116), indicating the extent and sequence of cold working; these designations apply exclusively to non-heat-treatable alloys [10]. Heat-treated tempers (T) denote alloys that have undergone solution heat-treatment and quenching, often followed by artificial or natural aging, and may also include subsequent cold deformation steps to achieve the final temper [10]. Table 3 summarizes the principal metallurgical temper designations for aluminum commonly used in structural engineering applications [6].

The metallurgical temper designations used for aluminum in structural applications [6] are summarized in Table 3 below, along with their meanings:

Tab.3: The metallurgical temper designations used for aluminum in structural applications [6]

Temper	Description
H111	Annealed through appropriate working procedures, with a slight degree of cold work.
H12	Hard wrought – 1/4 hardened.
H14	Hard wrought – 1/2 hardened.
H18	Hard wrought – 4/4 hardened. (fully hardened)
H22	Strain hardened and partially aged – 1/4 hardened.
H32	Strain hardened and stabilized – 1/4 hardened.
H42	Strain-hardened and painted or lacquered - 1/4 hardened.
T4	Solution-heat-treated and naturally aged.

T5	Cooled from an elevated temperature shaping process and then artificially aged.
T6	Solution heat-treated and then artificially aged.
T61	Solution-heat-treated and intentionally under-aged to improve machinability (not fully artificially aged).
T66	Solution heat-treated and then artificially aged - mechanical property level higher than T6 achieved through special control of the process (6000 series alloys).
T651	Solution heat-treated, stress-relieved by controlled stretching (permanent set 0.5% to 3% for sheet, 1.5% to 3% for plate, 1% to 3% for rolled or cold-finished rod and bar, 1% to 5% for hand or ring forging and rolled ring) and then artificially aged. The products receive no further straightening after stretching.
T7	Solution heat-treated and then artificially overaged.

These temper designations ensure that engineers select the appropriate combination of strength, ductility, and dimensional stability for aluminum structural components. The criteria for selecting the appropriate alloy are summarized in Table 4, based on load-bearing capacity, weldability, corrosion resistance, machinability, and finish quality.

Tab. 4: Selection criteria for aluminum alloys based on mechanical, fabrication, and durability properties [9].

Criterion	Deformation-hardened			Age-hardened		
	1xxx	3xxx	5xxx	6xxx	2xxx	7xxx
*UTS (MPa)**	50–150	100–260	100–340	150–310	300–450	320–600
TIG/MIG welding	Allowed	Allowed	Allowed	Allowed	Not allowed	Not allowed
Anodizing (surface finish)	Allowed	Not allowed	Allowed	Allowed	Not allowed	Not allowed

Corrosion resistance	Good	Good	Very good	Very good	Poor	Poor
Extrusion machinability	Good	Good	Poor	Very good	Poor	Poor

* UTS = Ultimate Tensile Strength

The EN AW-6xxx series is by far the most widely used group of aluminum alloys in structural engineering, owing to its excellent combination of formability, strength, and corrosion resistance. These alloys respond exceptionally well to thermo-mechanical processing (rolling, extrusion, and forging) and maintain high resistance to atmospheric and salt-water corrosion. In addition, they exhibit good weldability under gas-tungsten arc (TIG) and brazing processes, and they can be cold-formed (for example, bending or deep-drawing) in both the fully annealed (O) and the solution-annealed, naturally aged (T4) conditions [2].

Magnesium and silicon are the principal alloying elements of the 6xxx series. Magnesium lowers the melting point to approximately 541 °C, increases overall strength, and improves corrosion resistance in marine environments, while silicon further reduces the melting point and enhances ductility. Together, these elements form magnesium silicide (Mg_2Si), which enables the series' characteristic age-hardening response [9].

Because 6xxx alloys achieve their best mechanical and physical properties through a controlled sequence of solution heat-treatment, quenching, and artificial aging, they fall into the category of thermo-mechanically treatable alloys [10]. Artificial aging is typically conducted at temperatures between 100 °C and 200 °C, with each step of the process—solution annealing, quenching, and aging—having a direct and predictable effect on the final strength, toughness, and dimensional stability of the alloy.

2.3 Mechanical properties

The elastic (Young's) modulus of pure aluminum is 69 GPa, with typical aluminum alloys ranging from 69 GPa to 72 GPa; hence, a value of 70 GPa is conventionally adopted for structural calculations. This stiffness is roughly one-third that of conventional structural steel, which means aluminum-alloy members exhibit significantly greater elastic deflections and are more prone to both local (e.g., flange or web buckling) and global

(e.g., overall member or frame instability) failure modes under equivalent loading conditions [11].

Tab.5: Comparison of Aluminum and Steel Properties [11]

Property	Aluminum	Steel
Density, ρ [kg/m³]	2 700	7 850
Melting point [°C]	658	1 450–1 530
Coefficient of linear thermal expansion, α [K^{-1}]	24×10^{-6}	12×10^{-6}
Specific heat capacity, c [cal · g^{-1} · $°C^{-1}$]	0.225	0.12
Thermal conductivity, k [cal · cm^{-1} · s^{-1} · $°C^{-1}$]	0.52	0.062
Electrical resistivity, ρ_e [μΩ · cm]	2.84	15.5
Young's modulus, E [N/mm² (MPa)]	68 500	206 000

Aluminum's lower density and melting point, combined with its higher thermal expansion and conductivity, distinguish it sharply from steel. Its significantly lower Young's modulus (about one-third compared to the steel) also drives the need for careful consideration of deflections and stability in aluminum structures.

The true Poisson's ratio for aluminum is approximately 0.33, higher than the commonly adopted value of ν = 0.30, which was first measured in a 1948 Cambridge study [12]. The shear modulus for aluminum alloys is G = 27 GPa[6].

Yield strength varies widely across aluminum alloys, from as low as about 10 MPa for commercially pure aluminum to nearly 500 MPa for high-strength 7xxx-series alloys. Because aluminum's stress–strain response is distinctly nonlinear, a clear yield "knee" is often absent. For design, therefore the conventional 0.2 % offset yield strength is used, f_0, defined in EN 1999-1 as the stress at which 0.2 % permanent (plastic) strain occurs [6].

According to EN 1999-1-1 [6], the complete stress–strain curve for aluminum alloys is approximated by the Ramberg–Osgood expression:

$$\varepsilon = \frac{\sigma}{E} + 0.002 \left(\frac{\sigma}{f_{0.2}}\right)^n$$

where n is the strain-hardening exponent that governs the curvature of the stress–strain curve in the post-yield region. The value of n depends on the specific alloy and temper, and is typically tabulated alongside other mechanical properties.

In Fig. 3, experimentally measured σ–ε curves for aluminum alloys 7020 T6 and 6060 T5 are compared with those of steels Č0561 and Č0361 [13].

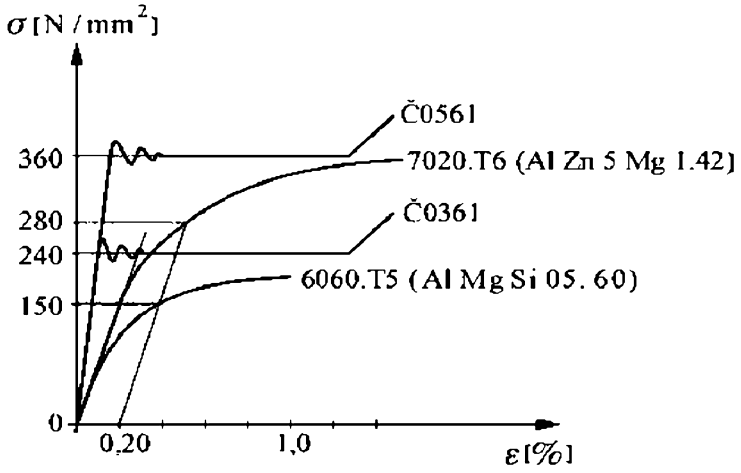

Fig.3: True Stress–Strain Curves of Aluminum Alloys EN AW-7020 T6 and EN AW-6060 T5 Compared to Steels Č0561 and Č0361 [13]

Fig. 4 illustrates a family of Ramberg–Osgood curves for different values of n. These comparisons underscore both the lower stiffness and the more gradual yield transition characteristic of aluminum alloys, forming more accurate deformation and stability assessments in structural design [6].

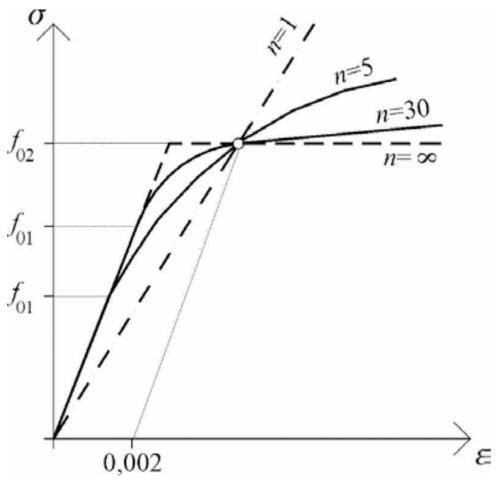

$$n = \frac{\ln 2}{\ln\left(f_{02} / f_{01}\right)} \tag{1}$$

$$\varepsilon = \frac{\sigma}{E} + 0{,}002\left(\frac{\sigma}{f_{02}}\right)^{n} \tag{2}$$

Fig.4: Ramberg–Osgood model of the σ–ε curve [6]

Fig. 5 presents the elastic modulus E and corresponding load-bearing parameters for aluminum alloys EN AW-5083 and EN AW-6082, both within the heat-affected zone (HAZ) and in the base material outside the HAZ [14]. These data illustrate the reduction in stiffness and strength induced by welding, quantifying the drop in the Yield and Ultimate Strength within the HAZ compared to unaffected regions. Such comparisons are essential for accurately modelling welded connections and ensuring the safety and

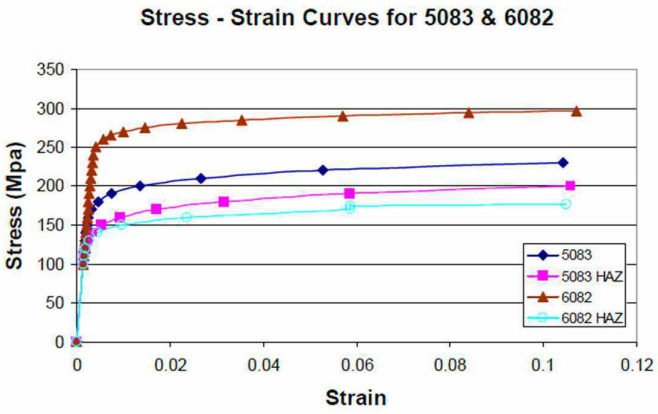

serviceability of aluminum structures.

Fig.5: Stress–Strain Curves for EN AW-5083 H111 and EN AW-6082 T6 [14]

2.4 Hollow-section truss girders

Hollow-section trusses are widely used in both bridge and building construction for elements such as stiffeners, roof beams, floor girders, crane runways, and bracing systems. These hollow-section structures (HSS – Hollow Section Structures) employ circular (CHS), square (SHS), or rectangular (RHS) hollow sections. Compared to traditional hot-rolled open-section trusses, HSS trusses offer several key advantages [15]:

- Enhanced load capacity: Hollow sections have uniform geometric properties about both principal axes, and they exhibit significantly higher axial compressive strength than comparable open profiles.
- Material efficiency: The uniform mass distribution around the centroid reduces slenderness for a given span and loading, often yielding up to a 25 % weight saving. Larger radii of gyration in HSS profiles contribute to lower effective slenderness and lighter members.
- Reduced aerodynamic drag: The streamlined cross-section of hollow profiles minimizes wind, water, and wave loads compared to open-section members.
- Space for infill: Filling the interior of a hollow section with concrete can increase both fire resistance and load capacity without altering the external dimensions.
- Corrosion-protection savings: With up to two-thirds less perimeter than equivalent open sections, HSS members require up to 40 % less coating area, reducing maintenance costs.
- Faster installation: Lighter, compact sections simplify handling, transport, and on-site assembly relative to conventional truss elements.

Statically, hollow-section trusses are most often modelled as simply supported or continuous beams. Their depth depends on span, loading, and allowable deflection; a span-to-depth ratio of 10–15 is typically recommended.

When designing aluminum HSS trusses, particular attention must be paid to the ultimate strength of both tension and compression members, stability against local and global

buckling, the behavior of welded connections, and the effects of welding heat on member capacity.

2.5 Welded connections

The simplest method for connecting elements in a truss structure made of hollow section profiles is direct welding of brace members to the chord members. In addition to this, connections with welded gusset plates attached to the chord allow the use of bolts within the truss joint as an alternative fastening method [16].

Welded joints in truss structures composed of hollow sections can be categorized as follows [17], [18]:

- Direct connections – either unreinforced or reinforced – where brace members are welded directly to the chord.
- Indirect connections, where both chords and brace members are connected via an intermediate gusset plate, using bolts, rivets, or welds.

Due to the unique material behavior of aluminum alloys—except those in the annealed (O) or T4 temper conditions, the calculation of welded connections in aluminum is not specifically covered in EN 1999-1-1 [6]. Instead, designers often rely on the provisions given in EN 1993-1-8 [19], which is the design standard for welded connections in steel structures. This standard defines the most common joint types and serves as a reference for aluminum by analogy.

Compared to indirect welded joints, directly welded connections provide greater structural integrity and technical safety. The force transfer occurs directly from one member to another, whereas in indirect welds, the force path is routed through a gusset plate [21].

Based on the geometry of the connected members, direct welded joints (Fig. 6) are typically classified into:

- Planar joints: X, T, Y, N, and K joints;
- Special joints: KT, DK, DY joints;
- Spatial joints: XX, TT, KK joints [21].

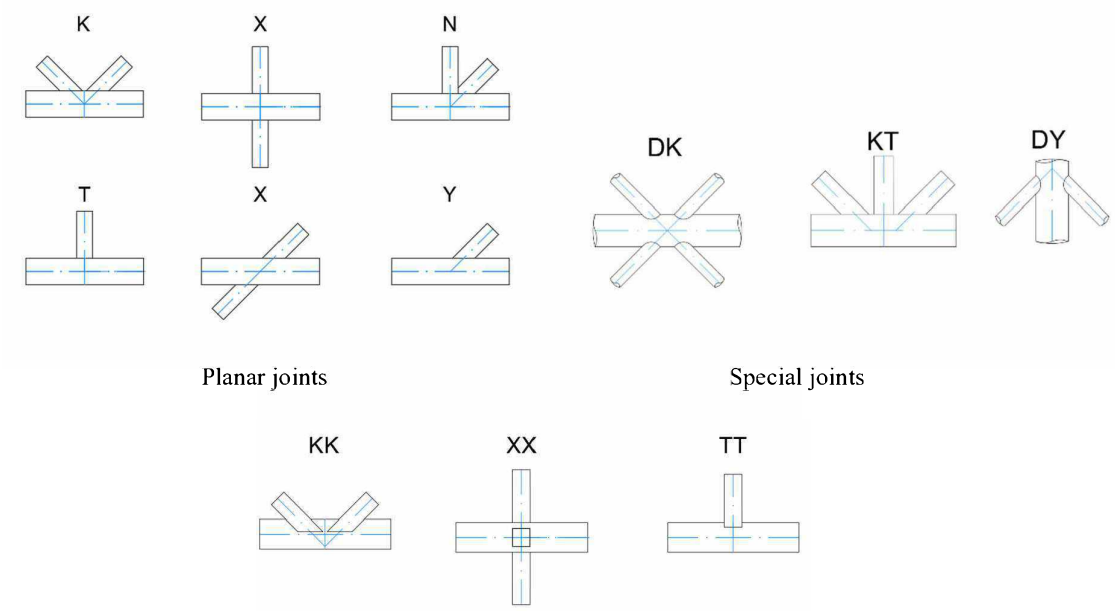

Fig.6: Welded joints geometrical configurations [21]

The configuration of a welded joints, beyond its geometric form, also depends on parameters such as gap (+g), overlap (λ = –g), eccentricity (±e), and the inclination angle of the brace members (θ_i), as well as the internal force distribution within the joint (Fig. 8) [21]. This can be illustrated through typical examples of K-, Y-, and X-type joints (Fig. 7).

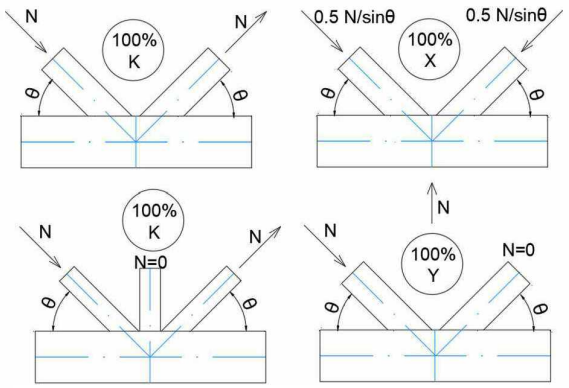

Fig.7: Welded Joint Configurations [21]

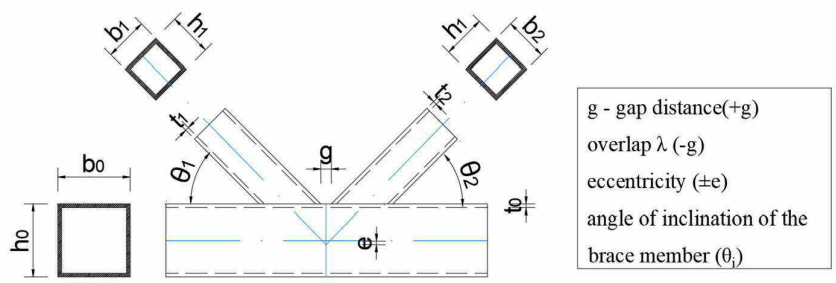

Fig.8. Geometric Parameters Required for Determining Joint Load Bearing Capacity [21]

The joint eccentricity (±e) arises from the formation of a gap between adjacent brace members or their overlap, typically introduced to increase the joint's resistance or to meet fabrication requirements (such as straight cutting) [21].

Eccentricity is considered positive (+e) when the centerlines of the brace members intersect below the axis of the chord member. Conversely, it is negative (–e) when the intersection occurs above the centroidal axis of the chord member [21].

The permissible eccentricity range is defined as:

$$-0.55d_0<e<0.25d_0$$

where d_0 is the outer diameter of the hollow section [21].

Failure Modes and Analytical Failure Models for Hollow-Section Joints

The resistance of a joint section can be assessed using several design criteria, the most commonly applied being:

- (a) Ultimate limit state (ULS)
- (b) Deformation limit state
- (c) Visual identification of cracks

The ultimate limit state is typically well defined for members under compression, where the stress–strain (σ–ε) diagram shows a clear peak followed by a decline in strength with increasing deformation [20]. However, for some welded connections, the σ–ε response may not show a distinct peak. Instead, the strength may continue to increase with strain, leading to a limit state defined by excessive deformation rather than a loss of strength [21].

To ensure safety in such cases, particularly for joints with limited ductility, the compressive ultimate load is adopted as the governing design criterion [21].

To further control joint behavior, a deformation limit state is introduced, defined using the width (b_0) or diameter (d_0) of the chord member. Based on the work of Lu et al. (1994) [22], widely adopted in current design standards, the following strain limits apply:

- 3% of b_0 for square (SHS) and rectangular (RHS) hollow sections
- 3% of d_0 for circular (CHS) hollow sections

These limits are based on the understanding that serviceability limit states, such as surface cracking, are not critical in determining connection strength. It is assumed that visible cracking will not occur under typical service conditions [21].

The deformation limit is typically assessed based on localized denting or bulging of the chord at the intersection with brace members [21].

For serviceability limit, a more conservative strain limit is defined [21]:

- 1% of b_0 for SHS and RHS profiles
- 1% of d_0 for CHS profiles

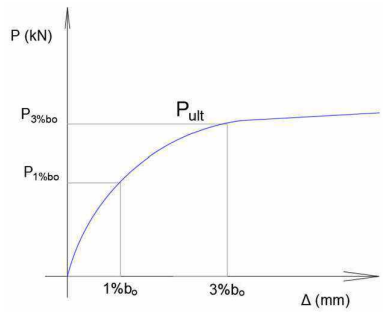

Fig. 9: Adopted values for the serviceability and ultimate limit states [21]

2.6 Primary failure modes in hollow circular section joints

By analyzing how loads are transferred within a joint, it is possible to identify critical failure locations and corresponding failure modes. These modes are governed by the local stiffness distribution and material properties, which together determine the joint's behavior under load. The lowest load that causes failure at any critical location defines the ultimate load-bearing capacity of the joint [21].

Experimental studies on the behavior of welded joints in truss girders composed of hollow sections, notably those by Wardenier and Stark (1978) and Kurobane (1980/81), have shown that the failure mechanism depends on several factors. These include the type of joint, geometry and dimensions of the chord and brace members, key geometrical parameters (β, γ, τ, g, λ_{ov}, θ), the type and magnitude of loading in the chord, and the material quality of the steel used [7].

Depending on these variables, joint failure may occur through one or more of the following mechanisms [21] (see Fig. 10):

- Chord face plastification: Plastic failure of either the outer face of the chord or its entire cross section due to concentrated loading from the brace;
- Punching shear failure: Local shear rupture of the chord wall under the brace, typically manifesting as a crack that leads to separation of the brace from the chord;
- Brace failure with reduced effective width: Fracture in the brace member itself, often initiated by weld cracking or rupture due to a reduced effective area for load transfer;
- Chord shear failure: Overall shear failure of the chord cross section, particularly under high axial or out-of-plane loading;
- Local buckling: Instability and local deformation (buckling) of either the brace or the chord wall in the region of the joint;
- Chord sidewall or web failure: Localized yielding, crushing, or instability (e.g., denting or buckling) of the side walls or internal webs of the chord beneath compressive brace loading—especially critical in thin-walled or heavily loaded members.

These failure modes reflect the complex interaction between member geometry, loading conditions, and material response, and must be carefully considered in the analytical and numerical modeling of hollow-section joints.

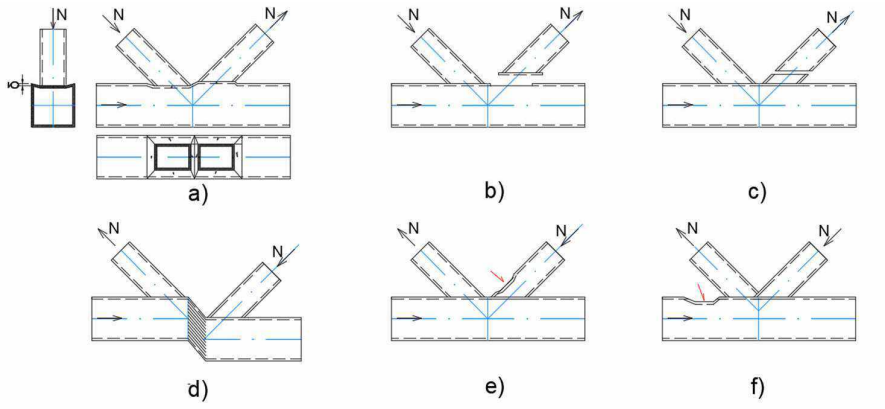

Fig. 10: Failure Modes in Truss Joints [21]

By adhering to the design recommendations and limitations outlined in [21], the occurrence of certain failure modes can be effectively prevented. For instance, selecting an appropriate weld size reduces the risk of weld cracking, while proper choice of the diameter-to-thickness (d/t) ratio minimizes the possibility of local buckling.

The most common and cost-effective method for connecting square hollow sections is through direct connections, without the use of end plates or additional fittings. This approach also proves to be the most practical in terms of maintenance and corrosion protection. Connections between box sections are straightforward to fabricate, as the member ends only require flat cuts. However, despite their fabrication simplicity, the load transfer within these joints is more complex, particularly when compared to circular hollow sections, due to non-uniform stiffness distribution within the joint region [7].

Most observed failure modes can be directly associated with analytical models, which provide a basis for evaluating the influence of various parameters on the joint's load-bearing capacity. As a result, a set of design rules has been established, grounded in both analytical modeling and extensive experimental validation [7].

For rectangular and square hollow sections (RHS/SHS), it is essential to evaluate several possible failure modes during structural design, as specified in [19]. These include:

- Local failure of the brace due to yielding or local buckling;
- Plastification of the chord face;
- Punching shear failure of the chord wall;
- Failure of the chord side walls;

- Chord shear failure.

Due to the wide variety of geometric configurations and cross-sectional orientations possible in RHS connections, multiple failure modes must often be considered. This results in a more complex verification process. However, in square hollow section (SHS) joints, it is often sufficient to check only one or two dominant failure mechanisms [19].

Typical failure modes [19] in RHS joints:

- Local brace failure usually occurs in joints with thin-walled braces and is particularly common in overlapped joints;
- Chord face plastification is the most frequently observed failure mode in T, Y, X, K, and N joints, especially when the width ratio β (brace width to chord width) is less than 0.85;
- Punching shear failure of the chord wall can develop in joints with either very low or very high β values. For this failure to occur, the brace width must exceed a certain threshold relative to the chord face dimensions;
- Chord side wall failure typically appears in T, Y, and X joints, particularly when β approaches or equals 1.0, which leads to increased loading on the chord walls adjacent to the brace;
- Chord shear failure may arise in K-type joints with gaps, especially when β is large, or in overlapped K joints where the chord has a low height-to-width ratio (h_0 / b_0).

Analytical models are used for RHS connections to represent the joint's mechanical behavior and define the key parameters that govern its capacity. These models are based on a combination of experimental testing and semi-empirical equations, which have been developed to accurately predict the load-bearing capacity of hollow-section joints. The corresponding design parameters and limit values are summarized in Tab. 5 [19].

To determine the load-bearing capacity of rectangular hollow section (RHS) joints, several analytical failure models are employed, as summarized in Tab. 6 [19]. Each model corresponds to a specific failure mechanism observed in experimental testing [19]:

- Yield Line Model: Used to evaluate joint capacity based on the plastification of the chord face;
- Punching Shear Model: Assesses failure due to shear rupture of the chord wall beneath the brace;
- Local Brace Failure Model: Captures local yielding or buckling of the brace member, typically in joints with thin-walled elements;
- Chord Side Wall Bearing or Buckling Model: Evaluates the stability or bearing capacity of the chord side walls under concentrated loading;
- Chord Shear Model: Accounts for overall shear failure of the chord cross-section under high in-plane loading.

For square hollow section (SHS) joints—within a defined range of applicability—the joint resistance can typically be assessed using a single analytical model, as outlined in Tab. 7. [19].

It this case, yield line model is the primary model for determining the capacity of SHS joints, based on the formation of yield lines and chord face plastification [19].

These models provide the foundation for rational joint design and are integrated into current design codes through semi-empirical equations calibrated against experimental data.

Tab.5: Validity Range for T, Y, X, and K Joints with CHS and RHS Braces [19]

Parameter	T, Y, or X Joints	K Joints with Overlap
Brace-to-Chord Width Ratio	RHS brace: $b_i/b_0 \geq 0.1 + 0.01 b_0/t_0$ or ≥ 0.25 CHS brace: $d_i/d_0 \geq 0.1 + 0.01 d_0/t_0$ and $0.25 \leq d_i/b_0 \leq 0.80$	
RHS Chord	Compression: class 1 or 2 and $b_0/t_0 \leq 40$, $h_0/t_0 \leq 40$ Tension: $b_0/t_0 \leq 40$ and $h_0/t_0 \leq 40$	
RHS Brace	Compression: class 1 or 2 and $b_i/t_i \leq 40$, $h_i/t_i \leq 40$ Tension: $b_i/t_i \leq 40$ and $h_i/t_i \leq 40$	
CHS Brace	Compression: class 1 or 2 and $d_i/t_i \leq 50$ Tension: $d_i/t_i \leq 50$	

Gap	N/A	$0.5(1-\beta)b_0 - g \leq 1.5(1-\beta)b_0$ and $g \geq t_1 + t_2$
Eccentricity	N/A	$e \leq 0.25h_0$
Height-to-Width Ratio	$0.5 \leq h_i/b_i \leq 2.0$	
Brace Angle	$\theta_i \geq 30°$	
Yield Strength Limit	$f_{y1} \leq f_{y0}$	$f_y \leq 0.8f_u$, $f_y \leq 460$ N/mm² (use 0.9 reduction factor if $355 < f_y \leq 460$ N/mm²)
Note: For CHS braces, multiply the above capacities by $\pi/4$ (except for the chord shear criterion), and replace b_i and h_i with d_i ($i = 1$ or 2).		

Tab.6: Load-bearing capacity for K and N Joints [19]

Joint Type	Load-bearing capacity (i = 1 or 2)
K and N Joints with Gap	Chord Face Plastification: $N_{i,Rd} = \frac{8.9 \cdot k_n \cdot f_{y0} \cdot t_0^2 \sqrt{\gamma}}{\sin\theta_i}\left(\frac{b_1 + b_2 + h_1 + h_2}{4 \cdot b_0}\right) / \gamma_{M5}$ Chord Shear: $N_{i,Rd} = \frac{f_{y0} \cdot A_v}{\sqrt{3} \cdot \sin\theta_i} / \gamma_{M5}$ $N_{0,Rd} = [(A_0 - A_v) \cdot f_{y0} + A_v \cdot f_{y0} \cdot \sqrt{(1 - (f_u b / f_u A)^2)}] / \gamma_{M5}$ Brace Member Failure: $N_i,Rd = f_{y,i} \cdot (2h_i - 4t_i + b_i + b_{e,ff}) / \gamma_{M5}$ Tear-Out Failure (for $\beta \leq (1 - 1/\gamma)$):

	$N_{i,Rd} = \frac{f_{y0} \cdot t_0}{\sqrt{3} \cdot \sin\theta_i} \left(\frac{2h_i}{\sin\theta_i} + b_i + b_{e,p} \right) / \gamma_{M5}$

For CHS brace members, multiply the above load-bearing capacities with $\pi/4$. Replace b_1 and h_1 with d_1, and b_2 and h_2 with d_2, except in the case of chord shear resistance.

$A_v = (2h_0 + \alpha \cdot b_0) \cdot t_0$

For square or rectangular brace members:

$\alpha = 1 / \sqrt{(1 + (4g^2 / 3b_0^2))}$, where g is the gap

For CHS brace members: $\alpha = 0$

Effective width:

$b_{eff} = (10 / b_0) \cdot (f_{y0} / f_{y,i}) \cdot b_i$ (limited to b_i)

$b_{e,p} = (10 / b_0) \cdot (f_{y0} / f_{y,i}) \cdot b_i$ (limited to b_i)

For coefficient k_n:

If $n > 0$ (compression): $k_n = \min(1.3 - 0.4n / \beta, 1.0)$

If $n \leq 0$ (tension): $k_n = 1.0$

Tab.7: Design Resistance for T, Y, X, and K/N Joints (Overlap and Gap) [19]

Joint Type	Design Resistance (i = 1 or 2, j = overlapped brace)
T, Y, and X Joints Chord Face Failure ($\beta \leq 0.85$)	$N_{1,Rd} = \frac{k_n \cdot f_{y0} \cdot {b_0}^2}{(1 - \beta) \cdot \sin\theta_i} \left(\frac{2\beta}{\sin\theta_i} + 4\sqrt{1 - \beta} \right) / \gamma_{M5}$

K and N Joints with Gap Chord Face Failure ($\beta \leq 1.0$)	$N_{1,Rd} = \frac{8.9 \cdot \gamma^{0.5} \cdot k_n \cdot f_{\gamma 0} \cdot t_0^2}{\sin\theta_i} \left(\frac{b_1 + b_2}{2b_0}\right) / \gamma_{M5}$
K and N Joints with Overlap (j = overlapped brace)	Brace Failure: $25\% \leq \lambda_{ov} \leq 50\%$ $N_{1,Rd} = f_{\gamma,i} \cdot t_i \left(b_{eff} + b_{e,ov} + 2h_i \frac{\lambda_{ov}}{50} - 4t_i\right) / \gamma_{M5}$ Brace Failure: $50\% < \lambda_{ov} \leq 80\%$ $N_{i,Rd} = f_{\gamma,i} \cdot (b_{eff} + b_{e,ov} + 2h_o - 4t_i) / \gamma_{M5}$ Brace Failure: $\lambda_{ov} > 80\%$ $N_{i,Rd} = f_{\gamma,i} \cdot (b_i + b_{e,ov} + 2h_i - 4t_i) / \gamma_{M5}$

Parameters:

$b_{eff} = (10 / b_o) \cdot (f_{\gamma o} / f_{\gamma,i}) \cdot b_i$ (limited to b_i)

$b_{e,ov} = (10 / b_o) \cdot (f_{\gamma,j} / f_{\gamma,i}) \cdot b_j$ (limited to b_j)

For coefficient k_n:

If $n > 0$ (compression): $k_n = \min(1.3 - 0.4n / \beta, 1.0)$

If $n \leq 0$ (tension): $k_n = 1.0$

For CHS brace members, multiply the above resistances by $\pi/4$, and replace b_1 and h_1 with d_1, and b_2 and h_2 with d_2.

Class 1 cross-sections are those capable of forming a plastic moment resistance with sufficient rotation capacity required for plastic analysis, without any reduction in load-bearing capacity [19].

Class 2 cross-sections are capable of developing the full plastic moment resistance, but their rotation capacity is limited due to the onset of local buckling [19].

2.7 Welding

Welding is a process of joining two or more similar or dissimilar materials, with or without the use of filler material, to create a homogeneous welded joint.

There are various welding techniques, including gas welding, laser welding, and friction welding. However, the most commonly used methods in structural applications are the arc welding processes known as TIG (Tungsten Inert Gas) and MIG (Metal Inert Gas) [23].

The MIG welding process involves a consumable wire electrode, typically 1.5 mm in diameter, which is continuously and automatically fed through a welding gun and melted by an electric arc [23]. The weld pool is shielded from atmospheric contamination by an inert gas, usually argon [23]. MIG welding is suitable for materials with a minimum thickness of approximately 4 to 5 mm. Its advantages include high welding speed, precision, and the ability to weld in various positions. However, the process requires expensive equipment and involves the potential hazard of shielding gases. A similar process, MAG (Metal Active Gas) welding, uses active gases such as CO_2 instead of inert gases.

In contrast, TIG welding utilizes a non-consumable tungsten electrode and an inert shielding gas, typically argon or helium. The process is generally carried out using alternating current. TIG welding allows for high-quality, aesthetically clean, and precise welds and is particularly well-suited for thin plates and sheet metal.

2.8 Heat-affected zone (HAZ)

The heat-affected zone (HAZ) refers to the region of the base material surrounding the weld that undergoes changes in mechanical and microstructural properties due to the influence of welding heat. This zone typically experiences a reduction in strength and a loss of properties originally gained through heat treatment or mechanical processing. The HAZ must always be considered in the design and structural analysis of welded components.

In the calculation of welded structures using artificially aged, precipitation-hardened aluminum alloys, it is essential to account for the reduction in mechanical properties occurring near the weld seam. An exception to this rule applies to materials in the annealed condition (O-temper), or when the material is in the as-fabricated condition (F-temper) and the design strength is based on the properties of the O-temper [6].

The reduction in strength predominantly affects the 0.2% proof stress (conventional yield strength) rather than the ultimate tensile strength. The extent of the HAZ is localized around the weld, see Fig. 11[6].

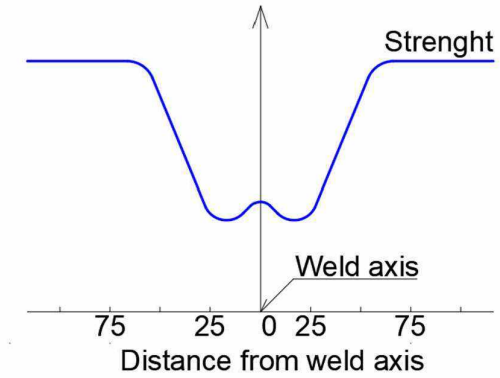

Fig. 11: Material behavior in the heat-affected zone (HAZ) [1]

According to EN 1999-1-1 [6], it is conservatively assumed that the reduction in strength is uniform across the entire HAZ, and this reduction is considered isotropic, extending equally in all directions from the weld, as illustrated in Fig. 12 [6].

Note: For distances less than $3 \cdot b_{haz}$, it is assumed that the HAZ extends across the entire width of the outer part of the joint [6].

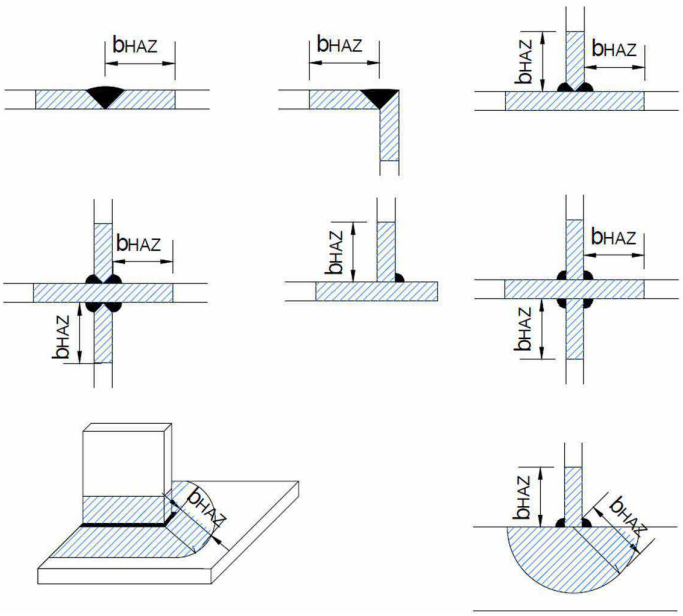

Fig. 12: Width of HAZ [6]

The influence of welding has a greater impact on the 0.2% proof stress (f_0) than on the ultimate tensile strength (f_u) of aluminum alloys [15].

To accurately determine the load-bearing capacity of welded members, the following parameters at the weld location must be considered [24]:

- The extent of material softening around the weld;
- The mechanical properties of the material within the heat-affected zone (HAZ);
- The distribution of residual stresses.

The variation in mechanical properties near the weld is typically represented by the distribution of the 0.2% proof stress, and three distinct zones can be identified in the material based on their exposure to thermal effects, Fig.13 [24]:

- Zone A – fully within the heat-affected zone (complete degradation of properties);
- Zone B – partially affected by the HAZ (intermediate reduction in strength);
- Zone C – unaffected by welding heat, retains original material properties.

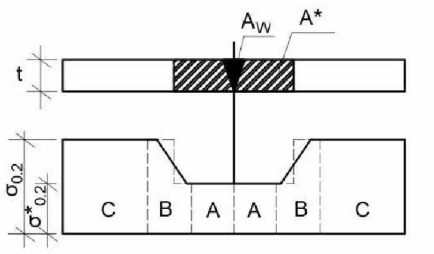

Fig. 13: Extent of the heat-affected zone (HAZ) [24]

The actual extent of the heat-affected zone (HAZ) is represented by the combined width of Zones A and B [24]. However, due to the complex nature of heat-induced microstructural changes, the stress distribution within the HAZ is difficult to model analytically. To address this, a stepwise transition model has been proposed, which allows a bit conservative but yet practical estimation of strength by acknowledging the load-carrying capacity of material regions that are only partially affected by welding.

This transitional region is referred to as the Reduced Strength Zone (RSZ) and is defined as the sum of Zone A and half of Zone B [24].

In 1962, Hill, Clark, and Brugraber [25] [24] proposed the "1-inch rule", which laid the foundation for strength assessment in welded aluminum structures. This rule was derived from hardness testing on various aluminum alloys (3003, 5052, 5154, 5356, and 6061), with welded joints of differing types and thicknesses (up to a maximum of 2 inches or 50.8 mm).

Subsequent research at the University of Cambridge refined this rule. Wong [26] [24] studied the effects of welding on 13 specimens of alloy 6082 and 8 specimens of alloy 7019 with butt welds. The tested plate thicknesses were 6.7 mm and 10 mm. Based on hardness measurements, the area of the reduced strength zone, A*, was found to correlate with the weld area (A_w) for both alloys as follows:

$$A^*=10 \cdot A_w \quad (4)$$

However, this relationship was found to be unreliable for 7000 series alloys due to the limited number of tested specimens. In 1985, Robertson [27] [24] conducted extensive testing on EN AW-6082 T6 and EN AW-7019 T6 alloys, analyzing the effects of welding on thin, medium, and thick plates with butt and fillet welds. For thin plates joined by fillet welds, he proposed the following empirical relationships:

$A^* = 9.6 \cdot A_w$ for EN AW-6082

$A^* = 13.8 \cdot A_w$ for EN AW-7019

According to EN 1991-1 [6], the influence of the HAZ is expressed through the b_{haz} distance measured from the weld, and specific values are provided depending on the welding method and material thickness (see Tab. 8).

Tab. 8: b_{haz} values based on element thickness and welding method [6]

Thickness of element t (mm)	MIG b_{haz} (mm)	TIG b_{haz} (mm)
$0<t\leq6$	20	30
$6<t\leq12$	30	30 (do 35)
$12<t\leq25$	35	35 (do 40)
$t>25$	40	40 (do 50)

To account for the loss of strength in the base material within the heat-affected zone (HAZ), reduction coefficients are introduced in the structural design equations:

$$f_{o,haz} = \rho_{o,haz} \cdot f_o$$

$$f_{u,haz} = \rho_{u,haz} \cdot f_u$$

where:

- $f_{o,haz}$ and $f_{u,haz}$ are the yield and ultimate tensile strengths within the HAZ,
- f_o and f_u are the corresponding strengths of the unaffected base material,
- $\rho_{o,haz}$ and $\rho_{u,haz}$ are reduction coefficients for yield and ultimate strengths, respectively.

2.9 Microstructure of the material in the HAZ

Aluminum alloys from the 6xxx series in the T6 temper condition exhibit a tendency for aging during welding. When examining the microstructure of a welded element made from a base metal of the 6xxx series in the T6 condition and a 5356 filler rod, three distinct zones can be observed: the Fusion Zone (FZ), the Heat-Affected Zone (HAZ), and the Base Material (BM) zone, which remains unaffected by the welding process, Fig. 14 [28].

The HAZ, acting as an isothermal transition region, can itself be subdivided into two subzones [28]. The first is the Partially Melted Zone (PMZ), located adjacent to the fusion boundary. This region approaches the melting point while experiencing a high cooling rate, resulting in natural aging processes [28].

The second subzone lies between the PMZ and the unaffected base material and is known as the Over-Aged Zone (OAZ). This subzone is exposed to a range of elevated temperatures lower than those in the PMZ, where both aging and over-aging phenomena occur [28].

Within the HAZ, the temperature ranges between the artificial aging temperature and the melting point of the alloy. Due to thermodynamic instability, this zone undergoes significant microstructural transformation, which directly impacts the material's mechanical properties [28].

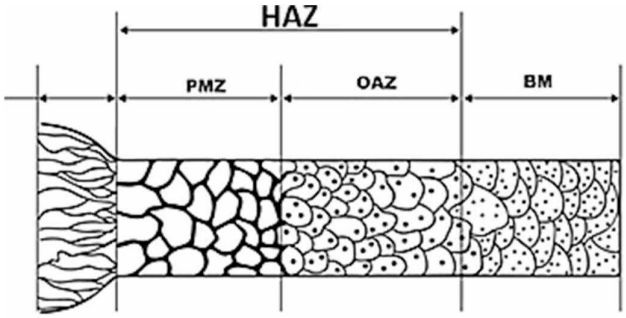

Fig. 14: Schematic Representation of the Heat-Affected Zone (HAZ) [28]

The Heat-Affected Zone (HAZ) in heat-treated aluminum alloys differs significantly from that in non-heat-treated alloys. In heat-treated alloys, the strength within the HAZ can be substantially reduced, especially when excessive heat input is applied during welding [25]. Therefore, it is critical to carefully control the welding temperature, avoid excessive preheating, and minimize the width of the weld passes, all of which help reduce overall heat input and preserve the mechanical integrity of the joint [28].

2.10 Hardness Testing

A straightforward method for assessing strength within the Heat-Affected Zone (HAZ) is through hardness testing. For the aluminum alloy EN AW-6082, which is the subject of this investigation, Dieter (1988) [30] and Matusiak (1999) [31] proposed a linear

relationship between hardness and tensile strength for Vickers hardness testing and uniaxial tensile tests. The following empirical relationships were suggested [30] [31]:

$$f_{0.2}(MPa) = 3.6HV - 81 \quad (9)$$

$$f_u(MPa) = 2.6HV + 54 \quad (10)$$

Where:

- HV is the Vickers hardness,
- $f_{0.2}$ is the 0.2% proof stress (yield strength),
- f_u is the ultimate tensile strength.

In [32], the procedure for measuring hardness within the HAZ and corresponding results are presented. Vickers hardness was measured using a 5 kg load applied along the central line of the cross-section, with 1 mm spacing between measurement points. The minimum hardness was observed within the HAZ, approximately 10 mm from the weld center. This minimum value was found to be around 65% of the hardness of the unaffected base material. Interestingly, the minimum hardness value in the base material was nearly equal to that in the weld metal.

Fig. 14 and 15 show the extent of the HAZ and the specimens used for Vickers hardness testing, while Fig. 16 presents representative hardness profiles within the HAZ for the alloys 6082-T6, 7020-T6, and 5083-H22.

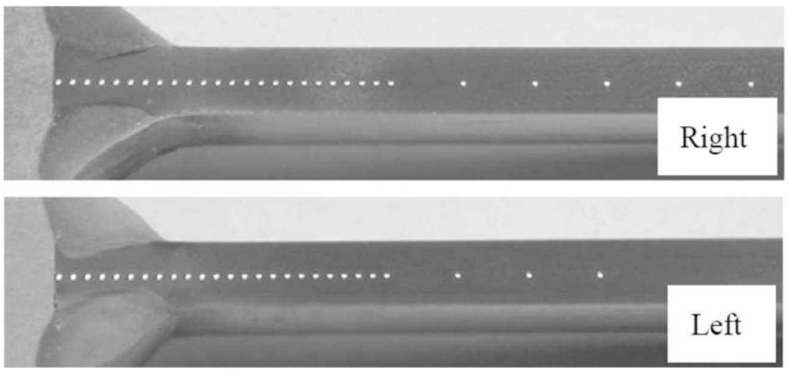

Figure 14. Extent of the Heat-Affected Zone (HAZ) Along the Member [29]

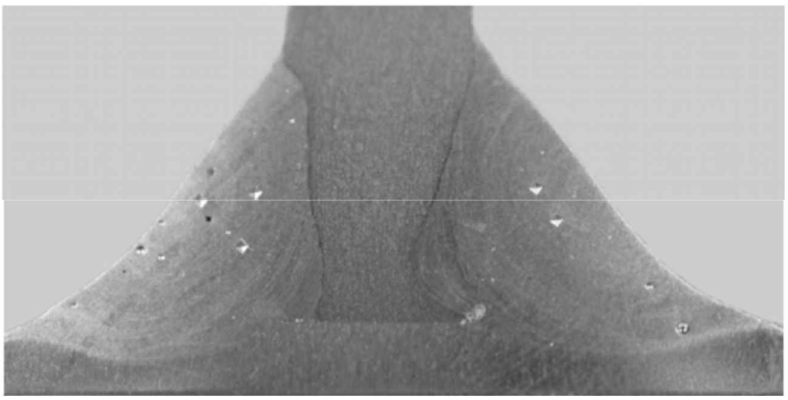

Figure 15. Extent of the Heat-Affected Zone (HAZ) [29]

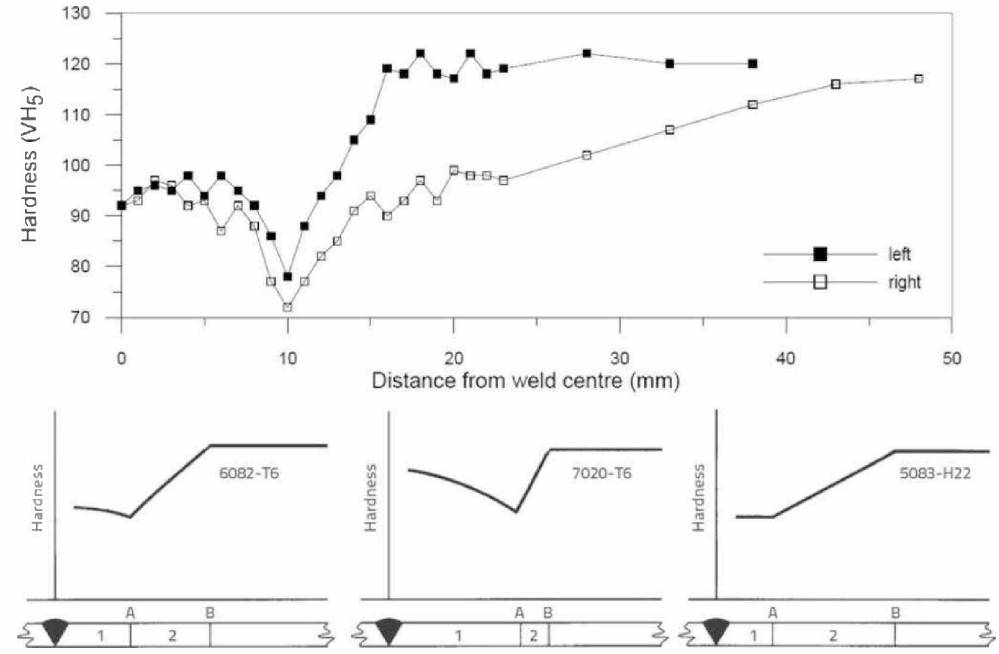

Figure 16. Typical Hardness Profiles in the Heat-Affected Zone (HAZ) for Alloys 6082-T6, 7020-T6, and 5083-H22 [23]

3 Previous research

Previous studies in this field can generally be classified into two main categories: investigations concerning the structural performance of joints in truss systems [33-64] and research into the mechanical behavior of aluminum alloys within the heat-affected zone (HAZ) [65-74]. While the research concerning the structural performance of joints has predominantly focused on steel trusses [33-64], there is limited research regarding alumiuim trusses [15, 75-80].

3.1 Mechanical behavior in the HAZ

Aluminum alloys, especially those from the 6000 and 7000 series, exhibit sensitivity to thermal input during welding processes, which induces notable softening in the HAZ. Lai and Nethercot (1993) [40] emphasized that the presence of transverse welds can significantly diminish the axial load-bearing capacity of welded aluminum columns, particularly when HAZ zones are centrally positioned. Zhu and Young [41] (2006) confirmed that 0.2% proof stress could reduce by up to 50% near welded zones.

European design standards, such as EN 1999-1-1 [6], account for this degradation through reduction coefficients applied to the mechanical properties. Hill, Clark, and Brugraber (1962) [25] initially proposed the "one-inch rule," which was substantiated by Wong (1985) [26] and later refined by Robertson (1985) [27], offering a practical method for estimating the softening area based on weld dimensions and hardness measurements.

Robertson [27] introduced expressions for RSZ (reduced strength zone) calculations for EN AW 6082 and 7019 alloys. Kos (2019) investigated welding performance using ER5356 and ER4043 filler materials and recommended using multiple-pass techniques and inter-pass temperature control to mitigate softening. Schellekens (2020) [42] studied ductility reductions post-welding and proposed a numerical model for parametric simulations.

Collette (2007) [43] reviewed the influence of fusion welding on aluminum ship structures and concluded that plastification tends to accumulate rapidly in HAZ regions, significantly impacting structural design criteria. Meini (2014) [44] and Stamenkovic et al. (2021) [45] both emphasized the effects of heat treatment and weld configuration on hardness distribution and residual stress across the welded zone.

Astarita et al. (2016) [46] demonstrated that FSW (friction stir welding) produced joints with less degradation compared to conventional TIG methods in AA6061 T6 specimens. Further studies by Macdonald and Haagensen (2009) [47] and Kos et al. (2019) [48] reinforced the use of hardness testing to map HAZ boundaries and correlate them with strength loss.

3.2 Load-bearing capacity of joints in truss girders

Several investigations addressed the strength and stiffness of aluminum truss joints, especially those using CHS (circular hollow section) and RHS (rectangular hollow section) profiles. Kalac et al. (2022) [49-51] conducted experimental analysis on aluminum X and K joints formed from EN AW 6082-T6, revealing that geometry factor such as β (brace-to-chord width ratio) significantly impact ultimate capacity. Đuričić (2018) [15] proposed analytical models and nomograms for aluminum K and T joints based on EN 1993-1-8 steel design equations with appropriate modification factors. But most of the research in this field is based on the investigation of steel truss girders and predominantly on the fatigue behavior of these joints.

Van Wingerde, Packer, and Wardenier (2001) [52] developed simplified SCF (stress concentration factor) equations for CHS and RHS K-joints, supported by FE simulations and test data. Feng and Young (2011) [53] validated FE models of cold-formed SHS and RHS stainless steel joints, noting discrepancies in Eurocode-based design formulas when applied to plastified brace zones.

Chen et al. (2016, 2017, 2019) [53-57] explored composite steel-concrete-aluminum configurations in SHS and CHS joints. Concrete infill improved ductility and stiffness, particularly when chord elements were filled. Packer (1980), Davies (1978), [58-64] and others introduced yield-line and punching shear models that remain foundational for aluminum tubular joint evaluation.

Al Zamzami et al. (2018) [65] investigated hybrid joints and concluded that failures invariably occur in aluminum HAZ regions. Cornacchia and Cecchel (2020) [58] found that innovative welding processes such as fiber-laser MIG reduced porosity and microstructural defects compared to conventional MIG.

Baskutis et al. (2019) [67] correlated weld current with HAZ geometry and observed long-term hardness recovery due to natural aging in 6082-T6 alloys.

F. Soetens [75] presented an extensive review of welded connections in aluminum structures, including design principles, types of welded joints, and experimental results on strength and failure modes. The work focused on the effects of material properties and joint geometry on structural performance and provides guidelines for safe design.

S. de Jongh et al. [76] investigated the load-bearing capacity of welded X-joints made of rectangular hollow aluminum sections. It combined experimental testing and analytical modeling, providing resistance curves and recommendations for design in structural applications. The paper highlighted the influence of weld geometry and material grade on joint strength.

Manders et al. [77] analyzed punching shear failures in welded RHS aluminum joints through experimental tests and numerical simulations. The study quantified critical parameters affecting punching resistance, such as weld configuration and section thickness, and proposes analytical expressions for design.

Ziemian and Ziemian [79] conducted a numerical study of transverse welds in aluminum I-shaped columns. The paper examined how weld placement affects global and local member strength, stresses, and buckling behavior. Results provided guidance for optimizing weld locations in design.

Matusiak [80] investigated the strength and ductility of various welded aluminum alloy structures. The thesis combined experimental testing and analytical modeling to evaluate failure modes, material softening in heat-affected zones, and the influence of weld geometry. It provided recommendations for design and practical applications in structural engineering.

Cumulative research demonstrates that HAZ degradation due to welding significantly affects the mechanical integrity and structural reliability of aluminum joints. Despite advancements in modeling and testing, most standards are still based on extrapolated steel behavior. There is a clear need for aluminum-specific analytical models and design criteria, especially for fatigue, chord face plastification, sidewall failure, and mixed-

material (hybrid) joints. Few studies have investigated the interactive effects of eccentricity, local buckling, and pre-existing imperfections in aluminum joint behavior.

This dissertation builds upon the analytical frameworks developed by Đuričić (2018) [15] and integrates newer insights into modeling, experimental validation, and parametric sensitivity analysis, aiming to refine the understanding and predictability of welded truss joints in aluminum structures.

4. Original research

As part of this doctoral research, a comprehensive experimental, numerical, and theoretical investigation was conducted on welded aluminum truss girders composed of CHS and SHS profiles. The scope of the study included:

1. Analysis of mechanical properties and HAZ mapping

   Characterization of mechanical properties and indirect mapping of the heat-affected zone (HAZ) through hardness measurements and application of the Digital Image Correlation (DIC) method.

2. Analysis of X-Joint (Integrated System: SHS–SHS)

   Investigation of an X-joint composed of SHS braces and SHS chord as an integral part of the aluminum truss girder.

3. Analysis of Isolated X-Joint (SHS–SHS)

   Investigation of an isolated X-joint with SHS brace and SHS chord members.

4. Analysis of X-Joint (Integrated System: CHS–SHS)

   Investigation of an X-joint formed by CHS braces and an SHS chord, considered within the full truss girder configuration.

5. Analysis of Isolated X-Joint (CHS–SHS)

   Investigation of an isolated X-joint composed of CHS braces and an SHS chord member.

6. Analysis of K-Joint (Integrated System: SHS–SHS)

   Investigation of a K-joint composed of SHS braces and SHS chord, tested as part of the overall truss structure.

7. Analysis of K-Joint (Integrated System: CHS–SHS)

   Investigation of a K-joint with CHS braces and an SHS chord within the assembled aluminum truss system.

8. Global Deformation Analysis of the Truss Girder

Full-scale assessment of global deformation behavior of the welded aluminum truss under load.

4.1 Experimental investigation

The experimental investigations were conducted in two stages at two institutions: the Laboratory for Material Testing at the Faculty of Civil Engineering, University of Montenegro (Podgorica), and the Laboratory for Material Testing at the Chair of Metal Structures, Technical University of Munich. Sample preparation was carried out at Remid Vis, a specialized company for metal forming and cutting. Welding procedures were performed by the company HIPERION, under the supervision of a certified welding engineer.

Experimental testing of the mechanical characteristics of the material, as well as mapping of the heat-affected zone (HAZ) using the Digital Image Correlation (DIC) method, was conducted at the Technical University of Munich. The experimental investigation of the truss girders and isolated welded joints was performed at the University of Montenegro. This experimental investigation was a multi-phase process requiring several preparatory stages prior to the mechanical testing:

1. Material Selection

   The selection of the aluminum alloy was based on mechanical properties, weldability, formability, and market availability. EN AW 6082-T6 was ultimately selected due to its favorable balance of strength and welding characteristics.

2. Sample Preparation

   Cutting of the aluminum specimens was performed using a band saw in combination with a cooling emulsion to minimize thermal input and avoid microstructural changes that could influence mechanical performance. This method was chosen to preserve the original properties of the thermally sensitive aluminum alloy.

3. Welding Process Selection

   Given the specific challenges of welding aluminum—including its lower melting point, high thermal conductivity, and surface oxidation—a meticulous approach was necessary for process selection. Several trial welds were conducted to verify weld quality and process parameters. The TIG process with ER5356 rod was

ultimately adopted, optimized for compatibility with EN AW 6082-T6. Welding was executed by certified personnel from HIPERION, following standardized parameters.

4. Instrumentation and Measurement Setup

   The experimental program involved simultaneous measurement of local and global deformations. Local deformations were monitored at the weld toe on the chord face, while the joint was loaded as an integral part of a truss girder. To achieve aqurate data, a custom measurement system was designed and fabricated. This setup included displacement transducers, a calibrated data acquisition unit, and structural support elements adapted for aluminum joint testing.

4.1.1 Material selection

For the purposes of this research, EN AW-6082 T6 aluminum alloy has been selected due to its highest tensile strength among the 6xxx series alloys which are commonly used in construction industry. This alloy is artificial aged wrought aluminum alloy in which dominant alloying elements are magnesium and silicon. The detailed tables of chemical composition and mechanical properties of EN AW-6082 T6 are presented, tab. 8 and tab 9.

Tab. 8: Chemical composition of EN AW-6082 T6 [8]

Chemical composition of EN AW-6082 T6										
Element	Si	Fe	Cu	Mn	Mg	Cr	Ni	Zn	Ti	Others
Standard EN 573-3	0.70–1.30	≤ 0.50	≤ 0.10	≤ 0.40	0.60–1.20	≤ 0.25	–	≤ 0.20	–	≤ 0.10

Tab. 9: Mechanical Properties of EN AW-6082 T6 [6]

Mechanical Properties of EN AW-6082 T6					
Thickness EN 1991-1-1	Tensile Strength, f_u (MPa)	Yield Strength, f_y (MPa)	Elongation, A (%)	Elongation at 50 mm, A50	Brinell Hardness, HB
≤ 5 mm	290	250	8	6	95
> 5 mm to ≤ 25 mm	310	260	10	8	–

4.1.2 Sample Preparation

Cutting of the specimens was performed using a band saw in combination with a cooling emulsion, in order to minimize heat input and prevent thermal effects on the material's microstructure, see Fig. 17.

Fig. 17: Cutting of the aluminum profiles

4.1.3 Weld testing

Prior to welding aluminum, and after each deposited weld pass, thorough cleaning was conducted to reduce the presence of aluminum oxide (Al_2O_3). This was achieved through mechanical brushing using a stainless-steel wire brush. Following mechanical cleaning, welding was performed promptly to minimize re-oxidation of the surface. Brushing continued until the surface lost its luster, as a shiny appearance typically indicates the continued presence of surface oxide layers.

Before welding, the surfaces surrounding the joint were thoroughly dried. In addition, brief purging of the welding hose was carried out using the torch trigger to further reduce internal moisture, which is known to contribute to porosity in aluminum welds.

To avoid introducing defects during initial arc ignition, a preliminary weld bead was deposited on a separate test piece before initiating the weld on the actual specimen.

For welding the EN AW-6082 T6 alloy, ER 5356 (AlMg5) filler rod was used. The shielding gas employed for the TIG welding process was high-purity argon, Fig. 18.

Fig.18: Welding of aluminium truss girders

The specimens used for hardness testing were prepared according to the following procedure:

- Grinding of the sample surface with P80 grit sandpaper in two perpendicular directions;
- Further grinding with P320 grit sandpaper in two perpendicular directions;
- Degreasing of the sample surface using nitro thinner.

The testing setup for evaluating the load-bearing capacity of the T-joint and the welded connection consisted of the following:

- A steel beam: IPE 140, length = 1200 mm;
- Two clamps: M12 bolts, strength grade 8.8, length = 500 mm, with L-shaped brackets (50×4×50 mm).

Measuring equipment, Fig. 19, consisted from:

- Displacement transducer;
- Data acquisition system (data logger);
- Analog gauge integrated with the testing machine;
- Portable hardness tester: SADT HARTIP 1500.

Fig. 19: Measuring Equipment

Two welded aluminum T-joint specimens were tested under vertical tensile loading to evaluate weld. Specimen 1, fabricated using the TIG welding process, exhibited local deformation at the weld toe but did not reach the ultimate load-bearing limit. Instead, failure occurred in the heat-affected zone (HAZ) of the chord due to localized moment-induced fracture.

Specimen 2, welded using the MIG process, reached its ultimate load-bearing capacity through plastification of the chord's upper surface, with a measured failure load of 64 kN. The fracture occurred in the HAZ of the chord, indicating that thermal degradation due to welding significantly reduced ductility and cross-sectional integrity.

In both tests, local deformation was monitored, and critical displacement was defined as 3% of the chord width. Results confirmed that failure was governed by the condition of the HAZ, with the MIG-welded joint showing slightly higher structural performance and the welds performed well without visible cracks, see Fig. 20.

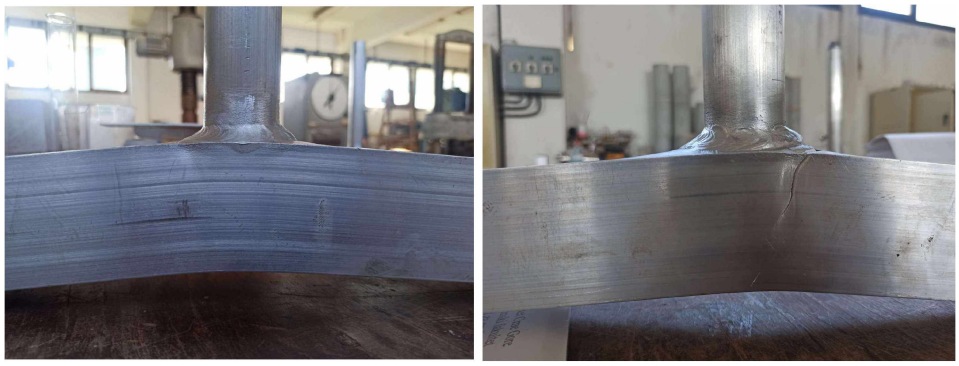

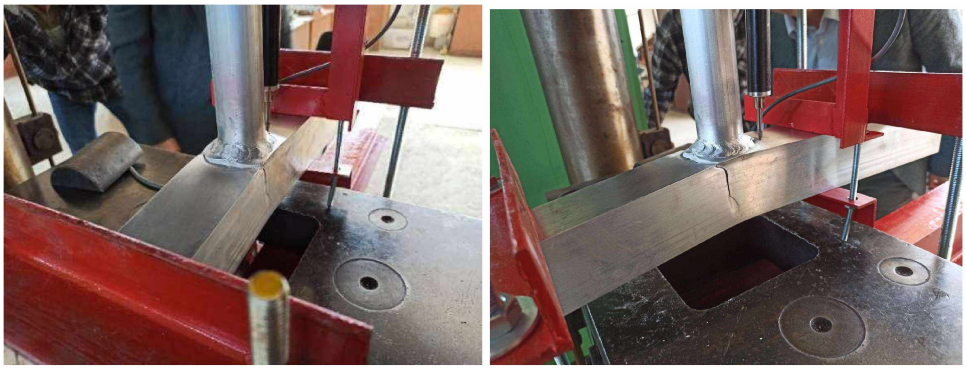

Fig. 20: Tested samples

4.1.4 Hardness Testing

The purpose of the hardness measurements was to determine the extent of the heat-affected zone (HAZ). Two approaches were considered:

1. Stationary (destructive) method – involves cutting the specimen into smaller plates of defined dimensions and is suitable only under controlled laboratory conditions.
2. Dynamic method – based on measuring the rebound velocity of a ball impacting the surface of the specimen.

For this study, the dynamic method was applied using a portable hardness tester to measure Vickers hardness (HV) within the HAZ. On Specimen 1, measurement lines were marked such that the points were at equal perpendicular distances from the weld seam. Line 1D was positioned approximately 5.0 mm from the seam. The calibration of the portable hardness tester was verified using the standard reference block provided with the device. Surface preparation of the specimen was conducted in accordance with the previously described methodology, see Fig. 21.

Fig. 21: Tested sample

The Tab.10 presents the Vickers hardness values (HV) measured along several lines perpendicular to the weld seam at varying distances. Measurements were taken on both sides of the chord axis, as well as directly on the axis.

Tab. 10: Hardness results of HAZ using the dynamic method

Line ID	Distance from Weld Seam (mm)	Left Edge of Chord (HV)	On Chord Axis (HV)	Right Edge of Chord (HV)
1D	5	N/A	N/A	N/A
2D	10	82	57	82
3D	15	87	62	88
4D	20	87	59	87
5D	25	88	47	94
6D	30	94	48	86

The values on the left and right edge clearly illustrate the softening effect in the HAZ. Based on the presented results, no consistent trend in hardness variation was observed with increasing distance from the weld edge in the chord axis. Therefore, it can be concluded that hardness measurements obtained using a portable hardness tester do not yield valid or reliable results in this context.

Further analysis suggests that the inaccuracy of these results may be attributed to the geometry of the specimen and the inability to provide a non-deformable backing beneath the tested surface. To accurately determine the extent of the HAZ, it is necessary to perform testing using a stationary (laboratory-based) hardness method or by preparing micro-specimens and conducting direct tensile tests on a universal testing machine.

Analysis of Mechanical Properties and HAZ Mapping

A comprehensive approach incorporating advanced characterization techniques was adopted to ensure reliable evaluation of the mechanical behavior of the selected material. Both tensile and hardness tests were performed as part of quality control, providing insight into the effects of welding on local and global mechanical properties. The tensile test specimens were prepared in accordance with EN ISO 6892-1:2019 [81], and dimensions were tailored to comply with the capabilities of the available testing apparatus, as shown in Fig. 21.

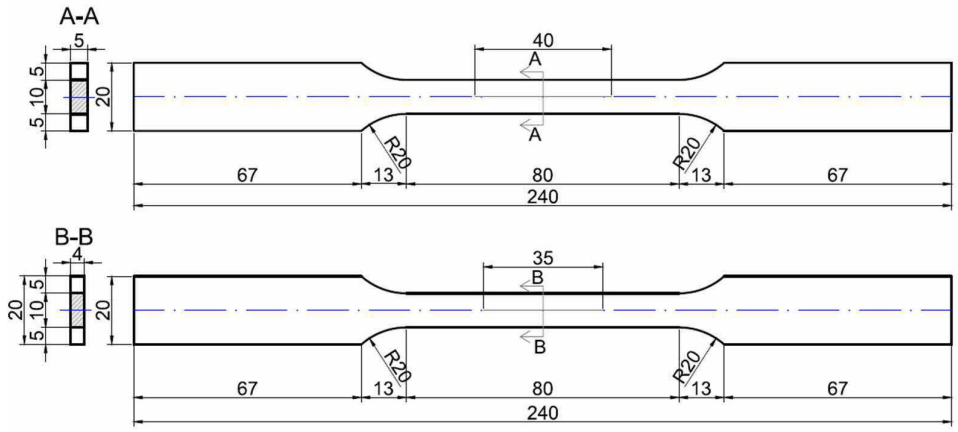

Fig. 21: The shape and dimensions of the tensile test coupons.

The experimental methodology was designed to characterize both the local and overall mechanical responses of the welded and non-welded specimens. In order to obtain a comprehensive dataset, two sets of dog-bone specimens were prepared from an EN AW-6082-T6 aluminum alloy.

The first set consisted of specimens made entirely from the base material, while the second set comprised specimens extracted from a MIG-welded joint produced using an ER5356 filler wire.

For the welded specimens, careful cutting procedures were followed to ensure that the welded region was centered within the gauge section. This step was crucial to accurately capture the effect of the weld on the mechanical properties during testing. All specimens were machined to standard dog-bone geometries to ensure uniformity in tensile testing and to facilitate direct comparison between the base material and the welded joints as shown in Fig. 22.

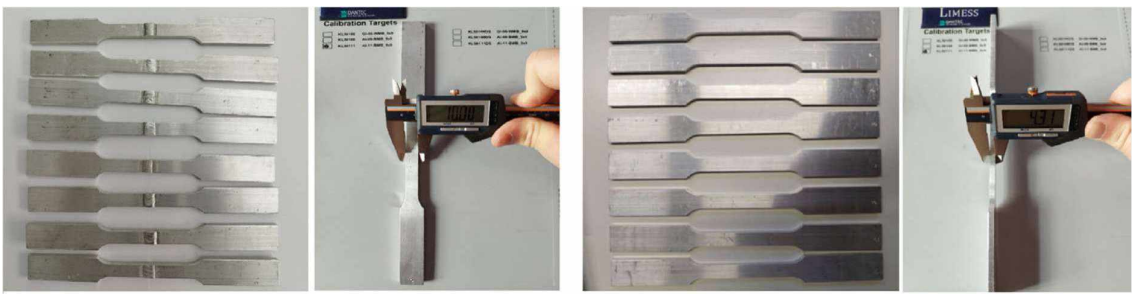

Fig. 22: Measuring geometrical imperfections.

Tensile tests were conducted using a 100 kN Instron universal testing machine (see Fig. 23). A Digital Image Correlation (DIC) system was employed to obtain full-field strain measurements throughout the tests. The DIC system was carefully synchronized with the load-cell data, ensuring a consistent correlation between applied force and localized strain behavior. The captured image sequences were subsequently processed to generate high-resolution strain maps at discrete loading intervals. These maps enabled precise tracking of strain localization and provided insight into early plastification phenomena, particularly in the softened regions around the weld.

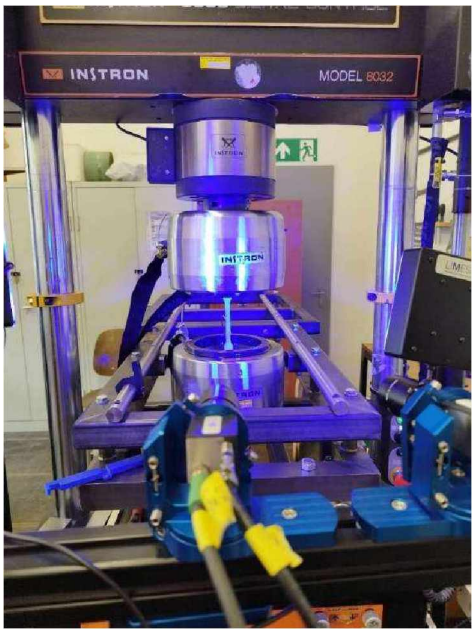

Fig. 23. Testing setup.

As illustrated in Fig. 24 the welded specimens displayed pronounced strain localization in the HAZ, with strain values exceeding the elastic limit in these regions while remaining lower in the unaffected base material. This localized deformation ultimately led to failure occurring in the vicinity of the weld, which aligned with expectations. In contrast, the non-welded specimens exhibited a more uniform strain distribution along the specimen length, and no clear failure initiation zone was observed prior to full cross-sectional plastification.

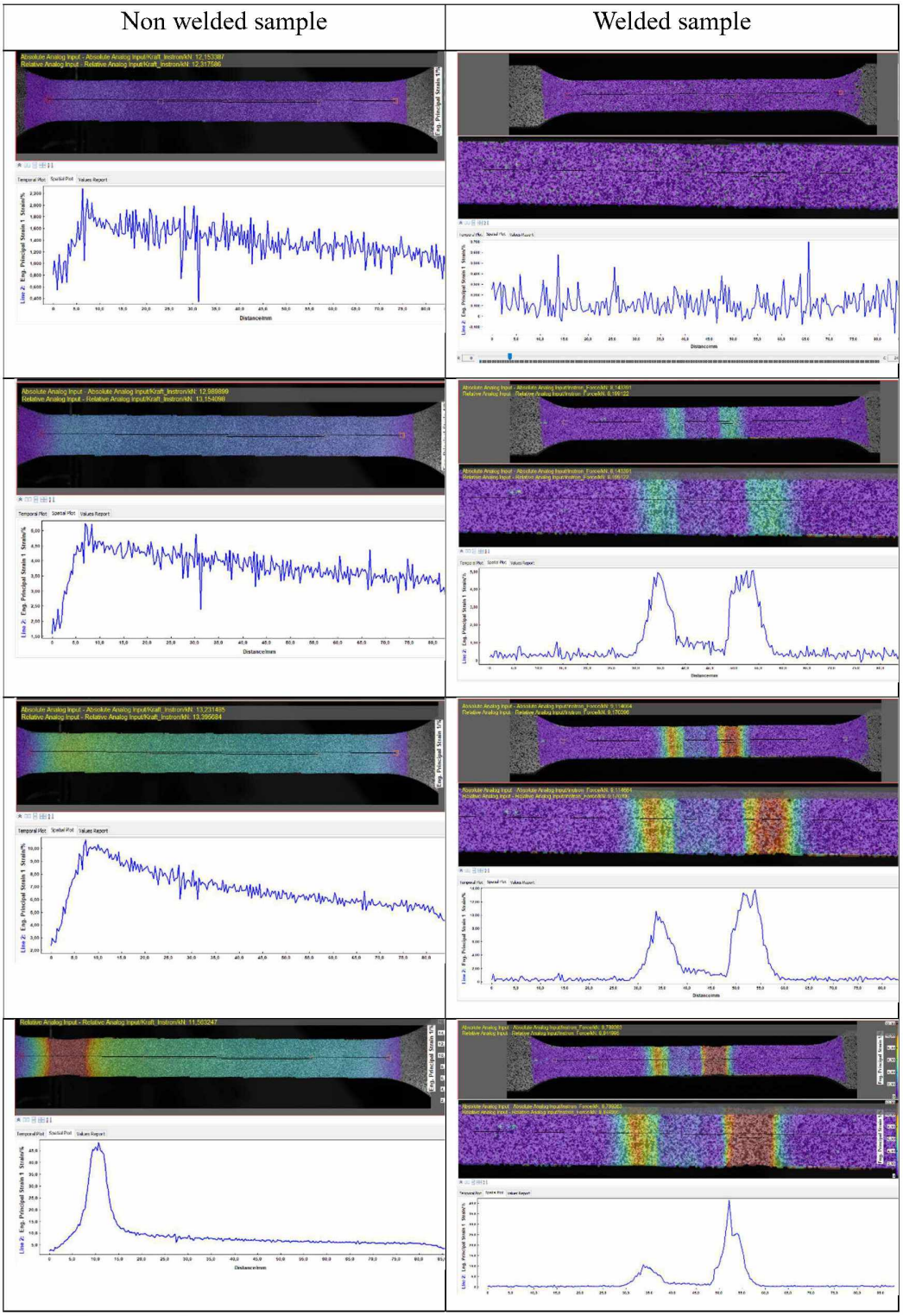

Fig. 24: DIC images of strain distribution across the welded and non-welded specimen.

Tensile test coupons experimental results are presented in Tab. 11.

Tab. 11. Tensile test coupons experimental results

Profile	f_0 (MPa)	$f_{0,HAZ}$ (MPa)	f_u (MPa)	$f_{u,HAZ}$ (MPa)	A (%)
prEN 1999-1-1	250	125	290	185	8
SHS 40	254	127	301	193	10.7
SHS 50	263	131	314	199	10.7
SHS 60	252	126	297	189	11.4
SHS 100	251	126	294	187	12.3

Hardness tests [51] were conducted using the Vickers hardness test. The testing method was HV1, a low-force hardness scale, with an applied test force of 9,807 N, as shown in Figs. 25 and 26. In the following figures, the values of $d1$ and $d2$ are expressed in millimeters.

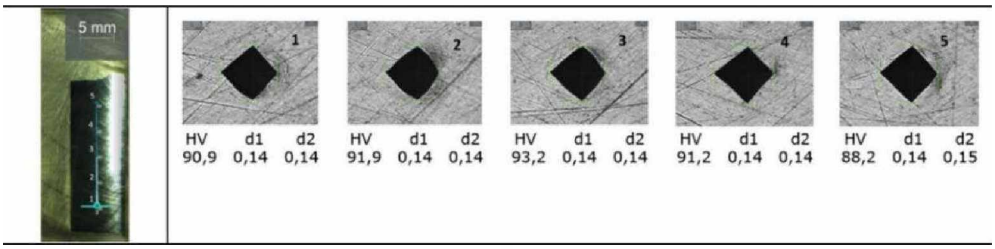

Fig. 25. Hardness test results for the non-welded specimen.

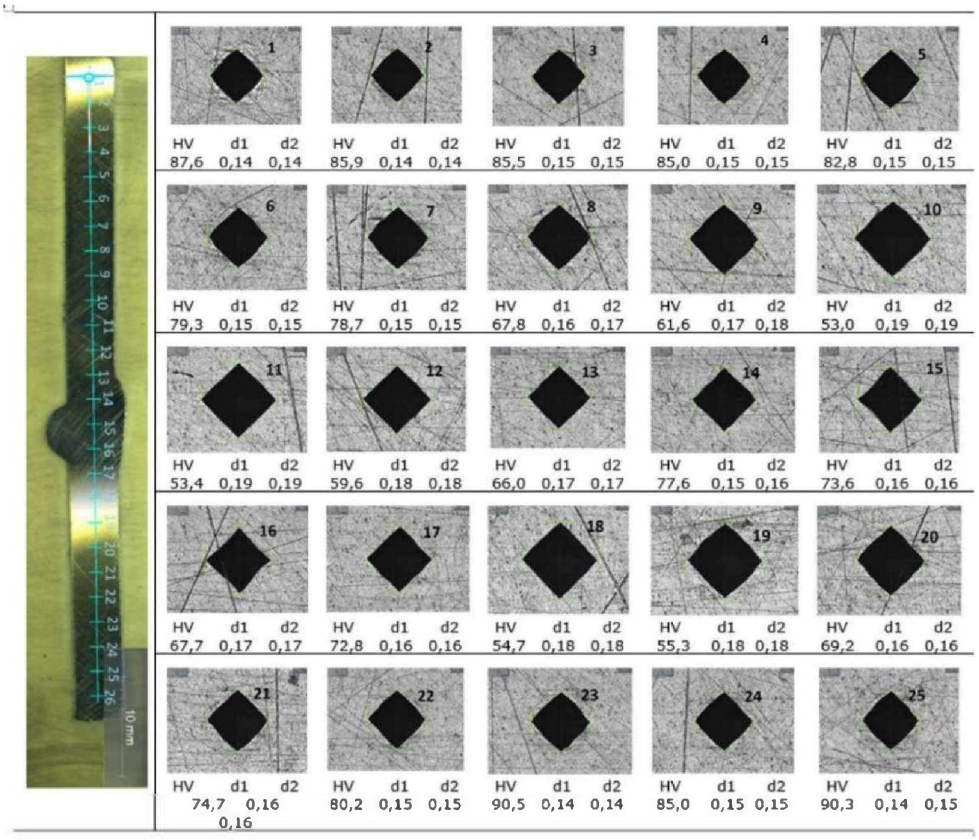

Fig. 26: Hardness test results for the welded specimen.

In Fig. 27. [51] the hardness test outcomes are presented graphically. Within this figure, the welded specimen is distinguished by the demarcation of the HAZ and the fusion zone, in contrast to the non-welded specimen, which is characterized as the base material area.

The outcomes of these tests, including values for yield stress in the base material (f_0), yield stress in the HAZ ($f_{0,HAZ}$), ultimate strength in the base material (f_u), ultimate strength in the HAZ ($f_{u,HAZ}$), and maximum elongation in the base material (A), have been presented in Table 2.

It is known that in the EN AW-6082 T6 alloy [51], the yield strength in the HAZ decreases by up to 50% as a result of material softening during the welding process. The findings from the tensile and hardness tests on both the welded and non-welded specimens, derived from an identical sample, comply with this fact.

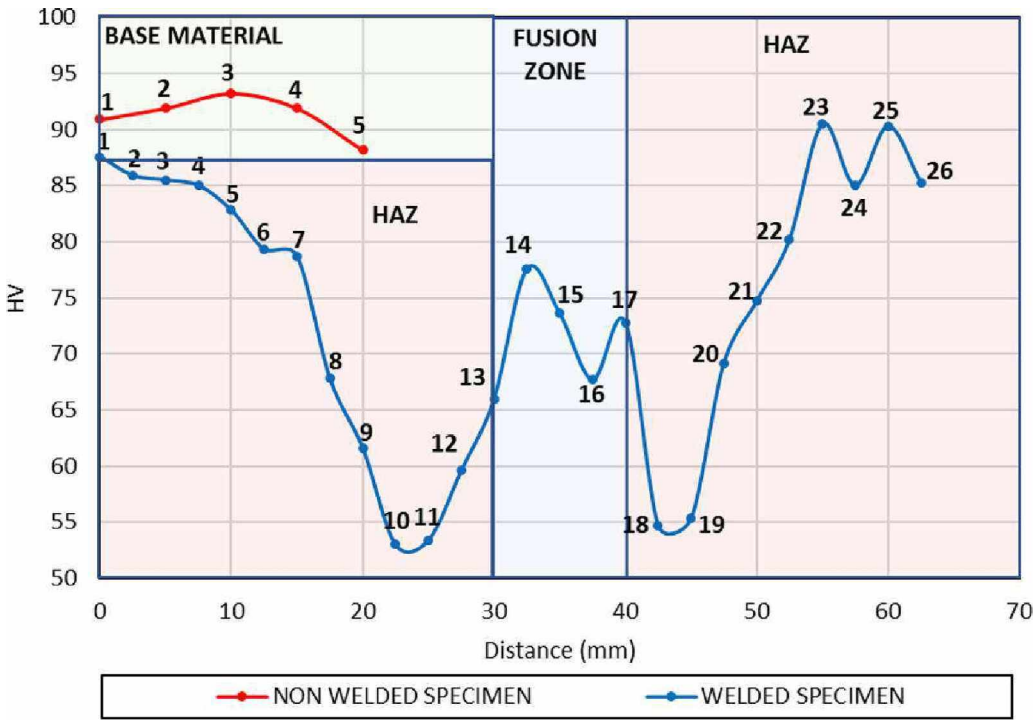

Fig. 27. Hardness test results for the welded and non-welded specimens.

4.1.5 Investigation of welded truss girders

Six truss girders manufactured from the aluminum alloy EN AW-6082-T6 in total were investigated in this experiment. Brace members and chord members were joined together directly using TIG welding with the filler rod ER 5356 (AlMg5) [51].

The truss girders [51] had a height of 600 mm and a 3000 mm span. All tested truss girders had the same chord members, which were SHS 100×5 profiles, Fig. 28. In order to carry out the parametric analysis, the brace members' shape and size were altered. Circular hollow sections (CHS) with cross-sectional diameters of 40, 50, and 60 mm were used to construct three truss girders. Brace members from SHS profiles with widths of 40, 50, and 60 mm were used to construct the other three truss girders. The joints were centered without eccentricities e=0 and there was a gap whose size depended on brace member dimensions. The brace members have been joined to the chord members at the angle θ_i=45°. Regarding this, the β coefficient varied from 0.4 (SHS40 and CHS40) to 0.6 (SHS60 and CHS 60), which refers to the ratio of the width or diameter of the brace member to the width of the chord member. The joints met all the requirements of EN 1993-1-8 [3] and were both centric and with a gap.

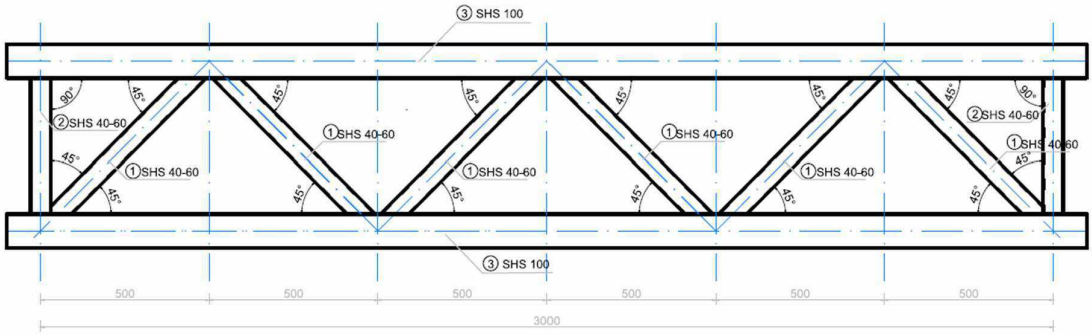

Fig. 28: Geometry of aluminum truss girder.

Specimen labeling

The truss girders [51] have been designated based on the brace member cross-section from which they are constructed. Therefore, the truss girders are labeled as SHS 40, SHS 50, SHS 60, and CHS 40, CHS50, CHS 60.

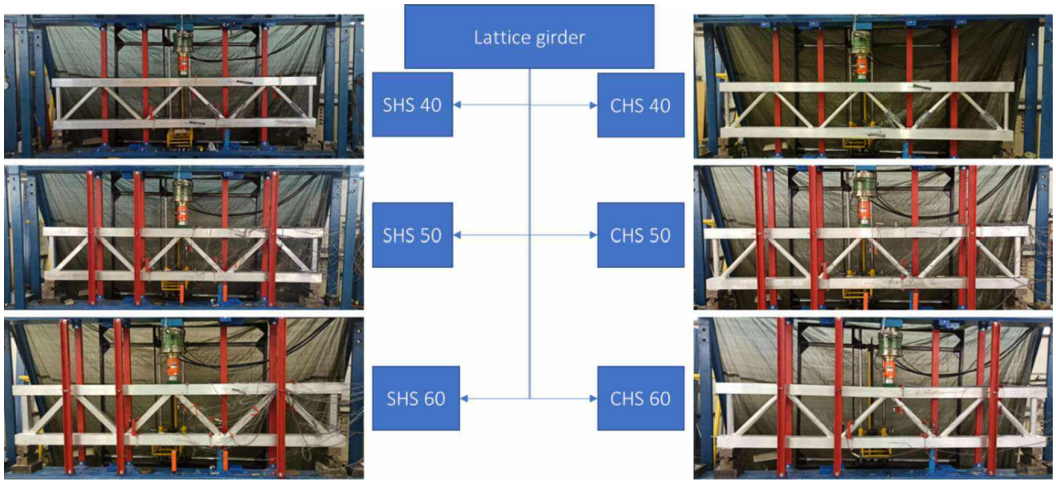

Fig. 29: Labeling of truss girders

The joints [51] have been designated based on the type of the joint, position inside truss girder and axial chord force direction in the joint. K-joints are designated as KTL- (left-positioned) and KTR- (right-positioned) in the tensioned chord members. K-joints in the compression chord member are designated as KC. The positions of designated X joint and K-joints are shown in Fig. 30.

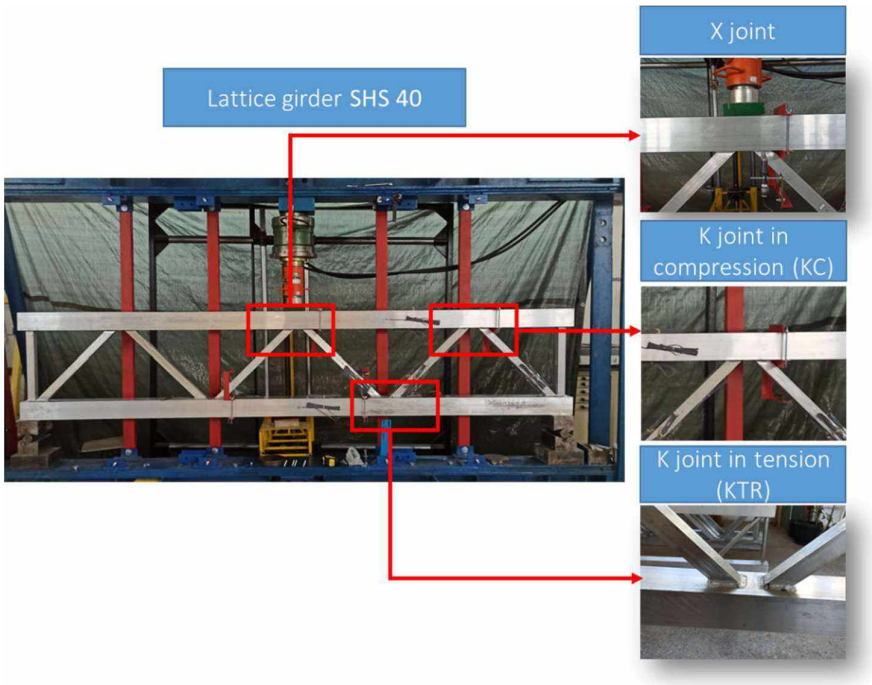

Fig. 30: Designation of the joints inside truss girder.

Testing setup

The truss girder [51], shown in Fig. 31, was simply supported (I, II) within the testing frame (III) and subjected to a single force (IV) applied at the midpoint of its length. Deflections of the Y-joints (I, II) were prevented. In the case of buckling, the lateral displacement of the compression chord member of the truss girder was prevented every 500 mm using bolts connected to UPE profiles (V). A load cell (A), mounted on a steel plate (120×30×100 mm), received the load from the hydraulic press (IV) above. Linear transducers were used to measure the local deflection of the chord members' surfaces. Specifically, the ones installed at the tension chord (C, E) measured local deflections at the KTL- and KTR-joints and the transducer installed at the compression chord (D) measured the local deflection of the KC-joint. Transducers installed on the testing frame (F, G) were used to measure the overall deflection of the girder. Additionally, transducer A measured the local deflection of the X-joint.

Based on Hooke's law, linear relationships between normal stress and strains can be applied for stresses below the proportionality limit of the stress–strain (σ–ε) curve [51]. This assumption was validated by comparing the measured strain values with the σ–ε curves obtained from the coupon testing previously mentioned.

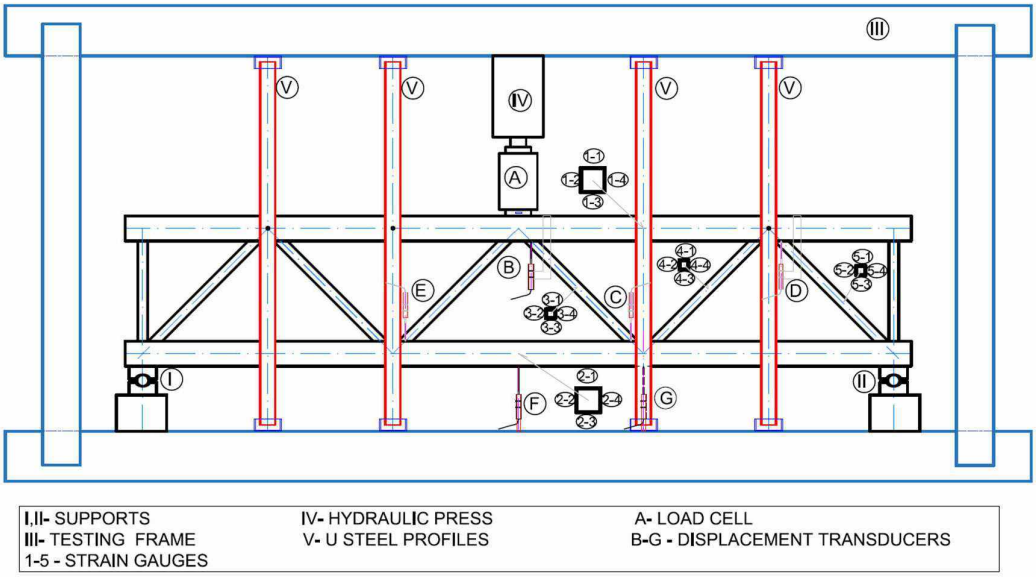

Fig. 31: Schematic disposition of testing an aluminum truss girder.

Strains [51] were measured using FLAB-5-23-5LJCT-F (TML) strain gauges installed at the center of the members' faces, specifically at the midpoint of the spans of both the brace and chord members, as shown in Fig. 32. Strain gauges were labeled numerically from 1 to 5 and placed at the span's midpoint: the compression chord member (1.1–1.4), the tension chord member (2.1–2.4), the compression brace members (3.1–3.4, 5.1–5.4), and the tension brace member (4.1–4.4).

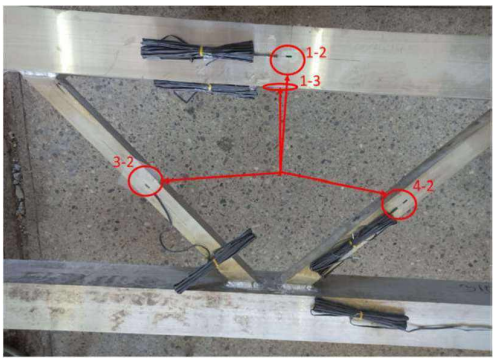

Fig. 32: Location of strain gauges of testing aluminum truss girder.

After positioning the truss girder [51] in the testing frame, an initial preload of approximately 0.5 kN was applied to allow the girder to settle into its optimal position. The loading was then increased incrementally at a rate of 2 kN/min using a hydraulic press, with data acquisition equipment recording the results until plastification of the K-joints was observed, defined by joint deflections without further load increase, see Fig. 33. Maximum joint deformation occurred at the contact point between the compression brace member and the chord. In specimens with SHS 60 brace members, the collapse of welds in the tension brace members was also observed as the critical failure mode. Therefore, in the SHS 60 truss girder, the K-joint face plastification failure mode did not occur.

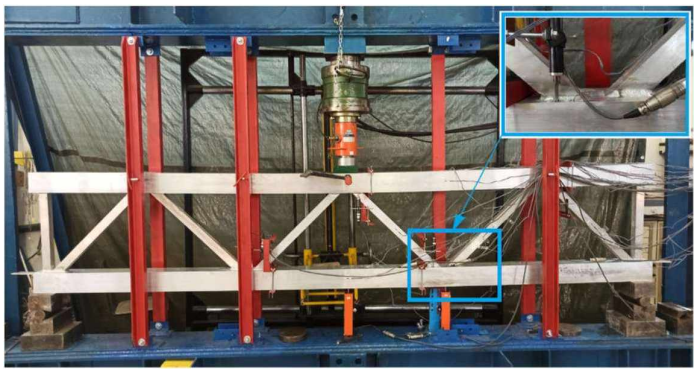

Fig. 33: Deformed shape of SHS 40 truss girder.

Experimental results and discussion

Based on the experimental results [51], for truss girders with a geometric ratio coefficient β of 0.4 and 0.5, the failure modes predicted by EN 1993-1-8 [19] align well with the observed critical failure mechanisms, particularly chord face plastification. However, for truss girders with β=0.6, the current upper limit for critical chord face plastification failure should be re-evaluated in the context of welded hollow section joints.

Moreover, weld quality control emerges as a crucial factor, [51] particularly for joints involving circular hollow section (CHS) profiles. In the case of the CHS 60 truss girder, a crack initiated within the weld was identified as the critical failure mode, which diverged from theoretical assumptions based solely on geometrical and material parameters.

It is also worth noting that local joint failure does not necessarily result in immediate global failure of the entire truss girder, especially for configurations with lower β values. For instance, in the experiment with β=0.4, the structure retained a degree of global integrity despite localized damage at the joint, see tab. 11.

Table 11. Failure modes for investigated truss girders

Truss girder	Critical failure mode	II Failure mode	III Failure mode	IV Failure mode
SHS 40	X joint chord face plastification	X joint side wall chord profile buckling	K joint chord face plastification	
SHS 50	X joint chord face plastification	X joint side wall chord profile buckling	K joint chord face plastification	Weld falure in tensioned brace
SHS 60	X joint chord face plastification	X joint side wall chord profile buckling		

CHS 40	X joint chord face plastification	K joint chord face plastification	Weld falure in tensioned brace	
CHS 50	X joint chord face plastification	X joint side wall chord profile buckling	K joint chord face plastification	Weld falure in tensioned brace
CHS 60	Weld falure in tensioned brace			

Truss girders with lower values of coefficient β have shown higher ductility capacity or deformation capability compared to ones with higher values, as shown in the Fig. 34. Regarding the shape of brace members for the same values of coefficient β, it could not be stated what is the more favorable options regarding global ductility as CHS truss girders are more prone to weld failure and the plastification of the joints didn't occur in some of the cases.

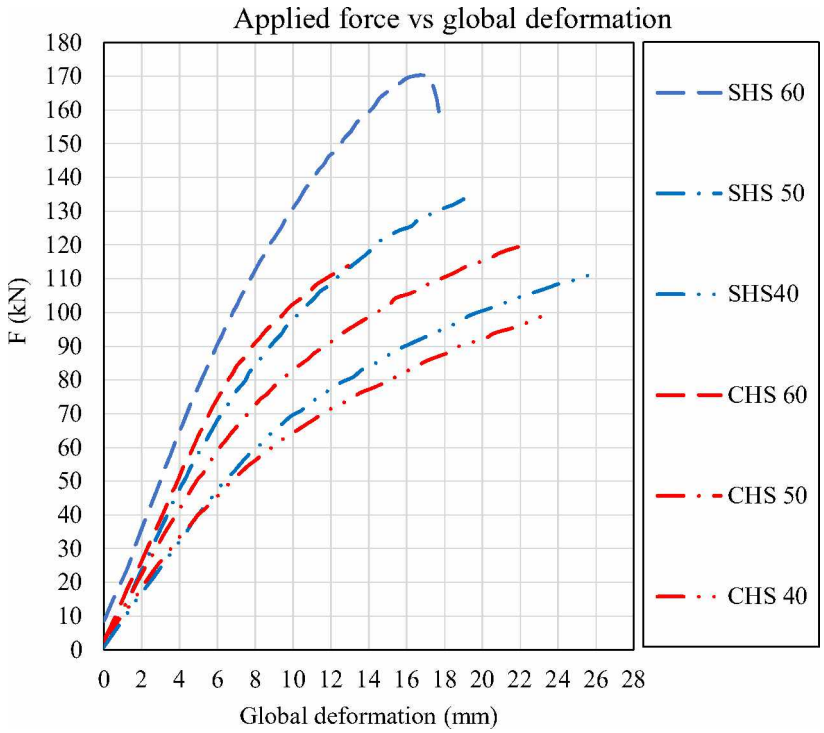

Fig.34: Applied force- global deformation curves

SHS joints

Tab. 12. presents the experimental results of load-bearing capacities of welded SHS aluminum joints and compares them with theoretical predictions derived from EN 1993 and EN 1999 design standards. Four joints were evaluated (X, KTL, KTR, and KC) across three different cross-section sizes: SHS 40, SHS 50, and SHS 60. Column (1) shows the experimental force inside joint corresponding to 1% chord face deformation ($P_{1\%bo}$) or force at serviceability limit, column (2) gives the experimentally measured ultimate force (Pult, exp), while columns (3) and (4) present the theoretical load-bearing capacities of joints calculated using EN 1993-1-8 + EN 1999-1-1 combined and EN 1993-1-8 alone, respectively. The subsequent columns display absolute and percentage differences between experimental and theoretical values, thereby offering insight into the adequacy of current design models.

Tab. 12: The results of load-bearing capacities of welded SHS aluminum joints.

		$P_{1\%bo}$	$P_{ult, exp}$	$P_{ult, EN1993 +EN 1999}$	$P_{ult, EN1993}$	Difference			
SHS 40	Joint	(1)	(2)	(3)	(4)	(3)-(2)	((3)-(2))%	(4)-(2)	((4)-(2))%
	X	31.715	43.306	31.155	62.311	-12.151	-28.058	19.005	43.885
	KTR	43.612	58.818	55.617	111.234	-3.201	-5.442	52.416	89.115
	KTL	48.497	64.651	55.617	111.234	-9.034	-13.973	46.583	72.053
	KC	44.1	60.565	55.617	111.234	-4.948	-8.169	50.669	83.660
		$P_{1\%bo}$	$P_{ult, exp}$	$P_{ult, EN1993 +EN 1999}$	$P_{ult, EN1993}$	Difference			
SHS 50	Joint	(1)	(2)	(3)	(4)	(3)-(2)	((3)-(2))%	(4)-(2)	((4)-(2))%
	X	43.827	63.597	37.500	75.001	-26.096	-41.034	11.404	17.931
	KTR	N/A	N/A	N/A	N/A	N/A	N/A	N/A	N/A
	KTL	70.000	93.719	69.521	139.043	-24.197	-25.819	45.324	48.361
	KC	71.333	92.668	69.521	139.043	-23.146	-24.977	46.375	50.044
		$P_{1\%bo}$	$P_{ult, exp}$	$P_{ult, EN1993 +EN 1999}$	$P_{ult, EN1993}$	Difference			
SHS 60	Joint	(1)	(2)	(3)	(4)	(3)-(2)	((3)-(2))%	(4)-(2)	((4)-(2))%
	X	86.08	99.487	46.701	93.403	-52.785	-53.057	-6.084	-6.115
	KTR	N/A	N/A	N/A	N/A	N/A	N/A	N/A	N/A
	KTL	N/A	N/A	N/A	N/A	N/A	N/A	N/A	N/A
	KC	N/A	N/A	N/A	N/A	N/A	N/A	N/A	N/A

The results demonstrate varying degrees of agreement between experimental findings and theoretical predictions, with clear trends based on joint type and section size. For

SHS 40 joints, the EN 1993 + EN 1999 approach underestimates the ultimate load by 5–28%, while EN 1993 alone consistently overestimates it by up to 89%. Notably, the X-joint shows a substantial discrepancy of 28.06% between the experimental and combined-code prediction, highlighting its sensitivity to local effects not fully captured in the codes. As the profile size increases to SHS 50, the differences become more pronounced. In the case of the X-joint, the combined-code approach underpredicts by over 41%, which raises questions about its applicability for larger sections without calibration. On the other hand, KTL and KC joints yield deviations of around 25%, which, while significant, are more manageable and consistent with prior research.

These findings suggest that standard design equations become increasingly conservative or inconsistent as joint geometry and cross-sectional dimensions scale up, especially in the presence of HAZ and geometrical complexities, Figs. 35.-38. The absence of test results for K-type joints in SHS 60 underscores potential challenges in joint fabrication or measurement for these configurations. For the reference value $P_{ult,exp}$ is adopted.

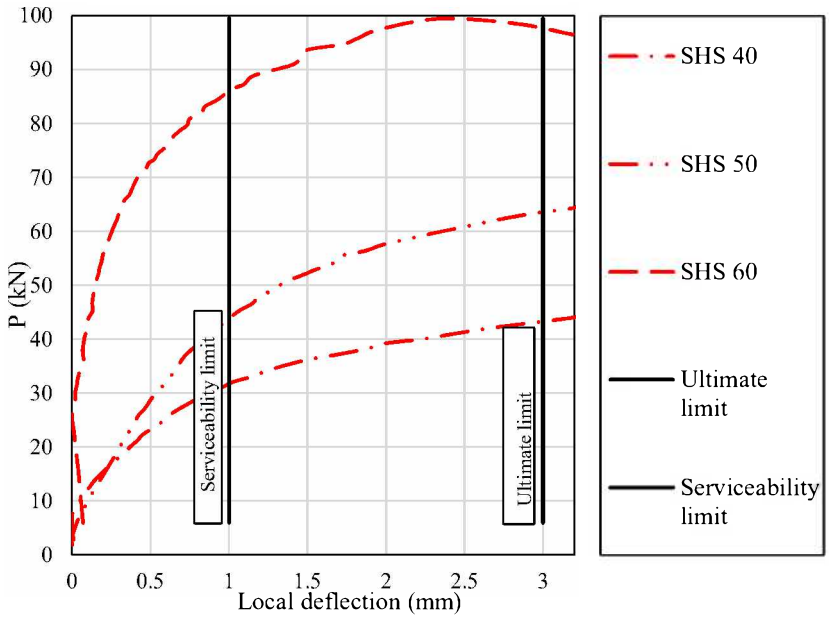

Fig.35: X joint: axial force versus local deflection

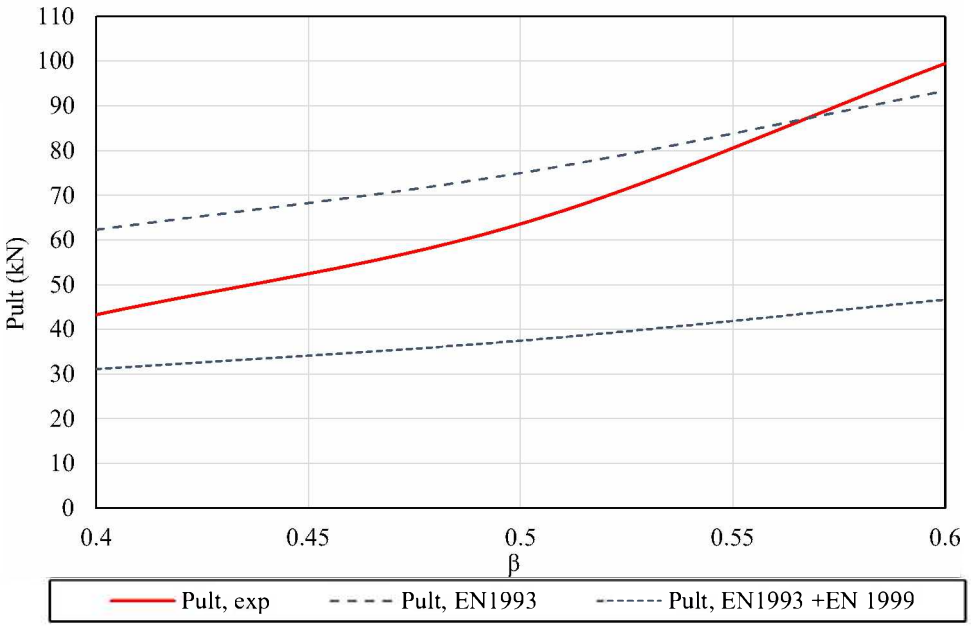

Fig.36: Ultimate load P_{ult} versus β ratio for SHS X-joints: comparison between experimental results and predictions from EN 1993 and combined EN 1993 + EN 1999 design provisions.

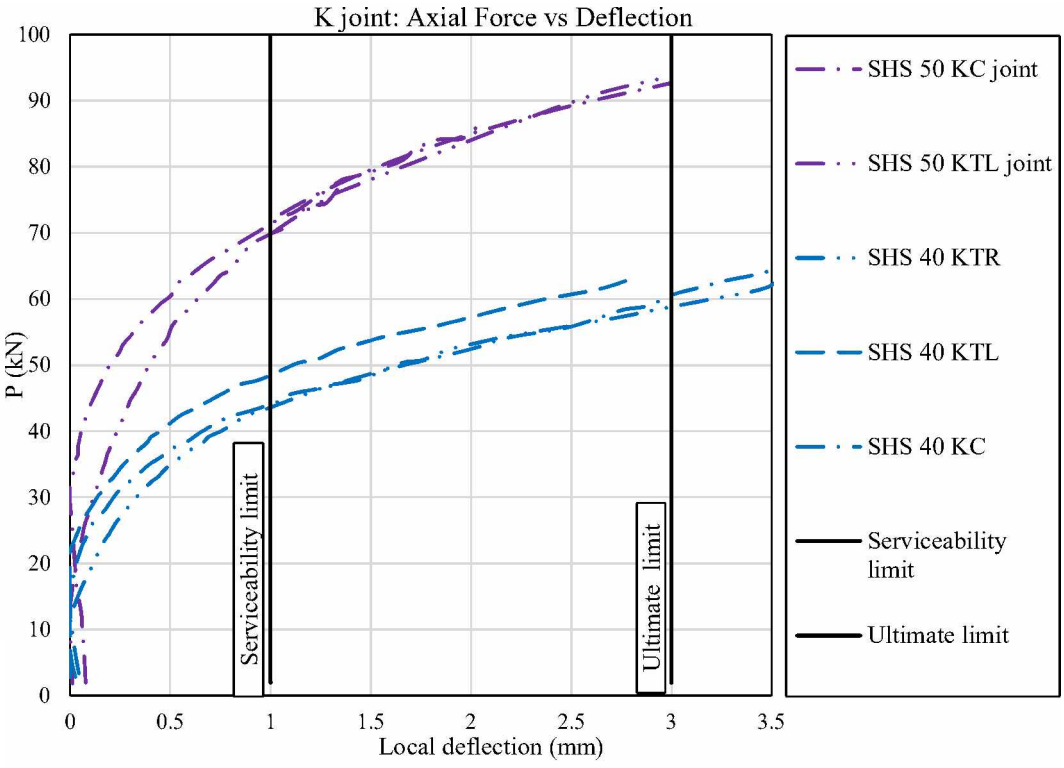

Fig. 37: SHS K joint: axial force versus local deflection

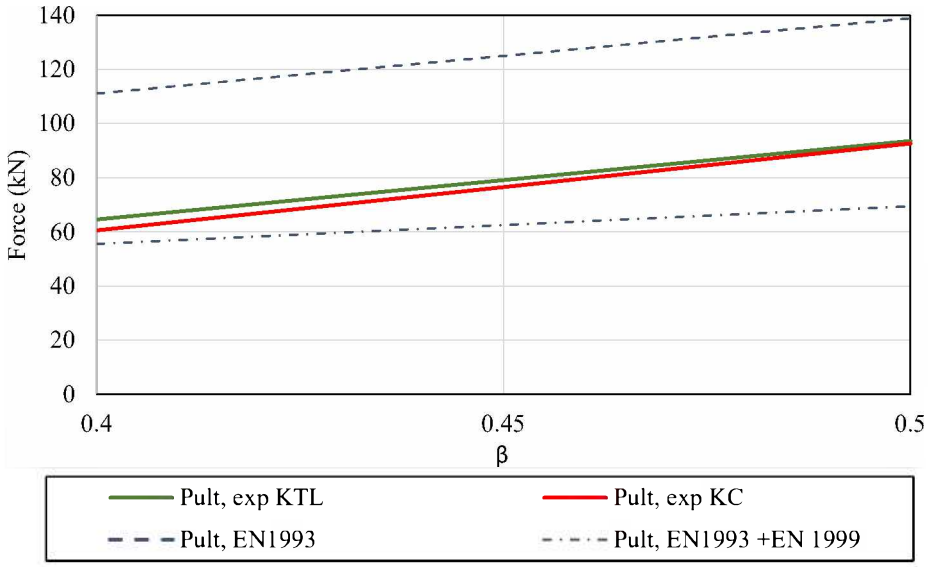

Fig.38: Ultimate load P_{ult} versus β ratio for SHS K-joints: comparison between experimental results and predictions from EN 1993 and combined EN 1993 + EN 1999 design provisions.

Tab. 13. presents a comparison between experimentally measured vertical concentrated external forces at mid-span (F) of truss girders with various welded SHS joint configurations and theoretical force capacities predicted by Eurocode standards (EN 1993 and EN 1993 + EN 1999). The table includes joints of types X, KTR, KTL, and KC across SHS 40, SHS 50, and SHS 60 sections. The differences between experimental and theoretical values are provided both in absolute terms and as percentages to evaluate the conservativeness of the code-based predictions.

Tab. 13: The results of applied concentrated load in the moment when the SHS joint load-bearing capacity is reached.

		$F_{measured}$	$F_{teor+EN1993}$	$F_{teor+EN1993+EN1999}$	Difference			
	Joint	(5)	(6)	(7)	(5)-(6)	((5)-(6))%	(5)-(7)	((5)-(7))%
SHS 40	X	80.9	88.121	44.060	-7.221	-8.194	36.839	45.537
	KTR	108.6	157.309	78.654	-48.709	-30.963	29.945	27.574
	KTL	114.3	157.309	78.654	-43.01	-27.340	35.645	31.185
	KC	99.3	157.309	78.654	-58.01	-36.875	20.645	20.7910
		$F_{measured}$	$F_{teor+EN1993}$	$F_{teor+EN1993+EN1999}$	Difference			
	Joint	(5)	(6)	(7)	(5)-(6)	((5)-(6))%	(5)-(7)	((5)-(7))%
SHS 50	X	80.9	106.067	53.033	-25.167	-23.727	27.866	34.445
	KTR	N/A	N/A	N/A	N/A	N/A	N/A	N/A
	KTL	185.041	196.636	98.318	-11.595	-5.896	86.723	46.867
	KC	155.245	196.636	98.318	-41.391	-21.050	56.927	36.669
		$F_{measured}$	$F_{teor+EN1993}$	$F_{teor+EN1993+EN1999}$	Difference			
SHS 60	Joint	(5)	(6)	(7)	(5)-(6)	((5)-(6))%	(5)-(7)	((5)-(7))%

	X	169.900	132.910	66.455	36.990	27.831	103.445	60.886
	KTR	N/A	N/A	N/A	N/A	N/A	N/A	N/A
	KTL	N/A	N/A	N/A	N/A	N/A	N/A	N/A
	KC	N/A	N/A	N/A	N/A	N/A	N/A	N/A

The results in tab. 13. indicate that Eurocode predictions—based on EN 1993 alone or in combination with EN 1999—do not always reflect the actual behavior of welded SHS joints in aluminum truss girders.

A critical factor contributing to this divergence is the distribution of internal forces within the truss girder system. In real structural configurations, chord members are not isolated elements, they continue through the joint and, consequently, exhibit not only axial load-bearing behavior but also shear and bending resistance. These additional capacities, stemming from the continuity and stiffness of the chord, are not fully captured in simplified or isolated joint models typically used in standard design codes.

Therefore, evaluating the joint as an integral component of the global structural system, rather than as an isolated element, is essential for accurate assessment of structural performance. This integrated approach accounts for interaction effects, moment transfer, and real boundary conditions—factors which substantially influence joint strength and failure modes in practice.

CHS joints

The presented tab. 14 compares the experimentally determined ultimate load-bearing capacities of welded aluminum joints with theoretical predictions derived from EN 1993 and the combined application of EN 1993 and EN 1999. The table includes X, KTR, KTL, and KC joints fabricated from circular hollow section (CHS) aluminum profiles with diameter of 40 mm, 50 mm, and 60 mm.

Tab. 14: The results of load-bearing capacities of welded CHS aluminum joints.

		$P_{1\%bo}$	$P_{ult,\ exp}$	$P_{ult,\ EN1993+EN\ 1999}$	$P_{ult,\ EN1993}$	Difference			
	Joint	(1)	(2)	(3)	(4)	(3)-(2)	((3)-(2))%	(4)-(2)	((4)-(2))%
CHS 40	X	26.757	44.545	24.457	48.914	-20.088	-45.096	4.369	9.808
	KTR	39.498	52.623	43.659	87.319	-8.963	-17.033	34.696	65.933
	KTL	37.275	52.923	43.659	87.319	-9.264	-17.504	34.396	64.992
	KC	39.713	53.702	43.659	87.319	-10.042	-18.700	33.617	62.599

		$P_{1\%bo}$	$P_{ult,\ exp}$	$P_{ult,\ EN1993+EN\ 1999}$	$P_{ult,\ EN1993}$	Difference			
CHS 50	Joint	(1)	(2)	(3)	(4)	(3)-(2)	((3)-(2))%	(4)-(2)	((4)-(2))%
	X	41.904	56.467	29.438	58.876	-27.029	-47.867	2.409	4.266
	KTR	57.951	71.951	54.574	109.149	-17.376	-24.150	37.198	51.699
	KTL	58.788	73.101	54.574	109.149	-18.526	-25.343	36.048	49.312
	KC	54.754	71.531	54.574	109.149	-16.956	-23.705	37.618	52.589
		$P_{1\%bo}$	$P_{ult,\ exp}$	$P_{ult,\ EN1993+EN\ 1999}$	$P_{ult,\ EN1993}$	Difference			
CHS 60	Joint	(1)	(2)	(3)	(4)	(3)-(2)	((3)-(2))%	(4)-(2)	((4)-(2))%
	X	43.524	72.268	36.660	73.321	-35.607	-49.271	1.053	1.457
	KTR	N/A	N/A	N/A	N/A	N/A	N/A	N/A	N/A
	KTL	N/A	N/A	N/A	N/A	N/A	N/A	N/A	N/A
	KC	N/A	N/A	N/A	N/A	N/A	N/A	N/A	N/A

The tab. 14. clearly highlights the discrepancies between experimentally obtained and theoretically predicted ultimate loads for welded CHS joints. In nearly all cases, theoretical models, particularly those based solely on EN 1993, overestimate the joint capacities. However, when the combined approach using both EN 1993 and EN 1999 is applied, the models tend to underestimate the actual joint capacity, with some differences exceeding 45%.

For instance, the X-joint made from CHS 40 shows an experimental ultimate capacity of 44.545 kN, while the combined EN 1993+1999 prediction gives only 24.457 kN, underestimating the capacity by 45.1%. On the other hand, the same joint evaluated by EN 1993 alone slightly overestimates the strength by about 9.8%.

As the profile size increases, especially for CHS 60, the underestimation becomes more severe for EN 1993+1999 predictions, particularly in X-joints, where the discrepancy reaches nearly 49.3%. This suggests that for larger aluminum profiles, current code-based prediction models may not fully capture the complex behavior of welded joints, including local effects such as chord face plastification and HAZ softening.

Tab. 15 presents a comparison between experimentally measured vertical concentrated external forces at mid-span (F) of truss girders with various welded CHS brase joint configurations and theoretical load-bearing capacities predicted by Eurocode standards (EN 1993 and EN 1993 + EN 1999). The table includes joints of types X, KTR, KTL,

and KC across SHS 40, SHS 50, and SHS 60 sections. The differences between experimental and theoretical values are provided both in absolute terms and as percentages to evaluate the conservativeness of the code-based predictions.

Tab. 15: The results of applied concentrated load in the moment when the CHS joint load-bearing capacity is reached.

	Joint	$F_{measured}$	$F_{teor+EN1993}$	$F_{teor+EN1993+EN1999}$	Difference			
		(5)	(6)	(7)	(5)-(6)	((5)-(6))%	(5)-(7)	((5)-(7))%
CHS 40	X	82.3	69.175	34.588	13.125	18.973	47.712	57.974
	KTR	100.3	123.488	61.744	-23.188	-18.777	38.556	38.441
	KTL	100.3	123.488	61.744	-23.188	-18.777	38.556	38.441
	KC	88.3	123.488	61.744	-35.188	-28.494	26.556	30.074
	Joint	$F_{measured}$	$F_{teor+EN1993}$	$F_{teor+EN1993+EN1999}$	Difference			
		(5)	(6)	(7)	(5)-(6)	((5)-(6))%	(5)-(7)	((5)-(7))%
CHS 50	X	99.9	83.263	41.631	16.637	19.9813	58.2685	58.327
	KTR	128.288	154.36	77.180	-26.072	-16.890	51.108	39.838
	KTL	130.383	154.36	77.180	-23.977	-15.533	53.203	40.805
	KC	115.6	154.36	77.180	-38.76	-25.110	38.42	33.235
	Joint	$F_{measured}$	$F_{teor+EN1993}$	$F_{teor+EN1993+EN1999}$	Difference			
		(5)	(6)	(7)	(5)-(6)	((5)-(6))%	(5)-(7)	((5)-(7))%
CHS 60	X	127.947	103.692	51.846	24.255	23.391	76.101	59.478
	KTR	N/A	N/A	N/A	N/A	N/A	N/A	N/A
	KTL	N/A	N/A	N/A	N/A	N/A	N/A	N/A
	KC	N/A	N/A	N/A	N/A	N/A	N/A	N/A

For CHS 40 joints, the experimentally measured loads exceed the theoretical predictions from both codes for the X-joint, by 19% (EN 1993) and 58% (EN 1993+1999) respectively. However, for K-type joints, theoretical predictions from EN 1993 are often higher than measured loads, with differences ranging from -19% to -28%, indicating conservative predictions for compressed and tensioned braces. Still, significant underestimation is noted when comparing with EN 1993 + EN 1999 (differences of 38–57%).

CHS 50 joints exhibit a similar trend. The experimental load in the X-joint exceeds EN 1993 and EN 1993 + EN 1999 predictions by 20% and 58%, respectively. For K-joints,

although the measured values are lower than EN 1993 predictions, the EN 1993 + EN 1999 models again substantially underestimate the actual behavior (by ~40–58%).

In the case of the CHS 60 X-joint, the measured load is significantly higher than both theoretical predictions, by 23% (EN 1993) and 59% (EN 1993 + EN 1999).

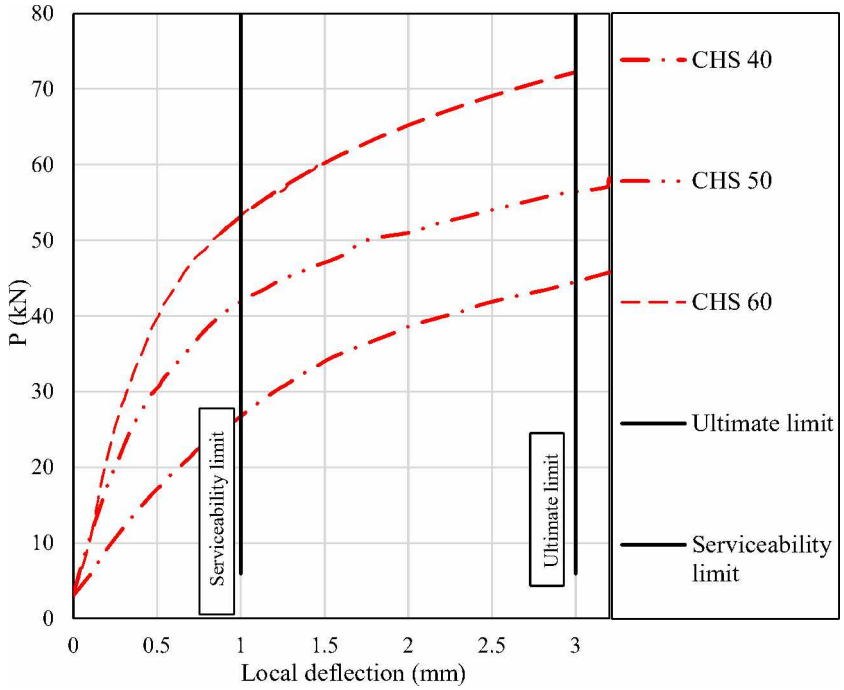

Fig. 39: X joint: axial force versus local deflection

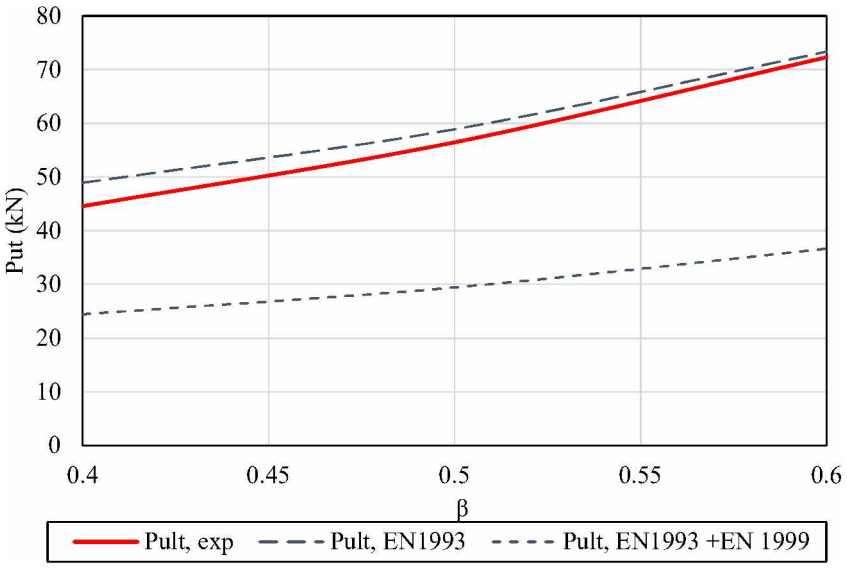

Fig. 40: Ultimate load P_{ult} versus β ratio for CHS X-joints: comparison between experimental results and predictions from EN 1993 and combined EN 1993 + EN 1999 design provisions.

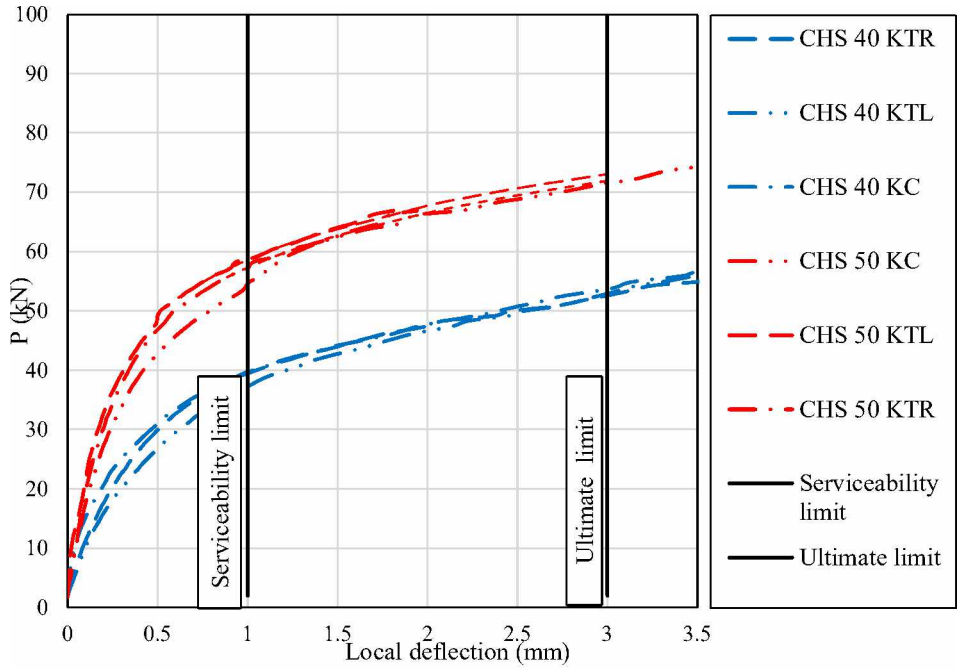

Fig. 41: K joint: axial force versus local deflection

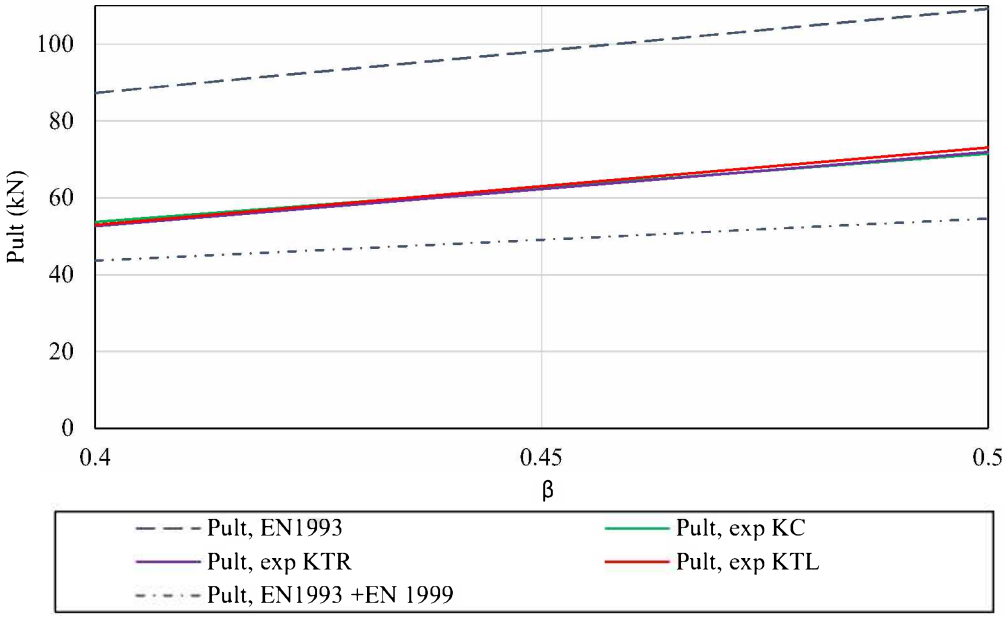

Fig. 42: Ultimate load P_{ult} versus β ratio for CHS K-joints: comparison between experimental results and predictions from EN 1993 and combined EN 1993 + EN 1999 design provisions.

4.1.6 Investigation of welded isolated X joints

Twelve isolated X joints, fig. 43, manufactured from the aluminum alloy EN AW6082 T6 in total were investigated in this experiment. Brace members and chord members were joined together directly using TIG welding with the filler rod ER 5356 (AlMg5).

The chord member had length of 600 mm while length of brace member was 300 mm. All tested X joints had the same chord member, which was SHS 100 × 5 profiles. In order to carry out the parametric analysis, the brace members' shape and size were altered. Circular hollow sections (CHS) with cross-sectional diameters of 40, 50, and 60 mm were used to construct six joints, each brace member repeated two times. truss girders. Brace members from SHS profiles with widths of 40, 50, and 60 mm were used to construct the other six joints. The joints were centered without eccentricities e=0. The brace members have been joined to the chord members at the angle θ_i=90°. Regarding this, the β coefficient varied from 0.4 (SHS40 and CHS40) to 0.6 (SHS60 and CHS 60), which refers to the ratio of the width or diameter of the brace member to the width of the chord member. The joints met all the requirements of EN 1993-1-8 [3] and were concentric.

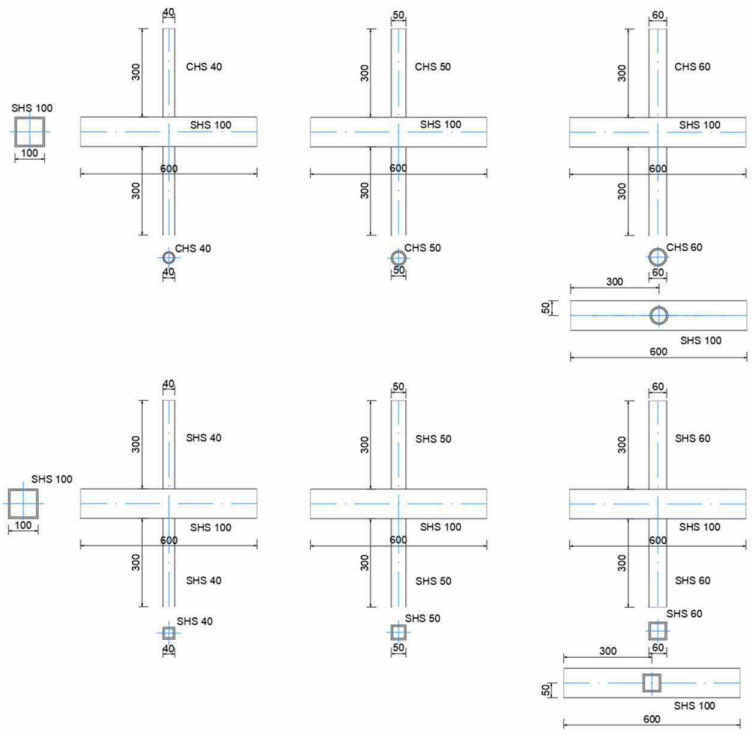

Fig. 43: Specimens of isolated X joints

Specimen labeling

The X joints have been designated based on the brace member cross-section from which they are constructed. Therefore, the truss girders are labeled as X SHS 40-1, X SHS 40-2, X SHS 50-1, X SHS 50-2, X SHS 60-1, X SHS 60-2, and X CHS 40-1, X CHS 40-2, X CHS 50-1, X CHS 50-2, X CHS 60-1, X CHS 60-2.

Fig. 44: Specimen labeling.

Experimental setup

The X joint, shown in Fig. 45, was installed in the testing frame (I) and subjected to a single axial force (II) applied at the top of the brace member. A load cell (III), mounted on the top of the brace member, received the load from the hydraulic press (II) above. Linear transducers were used to measure the local deflection of the chord members' surfaces (1,2).

After positioning the specimen in the testing frame, an initial preload of approximately 0.5 kN was applied to allow the specimen to settle into its optimal position. The loading was then increased incrementally at a rate of 1 kN/min using a hydraulic press, with data acquisition equipment recording the results until plastification of the X-joint was observed, defined by joint deflections without further load increase. Maximum joint deformation occurred at the contact point between the compression brace member and the chord.

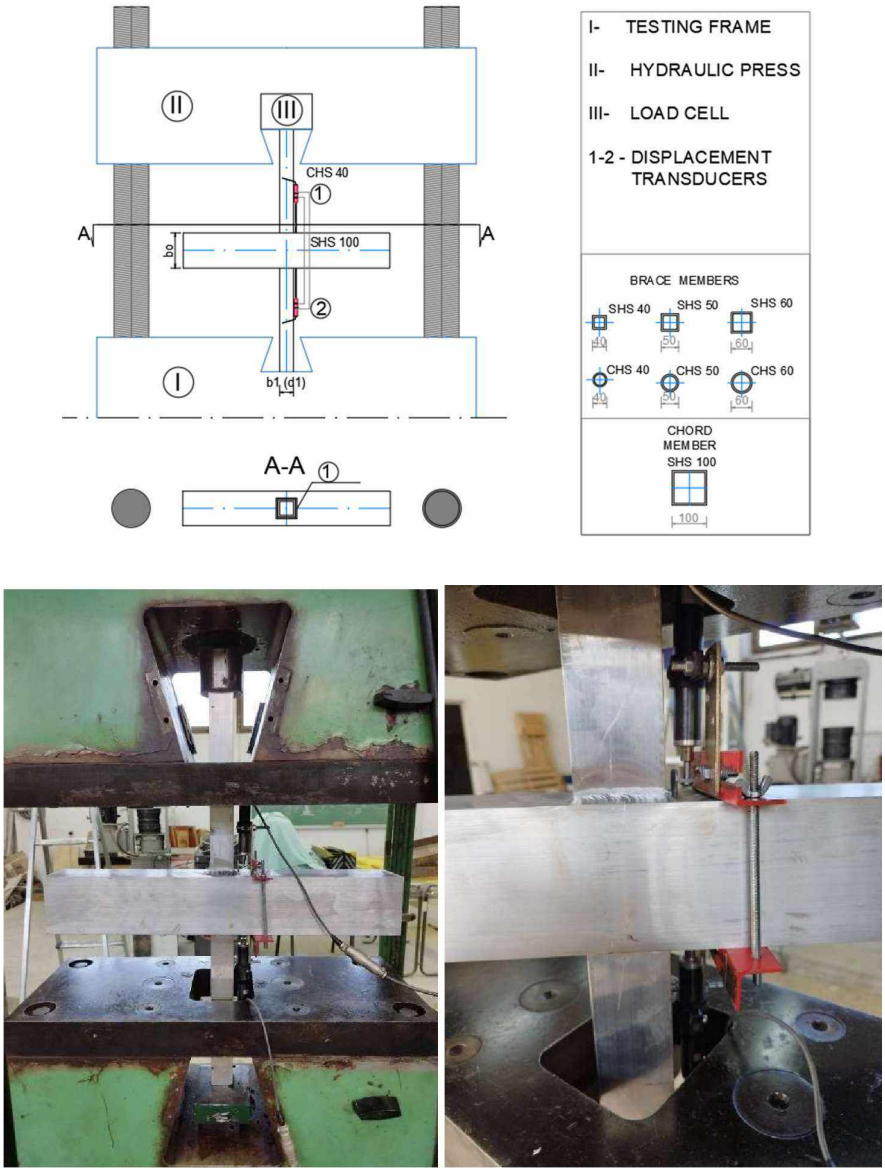

Fig. 45: Experimental setup

Experimental results and discussion

The Tab. 16 presents the experimental results for isolated SHS X-joints composed of EN AW-6082 T6 aluminum alloy, with square hollow section (SHS) brace members of varying sizes (40 mm, 50 mm, and 60 mm). Each joint was tested to determine its experimental ultimate load-bearing capacity ($P_{ult,exp}$)which was then compared with two theoretical predictions: one based on EN 1993 alone ($P_{ult,EN\ 1993}$) and another based on a combined model from EN 1993 and EN 1999 ($P_{ult,EN\ 1993\ +\ EN\ 1999}$).

Tab. 16: The experimental results of load-bearing capacites for isolated SHS X-joints compared to values obtained thru EN 1993 and EN 1999 codes.

X joint	$P_{1\%bo}$	$P_{ult,exp}$	$P_{ult,EN1993+EN1999}$	$P_{ult,EN1993}$	Difference			
	-4	-5	-6	-7	(5)-(6)	((5)-(6))%	(5)-(7)	((5)-(7))%
SHS40-1-1	19.09	32.89	20.304	40.608	12.586	38.267	7.718	19.006
SHS40-1-2	20.13	33.31	20.304	40.608	13.006	39.045	7.298	17.972
SHS40-2-1	17.03	30.55	20.304	40.608	10.246	33.538	10.058	24.769
SHS40-2-2	17.79	31.335	20.304	40.608	11.031	35.203	9.273	22.835
X joint	$P_{1\%bo}$	$P_{ult,exp}$	$P_{ult,EN1993+EN1999}$	$P_{ult,EN1993}$	Difference			
	-4	-5	-6	-7	(5)-(6)	((5)-(6))%	(5)-(7)	((5)-(7))%
SHS50-1-1	26.96	40.357	23.928	47.855	16.429	40.709	7.498	15.668
SHS50-1-2	28.89	43.326	23.928	47.855	19.398	44.772	4.529	9.464
SHS50-2-1	27.16	41.781	23.928	47.855	17.853	42.730	6.074	12.693
SHS50-2-2	28.83	47.43	23.928	47.855	23.502	49.551	0.425	0.888
X joint	$P_{1\%bo}$	$P_{ult,exp}$	$P_{ult,EN1993+EN1999}$	$P_{ult,EN1993}$	Difference			
	-4	-5	-6	-7	(5)-(6)	((5)-(6))%	(5)-(7)	((5)-(7))%
SHS60-1-1	41.43	55.801	29.139	58.278	26.662	47.781	2.477	4.250
SHS60-1-2	40.645	58.252	29.139	58.278	29.113	49.978	0.026	0.045
SHS60-2-1	35.905	53.703	29.139	58.278	24.564	45.740	4.575	7.850
SHS60-2-2	39.107	57.926	29.139	58.278	28.787	49.696	0.352	0.604

For SHS 40 joints, the experimental ultimate loads ranged between 30.55 kN and 33.31 kN, while the EN 1993 + EN 1999 predictions significantly underestimated the capacity, with differences up to ~39%. In contrast, predictions from EN 1993 alone slightly overestimated the joint capacity by about 18–25%, indicating a conservative design approach.

SHS 50 joints showed better agreement between experimental and EN 1993 predictions. The largest deviation from EN 1993 + EN 1999 occurred for sample SHS50-2-2, with a discrepancy of nearly 50%, while EN 1993 predicted the ultimate capacity almost exactly, differing by less than 1%.

SHS 60 joints followed a similar trend, with experimental values substantially exceeding EN 1993 + EN 1999 predictions by up to 49%. Notably, EN 1993 predictions were much

closer, with differences ranging from 0.03% to just over 7%, confirming its applicability for larger cross-sections.

These results suggest that the combined EN 1993 + EN 1999 model underestimates the capacity of welded SHS joints, particularly for joints with smaller β ratios, see Figs. 45 - 48. The EN 1993 model alone provides more reliable estimates across all tested configurations. This supports the hypothesis that welded SHS joints behave more robustly than currently assumed in aluminum design codes, particularly in concentric joint arrangements without eccentricities.

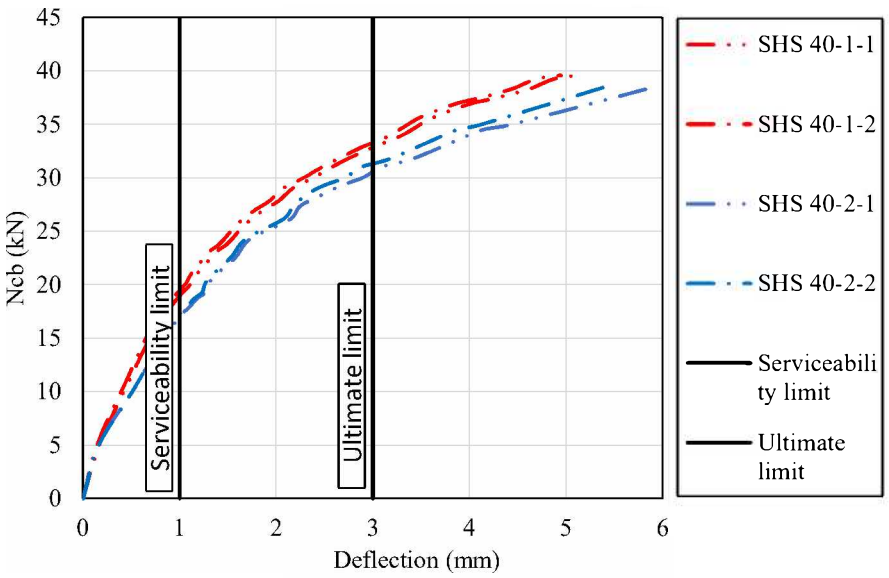

Fig. 45: Force-deflection curve for SHS 40 X-joint

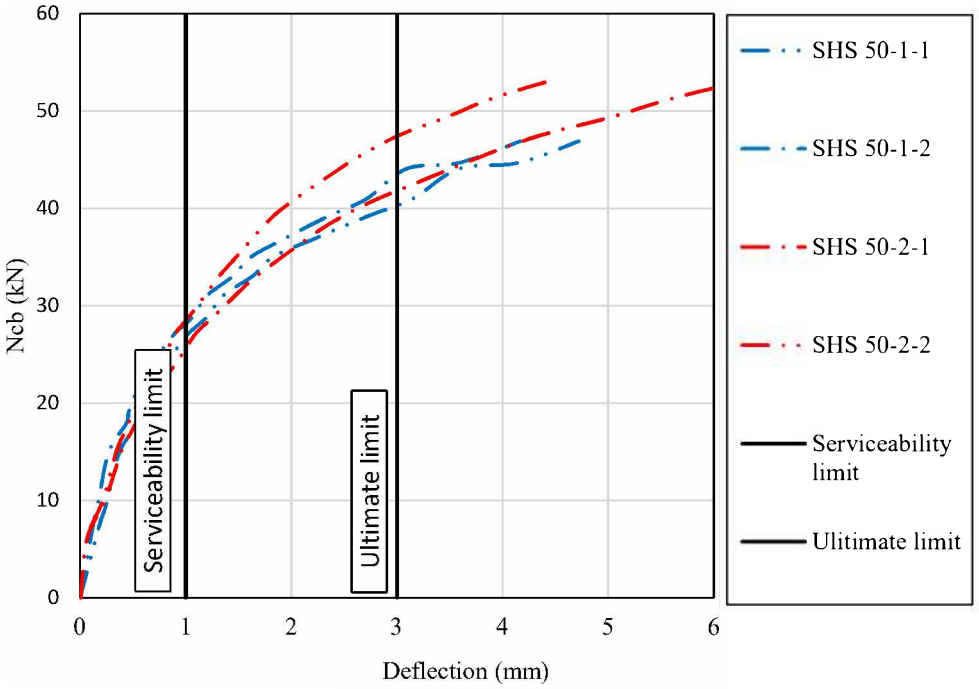

Fig. 46: Force-deflection curve for SHS 50 X-joint

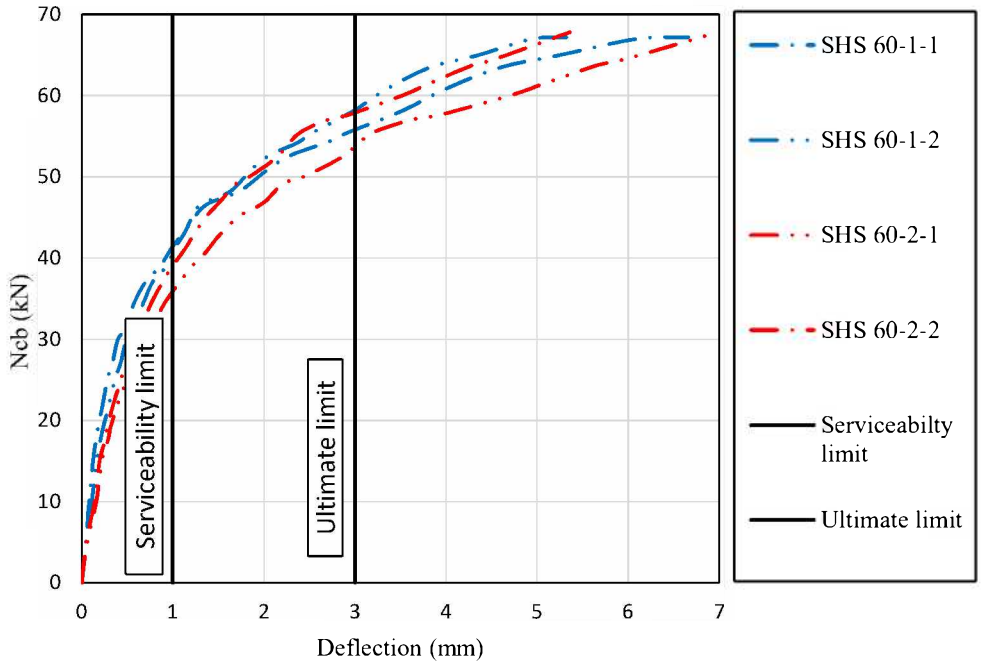

Fig. 47: Force-deflection curve for SHS 60 X-joint

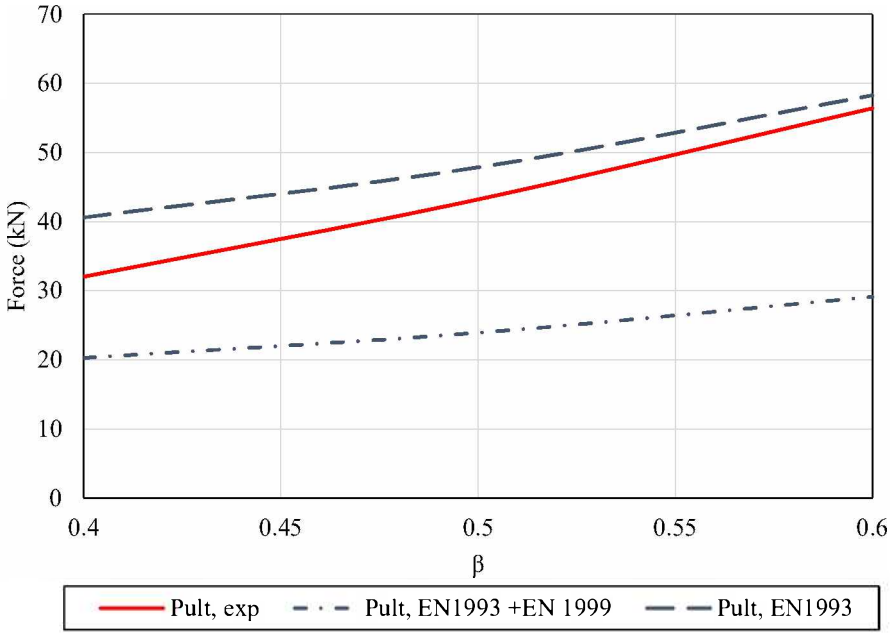

Fig. 48: Ultimate load P_{ult} versus β ratio for SHS isolated X-joints: comparison between experimental results and predictions from EN 1993 and combined EN 1993 + EN 1999 design provisions.

The tab.17 summarizes the experimental and theoretical ultimate load-bearing capacities of concentric X-joints composed of EN AW-6082 T6 aluminum alloy, where brace members are circular hollow sections (CHS) and the chord member is an SHS 100 × 5 profile. The brace diameters tested were 40 mm, 50 mm, and 60 mm, corresponding to β ratios of 0.4, 0.5, and 0.6, respectively. The theoretical capacities were calculated using both EN 1993 alone and in combination with EN 1999, allowing for a direct comparison with experimental findings.

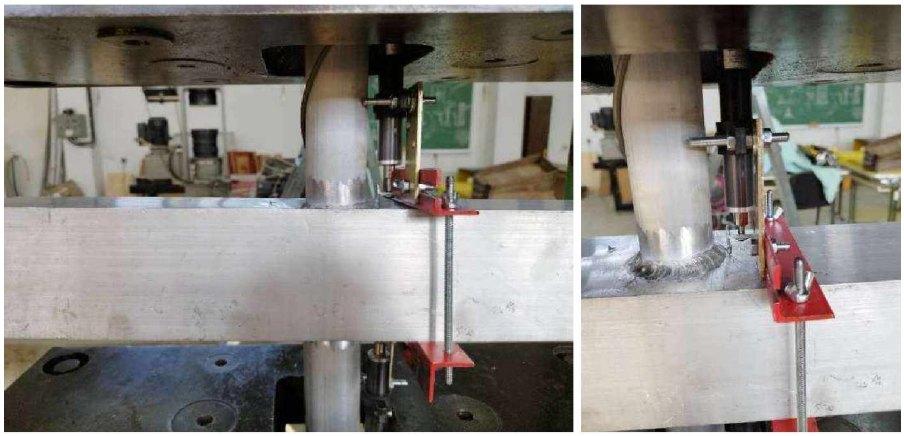

Fig. 49: Testing setup for isolated CHS X joints.

Tab. 17: The experimental results of load-bearing capacites for isolated CHS X-joints compared to values obtained thru EN 1993 and EN 1999 codes.

X joint	P_{serv} (kN)	$P_{ult, exp}$ (kN)	$P_{ult, EN1993 +EN 1999}$ (kN)	$P_{ult, EN1993}$ (kN)	Difference			
	-4	-5	-6	-7	(5)-(6)	((5)-(6))%	(5)-(7)	((5)-(7))%
CHS40-1-1	12.791	24.978	15.974	31.95	9.004	36.048	6.972	21.822
CHS40-1-2	13.177	25.999	15.974	31.95	10.025	38.559	5.951	18.626
X joint	P_{serv} (kN)	$P_{ult, exp}$ (kN)	$P_{ult, EN1993 +EN 1999}$ (kN)	$P_{ult, EN1993}$ (kN)	Difference			
	-4	-5	-6	-7	(5)-(6)	((5)-(6))%	(5)-(7)	((5)-(7))%
CHS50-1-1	22.372	36.146	18.793	37.586	17.353	48.008	1.44	3.831
CHS50-1-2	21.796	35.295	18.793	37.586	16.502	46.754	2.291	6.095
CHS50-2-1	23.038	34.567	18.793	37.586	15.774	45.633	3.019	8.032
CHS50-2-2	25.26	38.723	18.793	37.586	19.93	51.468	-1.137	-3.025
X joint	P_{serv} (kN)	$P_{ult, exp}$ (kN)	$P_{ult, EN1993 +EN 1999}$ (kN)	$P_{ult, EN1993}$ (kN)	Difference			
	-4	-5	-6	-7	(5)-(6)	((5)-(6))%	(5)-(7)	((5)-(7))%
CHS60-1-1	25.351	41.534	22.886	45.771	18.648	44.898	4.237	9.257
CHS60-1-2	29.36	47.397	22.886	45.771	24.511	51.714	-1.626	-3.552
CHS60-2-1	30.679	44.683	22.886	45.771	21.797	48.781	1.088	2.377
CHS60-2-2	31.91	46.23	22.886	45.771	23.344	50.495	-0.459	-1.003

For CHS 40 joints, the EN 1993 + EN 1999 predictions underestimated the joint capacity by over 36%, while EN 1993 alone slightly overpredicted the capacity by about 19–22%. This underlines the conservative nature of current aluminum joint codes, particularly when dealing with smaller-diameter brace members.

In CHS 50 joints, the experimental values exceeded EN 1993 + EN 1999 predictions by 45–51%, a significant deviation indicating that current combined-code approaches may not adequately capture the actual strength of such joints. However, EN 1993 alone predicted the ultimate capacities with greater accuracy, deviating by only ±3% to 8% in most cases.

The CHS 60 joints showed a similar trend. Experimental loads were on average 45–51% higher than those predicted by EN 1993 + EN 1999. EN 1993 estimates were much closer to the experimental values, with deviations ranging from -3.5% to +9.3%, indicating a better alignment between code predictions and real behavior for joints with larger brace diameters.

These findings highlight that theoretical predictions, particularly those using the combination of EN 1993 and EN 1999, tend to be overly conservative when applied to CHS-to-SHS welded aluminum X-joints, Figs. 50.-54. EN 1993 alone yields more realistic values, especially for larger β ratios. Consequently, this suggests the need for recalibration or refinement of aluminum joint models to better reflect actual performance, particularly under axial loading and when accounting for the structural integrity of full-scale truss systems.

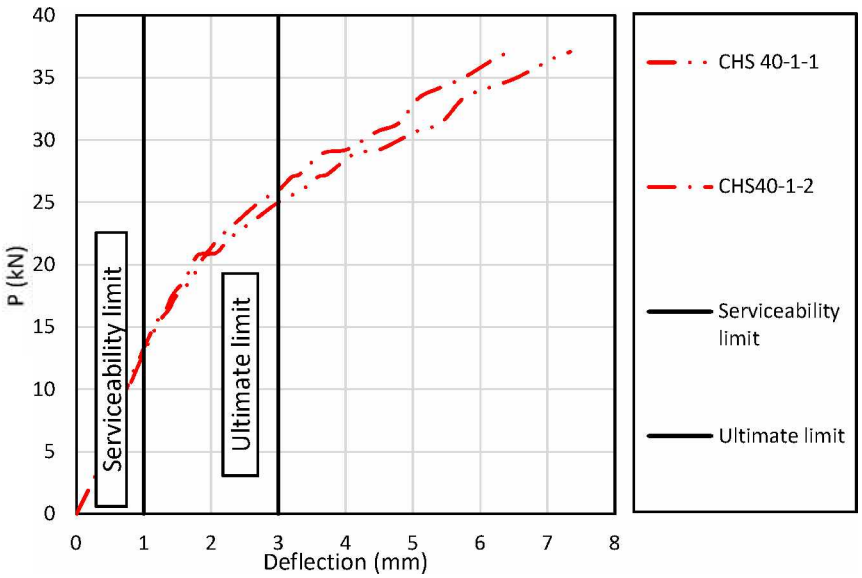

Fig. 50: Force-deflection curve for CHS 40 X-joint

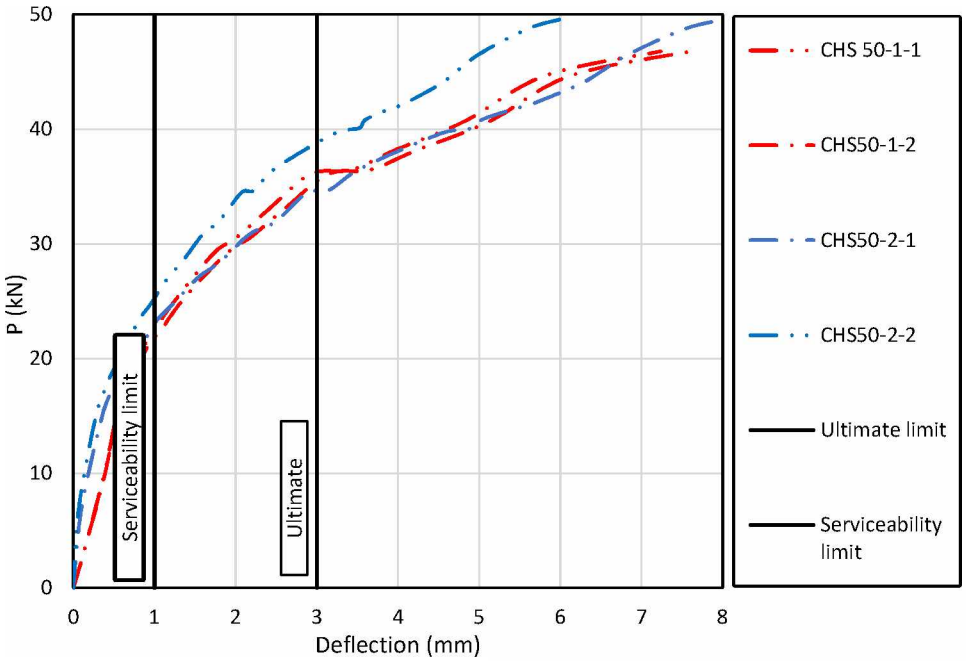

Fig. 51: Force-deflection curve for CHS 50 X-joint

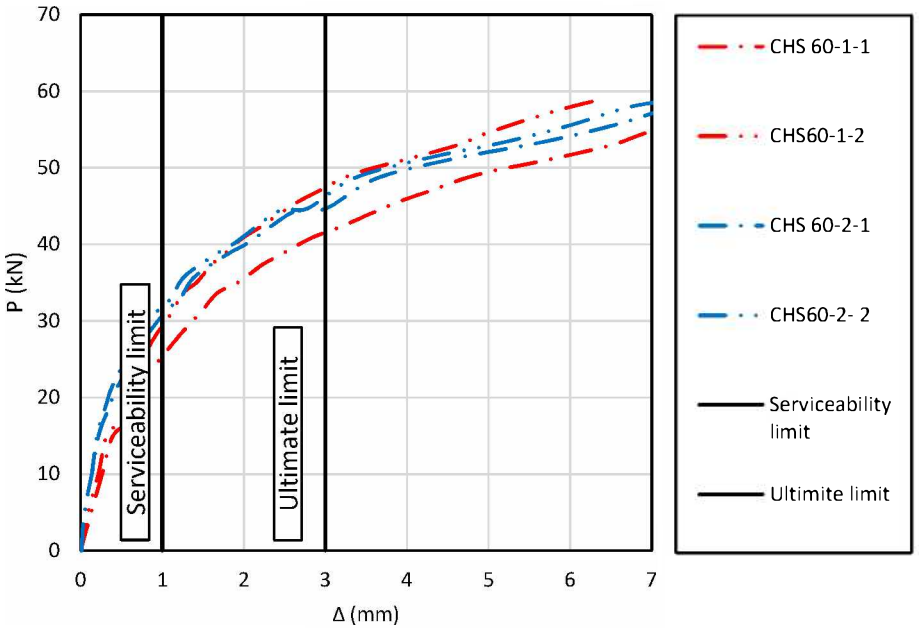

Fig. 52: Force-deflection curve for CHS 60 X-joint

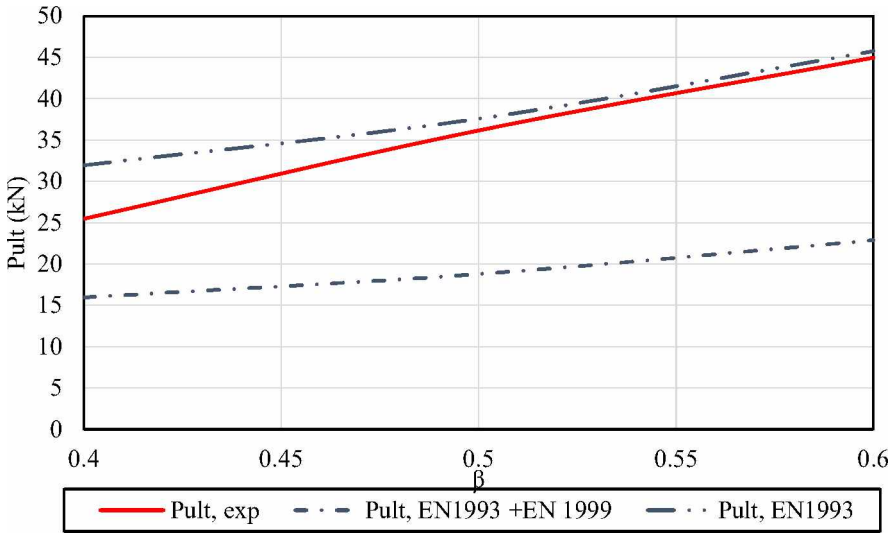

Fig. 53: Ultimate load P_{ult} versus β ratio for CHS isolated X-joints: comparison between experimental results and predictions from EN 1993 and combined EN 1993 + EN 1999 design provisions.

Fig. 54: Isolated CHS X joint- chord face plastification

Hardness measurements

The strength values [51] in the HAZ next to the weld were derived by hardness tests. In [30,31] a linear relationship for EN AW-6082-T6 (the material from which the specimens are made) between the Vickers hardness test and uniaxial tensile strength test is introduced by the following expressions:

$$f_o(MPa) = 3.6HV - 81$$

$$f_u(MPa) = 2.6HV + 54$$

Where HV [51] is the Vickers hardness, f_o is the yield strength and fu is the ultimate load-bearing capacity or strength. The following Table 3. presents the respective values for yield stress and tensile strength. HV is the Vickers hardness, fo is the yield strength and fu is the ultimate load-bearing capacity or strength.

The Vickers hardness values [51] presented in Tab. 18. are displayed graphically in the following Fig. 55. The lowest hardness values are near the weld toe, around HV 53, and gradually increase to HV 77 at a distance of 30 mm from the weld toe. These results are expected and relate to the HAZ reduction factor [6]. It can be seen that the values for the reduction coefficient $\rho_{o,HAZ}$ defined in prEN 1999-1-1 [6] are based on the value of reduction at the vicinity of the weld toe. That approach is convenient for simplified calculations in engineering practice.

The purpose of this hardness measurements [51] are to develop an FEM model in order to obtain a more accurate behavior of the observed structure, in this case the behavior of the joint, therefore the model of the HAZ zone is defined with two subzones, HAZ 1 and HAZ 2, based on the hardness test results. This approach is less conservative and gives more realistic and accurate results. HAZ 1 is adopted as the heat-affected zone where the HV is less than 60, which approximately corresponds to the width of the HAZ from the weld toe up to 20 mm and the area under the brace member and weld, while the rest of the HAZ is defined as HAZ 2 and is the area between 20 mm to 30 mm from the weld toe. The cumulative area of HAZ 1 and HAZ 2 is 30 mm, which, based on the welding method (TIG) and the thickness of the used elements, corresponds to the area b_{HAZ} defined in EN 1999-1-1 [6], see Table 1.

Tab. 18: Hardness test results and mechanic characteristics of a welded SHS 40 joint.

Angle	distance (mm)	5	10	15	20	25	30	35	40
0°	HV	53	59	66	69	77	77	77	80
	f_o (MPa)	*110*	132	156	166	196	196	196	208
	f_u (MPa)	*192*	208	225	232	254	254	254	262
22.5°	HV	57	61	74	74	77	74	74	74
	f_o (MPa)	110	132	156	166	196	196	196	208
	f_u (MPa)	202	213	247	247	254	247	247	247
45°	HV	66	66	74	77	77	80		
	f_o (MPa)	156	156	186	196	196	208		
	f_u (MPa)	225	225	247	254	254	262		

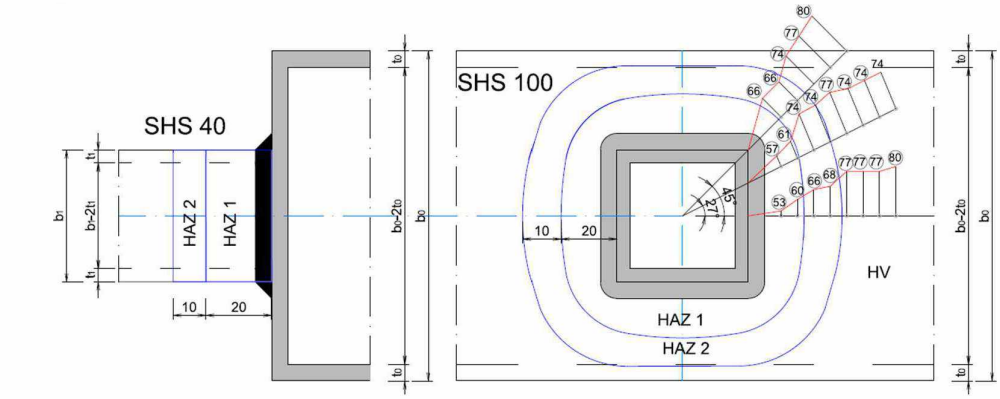

Fig. 55: Hardness test results for SHS T joint

4.2 Numerical investigation

4.2.1 Investigation of welded aluminiuim truss girders

The primary objective of the numerical investigation was to develop a validated finite element model that can be reliably used in engineering practice and research. This model will extend the experimental data and enable comprehensive parametric analyses aimed at deepening the understanding of the structural behavior of welded aluminum joints as shown in tab. 19.

Two critical dimensionless parameters will be systematically varied and evaluated:

- β– This parameter represents the ratio between the width (or diameter) of the brace member and the width of the chord member. It also implicitly accounts for the influence of the welded surface area of the brace member. For this investigation, β values ranged from 0.4 to 0.6, corresponding to the practical configurations tested in the experimental program.

- γ– This parameter is defined as the ratio between the width of the chord member and twice the wall thickness of the chord member. The parameter reflects the chord's local stiffness and its ability to distribute stresses around the joint area. The values of γ to be considered in this study were 10, 12, and 15, capturing a representative range of typical chord geometries.

The parametric study facilitated the identification of critical factors governing joint performance and supported the development of improved analytical models and design recommendations for welded aluminum structures.

Tab. 19: SHS joints configurations with geometric parameters and experimental test status.

Model no.	Chord	Brace	bo	to	bi	β	bo/to	γ	Experiment
1	SHS 100	SHS 40	100	5	40	0.4	20	10	Yes
2	SHS 100	SHS 50	100	5	50	0.5	20	10	Yes
3	SHS 100	SHS 60	100	5	60	0.6	20	10	Yes
4	SHS 120	SHS 50	120	5	50	0.416	24	12	No
5	SHS 120	SHS 60	120	5	60	0.5	24	12	No
6	SHS 120	SHS 70	120	5	70	0.583	24	12	No
7	SHS 150	SHS 60	150	5	60	0.4	30	15	No
8	SHS 150	SHS 70	150	5	70	0.466	30	15	No
9	SHS 150	SHS 80	150	5	80	0.533	30	15	No
10	SHS 150	SHS 90	150	5	90	0.6	30	15	No

Model geometry and boundary conditions

Numerical simulation [51] was executed using the FE method by the software ANSYS [82]. Only one-quarter of the specimen was modeled due to symmetry. Line C-C support was modeled as support with prevented displacement in the Y and X directions, whereas line B-B support was modeled as support with prevented displacement in the X direction, as shown in Fig. 56.

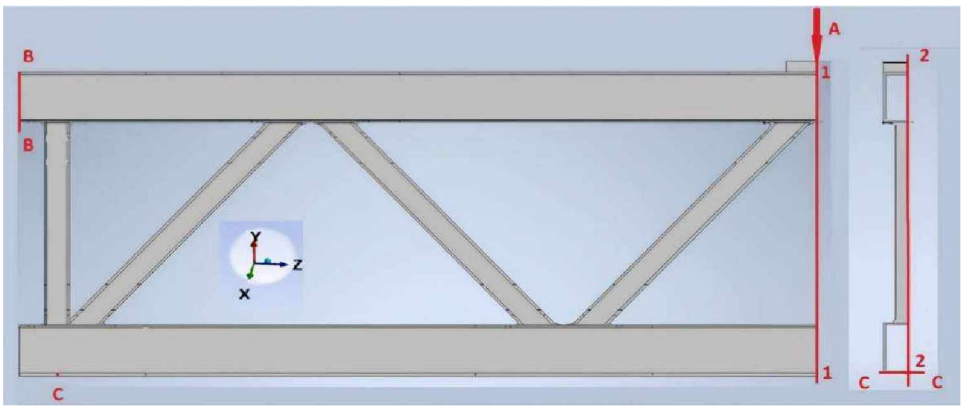

Fig. 56: Boundary and symmetry conditions of one-quarter of the specimen

In the ANSYS model [51], the HAZ zones with the softening influence were modeled. The area of the chord overlapping with the brace and extending 20 mm on both sides of the brace along the contour of the chord's cross-section was defined as HAZ 1 in the chord.
In the case of the brace member, HAZ 1 represented a 20-mm zone from the contact with the chord. HAZ 2 was defined as a 10-mm zone adjacent to HAZ 1, extending into both the chord and brace members. Multilinear diagrams were used for defining the material behavior in both zones, HAZ 1 and HAZ 2. The positions of the HAZs are presented in Fig. 57. Bonded contacts were used to model the interactions between the welds and heat-affected zones (HAZs), as well as between the HAZs and base material.

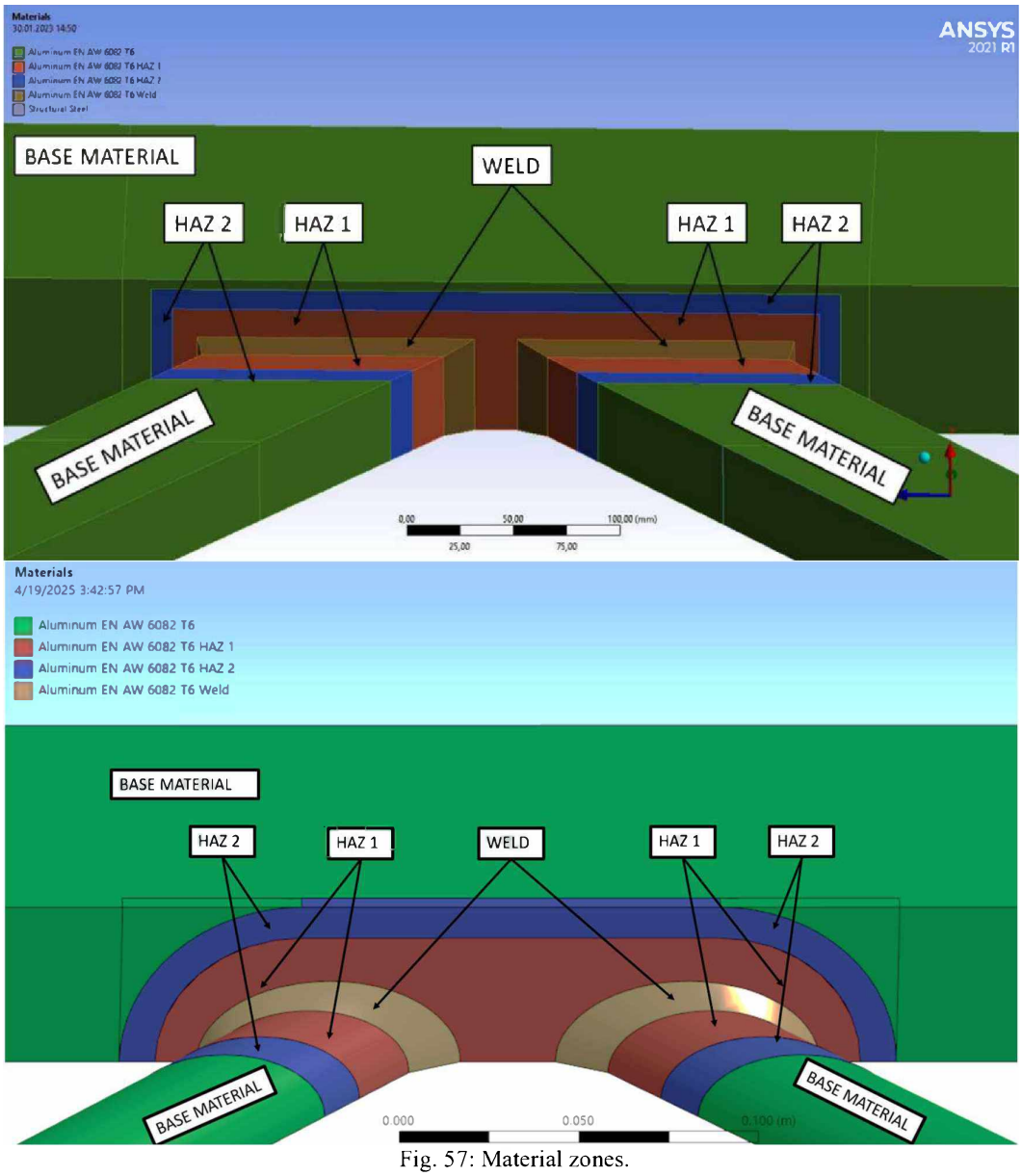

Fig. 57: Material zones.

Material definitions

The nonlinear behavior [51] of the material was taken into account, with the maximum deformations occurring within the plasticity domain. For numerical investigation, Ramberg–Osgood's equation of the stress– strain nonlinearity relation of a material [6] was applied for the welds and HAZ zones. The respective parameters are given in EN 1999- 1-1 [6], Annex E, while for the HAZ zone, the HAZ area and yield stress distribution due to the softening effect are taken from the mi-crohardness testing. Engineering stress–strain curves were transformed into true ones with the following well-known expressions:

$$\epsilon_{true} = ln(1+\epsilon_{eng})$$

and

$$\sigma_{true} = \sigma_{eng}(1+\epsilon_{eng})$$

The stress–strain curves [51] for the base material, heat-affected zones, and welds (multilinear isotropic) are presented in Fig. 58.

The characteristics of the material near the weld [51] were calculated using the Vickers method based on surface hardness testing. For all materials, an elasticity modulus E of 70 GPa was adopted.

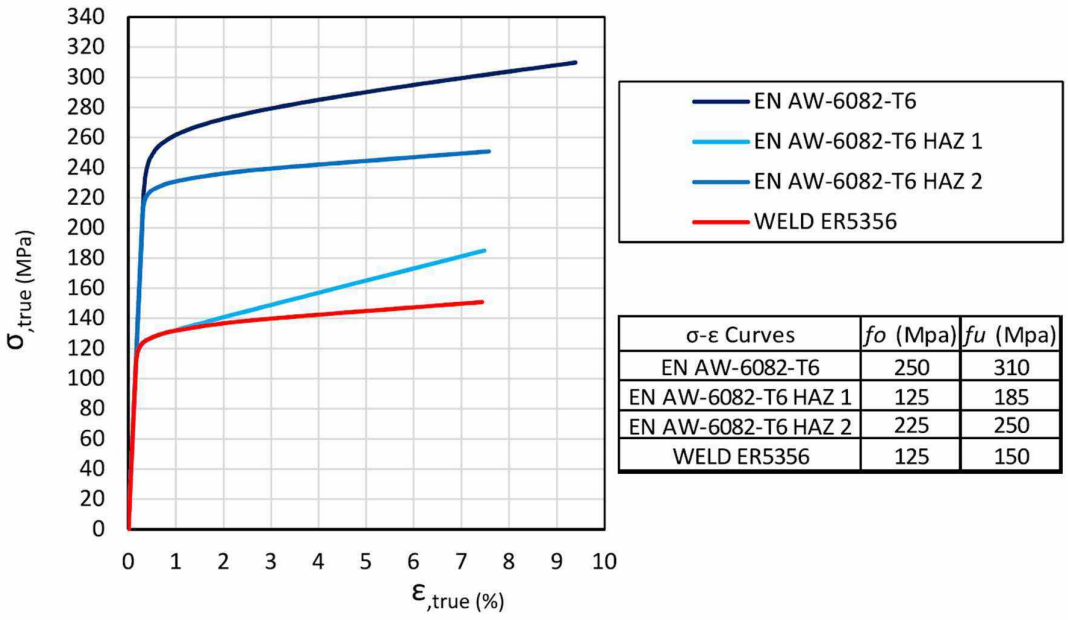

σ-ε Curves	*fo* (Mpa)	*fu* (Mpa)
EN AW-6082-T6	250	310
EN AW-6082-T6 HAZ 1	125	185
EN AW-6082-T6 HAZ 2	225	250
WELD ER5356	125	150

Fig. 58: True stress–strain curves.

Mesh Convergency

Convergence analysis has been executed on the model of the SHS 40 truss girder, see Fig. 59 and Tab. 20. The chord member was SHS 100 and the brace member was SHS 40. Modeling was done with solid bodies and based on symmetry rules the model was made for a quarter of a truss girder. Truss girder was modeled as a solid body and HEX 20 finite element were used dominantly. Meshing was done with a multi-zone function.

Bodies inside the model were separated as:

1. Base material- solid bodies of aluminum truss girder that are not affected by HAZ
2. Weld- Solid bodies of weld
3. HAZ 1- Heat affected zone close to weld, width 20mm
4. HAZ 2- Heat affected zone 2nd part, width 10mm

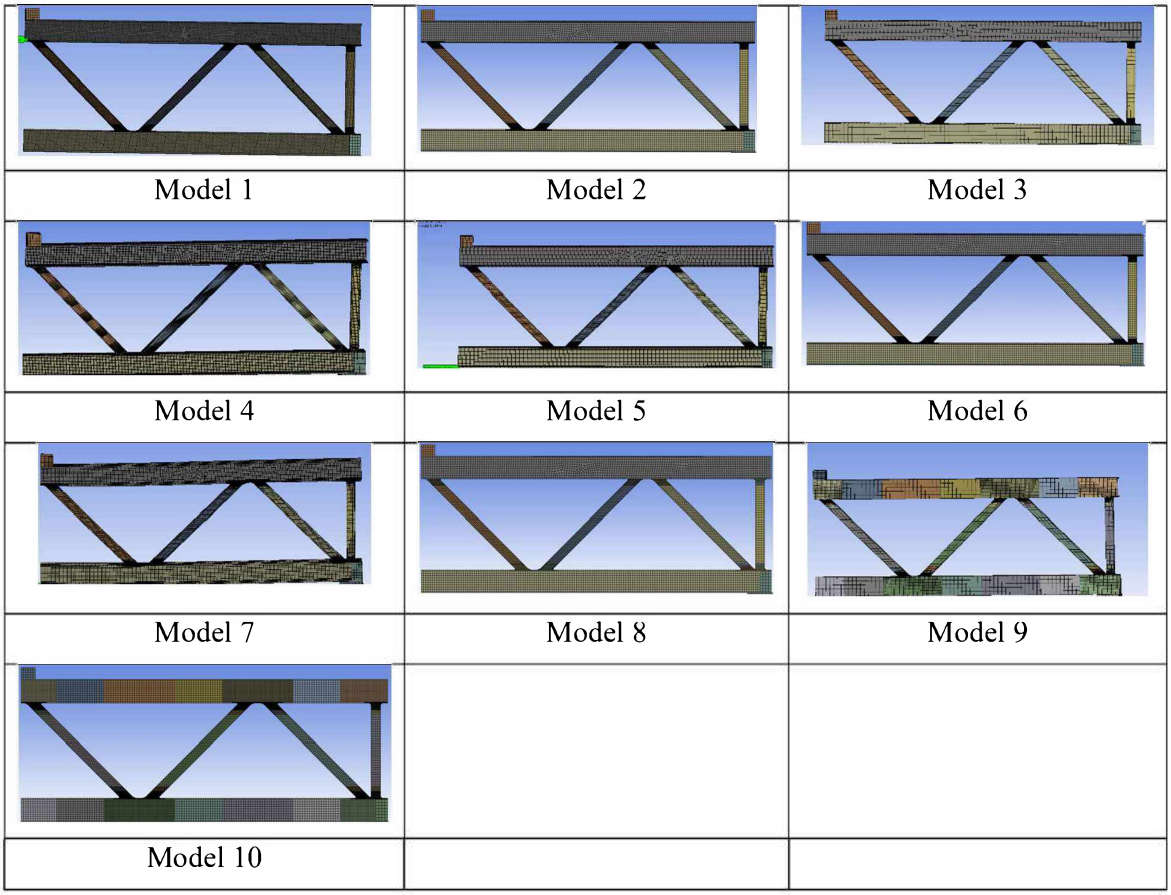

Fig. 59: Convergency FEM models

Tab. 20: Convergency analysis of the mesh

Model no.	Size of Finite elements				Elastic deformation F= 10 kN(40kN)									Local plastic deformation F=20kN(80 kN)	
							Ratio					Ratio			
	Base material (mm)	HAZ 1 (mm)	HAZ 2 (mm)	Weld (mm)	P2 (mm)	P1 (mm)	P1 (mm)	P1 %	P2 (mm)	P2 %	P1 - P2	(mm)	%	P1 (mm)	P2 (mm)
1	5	1	1	1	-4.765	-4.323	0.000	0	0.000	0	-0.442	0.000	0.00	-18.237	-18.774
2	10	1	1	1	-4.829	-4.386	0.064	1.33	0.063	1.44	-0.443	0.001	0.20		
3	20	1	1	1	-4.907	-4.464	0.143	2.91	0.142	3.17	-0.443	0.001	0.27		
6	10	1	2	1	-4.955	-4.500	0.191	3.85	0.177	3.94	-0.455	0.013	2.94		
4	5	2	2	2	-4.913	-4.437	0.148	3.01	0.114	2.57	-0.476	0.034	7.11		
5	10	2	2	2	-5.044	-4.558	0.280	5.55	0.235	5.16	-0.487	0.045	9.20	-17.929	-18.797
7	10	2	5	2	-5.051	-4.556	0.287	5.68	0.233	5.11	-0.496	0.054	10.84		
9	20/10	2	5	2	-5.157	-4.645	0.393	7.61	0.323	6.94	-0.512	0.070	13.67	-17.901	-18.882
8	10	5	5	5	-5.384	-4.870	0.620	11.51	0.547	11.24	-0.514	0.072	14.08		
10	10/5	2	2	2	-4.9778	-4.4905	0.2133	4.29	0.168	3.74	-0.487	0.045	9.32		

In the FEM analysis [51], solid finite HEX20 elements with reduced integration were used. These elements are characterized by 20 nodes, each with three degrees of freedom, and can be oriented in any spatial direction. For modeling the HAZ 1 and WELD zones, three layers of elements are applied across the member profile's wall thickness, while two layers are used for the HAZ 2 zone. The WELD zones are represented using TET 10 elements, which are characterized by 10 nodes, each with three degrees of freedom and capable of any spatial orientation. The width of the finite elements in the HAZ 1 and WELD zones is 2 mm, while the width of the finite elements in the HAZ 2 zone is 5 mm, the width of finite elements in the base material in proximity to the HAZ zones is 10 mm, and the width in the rest of the truss girder is 20 mm, as shown in Fig. 22. The gap

between the brace and the chord members is modeled such that the force is transferred only through the weld, see Figs. 60.-61.

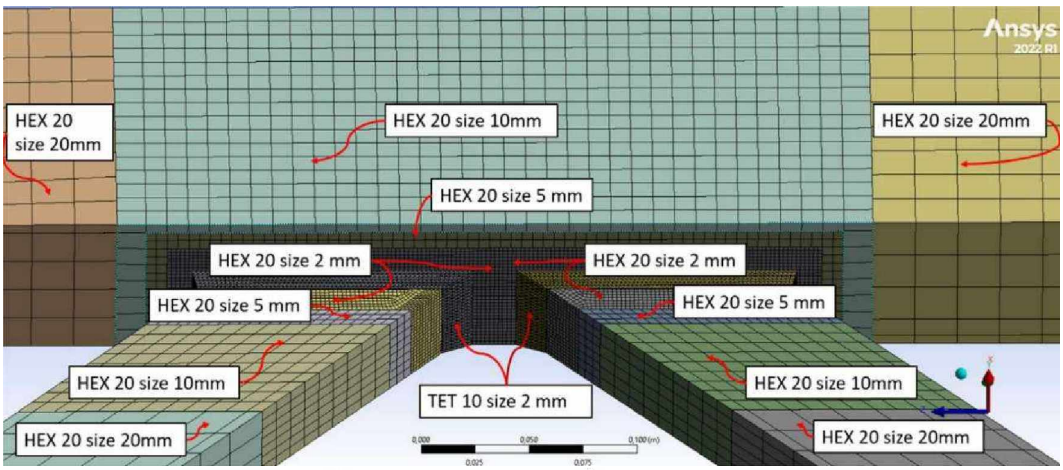

Fig. 60. Finite elements of the SHS K-joint.

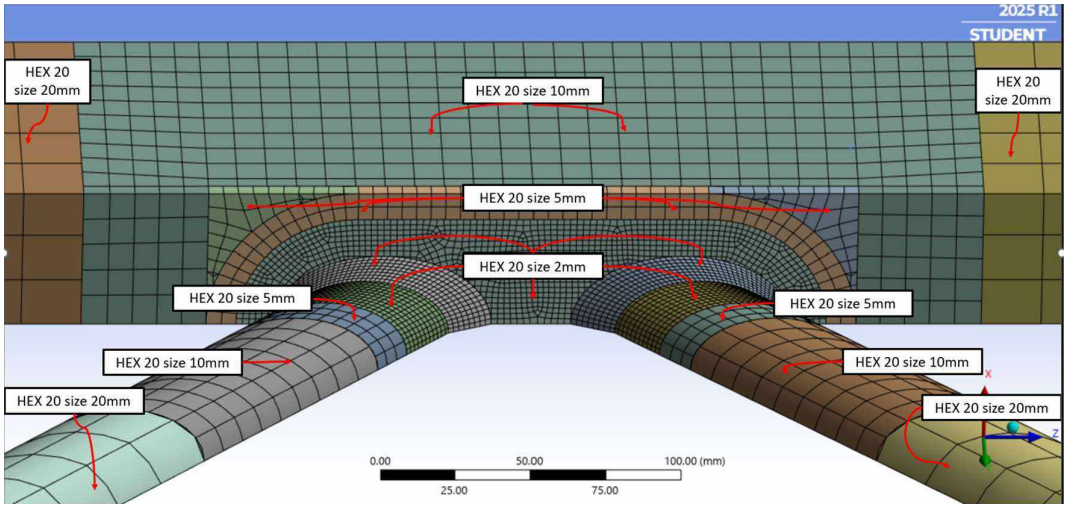

Fig. 61: Finite elements of the CHS K-joint.

SHS X joint

The tab. 21 presents the load-bearing capacities of SHS welded X-joints, derived from three different methodologies: numerical simulations, experimental testing, and theoretical calculations based on Eurocode standards EN 1993 and EN 1999. The results are categorized by the value of the parameter β (ranging from 0.4 to 0.6), which represents the ratio of the width of the brace member (b_1) to the width of the chord member (b_0).

- P_{serv}: Force at 1% deformation of the chord width which correspondents to the criteria for serviceability limit.
- P_{ult}: Ultimate load-bearing capacity at failure.
- $P_{ult,EN\ 1993}$: Theoretical design resistance based on Eurocode 1993 (steel structures).
- $P_{ult,EN1993+EN1999}$: Theoretical resistance corrected with aluminum-specific reduction factors from Eurocode 1999.

Tab. 21: Comparation of numerical results of load-bearing capacity of SHS X joints with experimental and values obtained thru EN 1993 and EN 1993 + EN1999

Type	Chord member	Brace member	β	P_{serv} (kN)	P_{ult} (kN)
Numerical results	SHS100	SHS 40	0.4	35.824	50.952
	SHS100	SHS 50	0.5	52.117	66.876
	SHS100	SHS 60	0.6	79.343	93.001
Experimental results	SHS100	SHS 40	0.4	31.715	43.306
	SHS100	SHS 50	0.5	43.827	63.597
	SHS100	SHS 60	0.6	86.080	99.487
EN1993	SHS100	SHS 40	0.4		62.311
	SHS100	SHS 50	0.5		75.001
	SHS100	SHS 60	0.6		93.403
EN1993 +EN 1999	SHS100	SHS 40	0.4		31.155
	SHS100	SHS 50	0.5		37.501
	SHS100	SHS 60	0.6		46.702

Numerical results align well with experimental results, especially for $\beta = 0.4$ and 0.5, where the difference in P_{ult} remains within ±6%. This validates the reliability of the numerical model for use in further parametric studies.

For $\beta = 0.6$, the experimental P_{ult} slightly exceeds the numerical prediction. This suggests that in higher β configurations, local effects or secondary stiffness contributions might not be fully captured in the numerical model and should be investigated further.

The trend of increasing P_{ult} with increasing β is consistent across all evaluation methods, confirming the strong correlation between brace size and joint capacity.

A notable discrepancy in P_{1+}values between experimental and numerical results at $\beta = 0.6$ suggests that early stiffness degradation or plastic deformations in the experiment may occur prior to those captured in simulations.

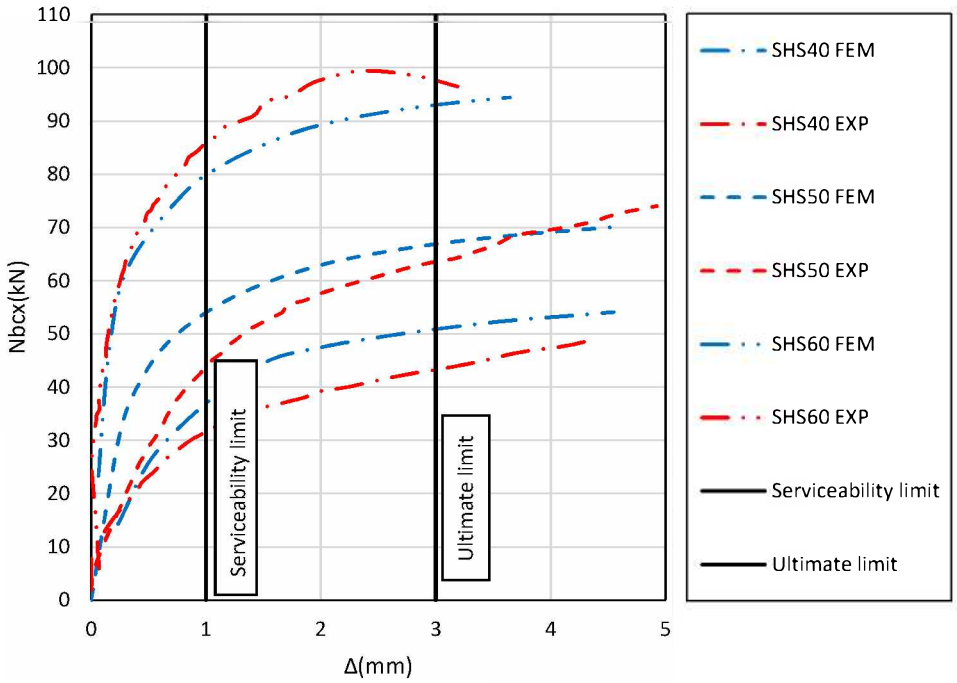

Fig. 62: Force-deflection curves for SHS X joints: experimental (EXP) and numerical (FEM).

In the Tab. 22 are presented numerical results of load-bearing capacities for aluminum X-joints in truss structures for different joint configurations. All joints are welded using SHS profiles for both the chord (horizontal member) and brace (inclined or vertical member). The data covers a wide range of brace-to-chord width ratios (denoted as $\beta = b_1/b_0$, where b_1 is the width of the brace member and b_0 is the width of the chord member), spanning from 0.40 to 0.60.

Tab. 22: Comparation of numerical results of load-bearing capacities of SHS X joints.

Type	Chord member	Brace member	β	P_{serv} (kN)	P_{ult} (kN)
Numerical results	SHS100	SHS 40	0.400	35.82	50.952
	SHS100	SHS 50	0.500	52.12	66.876
	SHS100	SHS 60	0.600	79.34	93.001
	SHS120	SHS50	0.416	34.77	49.629
	SHS120	SHS60	0.500	51.92	65.618
	SHS120	SHS70	0.583	67.34	84.063
	SHS150	SHS60	0.400	28.82	44.595
	SHS150	SHS70	0.467	34.89	50.320
	SHS150	SHS80	0.533	52.84	68.263
	SHS 150	SHS90	0.600	65.05	84.531

There is a consistent trend where increasing the β ratio leads to higher load-bearing capacities (P_{ult}).

For instance, in the SHS100 series: $\beta = 0.400 \rightarrow P_{ult} = 50.95$ kN

$\beta = 0.500 \rightarrow P_{ult} = 66.88$ kN

$\beta = 0.600 \rightarrow P_{ult} = 93.00$ kN

This demonstrates the importance of increasing brace width relative to the chord to enhance capacity, likely due to a larger welded contact area and reduced stress concentration at the weld toe. For the same β ratio, larger chords (from SHS100 to SHS150) tend to decrease the capacity.

At $\beta = 0.400$:

SHS100–SHS40 $\rightarrow P_{ult} = 50.95$ kN

SHS150–SHS60 $\rightarrow P_{ult} = 44.60$ kN

This counterintuitive result suggests that increasing chord size without adjusting brace size could reduce efficiency due to reduced local stiffness and increased flexibility in the wider face of the chord.

The difference between P_{serv} and P_{ult} increases with β, which indicates a greater post-elastic deformation capacity in joints with larger braces. At lower β (e.g., 0.400), the ratio P_{ult}/P_{serv} is around 1.42–1.55, while at $\beta = 0.600$, it reaches around 1.60–1.70.

Design codes may underestimate the load capacity for joints with higher β ratios unless adjustments are made.

These numerical results support the need to consider β as a critical design parameter and point toward the development of nonlinear models for more accurate strength prediction, especially when the $\beta > 0.5$, see Figs. 63,65.-66.

Joint capacity increases significantly with the brace-to-chord width ratio (β), indicating that this parameter plays a crucial role in joint strength and should be emphasized in design standards. Chord size alone does not linearly correlate with higher capacity; in some cases, larger chords with constant brace sizes show lower joint load-bearing capacity. The difference between initial yield and ultimate capacity highlights the ductility of these joints and suggests potential for using deformation-based performance

criteria. The tab. 22 data support the calibration and validation of finite element models used for parametric studies, confirming the reliability of numerical simulation for welded aluminum truss joints, see Fig. 64.

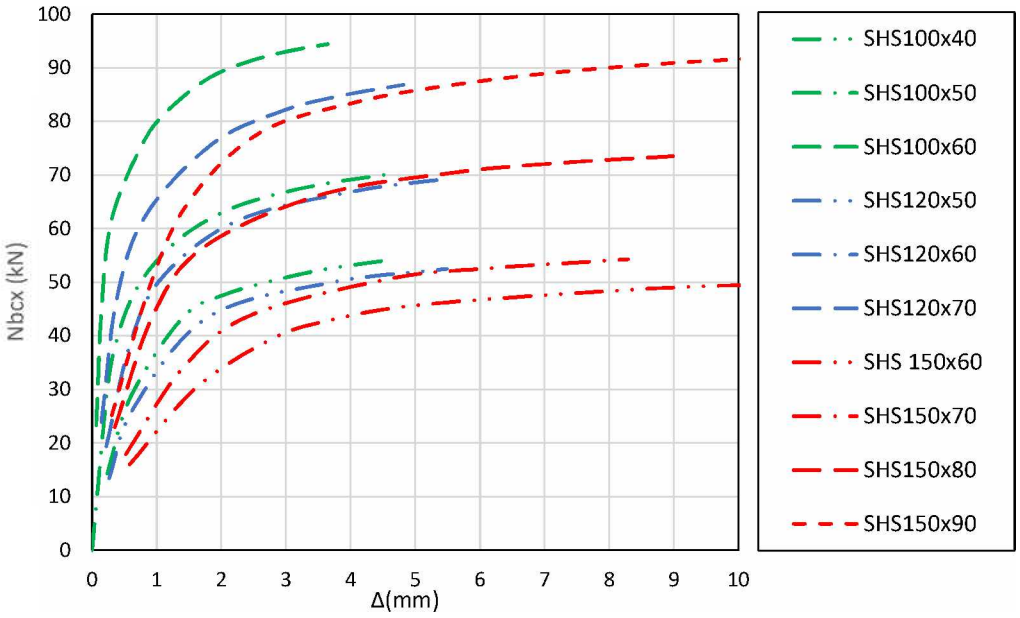

Fig. 63: Numerical force-deflection curves (FEM) for SHS X joints.

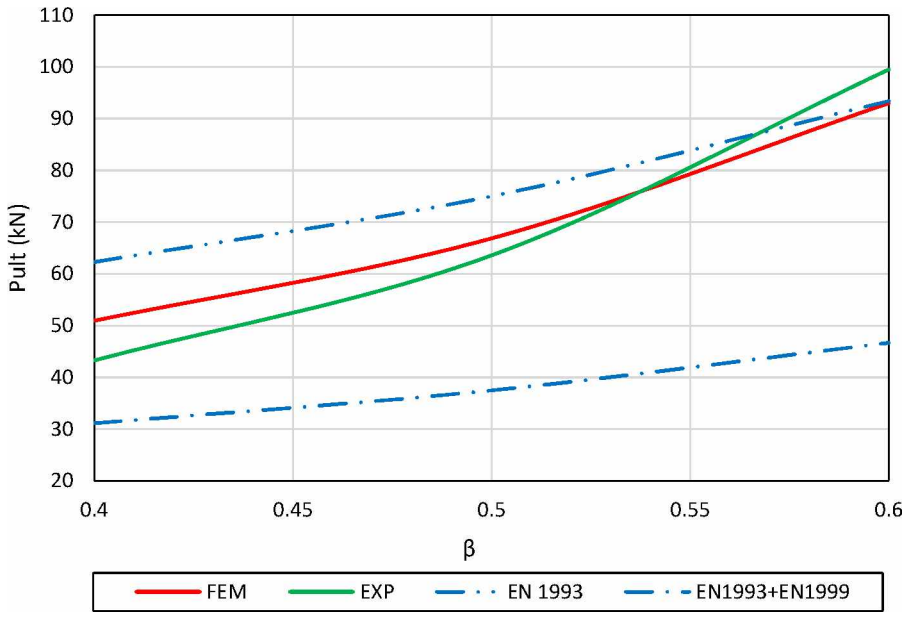

Fig. 64: Ultimate load P_{ult} versus β ratio for SHS X-joints for γ=10: comparison between numerical (FEM), experimental results (EXP) and predictions from EN 1993 (EN1993) and combined EN 1993 + EN 1999 design provisions (EN1993+EN1999).

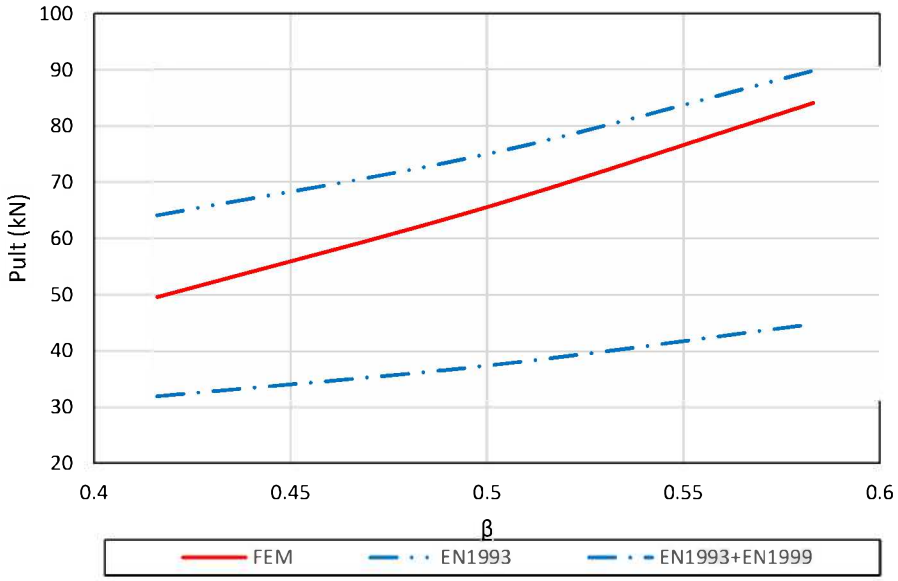

Fig. 65: Ultimate load P_{ult} versus β ratio for SHS X-joints for γ=12: comparison between numerical (FEM), experimental results (EXP) and predictions from EN 1993 (EN1993) and combined EN 1993 + EN 1999 design provisions (EN1993+EN1999).

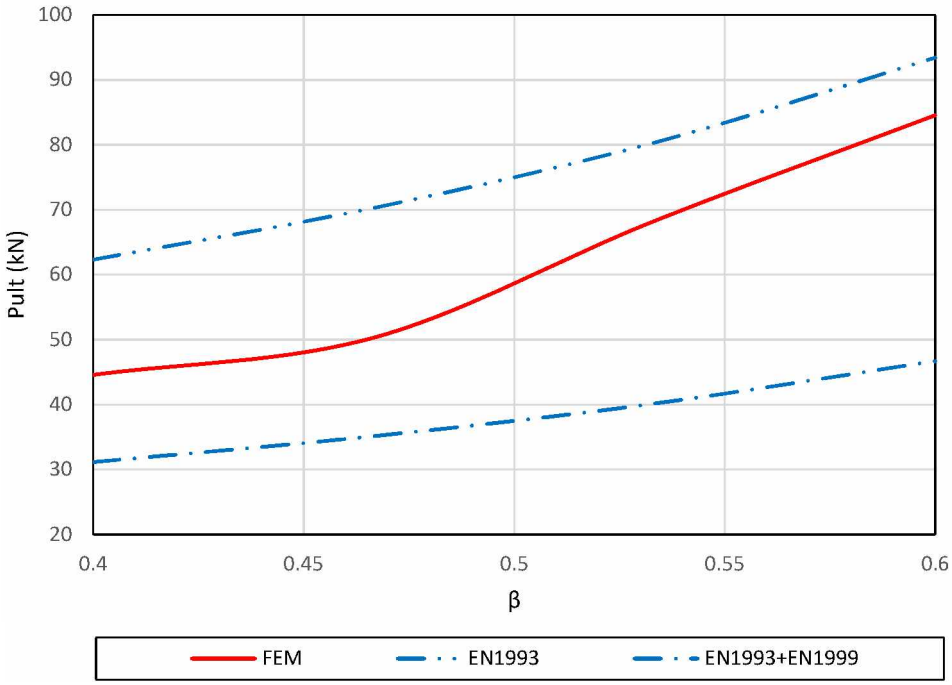

Fig. 66: Ultimate load P_{ult} versus β ratio for SHS X-joints for γ=15: comparison between numerical (FEM), experimental results (EXP) and predictions from EN 1993 (EN1993) and combined EN 1993 + EN 1999 design provisions (EN1993+EN1999).

SHS KC joint

The following tab. 23 compiles the load-bearing capacities of welded aluminum SHS K-joints with varying brace-to-chord width ratios.

Tab. 23: Comparation of numerical, experimental and code-based results of load-bearing capacities of SHS KC joints.

Type	Chord member	Brace member	β	P_{serv} (kN)	P_{ult} (kN)
Numerical results	SHS100	SHS 40	0.4	46.749	59.608
	SHS100	SHS 50	0.5	73.414	85.044
	SHS100	SHS 60	0.6	111.800	120.508
Experimental results	SHS100	SHS 40	0.4	44.1	60.565
	SHS100	SHS 50	0.5	71.333	92.668
	SHS100	SHS 60	0.6		
EN1993	SHS100	SHS 40	0.4		130.839
	SHS100	SHS 50	0.5		156.957
	SHS100	SHS 60	0.6		183.324
EN1993 +EN 1999	SHS100	SHS 40	0.4		65.419
	SHS100	SHS 50	0.5		78.478
	SHS100	SHS 60	0.6		91.662

As the β ratio increases, both numerical and experimental values of P_{ult} increase significantly, showing a positive correlation between brace width and joint capacity.

Numerical: P_{ult} rises from 59.6 kN (β = 0.4) to 120.5 kN (β = 0.6)

Experimental: P_{ult} increases from 60.6 kN to 92.7 kN (with missing data for β = 0.6)

The experimental results closely match the numerical predictions, indicating that the finite element model is well-calibrated and capable of predicting real joint behavior.

For example, at β = 0.5: Pult, numerical = 85.04 kN Pult, experimental = 92.67 kN

The difference is within an acceptable engineering margin (less than 10%).

EN 1993 predictions are highly conservative, showing load capacities over twice as high as those measured in experiments (e.g., 130.8 kN vs 60.6 kN at $\beta = 0.4$). This suggests overestimation if steel-based criteria are used directly for aluminum joints.

EN 1993 + EN 1999 values are closer to experimental and numerical results, but still slightly overestimate the capacity:

At $\beta = 0.5$: P_{ult} (exp) = 92.7 kN P_{ult} (EN1993+EN1999) = 78.5 kN

Difference = -15.3%, which is more acceptable but still requires attention.

Brace-to-chord ratio β is a dominant parameter influencing joint performance, with increased β leading to higher stiffness and capacity.

Experimental and numerical results are in strong agreement, validating the modeling approach and the assumptions used in the FE simulations.

EN 1993 standards significantly overestimate aluminum joint capacity if used directly, while EN 1993 + EN 1999 offers more realistic predictions, but it can still be very conservative.

These findings highlight the need for aluminum-specific design criteria, especially for welded SHS K-joints, to account for HAZ softening and joint geometry.

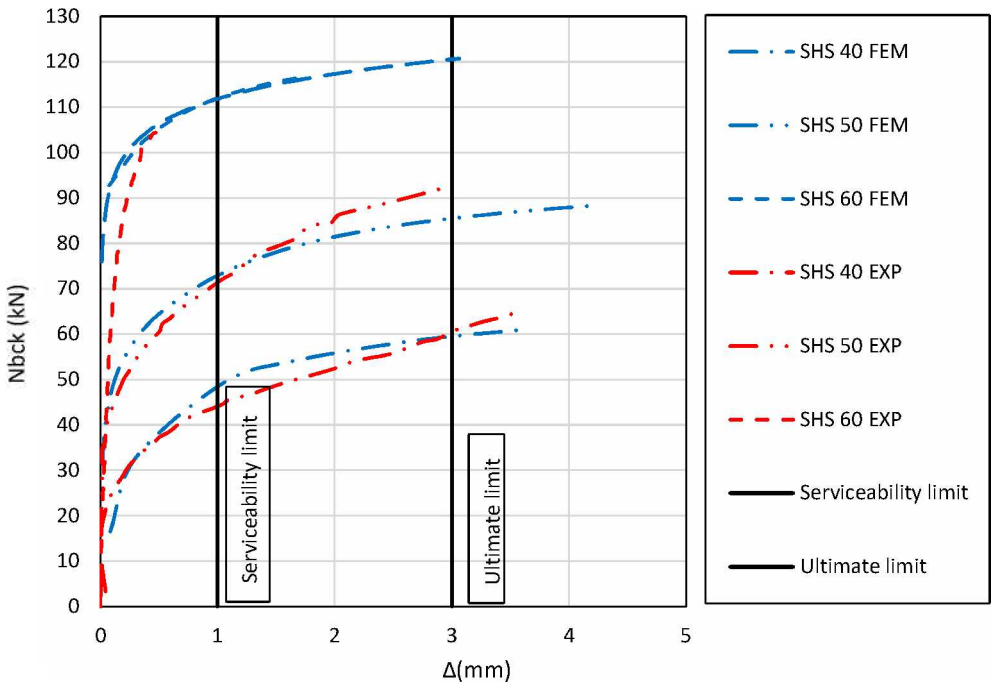

Fig. 67: Experimental (EXP) and numerical (FEM) force-deflection curves for SHS KC joints.

This tab. 24 presents the results of a numerical investigation into the load-bearing capacity of K-joints.

Tab. 24: Comparation of numerical (FEM) results of load-bearing capacities of SHS KC joints.

Chord member	Brace member	β	P_{serv} (kN)	P_{ult} (kN)
SHS100	SHS 40	0.4	46.749	59.608
SHS100	SHS 50	0.5	73.414	85.044
SHS100	SHS 60	0.6	111.800	120.508
SHS120	SHS50	0.416	47.138	62.497
SHS120	SHS60	0.50	71.579	85.777
SHS120	SHS70	0.583	67.340	118.280
SHS150	SHS60	0.40	39.466	59.852
SHS150	SHS70	0.466	48.136	69.030
SHS150	SHS80	0.533	78.413	103.160
SHS150	SHS90	0.60	115.225	136.282

As β increases, both P1%bo and Pult generally increase, confirming that larger brace sections provide more effective force transfer and improve joint capacity.

For SHS100:

$\beta = 0.4 \rightarrow$ Pult = 59.6 kN

$\beta = 0.5 \rightarrow$ Pult = 85.0 kN

$\beta = 0.6 \rightarrow$ Pult = 120.5 kN

This trend is consistent across other chord sizes (SHS120, SHS150).

Joint capacity is positively correlated with the β ratio, confirming the importance of brace width relative to chord width in force transfer efficiency.

Larger chord sizes improve joint strength, but the benefit depends on the relative stiffness between the chord and brace.

The results underline the need for tailored numerical and experimental analyses in the design of aluminum welded joints, particularly because standard steel-based codes (like EN 1993) may not account for the complex interaction between geometry and HAZ weakening in aluminum.

Future parametric studies could explore γ ($b_o/2t_o$) and other geometric or material parameters to refine design recommendations.

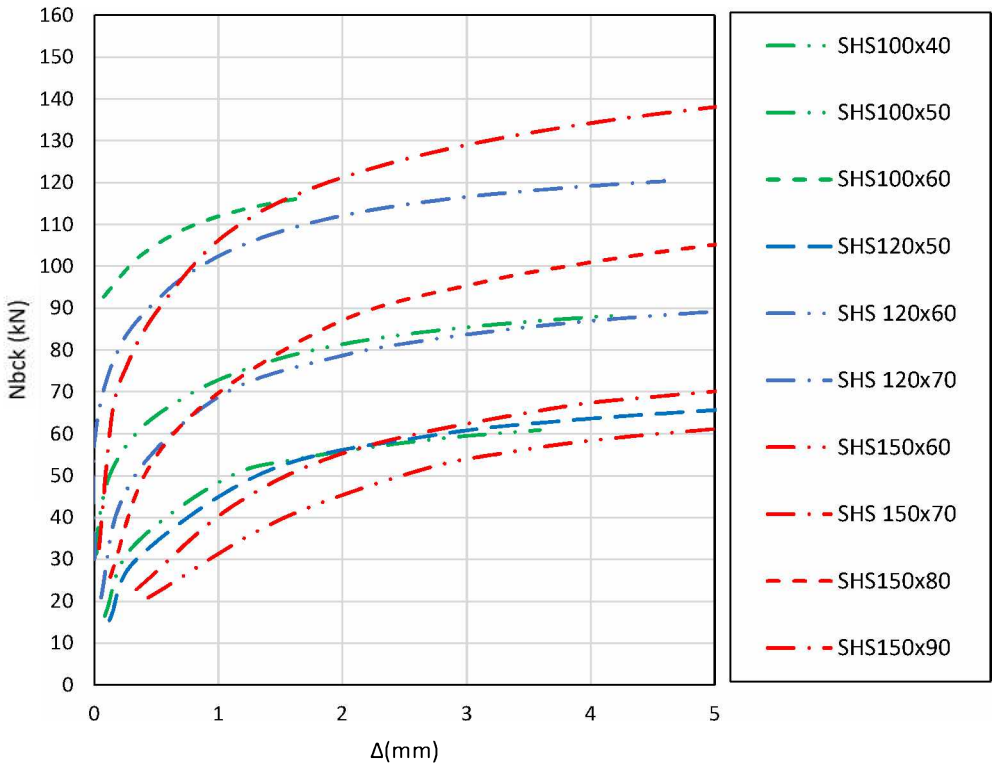

Fig. 68: Numerical (FEM) force-deflection curves for SHS KC joints.

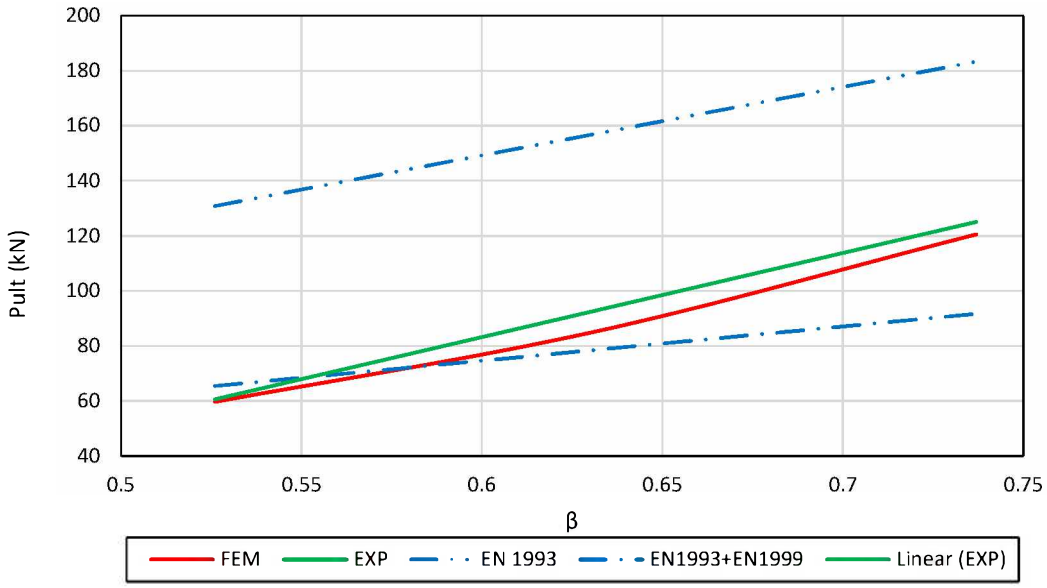

Fig. 69: Ultimate load P_{ult} versus β ratio for SHS KC-joints for γ=10: comparison between numerical (FEM), experimental results (EXP) and predictions from EN 1993 (EN1993) and combined EN 1993 + EN 1999 design provisions (EN1993+EN1999).

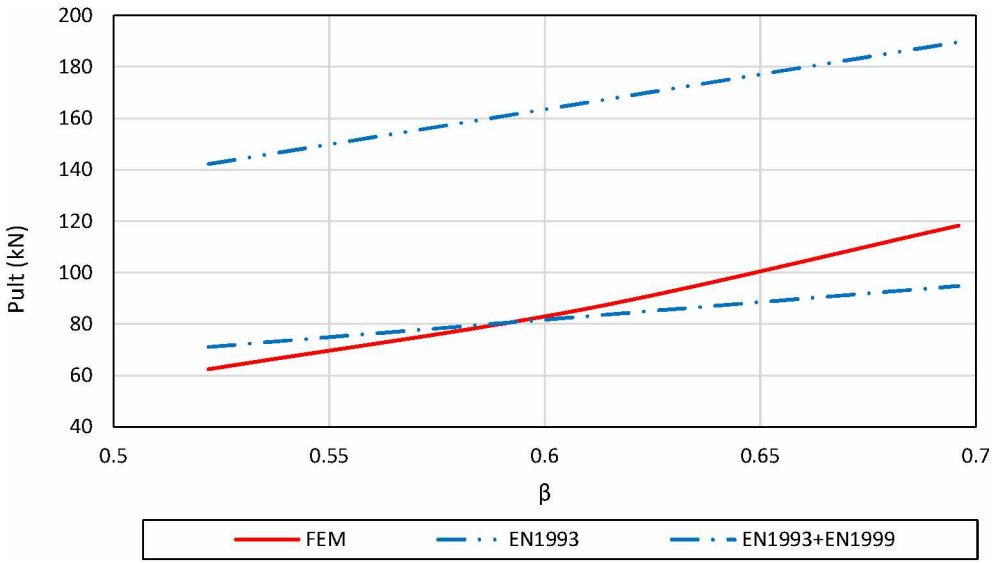

Fig. 70: Ultimate load P_{ult} versus β ratio for SHS KC-joints for γ=12: comparison between numerical (FEM), experimental results (EXP) and predictions from EN 1993 (EN1993) and combined EN 1993 + EN 1999 design provisions (EN1993+EN1999).

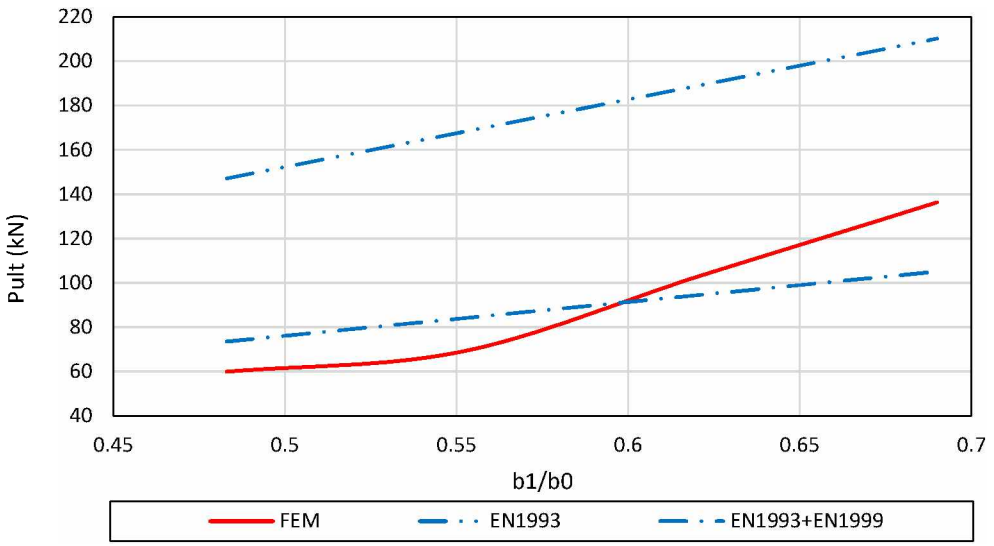

Fig. 71: Ultimate load P_{ult} versus β ratio for SHS KC-joints for γ=15: comparison between numerical (FEM), experimental results (EXP) and predictions from EN 1993 (EN1993) and combined EN 1993 + EN 1999 design provisions (EN1993+EN1999).

SHS KT joint

The tab. 25 presents load-bearing capacities (both at serviceability limit state – *P1%bo*, and at ultimate state – P_{ult}) for welded tensioned K-joints with square hollow section (SHS) brace and chord members according to the numeric, experimental and theoretical investigation.

Tab. 25: Comparation of numerical, experimental and code-based results of load-bearing capacities of SHS KT-joints.

Type	Chord member	Brace member	b1/b0	P_{serv} (kN)	P_{ult} (kN)
Numerical results	SHS100	SHS 40	0.4	50.231	67.203
	SHS100	SHS 50	0.5	67.558	83.906
	SHS100	SHS 60	0.6	102.531	114.362
Experimental results	SHS100	SHS 40	0.4	48.497	64.651
	SHS100	SHS 50	0.5	71.330	92.668
	SHS100	SHS 60	0.6		
EN1993	SHS100	SHS 40	0.4		130.839
	SHS100	SHS 50	0.5		156.957
	SHS100	SHS 60	0.6		183.324
EN1993 +EN 1999	SHS100	SHS 40	0.4		65.419
	SHS100	SHS 50	0.5		78.478
	SHS100	SHS 60	0.6		91.662

Increasing β from 0.4 to 0.6 results in a progressive increase in both P_{serv} and P_{ult}, confirming that joints with larger brace members relative to chord width carry tent to have higher load-bearing capacity.

Numerical P_{ult} grows from 67.2 kN (β=0.4) to 114.4 kN (β=0.6), while experimental P_{ult} follows a similar trend, reaching 92.7 kN for β=0.5.

Comparison Between Numerical and Experimental Results

Numerical results are in good agreement with experimental values:

For β=0.4: Numerical P_{ult} = 67.2 kN vs. Experimental P_{ult} = 64.7 kN (difference ≈ 3.9%).

For β=0.5: Numerical P_{ult} = 83.9 kN vs. Experimental P_{ult} = 92.7 kN (difference ≈ -9.5%).

No experimental value was available for β=0.6, but the trend suggests it would likely align closely with the predicted P_{ult} of 114.4 kN.

Code-based results vs. experimental results

Code-based values from EN 1993 alone are significantly higher than both experimental and numerical P_{ult}, often by more than 50%.

For β=0.4: EN 1993 P_{ult} = 130.8 kN vs. numerical = 67.2 kN → overestimation of 94.6%.

When adjusted with EN 1999, the theoretical values are much closer to reality:

For β=0.4: Pult EN1993+EN1999 = 65.4 kN, nearly matching the experimental and numerical values.

Serviceability limit values (P_{serv})

Experimental P_{serv} values are very close to the numerical ones (e.g., for β=0.4: 50.2 kN vs. 48.5 kN), indicating consistency in modeling local deformation thresholds.

Theoretical predictions based solely on EN 1993 significantly overestimate joint capacity due to their origin in steel joint behavior, which doesn't account for HAZ softening or aluminum's lower ductility. Using EN 1993 + EN 1999 leads to more realistic design predictions, validating the importance of aluminum-specific provisions. Joint stiffness and load-bearing capacity improve with increasing β, but the full capacity is limited by weld performance and HAZ behavior rather than just geometry. This comparison highlights the need for aluminum-specific design guidance and standards that integrate empirical and numerical data for more reliable joint behavior predictions.

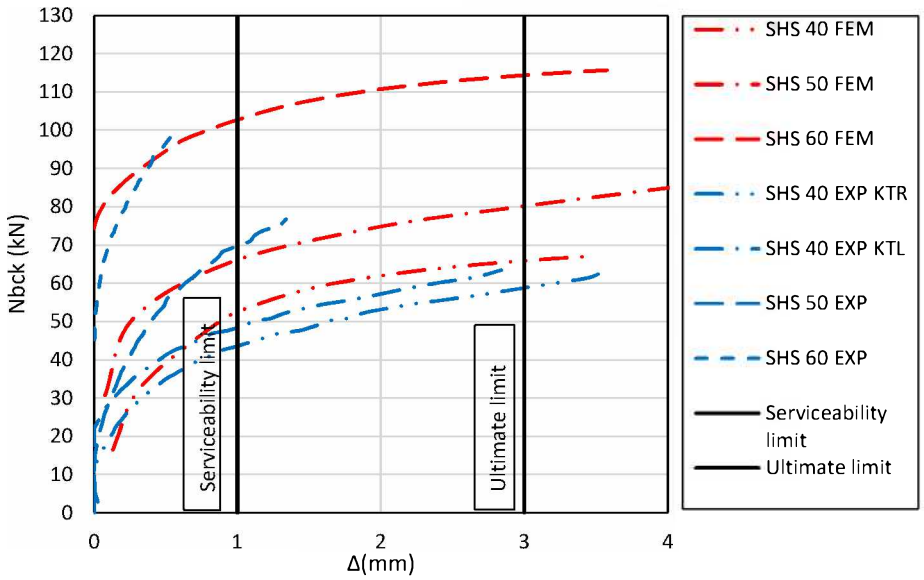

Fig. 72: Experimental (EXP) and numerical (FEM) force-deflection curves for SHS KT-joints.

This tab. 24 presents numerical simulation results (FEM) for welded KT-joints made from square hollow sections (SHS). The chord members have widths of 100 mm, 120 mm, and 150 mm, and the brace members range from SHS 40 to SHS 80.

Tab. 24: Comparation of numerical (FEM) results of load-bearing capacities of SHS KT joints.

Chord member	brace member	b1/b0	P_{serv} (kN)	P_{ult} (kN)
SHS100	SHS 40	0.4	50.231	67.203
SHS100	SHS 50	0.5	67.558	83.906
SHS100	SHS 60	0.6	102.531	114.362
SHS120	SHS50	0.416	43.05	55.99
SHS120	SHS60	0.50	64.648	75.506
SHS120	SHS70	0.583	94.33248	110.602
SHS150	SHS60	0.40	32.381	49.88
SHS150	SHS70	0.466	39.489	56.078
SHS150	SHS80	0.533	66.353	88.799

A higher β ratio leads to increased P_{ult}, which aligns with theoretical expectations. For instance:

SHS100 chord:

$\beta = 0.4 \rightarrow Pult = 67.2$ kN

$\beta = 0.6 \rightarrow Pult = 114.4$ kN

This trend is consistent across different chord widths (SHS100, SHS120, SHS150), indicating that brace size significantly affects the joint's axial and bending resistance.

For a fixed β ratio, increasing the chord size generally reduces the local deformation (P_{serv}) and ultimate load (P_{ult}) due to reduced stress concentration and improved stiffness:

At $\beta \approx 0.4$:

SHS100 $\rightarrow P_{ult} = 67.2$ kN

SHS120 $\rightarrow P_{ult} = 55.99$ kN

SHS150 $\rightarrow P_{ult} = 49.88$ kN

This suggests that larger chords may spread the stress more efficiently, but the stiffness increase limits localized plastification, reducing measured capacity in joint-localized failure modes.

The relationship between P_{serv} and P_{ult} is nonlinear, especially at higher β values. This reflects complex interaction effects like chord face plastification, local buckling, and weld behavior. Results emphasize that joint design should consider the full assembly context, especially the β ratio and chord size, which together control stiffness, local deformation, and failure mode. The P_{serv} values serve as early indicators of joint performance and potential serviceability concerns, while P_{ult} gives the structural limit.

Brace-to-chord width ratio (β) is the dominant parameter influencing both serviceability and ultimate load capacity of SHS-SHS welded K-joints.

These results validate the applicability of numerical modeling for parametric studies in aluminum joint behavior and highlight the need for β-sensitive design rules in aluminum joint standards.

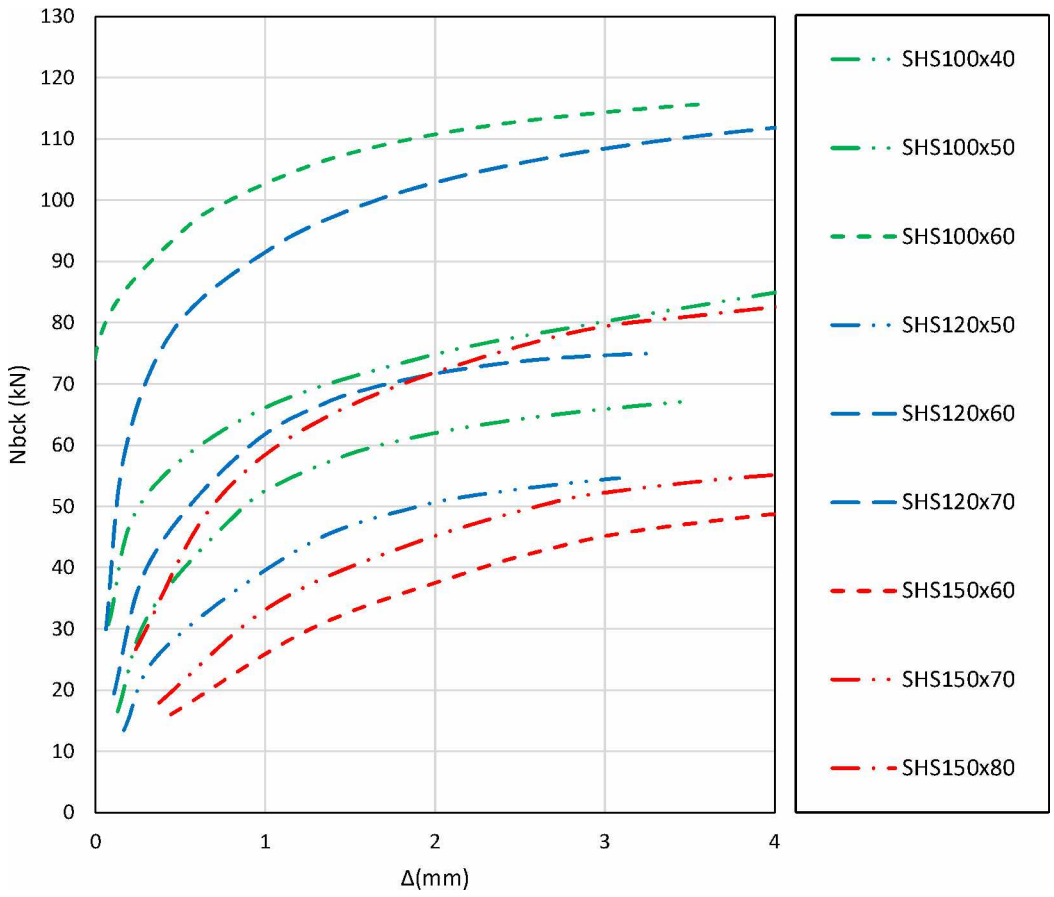

Fig. 73: Numerical (FEM) force-deflection curves for SHS KT joints.

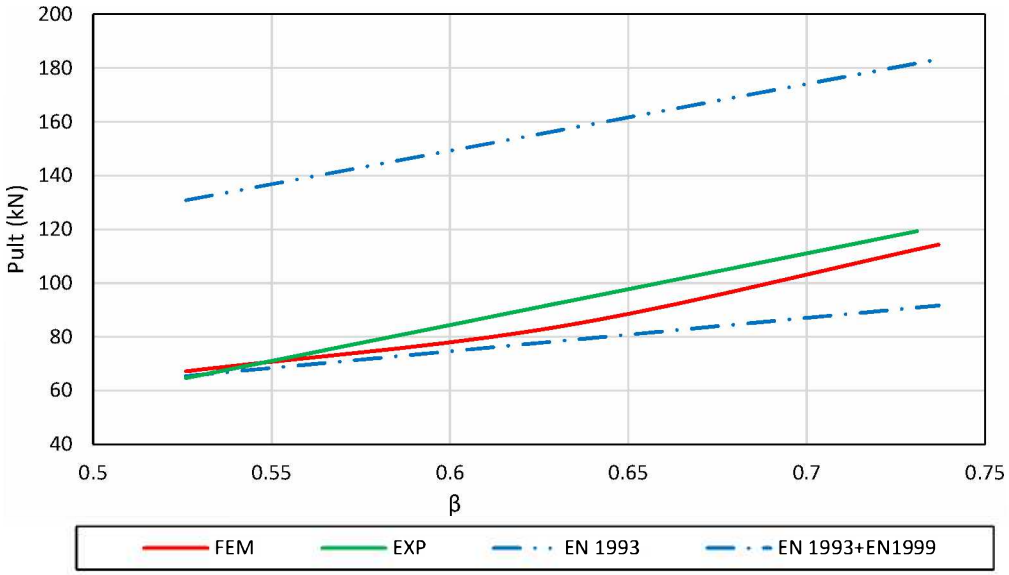

Fig. 74: Ultimate load P_{ult} versus β ratio for SHS KT-joints for γ=10: comparison between numerical (FEM), experimental results (EXP) and predictions from EN 1993 (EN1993) and combined EN 1993 + EN 1999 design provisions (EN1993+EN1999).

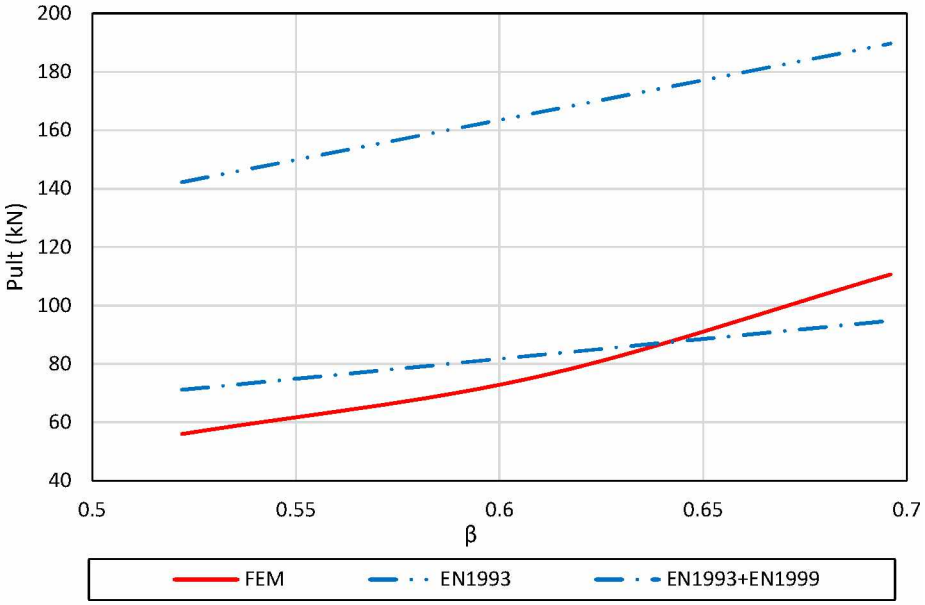

Fig. 75: Ultimate load P_{ult} versus β ratio for SHS KT-joints for γ=12: comparison between numerical (FEM), experimental results (EXP) and predictions from EN 1993 (EN1993) and combined EN 1993 + EN 1999 design provisions (EN1993+EN1999).

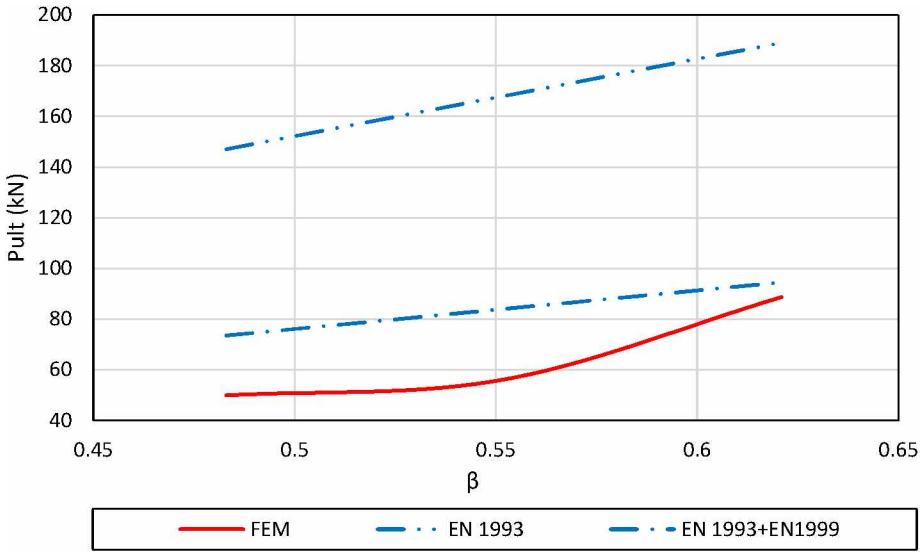

Fig. 76: Ultimate load P_{ult} versus β ratio for SHS KT-joints for γ=15: comparison between numerical (FEM), experimental results (EXP) and predictions from EN 1993 (EN1993) and combined EN 1993 + EN 1999 design provisions (EN1993+EN1999).

CHS X joint

In the tab. 25 are presented numerical (FEM), experimental (EXP) and code-based (EN 1993 and EN1993+EN1999) results of welded X-joints composed of square hollow section (SHS) chord members and circular hollow section (CHS) brace members.

Tab. 25: Comparation of numerical (FEM), experimental (EXP), code-based (EN 1993 and EN 1993+ EN 1999) results of load-bearing capacities of CHS X-joints.

Type	Chord member	brace member	β	P_{serv} (kN)	P_{ult} (kN)
Numerical results	SHS100	SHS 40	0.4	27.657	42.334
	SHS100	SHS 50	0.5	37.04	54.08
	SHS100	SHS 60	0.6	59.176	72.111
Experimental results	SHS100	SHS 40	0.4	26.757	44.545
	SHS100	SHS 50	0.5	41.904	56.467
	SHS100	SHS 60	0.6	53.204	72.268
Pult, EN1993	SHS100	SHS 40	0.4		48.938
	SHS100	SHS 50	0.5		58.905
	SHS100	SHS 60	0.6		73.358
Pult, EN1993 +EN 1999	SHS100	SHS 40	0.4		24.469
	SHS100	SHS 50	0.5		29.453
	SHS100	SHS 60	0.6		36.679

The numerical results show excellent agreement with experimental values:

For $\beta = 0.4$, P_{ult} differs by only ~4.95%;

For $\beta = 0.5$, P_{ult} differs by ~4.23%;

For $\beta = 0.6$, P_{ult} differs by only ~0.2%.

This high consistency suggests that the numerical model is well-validated and can be confidently used for further parametric studies. Both P_{serv} and P_{ult} increase with the β-ratio, confirming that larger brace diameters contribute to higher joint capacity due to increased contact area and load transfer efficiency. From $\beta = 0.4$ to $\beta = 0.6$, Pult increases by ~70% in the numerical model.

In the case of CHS X joints, EN 1993 only provides slightly conservative predictions at $\beta = 0.6$, EN1993 predicts P_{ult} = 73.358 kN vs 72.268 kN experimentally, a minor overestimation.

EN 1993 + EN 1999 significantly underestimates the ultimate capacity, especially at lower β-ratios at $\beta = 0.4$, prediction is only 55% of experimental value. This discrepancy highlights that current design codes may be overly conservative for welded aluminum joints and fail to reflect the actual load transfer mechanisms, especially in CHS braces welded to SHS chords. For CHS brace joints, experimental and numerical results align well, suggesting that weld quality and HAZ integrity dominate joint performance more than brace shape alone. This dataset reaffirms the reliability of validated numerical models in predicting both serviceability and strength limit states of welded aluminum CHS X-joints. It also demonstrates the limitations of current European standards in capturing realistic behavior, especially for aluminum applications with CHS braces.

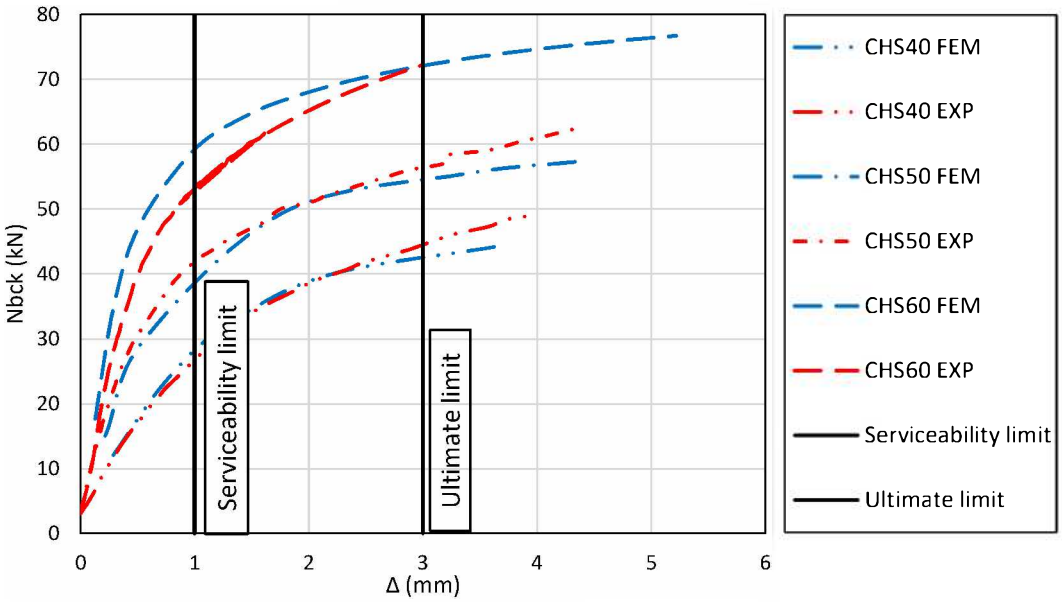

Fig. 77: Experimental (EXP) and numerical (FEM) force-deflection curves for CHS X-joints.

Tab. 26: Comparation of numerical (FEM) of results of load-bearing capacities of CHS X-joints.

Chord member	Brace member	β	P_{serv} (kN)	P_{ult} (kN)
SHS100	CHS 40	0.4	27.657	42.334
SHS100	CHS 50	0.5	37.04	54.08
SHS100	CHS 60	0.6	59.176	72.111
SHS120	CHS50	0.416	24.686	40.976
SHS120	CHS60	0.5	34.219	50.716
SHS120	CHS70	0.583	48.557	65.813
SHS150	CHS60	0.4	18.086	34.502
SHS150	CHS70	0.4666	24.07	40.319
SHS150	CHS80	0.5333	31.977	51.252
SHS 150	CHS90	0.6	43.971	65.188

In the tab. 26 are presented numerical results for a set of welded aluminum CHS X-joints. The key objective of this numerical study is to investigate the influence of joint geometry,

specifically, the β-ratio (brace-to-chord size ratio) on joint behavior under axial brace loading.

As expected, both P_{serv} and P_{ult} increase consistently with increasing β, regardless of the chord size. This shows that larger brace diameters contribute to improved load transfer efficiency, increased weld perimeter and load path, higher overall joint stiffness and load-bearing capacity.

For a given β ratio, increasing parameter γ (from SHS100 → SHS120 → SHS150) results in lower P_{serv} and P_{ult} values. Example at $\beta \approx 0.5$:

- SHS100–CHS50: P_{ult} = 54.08 kN
- SHS120–CHS60: P_{ult} = 50.716 kN
- SHS150–CHS80: P_{ult} = 51.252 kN

This numerical investigation confirms that both brace size and chord geometry critically impact the load-bearing performance of welded CHS X-joints in aluminum truss structures. The results reinforce the importance of careful proportioning (via β-ratio) and validate the feasibility of using numerical models to predict joint behavior and guide parametric studies in design optimization, Figs. 78. -81.

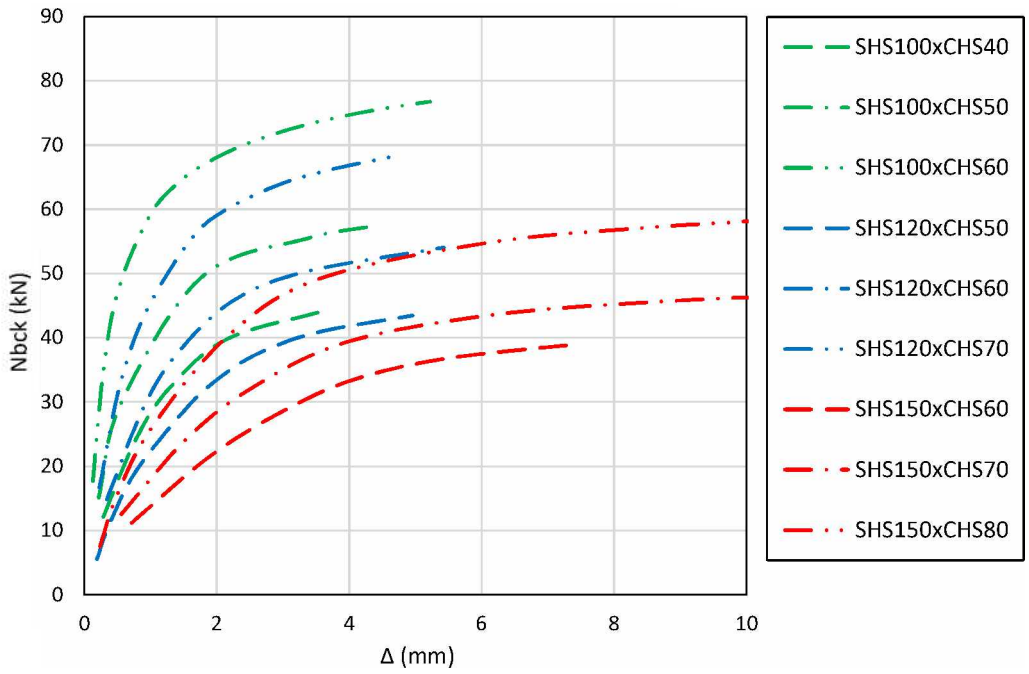

Fig. 78: Numerical (FEM) force-deflection curves for CHS X joints.

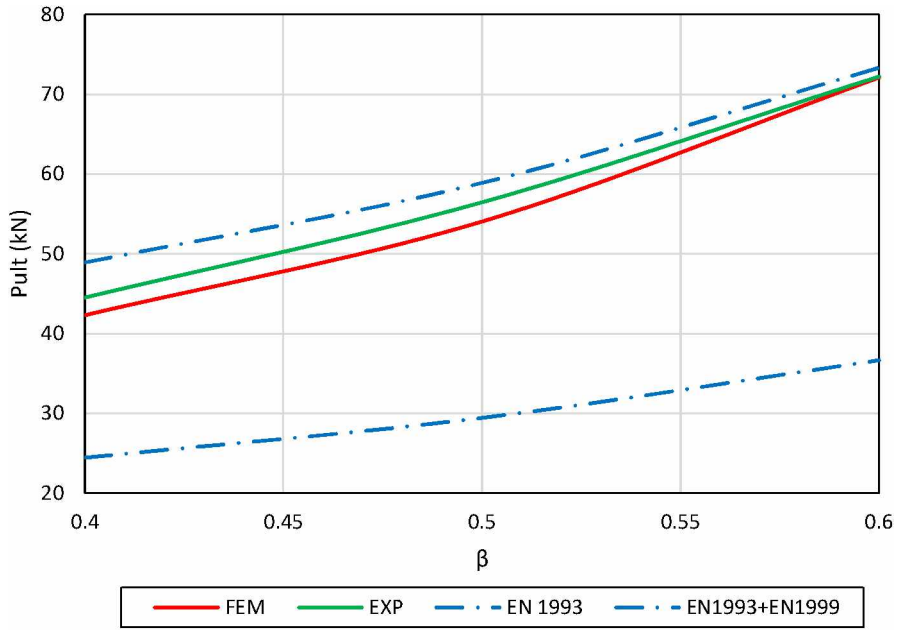

Fig. 79: Ultimate load P_{ult} versus β ratio for CHS X-joints for γ=10: comparison between numerical (FEM), experimental results (EXP) and predictions from EN 1993 (EN1993) and combined EN 1993 + EN 1999 design provisions (EN1993+EN1999).

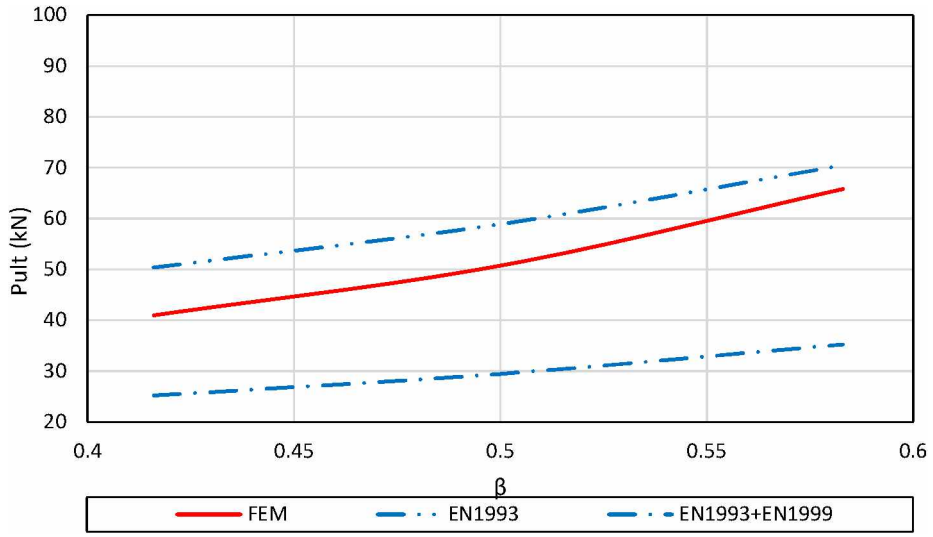

Fig. 80: Ultimate load P_{ult} versus β ratio for CHS X-joints for γ=12: comparison between numerical (FEM), experimental results (EXP) and predictions from EN 1993 (EN1993) and combined EN 1993 + EN 1999 design provisions (EN1993+EN1999).

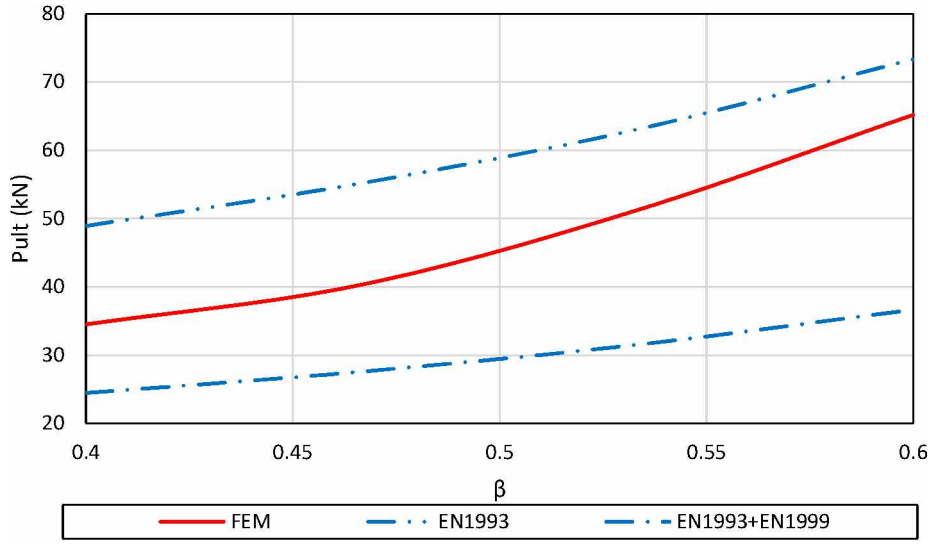

Fig. 81: Ultimate load P_{ult} versus β ratio for CHS X-joints for γ=15: comparison between numerical (FEM), experimental results (EXP) and predictions from EN 1993 (EN1993) and combined EN 1993 + EN 1999 design provisions (EN1993+EN1999).

CHS KC joint

This tab. summarizes and compares load-bearing capacities (P_{ult}) and service limit loads (P_{serv}) of KC joints composed of SHS 100 chord members and CHS brace members with varying diameters. The comparison includes values obtained from numerical simulations (FEM), experimental tests (EXP), and code-based results (EN 1993 and EN 1993 + EN 1999), with the primary focus on the parameter β.

Tab. 27: Comparation of results of load-bearing capacities of CHS KC-joints.

Type	Chord member	Brace member	β	P_{serv} (kN)	P_{ult} (kN)
Numerical results	SHS100	CHS 40	0.4	38.360	50.340
	SHS100	CHS 50	0.5	52.860	66.330
	SHS100	CHS 60	0.6	84.010	95.120
Experimental results	SHS100	CHS 40	0.4	39.713	53.702
	SHS100	CHS 50	0.5	54.754	71.531
	SHS100	CHS 60	0.6		
Pult, EN1993	SHS100	CHS 40	0.4		78.144
	SHS100	CHS 50	0.5		97.681
	SHS100	CHS 60	0.6		117.217
Pult, EN1993 +EN 1999	SHS100	CHS 40	0.4		39.072
	SHS100	CHS 50	0.5		48.841
	SHS100	CHS 60	0.6		58.609

This trend indicates that larger brace diameters contribute to higher joint stiffness and ultimate strength, due to increased load transfer area. EN1993 based results overestimates ultimate capacities compared to both experimental and numerical data. The overprediction reaches nearly 40–50%, especially at lower β. EN1993 + EN1999 results which includes HAZ softening, underestimates the strength, offering a conservative (but potentially uneconomical) design estimate. The numerical model shows strong correlation with experimental data, especially for β = 0.4 and 0.5, validating its applicability for further parametric studies.

The results highlight a critical gap in Eurocode 3 (EN1993) for predicting the behavior of aluminum KT joints, particularly due to inadequate consideration of HAZ effects and nonlinear local failures. EN1999 adjustments (which account for HAZ degradation) are safer but tend to be overly conservative. The findings support the need for aluminum-specific calibration of design standards, including numerical methods.

The numerical model effectively predicts the joint behavior and aligns well with experimental results for β = 0.4 and 0.5. Further experimental data for β = 0.6 would be valuable for validating the observed trends and confirming the limits of EN standards in this range.

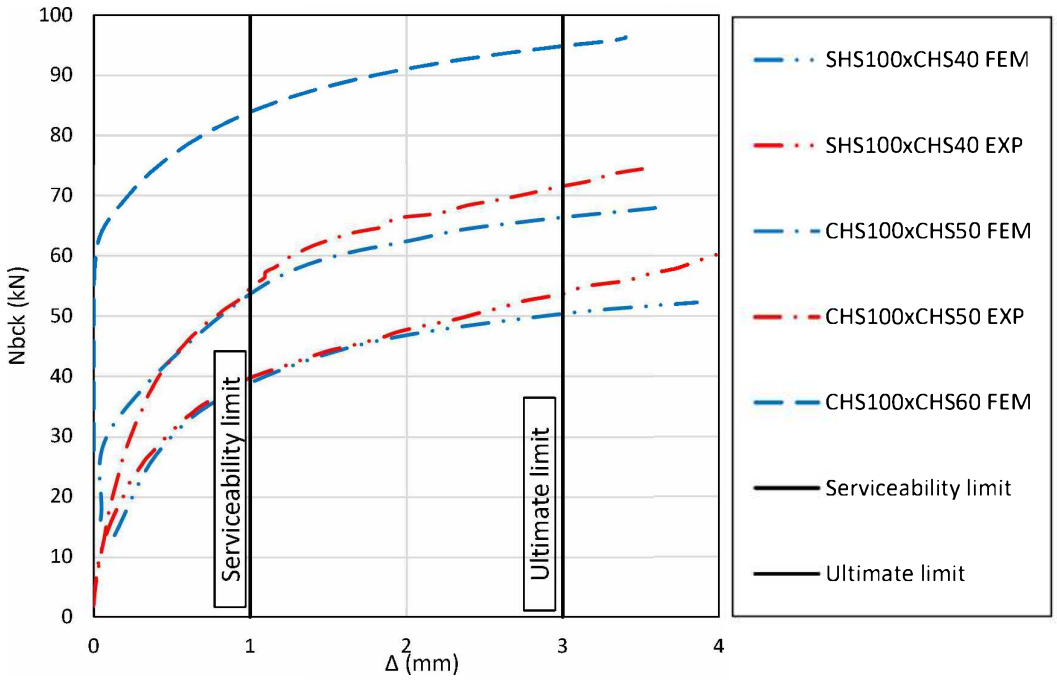

Fig. 82: Experimental (EXP) and numerical (FEM) force-deflection curves for CHS KC-joints.

This table presents numerical results of the ultimate load-bearing capacity (Pult) and load at 1% chord face deformation (P1%bo) for a series of KC-type welded aluminum joints. The joints are composed of square hollow section (SHS) chord members and circular hollow section (CHS) brace members, with variations in brace-to-chord diameter ratio ($\beta = b_1/b_0$) ranging from 0.4 to 0.6.

Tab. 28: Comparation of numerical results of the load-bearing capacities of CHS KC-joints.

Chord member	Brace member	β	P_{serv} (kN)	P_{ult} (kN)
SHS100	CHS 40	0.4	38.360	50.340
SHS100	CHS 50	0.5	52.860	66.330
SHS100	CHS 60	0.6	84.010	95.120
SHS120	CHS50	0.416	37.610	51.545
SHS120	CHS60	0.5	51.850	62.383
SHS120	CHS70	0.583	76.140	89.905
SHS150	CHS60	0.4	33.780	61.050
SHS150	CHS70	0.4666	39.480	61.714
SHS150	CHS80	0.5333	59.620	76.762
SHS 150	CHS90	0.6	77.530	98.403

For each chord profile group (SHS100, SHS120, SHS150), Pult increases as β increases:

- SHS100 group: P_{ult} increases from 50.3 kN (β = 0.4) to 95.1 kN (β = 0.6)
- SHS120 group: P_{ult} increases from 51.5 kN (β = 0.416) to 89.9 kN (β = 0.583)
- SHS150 group: P_{ult} increases from 61.0 kN (β = 0.4) to 98.4 kN (β = 0.6)

This trend confirms that larger brace diameters relative to the chord width enable better force transfer, thus increasing joint load-bearing capacity.

Comparing results across chord sizes for the same β:

At $\beta \approx 0.5$:

- SHS100: P_{ult} = 66.3 kN
- SHS120: P_{ult} = 62.4 kN
- SHS150: P_{ult} = 61.7 kN

The smaller chords (SHS100) seem to show slightly higher load-bearing capacity than SHS150 at the same β in some cases. This could indicate local stress concentration effects or HAZ weakening, which become more pronounced in larger, thinner-walled chords.

A higher P_{serv}/P_{ult} ratio indicates higher initial stiffness, which is beneficial for serviceability but may also suggest brittle failure modes.

Joint geometry (β) and chord size both play crucial roles in determining the ultimate strength of KC joints. For design purposes, increasing β (by increasing brace size) improves load capacity, but care must be taken with heat-affected zone (HAZ) softening, especially in larger chords.

This analysis of KC joints with CHS braces and SHS chords demonstrates a clear positive correlation between β and joint capacity, as shown in Figs. 83-86. However, the role of chord stiffness, welding effects, and geometry non-linearity must be accounted for in numerical modeling and design optimization. The data is valuable for calibrating analytical models or finite element simulations aimed at improving Eurocode-based design predictions for aluminum truss structures.

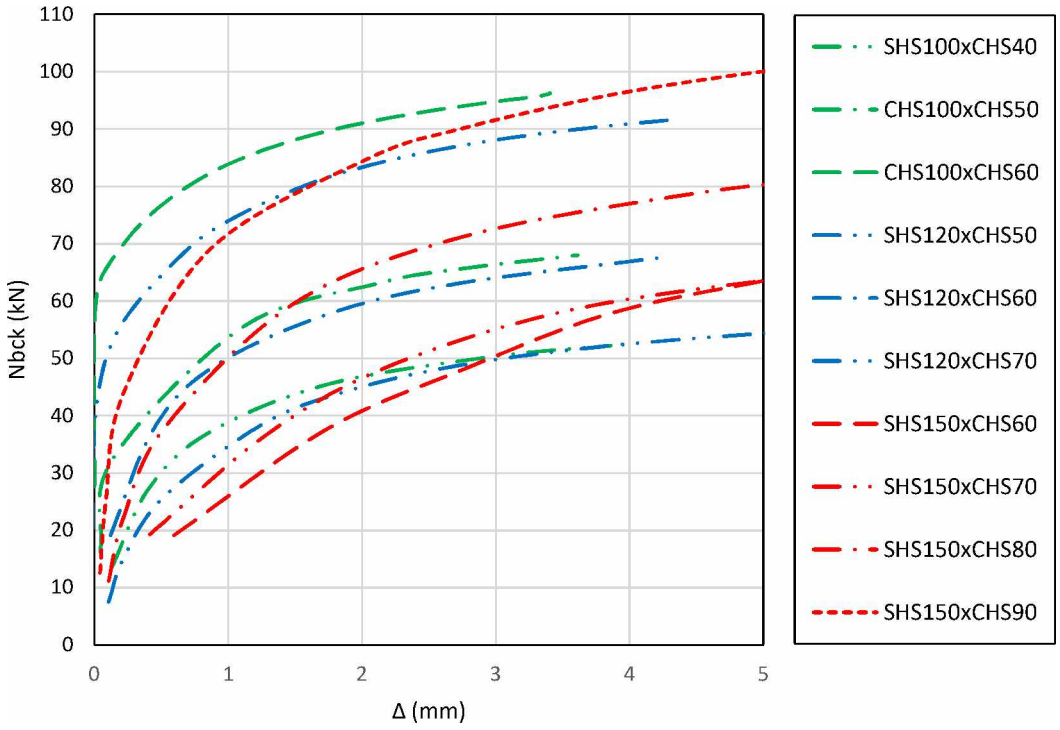

Fig. 83: Numerical (FEM) force-deflection curves for CHS KC-joints.

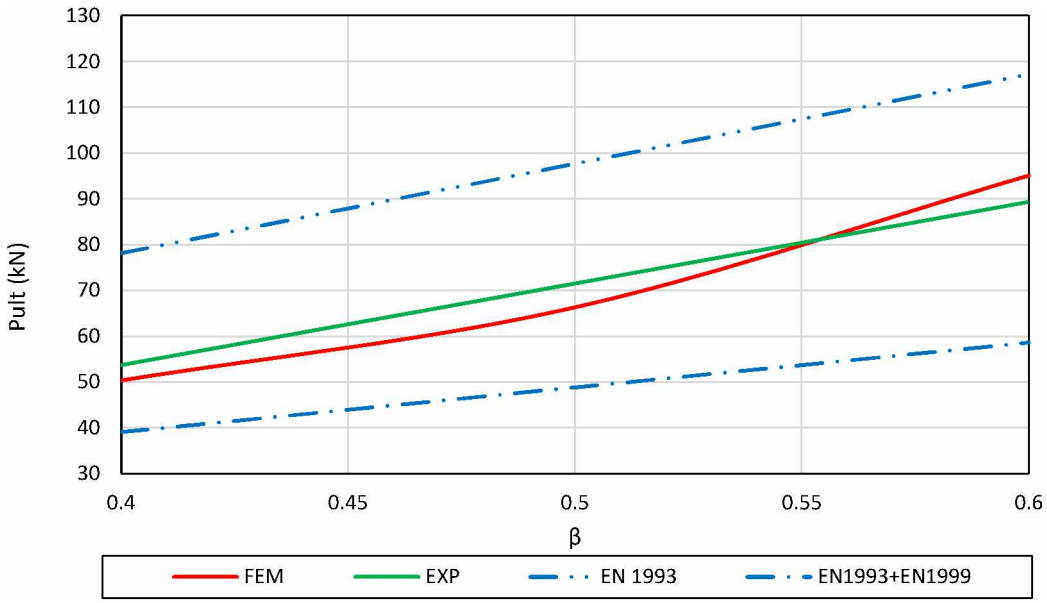

Fig. 84: Ultimate load P_{ult} versus β ratio for CHS KC-joints for γ=10: comparison between numerical (FEM), experimental results (EXP) and predictions from EN 1993 (EN1993) and combined EN 1993 + EN 1999 design provisions (EN1993+EN1999).

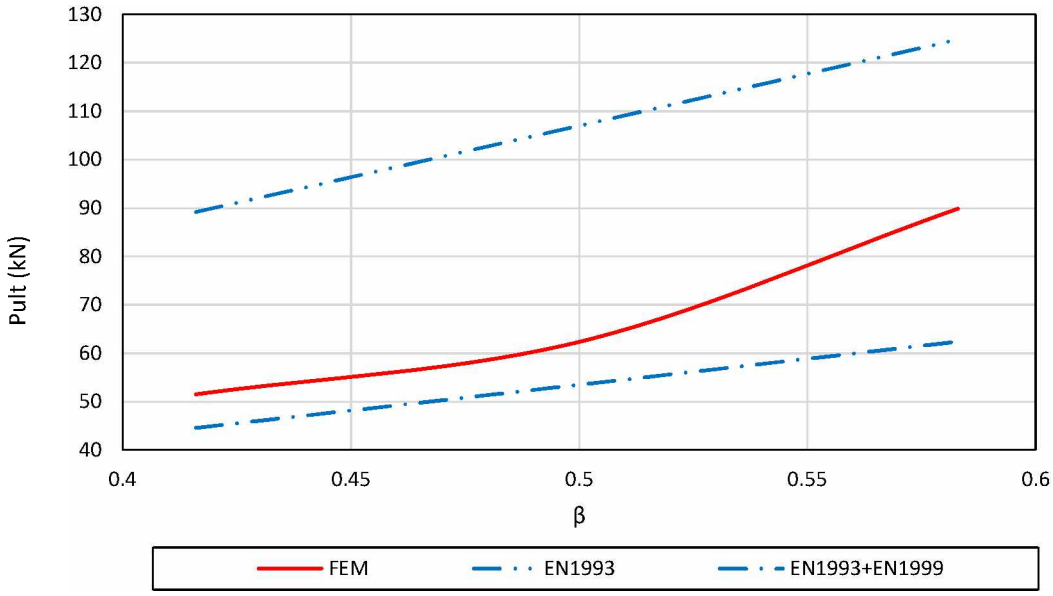

Fig. 85: Ultimate load P_{ult} versus β ratio for CHS KC-joints for γ=12: comparison between numerical (FEM), experimental results (EXP) and predictions from EN 1993 (EN1993) and combined EN 1993 + EN 1999 design provisions (EN1993+EN1999).

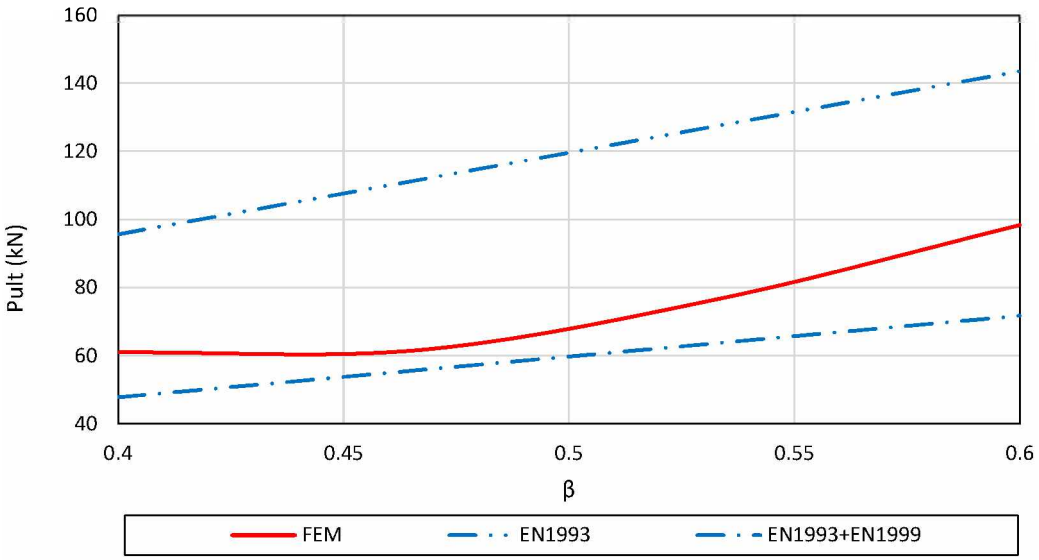

Fig. 86: Ultimate load P_{ult} versus β ratio for CHS KC-joints for γ=15: comparison between numerical (FEM), experimental results (EXP) and predictions from EN 1993 (EN1993) and combined EN 1993 + EN 1999 design provisions (EN1993+EN1999).

CHS KT joint

The tab. 29 below presents the load-bearing behavior of KT-type welded aluminum joints consisting of square hollow section (SHS) chord members and circular hollow section (CHS) brace members. The performance is assessed through numerical simulations (FEM), experimental investigations (EXP), and comparison of code-based results from EN 1993 and EN 1993 + EN 1999 design codes. The key parameter is the β ratio ranging from 0.4 to 0.6 in this study.

Tab. 29: Comparation of numerical results of the load-bearing capacities of CHS KT-joints.

Type	Chord member	brace member	β	P_{serv} (kN)	P_{ult} (kN)
Numerical results	SHS100	CHS 40	0.4	35.493	47.174
	SHS100	CHS 50	0.5	50.64	62.350
	SHS100	CHS 60	0.6	75.974	87.91
Experimental results	SHS100	CHS 40	0.4	37.275	52.923
	SHS100	CHS 50	0.5	58.788	73.101
	SHS100	CHS 60	0.6		
EN1993	SHS100	CHS 40	0.4		87.363
	SHS100	CHS 50	0.5		109.204
	SHS100	CHS 60	0.6		131.044
EN1993 +EN 1999	SHS100	CHS 40	0.4		43.682
	SHS100	CHS 50	0.5		54.602
	SHS100	CHS 60	0.6		65.522

The numerical results closely follow the experimental values, with small deviations in both P_{serv} (serviceability limit) and P_{ult} (ultimate load). For example, at $\beta = 0.4$, numerical P_{ult} is 47.17 kN, while experimental is 52.92 kN → only ~12.2% difference. For $\beta = 0.5$, numerical Pult is 62.35 kN, while experimental is 73.10 kN → ~14.7% difference.This consistency validates the reliability of the FE numerical model. EN 1993 predictions significantly overestimate the ultimate capacity compared to both experimental and numerical results. At $\beta = 0.4$, EN1993 predicts 87.36 kN vs. 52.92 kN experimental → ~65% overestimation. At $\beta = 0.5$, EN1993 gives 109.20 kN, compared to 73.10 kN experimentally → ~49.4% over.

EN 1993 + EN 1999 predictions are more conservative, and tend to underestimate the experimental results. Numerical simulations accurately replicate the joint behavior observed in experiments and are suitable for parametric investigations. Experimental results confirm that the β ratio significantly affects the joint stiffness and strength: higher β values generally lead to higher P_{ult}. EN 1993 overestimates the load capacity and may not be suitable for direct application to welded aluminum joints without modification. EN 1993 + EN 1999, incorporating aluminum-specific reductions, provides safer and more realistic predictions, though often is slightly conservative. For accurate design of KT-type joints, especially with CHS braces, validated numerical models or experimental data should supplement standard codes, particularly when safety margins and weld quality are critical.

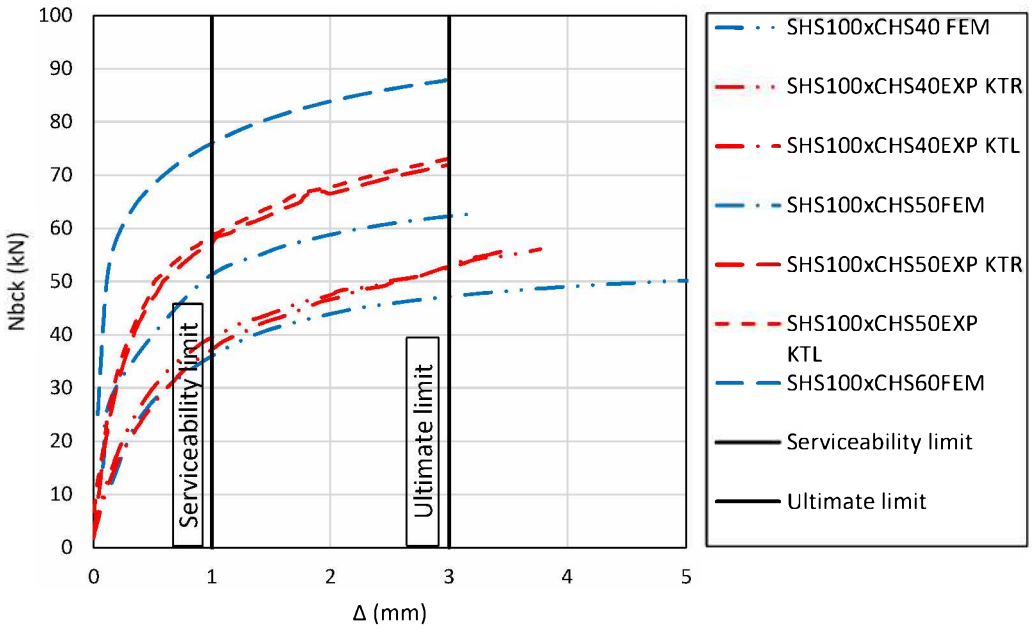

Fig. 87: Experimental (EXP) and numerical (FEM) force-deflection curves for CHS KT-joints.

KT joints

This tab. 30 presents the numerical results from the investigation of welded KT-joints formed by square hollow section (SHS) chord members and circular hollow section (CHS) brace members. The parametric variation is defined by the β which from 0.4 to 0.6, across three different chord sizes: SHS100, SHS120, and SHS150.

Tab. 30: Comparation of numerical results of the load-bearing capacities of CHS KT-joints.

Chord member	Brace member	β	P_{serv} (kN)	P_{ult} (kN)
SHS100	CHS 40	0.4	35.493	47.174
SHS100	CHS 50	0.5	50.640	62.350
SHS100	CHS 60	0.6	75.974	87.910
SHS120	CHS50	0.416	41.678	58.170
SHS120	CHS60	0.5	48.081	60.50
SHS120	CHS70	0.583	65.310	80.050
SHS150	CHS60	0.4	23.645	43.013
SHS150	CHS70	0.4666	33.890	49.670
SHS150	CHS80	0.5333	48.072	64.020
SHS150	CHS90	0.6	68.087	84.30

Across all chord sizes, increasing the β ratio leads to a consistent increase in both P_{serv} (service load) and P_{ult} (ultimate load). For SHS100, increasing β from 0.4 to 0.6 increased

P_{ult} from 47.17 kN to 87.91 kN, an 86.3% improvement. For SHS150, increasing β from 0.4 to 0.6 raised P_{ult} from 43.01 kN to 84.3 kN, showing a 95.9% improvement.

Joints with β = 0.4 consistently demonstrate the lowest ultimate capacities, suggesting that this ratio is at the lower limit for reliable load transfer in welded CHS-to-SHS connections. Especially noticeable in SHS150, where P_{ult} = 43.01 kN, compared to SHS100 at 47.17 kN.

The β ratio is the dominant parameter influencing load-bearing capacity in KT joints with CHS braces. Optimizing this ratio (approaching 0.6) maximizes the joint load-bearing capacity, see Figs. 88.-91.

While chord size positively correlates with load-bearing capacity, its influence is secondary to brace-to-chord geometry (β). These results provide valuable guidance for structural design of aluminum truss joints, particularly in identifying critical configurations that balance joint efficiency with material economy. Future standards should emphasize the interaction between brace size and chord stiffness, and promote validated numerical models to support designs beyond the conservative assumptions of current codes.

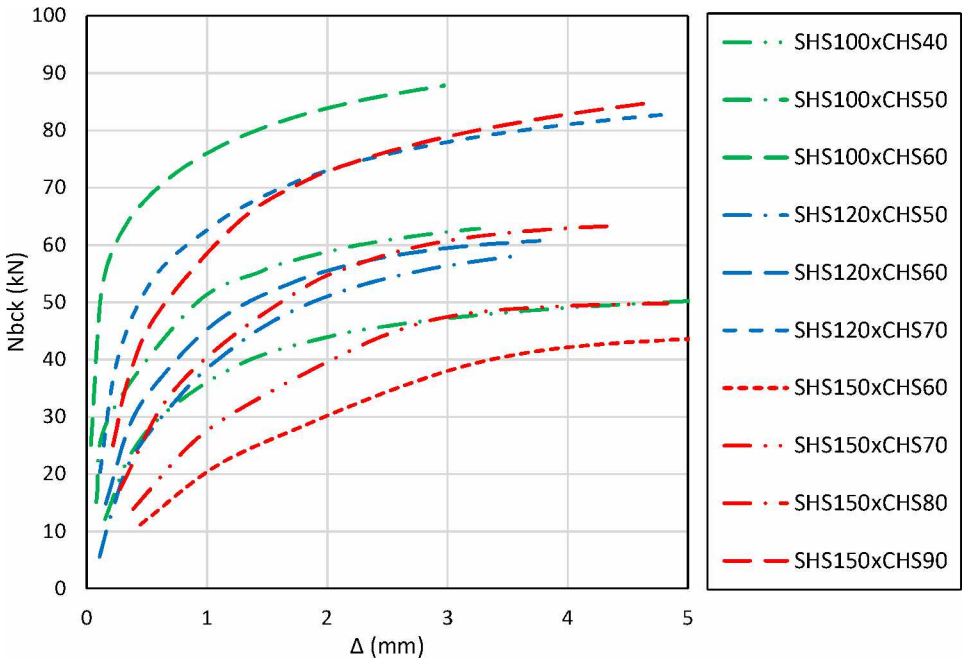

Fig. 88: Numerical (FEM) force-deflection curves for CHS KT-joints.

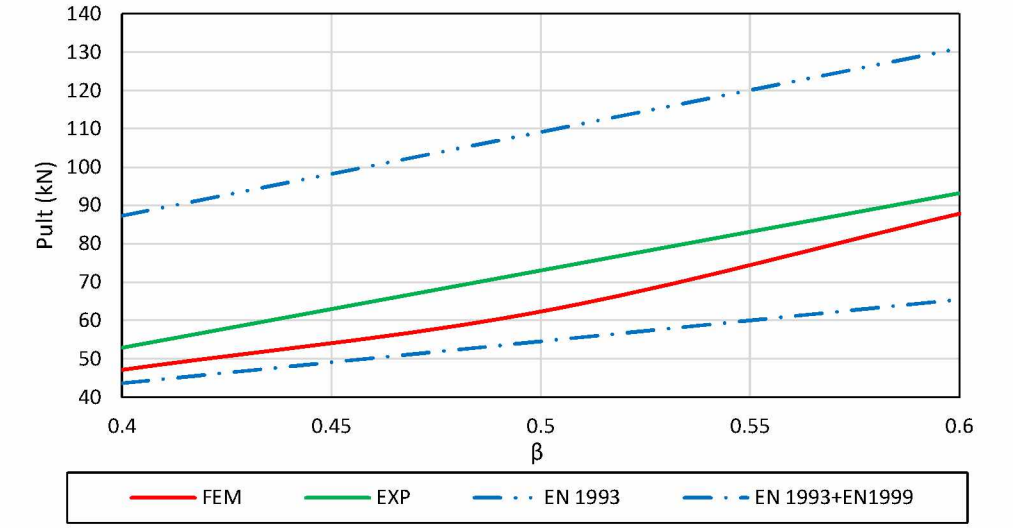

Fig. 89: Ultimate load P_{ult} versus β ratio for CHS KT-joints for γ=10: comparison between numerical (FEM), experimental results (EXP) and predictions from EN 1993 (EN1993) and combined EN 1993 + EN 1999 design provisions (EN1993+EN1999).

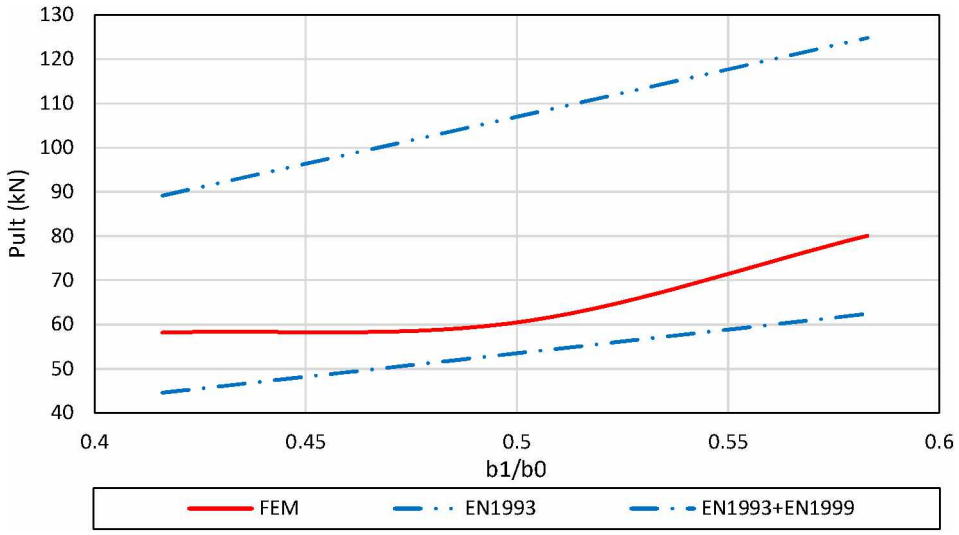

Fig. 90: Ultimate load P_{ult} versus β ratio for CHS KT-joints for γ=12: comparison between numerical (FEM), experimental results (EXP) and predictions from EN 1993 (EN1993) and combined EN 1993 + EN 1999 design provisions (EN1993+EN1999).

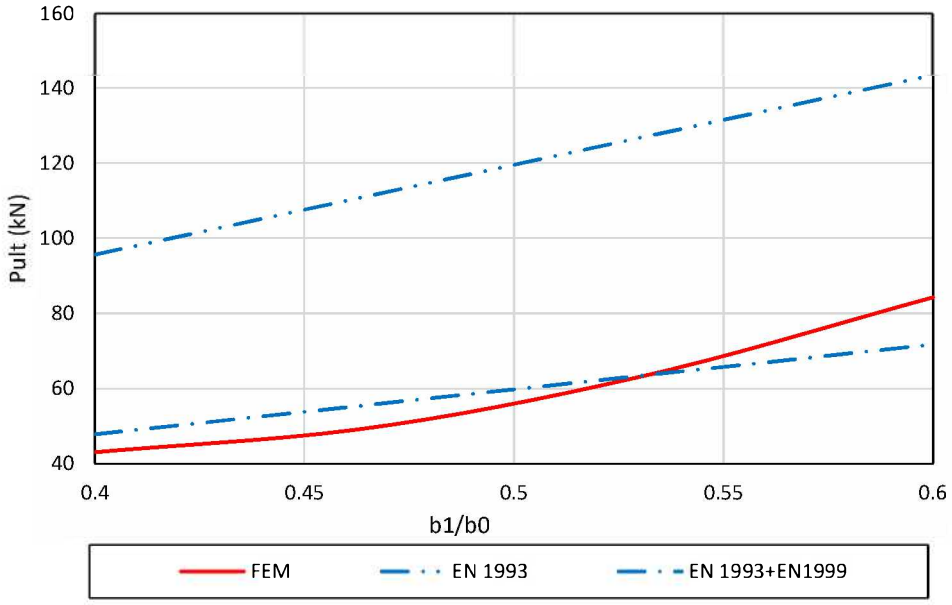

Fig. 90: Ultimate load P_{ult} versus β ratio for CHS KT-joints for γ=12: comparison between numerical (FEM), experimental results (EXP) and predictions from EN 1993 (EN1993) and combined EN 1993 + EN 1999 design provisions (EN1993+EN1999).

4.2.2 Investigation of isolated X joints

The primary objective of this numerical investigation was to develop a validated finite element model that can be reliably used in engineering practice and research and could be used for validation of analytical model which will be presented in the next chapter.

Two critical dimensionless parameters will be systematically varied and evaluated:

- β– This parameter represents the ratio between the width (or diameter) of the brace member and the width of the chord member. It also implicitly accounts for the influence of the welded surface area of the brace member. For this investigation, β values ranged from 0.4 to 0.6.
- γ– This parameter is defined as the ratio between the width of the chord member and twice the wall thickness of the chord member. The parameter reflects the chord's local stiffness and its ability to distribute stresses around the joint area. The values of γ to be considered in this study were 10, 12, and 15.

Numerical simulation was executed using the FE method by the software ANSYS [82]. Only one-eight of the specimen was modeled due to symmetry. Line A-A, B-B AND C-C are symmetry lines, as shown in Fig. 90.

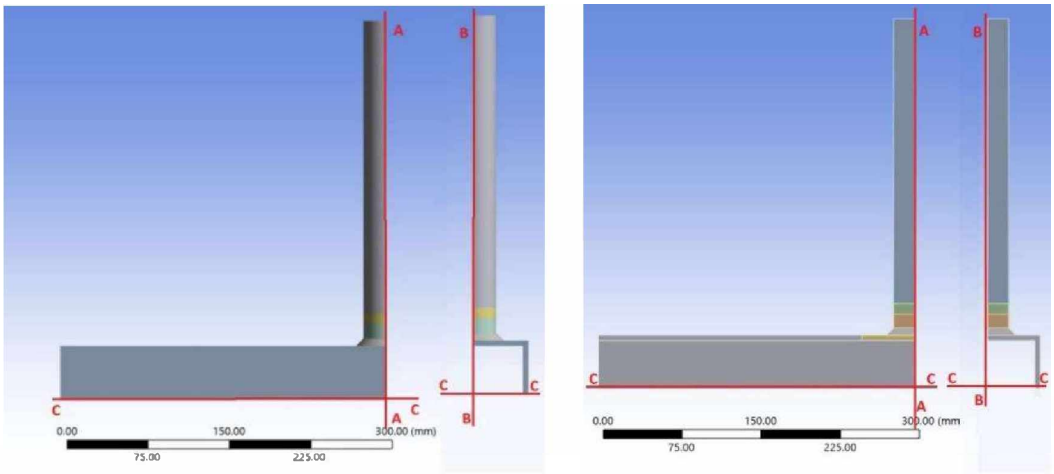

Fig. 90: Boundary conditions of one-quarter of the specimen

In the ANSYS model [51], the HAZ zones with the softening influence were modeled. The area of the chord overlapping with the brace and extending 20 mm on both sides of the brace along the contour of the chord's cross-section was defined as HAZ 1 in the chord. In the case of the brace member, HAZ 1 represented a 20-mm zone from the contact with the chord. HAZ 2 was defined as a 10-mm zone adjacent to HAZ 1, extending into both the chord and brace members. Multilinear diagrams were used for defining the material behavior in both zones, HAZ 1 and HAZ 2. The positions of the HAZs are presented in Fig. 91. Bonded contacts were used to model the interactions between the welds and heat-affected zones (HAZs), as well as between the HAZs and base material.

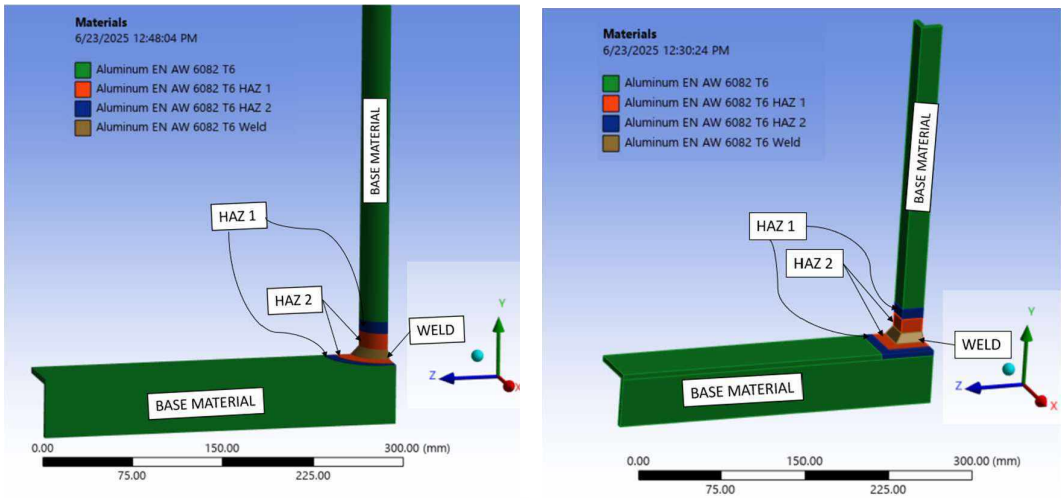

Fig. 91. Material zones.

Material definitions

The nonlinear behavior of the material [51] was taken into account, with the maximum deformations occurring within the plasticity domain. For numerical investigation, Ramberg–Osgood's equation of the stress– strain nonlinearity relation of a material [6] was applied for the welds and HAZ zones. The respective parameters are given in rEN 1999- 1-1 [6], Annex E, while for the HAZ zone, the HAZ area and yield stress distribution due to the softening effect are taken from the microhardness testing.

Mesh

The joint was modeled using solid elements, and by applying symmetry conditions, only one-eighth of the geometry was simulated. Joint was modeled as a solid body and HEX 20 finite element were used dominantly. Meshing was done with a multi-zone function.

Bodies inside the model were separated as:

1. Base material- solid bodies of aluminum truss girder that are not affected by HAZ;

2. Weld- Solid bodies of weld;

3. HAZ 1- Heat affected zone close to weld, width 20mm;

4. HAZ 2- Heat affected zone 2nd part, width 10mm ;

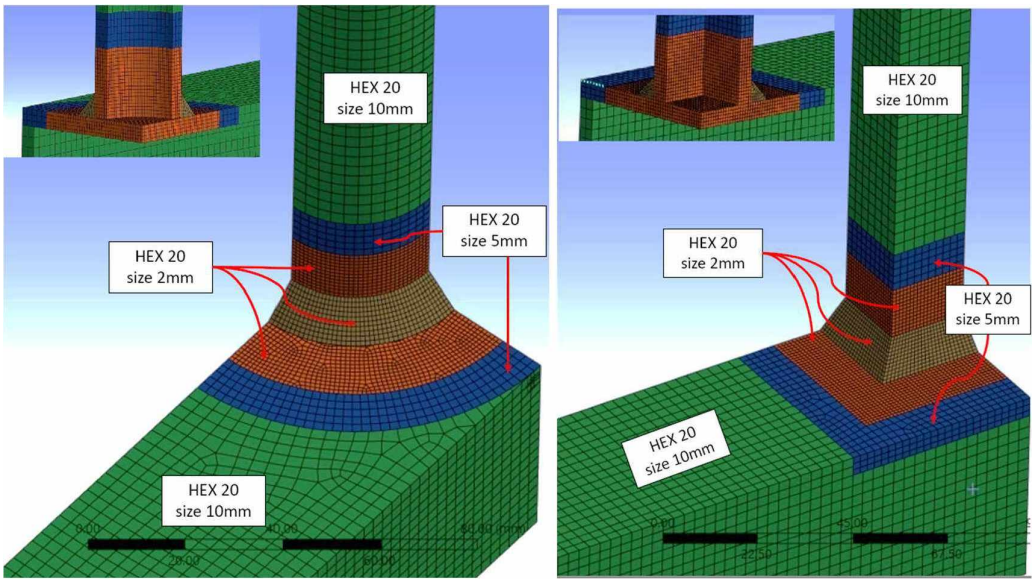

Fig. 93. Meshed isolated joints.

SHS X joint

These joints consist of square hollow section (SHS) profiles used both for the chord and the opposing brace members, which are welded symmetrically on opposite sides of the chord. Such X-joint configurations are typical in truss structures and truss frameworks, particularly in aluminum or steel space frames, where axial forces are transmitted through the central chord via aligned braces. Each joint configuration is characterized by the β-ratio which range is from 0.4 to 0.6. The results include joint capacities expressed in terms of P1%bo and P3%bo, which correspond to specific load levels normalized with respect to the chord width. These values represent the joint resistance at two deformation stages—typically associated with serviceability (e.g., 1% chord deformation) and ultimate limit states (e.g., 3% chord deformation), respectively.

The joint capacities were obtained through three primary methods: numerical simulations (NUM) using finite element analysis, experimental testing (EXP) on full-scale specimens, and code- based on current design standards. The analytical results follow two distinct approaches: one based solely EN 1993, which is tailored for welded steel joints, and another that combines EN 1993 and EN 1999, introducing adjustments for material behavior relevant to aluminum structures. This allows for an evaluation of how well existing steel design provisions can be adapted to welded aluminum X-joints.

The purpose of this comparative study is to examine the consistency between numerical, experimental, and code-based predictions, and to assess the applicability of current Eurocode formulations for the design of welded SHS X-joints, particularly in aluminum structures. The results also highlight the sensitivity of joint performance to variations in the β-ratio and provide insights into the structural efficiency and reliability of these connections under axial brace loading. This dataset forms a basis for validating modeling techniques and for proposing improvements to existing design methodologies.

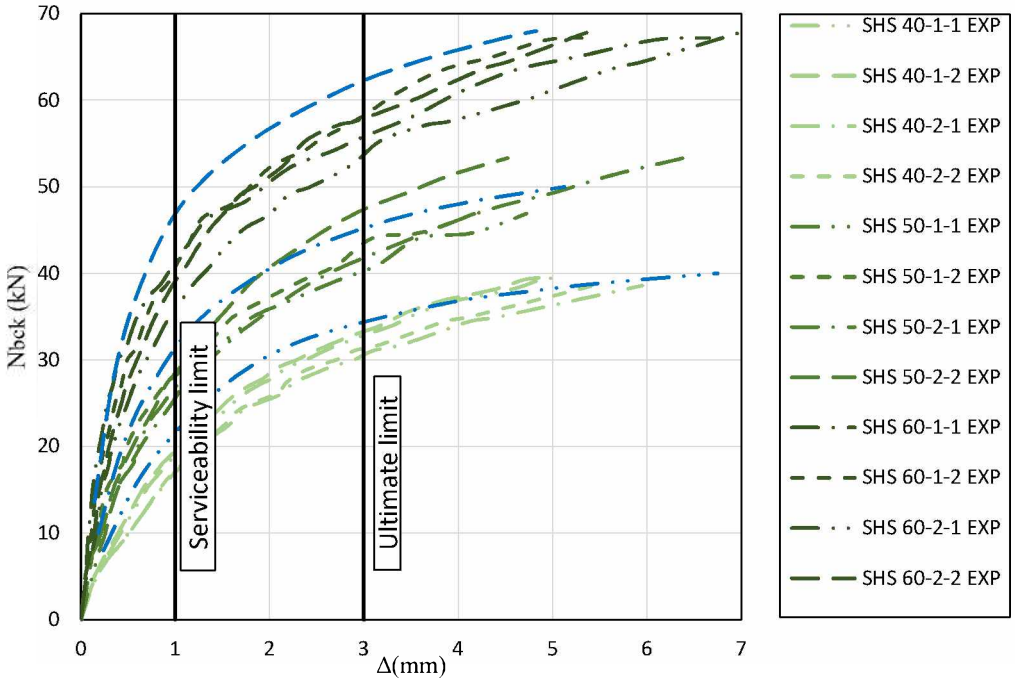

Fig. 94. Experimental (EXP) and numerical (FEM) force-deflection curves for SHS X-joints.

The tab. 32 presents a comparison between numerical, experimental and code-based (EN1993 and EN1993 + EN1999) results on the load-bearing behavior of isolated SHS X-joints subjected to axial loading, with a 90-degree angle between the brace and the chord members. The β ratio, defined as the ratio of the brace width to the chord width (b_1/b_0), ranges from 0.4 to 0.6 across the dataset.

Tab. 32: Comparation of numerical and experimental results of load-bearing capacity of isolated SHS X-joints.

	Chord	Brace	β	P_{serv} (kN)	P_{ult} (kN)
Numerical results	SHS 100	SHS40	0.4	21.581	34.164
		SHS50	0.5	28.386	45.097
		SHS60	0.6	47.6	62.105
Experimental results	SHS 100	SHS40	0.4	18.51	32.021
		SHS50	0.5	27.96	43.223
		SHS60	0.6	39.271	56.42
EN 1993	SHS 100	SHS40	0.4		40.608
		SHS50	0.5		47.855
		SHS60	0.6		58.278
EN 1993+EN 1999	SHS 100	SHS40	0.4		20.304
		SHS50	0.5		23.927
		SHS60	0.6		29.139
	SHS 120	SHS50	0.416	17.826	32.022

Numerical results		SHS60	0.5	26.651	42.384
		SHS70	0.5833	33.737	55.285
EN 1993	SHS 120	SHS50	0.416		41.661
		SHS60	0.5		47.855
		SHS70	0.5833		56.225
EN 1993+EN 1999	SHS 120	SHS50	0.416		20.830
		SHS60	0.5		23.927
		SHS70	0.5833		28.112
Numerical results	SHS 150	SHS60	0.4	14.191	27.486
		SHS70	0.4667	18.6	33.630
		SHS80	0.533	24.662	42.186
		SHS90	0.6	34.168	53.982
EN 1993	SHS 150	SHS60	0.4		40.608
		SHS70	0.4667		45.165
		SHS80	0.533		50.878
		SHS90	0.6		58.278
EN 1993+EN 1999	SHS 150	SHS60	0.4		20.304
		SHS70	0.4667		22.582
		SHS80	0.533		25.439
		SHS90	0.6		29.139

The presented dataset offers a detailed comparison of the load-bearing capacities of welded SHS X-joints under axial brace loading, where the braces are symmetrically connected to the chord at a 90-degree angle. Joint strength is evaluated using numerical simulations (NUM), experimental tests (EXP), and analytical predictions based on Eurocode 3 (EN 1993) and the combination of Eurocode 3 and Eurocode 9 (EN 1993+EN 1999)—the latter adjusted to reflect the mechanical behavior of aluminum alloys.

For joints with SHS 100 chord sections, as the β-ratio increases from 0.4 to 0.6, a consistent increase in joint capacity is observed. At $\beta = 0.4$, the experimental ultimate load (P_{ult}) is 32.02 kN, while the numerical simulation predicts 34.16 kN—an overestimation of around 7%. The EN 1993 prediction for this case is significantly higher at 40.61 kN, overestimating the test result by approximately 27%. In contrast, the EN 1993+1999 method gives a much lower value of 20.30 kN, underpredicting the capacity by nearly 37%. Similar trends are observed for $\beta = 0.5$ and 0.6, where EN 1993 consistently provides higher estimates than experiments, while EN 1993+1999 remains very conservative. For instance, at $\beta = 0.6$, the experimental capacity is 56.42 kN, the numerical result is 62.11 kN, EN 1993 predicts 58.28 kN, and EN 1993+1999 gives only 29.14 kN.

With SHS 120 chord joints, the same pattern holds. At $\beta = 0.416$, the numerical result ($P_{ult} = 32.02$ kN) is lower than the EN 1993 prediction (41.66 kN) but relatively close to the EN 1993+1999 value (20.83 kN). As β increases to 0.583, the numerical prediction reaches 55.29 kN and closely matches the EN 1993 result of 56.23 kN. However, the EN 1993+1999 value remains conservative at 28.11 kN—about 49% below the simulated capacity. This suggests that while EN 1993 becomes more accurate at larger β values, EN 1993+1999 continues to underpredict capacity across the full range.

For joints with the largest chord section (SHS 150), numerical results again increase with β, ranging from 27.49 kN ($\beta = 0.4$) to 53.98 kN ($\beta = 0.6$). At lower β values, EN 1993 substantially overestimates the capacity (e.g., 40.61 kN vs. 27.49 kN), while at higher β values it becomes more aligned with numerical predictions. For $\beta = 0.6$, the difference between EN 1993 (58.28 kN) and NUM (53.98 kN) is only around 8%. In contrast, EN 1993+1999 continues to provide significantly lower estimates (e.g., 29.14 kN), which may be overly conservative. This underlines a general trend: while EN 1993 may offer acceptable predictions at high β values and large chord sections, it tends to overestimate joint strength at lower β. The EN 1993+1999 method, designed to account for aluminum behavior, results in systematic underprediction of capacity—often by 30–50%.

Overall, numerical simulations demonstrate excellent agreement with experimental results, with deviations typically below 10%, confirming the reliability of finite element models for predicting the behavior of welded SHS X-joints, see Figs. 95-97. EN 1993, although originally developed for steel structures, provides relatively good predictions at higher β values but may not be safe or accurate for aluminum joints with small brace-to-chord ratios. EN 1993+EN 1999, though safe, appears overly conservative in most cases, potentially leading to inefficient use of material and unnecessarily heavy design solutions.

In conclusion, the dataset highlights the limitations of directly applying EN 19933 expressions to welded aluminum X-joints. The results underscore the need for calibrated or aluminum-specific design equations, especially for $\beta < 0.5$. Until such provisions are standardized, validated numerical simulations can serve as a reliable design tool. These findings support further refinement of current design codes to improve their accuracy and applicability to aluminum hollow section joints.

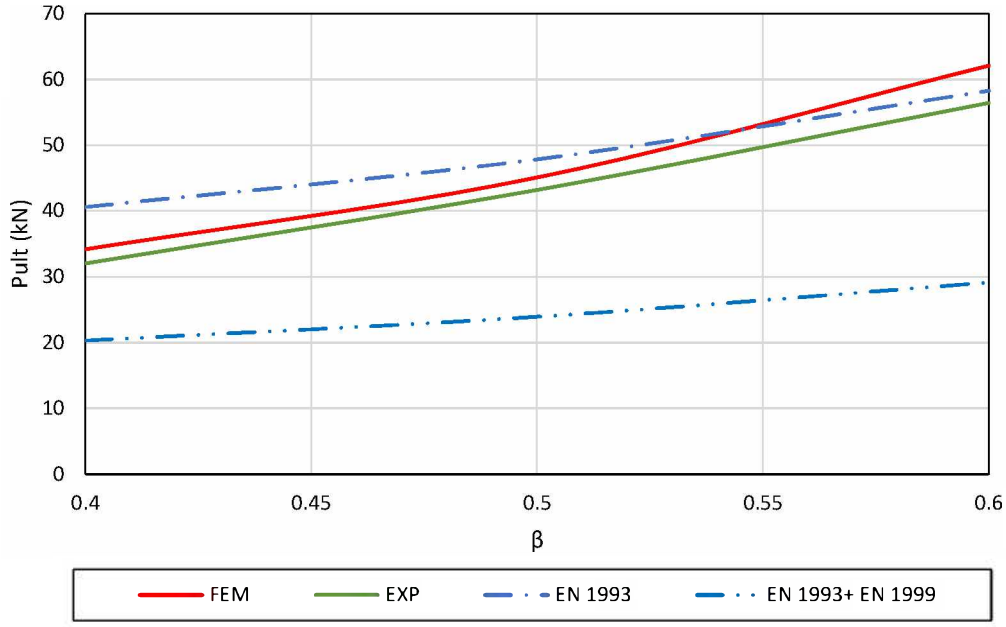

Fig. 95: Ultimate load P_{ult} versus β ratio for SHS X-joints for γ=10: comparison between numerical (FEM), experimental results (EXP) and predictions from EN 1993 (EN1993) and combined EN 1993 + EN 1999 design provisions (EN1993+EN1999).

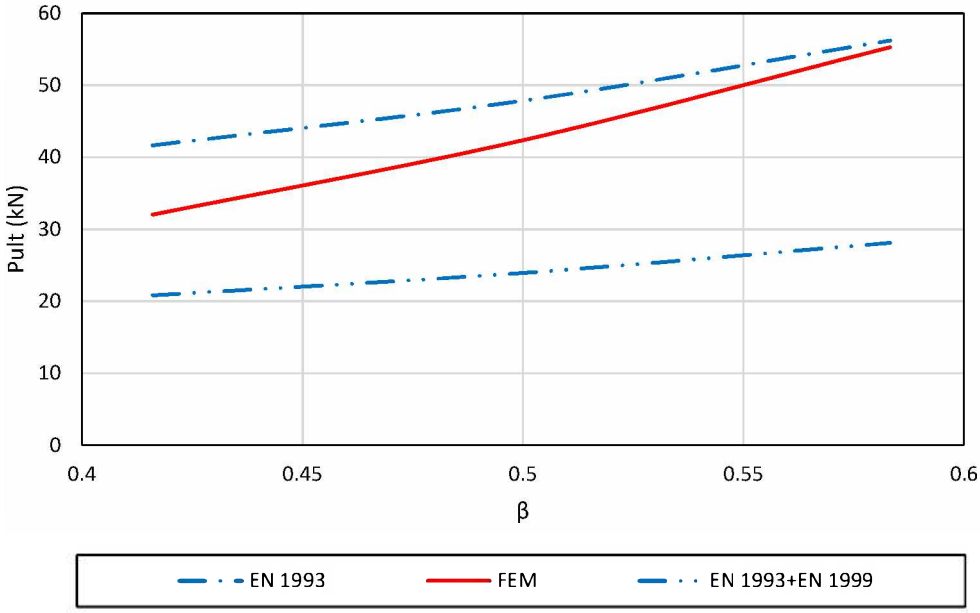

Fig. 96: Ultimate load P_{ult} versus β ratio for SHS X-joints for γ=12: comparison between numerical (FEM), experimental results (EXP) and predictions from EN 1993 (EN1993) and combined EN 1993 + EN 1999 design provisions (EN1993+EN1999).

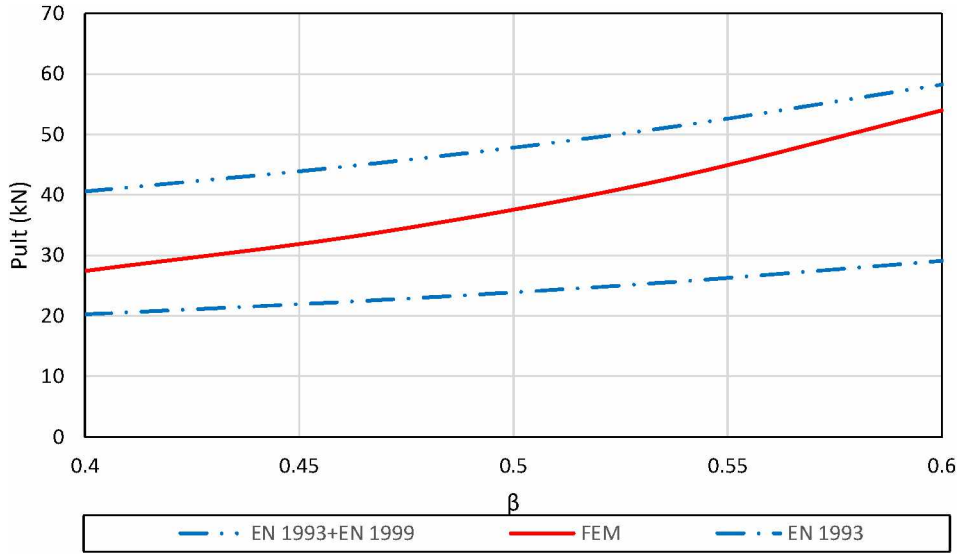

Fig. 97: Ultimate load P_{ult} versus β ratio for SHS X-joints for γ=15: comparison between numerical (FEM), experimental results (EXP) and predictions from EN 1993 (EN1993) and combined EN 1993 + EN 1999 design provisions (EN1993+EN1999).

CHS X joint

These X-joints are composed of SHS chord members and CHS brace members, arranged at a 90° angle. The chord members are of varying sizes: SHS 100, SHS 120, and SHS 150, and the brace members range from CHS40 to CHS90, resulting in β values (brace width to chord width ratio) from 0.4 to 0.6.

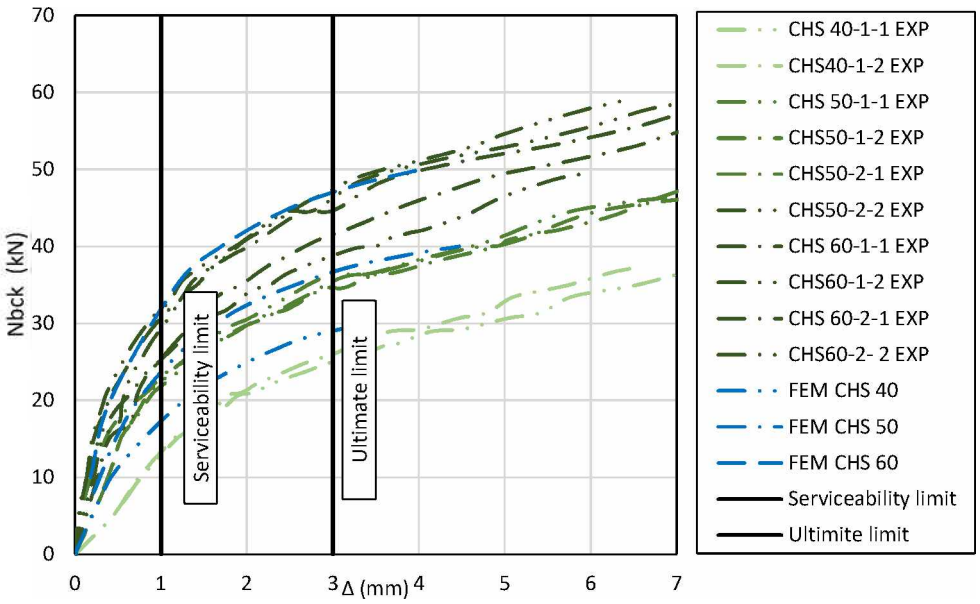

Fig. 98. Experimental (EXP) and numerical (FEM) force-deflection curves for SHS X-joints.

The tab. 33 presents an extensive comparison of load-bearing capacities for isolated CHS X-joints. Each row includes data from either numerical simulation (NUM), experimental testing (EXP), or code-based values calculated using EN 1993 and combined EN 1993 + EN 1999 design formulations. The key parameters under comparison are the load values corresponding to 1% and 3% deformation of the chord width — denoted as P_{serv} and P_{ult}.

For each geometry, the performance of the joints is evaluated by observing how P1%bo and P3%bo values differ between the predictive methods (NUM, EN standards) and actual test results (EXP). Notably, EN 1993 values are based on steel design provisions, while EN 1999 incorporates aluminum-specific behavior, offering more conservative values, especially for aluminum structures. This table helps assess how accurately various predictive methods reflect real-world joint behavior under axial loading.

Tab. 33: Comparation of numerical and experimental results of load-bearing capacity of isolated CHS X-joints.

	Chord member	Brace member	β	P_{serv}	P_{ult}
Numerical results	SHS 100	CHS40	0.4	16.79	28.883
		CHS50	0.5	23.455	36.691
		CHS60	0.6	31.424	46.899
Experimental results	SHS 100	CHS40	0.4	19.983	25.484
		CHS50	0.5	22.402	36.182
		CHS60	0.6	29.325	44.961
EN 1993	SHS 100	CHS40	0.4		31.877
		CHS50	0.5		37.566
		CHS60	0.6		45.748
EN 1993+ EN 1999	SHS 100	CHS40	0.4		15.938
		CHS50	0.5		18.783
		CHS60	0.6		22.874
Numerical results	SHS 120	CHS50	0.416	14.973	27.075
		CHS60	0.5	19.62	33.778
		CHS70	0.5833	26.651	42.369
EN 1993	SHS 100	CHS50	0.416		32.704
		CHS60	0.5		37.566
		CHS70	0.5833		44.137
EN 1993+ EN 1999	SHS 120	CHS50	0.416		16.352
		CHS60	0.5		18.783
		CHS70	0.5833		22.068
Numerical results	SHS 150	CHS60	0.4	11.5	22.623
		CHS70	0.4667	14.04	26.825
		CHS80	0.533	17.714	32.521

		CHS90	0.6	22.97	39.511
EN 1993	SHS 150	CHS60	0.4		31.877
		CHS70	0.4667		35.454
		CHS80	0.533		39.939
		CHS90	0.6		45.748
EN 1993+ EN 1999	SHS 150	CHS60	0.4		15.938
		CHS70	0.4667		17.7273
		CHS80	0.533		19.969
		CHS90	0.6		22.874

The data reveals several key trends regarding the accuracy and conservatism of the numerical model and Eurocode design provisions in predicting joint performance.

Starting with the SHS 100 chord, numerical results show a progressive increase in the load-bearing capacity as β increases from 0.4 to 0.6. For instance, at β = 0.6, the numerical P_{ult} reaches 46.899 kN, while experimental results are slightly lower at 44.961 kN. However, EN 1993 overestimates the strength (45.7 kN at β = 0.6), and EN 1993+EN 1999 is far more conservative, offering a much lower prediction (22.87 kN), capturing only about 51% of the experimental capacity. This discrepancy emphasizes the safety margin built into EN 1999 for aluminum joints, likely due to uncertainties in weld behavior and heat-affected zone softening.

When examining SHS 120 chord members, a similar pattern appears. For β = 0.5 (CHS60), the numerical model gives 33.778 kN at 3% deformation, closely followed by the EN 1993 prediction (37.566 kN). Again, EN 1993+1999 is more conservative at 18.78 kN — almost 50% lower than the numerical estimate. For the larger brace (CHS70, β = 0.5833), the numerical result reaches 42.369 kN, but EN 1993+1999 remains conservative at 22.07 kN.

The trend continues with the SHS 150 chord. At β = 0.6 (CHS90), the numerical model predicts 39.511 kN, while EN 1993 suggests 45.75 kN, which is an overestimation even compared to numerical predictions. Meanwhile, EN 1993+EN 1999 gives a conservative value of 22.87 kN, again approximately 50-55% of the numerical result. This consistent conservatism supports the notion that Eurocode provisions for aluminum intentionally underpredict joint resistance to ensure design safety, especially in absence of detailed test validation.

Interestingly, the experimental results (where available) tend to fall between the numerical and EN 1993 values. For example, for SHS 100 with CHS60 (β = 0.6), the experimental P_{ult} is 44.96 kN, just under the numerical value of 46.9 kN and almost equal to the EN 1993 prediction of 45.75 kN. This indicates that the numerical model provides a reasonably accurate upper-bound prediction of actual behavior, whereas EN 1993+1999 acts as a lower-bound envelope for conservative design.

Overall, we can conclude that numerical models provide realistic and moderately safe estimates, especially for aluminum joints with proper calibration see Figs. 98-101. Experimental results validate the numerical predictions within a ±10% range in most cases. EN 1993 provisions (based on steel behavior) often overpredict the capacity of aluminum joints, particularly for larger brace sizes. EN 1993 + EN 1999 combined design values are consistently conservative — underpredicting strength by 40–55%.

This analysis strongly supports the need for numerical simulations and/or physical testing when designing high-efficiency aluminum truss joints, especially if a more optimal balance between safety and material usage is desired beyond the conservative bounds of current standards.

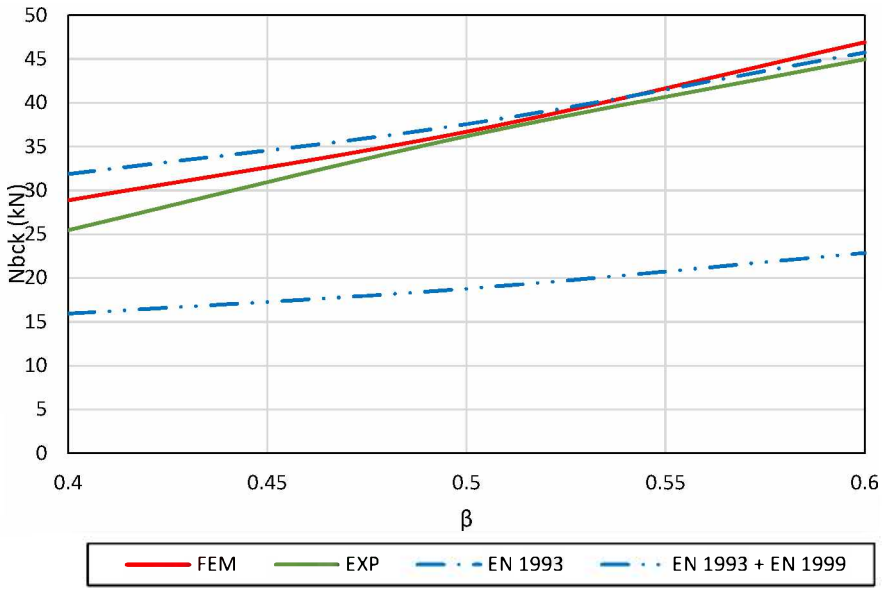

Fig. 99: Ultimate load P_{ult} versus β ratio for CHS X-joints for γ=10: comparison between numerical (FEM), experimental results (EXP) and predictions from EN 1993 (EN1993) and combined EN 1993 + EN 1999 design provisions (EN1993+EN1999).

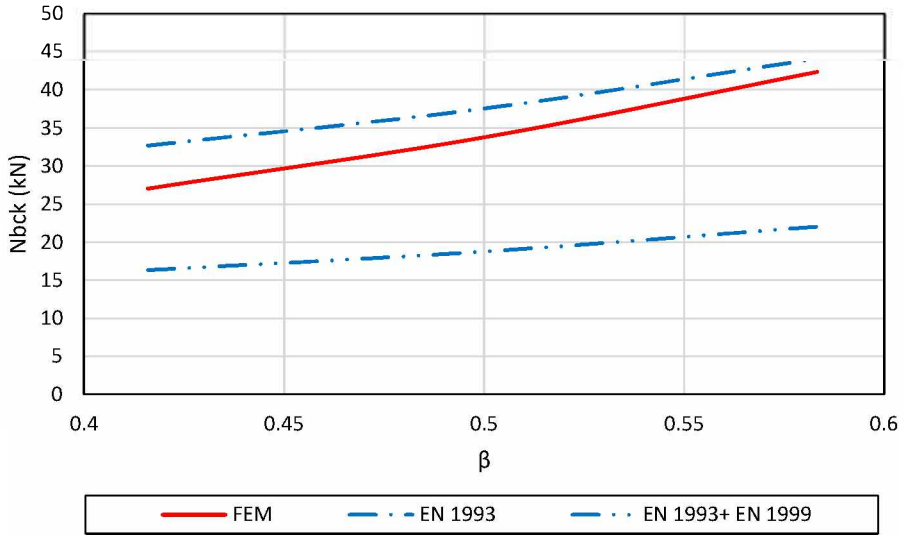

Fig. 100: Ultimate load P_{ult} versus β ratio for CHS X-joints for γ=12: comparison between numerical (FEM), experimental results (EXP) and predictions from EN 1993 (EN1993) and combined EN 1993 + EN 1999 design provisions (EN1993+EN1999).

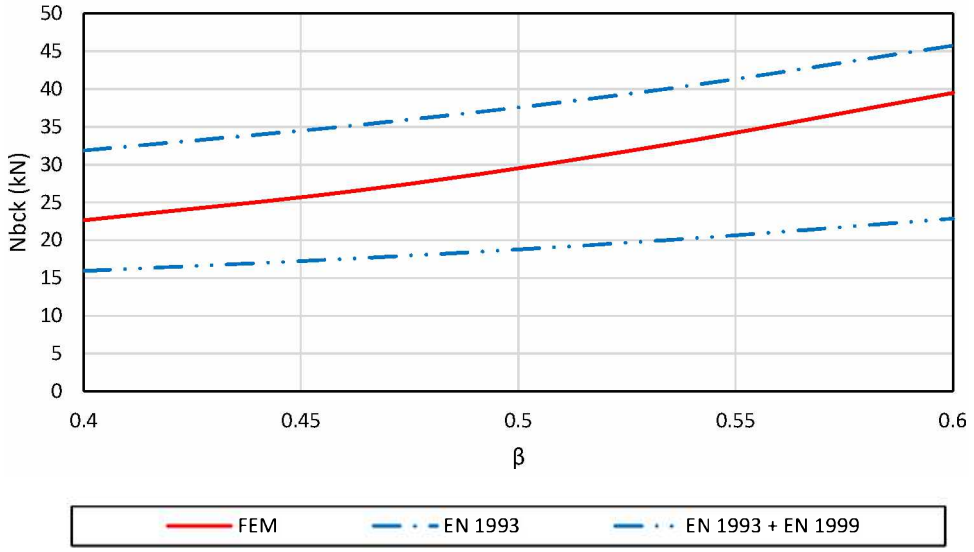

Fig. 101: Ultimate load P_{ult} versus β ratio for CHS X-joints for γ=15: comparison between numerical (FEM), experimental results (EXP) and predictions from EN 1993 (EN1993) and combined EN 1993 + EN 1999 design provisions (EN1993+EN1999).

4.3 Theoretical investigation

The load-bearing capacity of welded aluminum joints where β is less than 0.8 is predominantly governed by the plastification of the chord face in the vicinity of the brace intersection. Due to the relatively thin walls of hollow sections and the local stress concentrations caused by brace loading, yield line theory has emerged as a practical and reliable tool to estimate the plastic resistance of such connections. Yield line analysis [62,63], originally developed for reinforced concrete slabs, has been adapted successfully to the analysis of steel and aluminum structural connections, particularly in Rectangular Hollow Section (RHS) joints.

Previous research, notably the work of Cao, Packer, and Yang [61], established a comprehensive framework for yield line analysis in RHS connections subjected to axial loads. They introduced orthotropic plasticity concepts to account for axial preload effects and developed a general strength reduction factor [61]. However, their work primarily addressed steel connections and was focused on experimental correlations for RHS-to-plate joints. Additional foundational contributions were made by Johansen (1972) [62], Wood (1961) [63], and Zhao & Hancock (1993) [64], who investigated yield line formulations and orthotropic plate behavior in the presence of axial forces.

In this dissertation, a new analytical expression for evaluating the load-bearing capacity of aluminum welded RHS X-joints under concentrated loading has been developed which covers also the SHS X-joints. This expression is derived using the principle of virtual work and incorporates a refined yield line mechanism tailored for welded aluminum joints. Unlike previous models, the expression explicitly accounts for the range and influence of HAZ on each plastic hinge and provides a direct formulation for the minimum force required to initiate a yield line failure mechanism.

The derivation presented in this chapter demonstrates that by introducing specific parameters representing hinge locations and rotational compatibility and material softening effect in the HAZ area, the model achieves greater generality while maintaining compatibility with existing solutions in the literature. The final expression is suitable for parametric analysis, experimental validation, and numerical benchmarking.

4.3.1 Derivation of the Analytical Expression

The derivation is based on the equilibrium between external work and internal plastic dissipation along predefined plastic hinge lines. The assumed failure mechanism consists of five distinct yield lines formed on the chord face due to the action of a transverse brace load.

External Work

The external virtual work(W_{EXT})is calculated as the product of the applied force and the virtual displacement at the point of loading. Assuming unit displacement in the direction of loading and neglecting other external effects:

Internal Work

The internal plastic work (W_{INT}) is the sum of the plastic moment capacities multiplied by the rotation along each hinge line. The plastic hinge lines are denoted as:

- Line 1: Vertical hinge line perpendicular to the axis of the chord which width correspondents to the width of chord member;
- Line 2: Vertical hinge line represents intersection line between brace and chord member parallel to the Line 1 which width correspondents to the width of brace member;
- Line 3: Horizontal hinge line parallel to the axis of the chord located at the edge of chord member profile;
- Line 4: Horizontal hinge line parallel to the axis of the chord located at the intersection line between brace and chord member which width correspondents to the inclined projection of the brace member profile height;
- Line 5: Diagonal hinge lime inclined with respect to both axes.

The plastic moment per unit length is denoted as m_{pl} in base material and $m_{pl,HAZ}$ in HAZ material. The internal work along each line depends on the rotation angle φ_i and hinge length l_i.

Using geometric relationships, each φ_i is expressed in terms of virtual displacements and characteristic dimensions of the joint.

The developed expression for welded aluminum RHS X-joint, which part are also SHS X-joint, is defined as piecewise function depending on the area of HAZ and its influence on the hinge lines.

First case is the case when all the plastification zone is inside HAZ area which correspondents to the expression which is obtained as combination of EN 1993-1-8 and EN 1999-1-1, see Fig. 102. But for this expression, there has been defined limit of validity over which application of this expression will be conservative and will not represent true behavior of the joint.

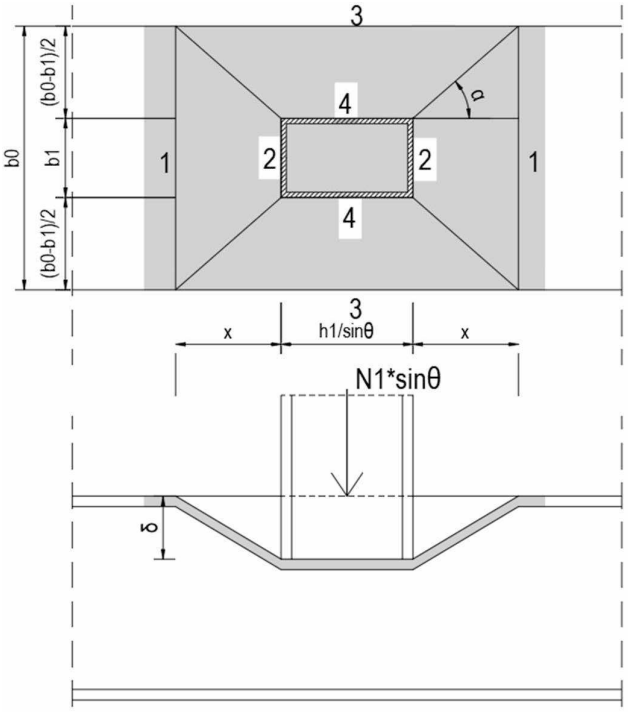

Fig. 102: First case when all the plastification zone is inside HAZ area

External force work

$$W_{EXT} = N_1 * \delta * sin\theta$$

Internal force work

$$W_{INT} = \sum_{i=1}^{5} l_i * m_{pl,HAZ} * \varphi_i$$

Plastic hinge line 1

$$\sum l_1 * m_{pl,HAZ} * \varphi_1 = 2 * b_0 * \frac{t_0^2 * f_{0.2}}{4} * \rho_{0,HAZ} * \frac{2 * \delta}{(b_0 - b_1) * ctg\alpha}$$

Plastic hinge line 2

$$\sum l_2 * m_{pl,HAZ} * \varphi_2 = 2 * b_1 * \frac{t_0^2 * f_{0.2}}{4} * \rho_{0,HAZ} * \frac{2 * \delta}{(b_0 - b_1) * ctg\alpha}$$

Plastic hinge line 3

$$\sum l_3 * m_{pl,HAZ} * \varphi_3$$

$$= 2 * \left(\frac{h_1}{sin\theta} + 2 * \frac{b_0 - b_1}{2} * ctg\alpha\right) * \frac{t_0^2 * f_{0.2}}{4} * \rho_{0,HAZ} * \frac{2 * \delta}{(b_0 - b_1)}$$

$$\sum l_3 * m_{pl,HAZ} * \varphi_3 = 4 * \left(\frac{\eta}{(1 - \beta) * sin\theta} + ctg\alpha\right) * \frac{t_0^2 * f_{0.2}}{4} * \rho_{0,HAZ} * \delta$$

Plastic hinge line 4

$$\sum l_4 * m_{pl,HAZ} * \varphi_4 = 2 * \left(\frac{h_1}{sin\theta}\right) * \frac{t_0^2 * f_{0.2}}{4} * \rho_{0,HAZ} * \frac{2 * \delta}{(b_0 - b_1)}$$

$$\sum l_4 * m_{pl,HAZ} * \varphi_4 = 4 * \left(\frac{\eta}{(1 - \beta) * sin\theta}\right) * \frac{t_0^2 * f_{0.2}}{4} * \rho_{0,HAZ} * \delta$$

Plastic hinge line 5

$$\sum l_5 * m_{pl,HAZ} * \varphi_5 = 4 * l_5 * \left(\frac{\delta}{l_5 * tg\alpha} + \frac{\delta}{l_5 * ctg\alpha}\right) * \frac{t_0^2 * f_{0.2}}{4} * \rho_{0,HAZ}$$

$$\sum l_5 * m_{pl,HAZ} * \varphi_5 = 4 * \delta * (tg\alpha + ctg\alpha) * \frac{t_0^2 * f_{0.2}}{4} * \rho_{0,HAZ}$$

$$W_{INT} = 2 * b_0 * \frac{t_0^2 * f_{0.2}}{4} * \rho_{0,HAZ} * \frac{2 * \delta}{(b_0 - b_1) * ctg\alpha} + 2 * b_0 * \frac{t_0^2 * f_{0.2}}{4} * \rho_{0,HAZ}$$

$$* \frac{2 * \delta}{(b_0 - b_1) * ctg\alpha} + 4 * \left(\frac{\eta}{(1 - \beta) * sin\theta} + ctg\alpha\right) * \frac{t_0^2 * f_{0.2}}{4} * \rho_{0,HAZ}$$

$$* \delta + 4 * \left(\frac{\eta}{(1 - \beta) * sin\theta}\right) * \frac{t_0^2 * f_{0.2}}{4} * \rho_{0,HAZ} * \delta + * \delta * (tg\alpha + ctg\alpha)$$

$$* \frac{t_0^2 * f_{0.2}}{4} * \rho_{0,HAZ}$$

$$W_{INT} = 8 * \delta * \frac{t_0^2 * f_{0.2}}{4 * (1-\beta)} * \rho_{0,HAZ} * \left(\frac{\eta}{sin\theta} + (1-\beta) * ctg\alpha + tg\alpha\right)$$

$$\boldsymbol{W_{EXT} = W_{INT}}$$

$$N_1 = \frac{2 * t_0^2 * f_{0.2} * \rho_{0,HAZ}}{(1-\beta) * sin\theta} * \left(\frac{\eta}{sin\theta} + (1-\beta) * ctg\alpha + tg\alpha\right)$$

Minimal value of N_1 is derived from condition $\frac{dN_1}{d\alpha} = 0$

$$\frac{dN_1}{d\alpha} = \frac{2 * t_0^2 * f_{0.2} * \rho_{0,HAZ}}{(1-\beta) * sin\theta} * \left((1-\beta) * \left(-\frac{1}{sin\alpha^2}\right) + \left(\frac{1}{cos\alpha^2}\right)\right) = 0$$

Solution:

$$\alpha = arctg(\sqrt{1-\beta})$$

Expresion for N_1

$$N_1 = \frac{t_0^2 * f_{0.2} * \rho_{0,HAZ}}{(1-\beta) * sin\theta} * \left(\frac{2 * \eta}{sin\theta} + 4 * \sqrt{1-\beta}\right)$$

Condition for validity

$$x = \frac{b_0}{2} * \sqrt{1-\beta} < b_{HAZ}$$

Second case is when the joint plastification partially occurs out of the HAZ area and the situation is more complex compared to the first case when the whole plastification of the joint occurs in the HAZ area, see Fig. 103.

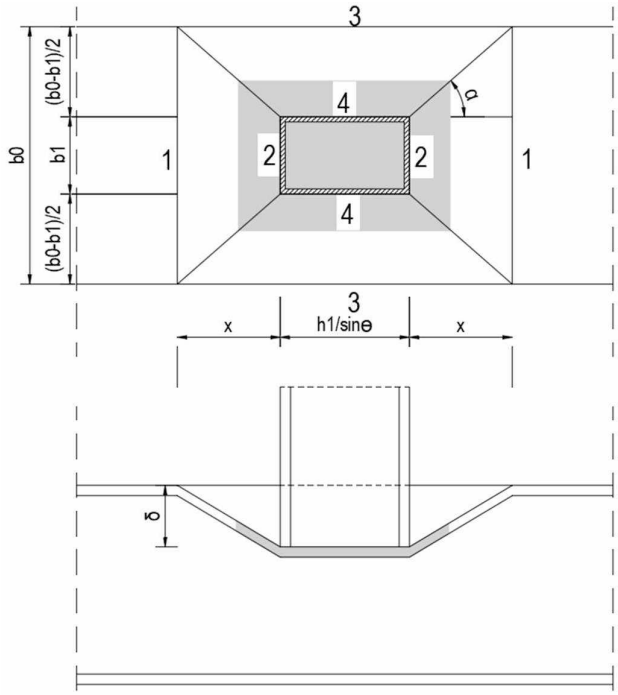

Fig. 103: Second case when all the plastification zone is inside HAZ area

External force work

$$W_{EXT} = N_1 * \delta * sin\theta$$

Internal force work

$$W_{INT} = \sum_{i=1}^{5} l_i * m_{pl,HAZ} * \varphi_i$$

Plastic hinge line 1

$$\sum l_1 * m_{pl} * \varphi_1 = 2 * b_0 * \frac{t_0^2 * f_{0.2}}{4} * \frac{2 * \delta}{(b_0 - b_1) * ctg\alpha}$$

Plastic hinge line 2

$$\sum l_2 * m_{pl,HAZ} * \varphi_2 = 2 * b_0 * \frac{t_0^2 * f_{0.2}}{4} * \rho_{0,HAZ} * \frac{2 * \delta}{(b_0 - b_1) * ctg\alpha}$$

Plastic hinge line 3

$$\sum l_3 * m_{pl} * \varphi_3 = 2 * \left(\frac{h_1}{sin\theta} + 2 * \frac{b_0 - b_1}{2} * ctg\alpha\right) * \frac{t_0^2 * f_{0.2}}{4} * \frac{2 * \delta}{(b_0 - b_1)}$$

$$\sum l_3 * m_{pl} * \varphi_3 = 4 * \left(\frac{\eta}{(1-\beta) * sin\theta} + ctg\alpha\right) * \frac{t_0^2 * f_{0.2}}{4} * \delta$$

Plastic hinge line 4

$$\sum l_4 * m_{pl,HAZ} * \varphi_4 = 2 * \left(\frac{h_1}{sin\theta}\right) * \frac{t_0^2 * f_{0.2}}{4} * \rho_{0,HAZ} * \frac{2 * \delta}{(b_0 - b_1)}$$

$$\sum l_4 * m_{pl,HAZ} * \varphi_4 = 4 * \left(\frac{\eta}{(1-\beta) * sin\theta}\right) * \frac{t_0^2 * f_{0.2}}{4} * \rho_{0,HAZ} * \delta$$

Plastic hinge line 5

$$l_{5,HAZ} = l_{5,tot} * \frac{2 * b_{HAZ}}{b_0 - b_1}$$

$$\sum l_{5,HAZ} * m_{pl,HAZ} * \varphi_5 \; + \; l_5 * m_{pl} * \varphi_5$$

$$= 4 * \left(l_{5,tot} * \left(\frac{2 * b_{HAZ}}{b_0 - b_1}\right)\right) * \left(\frac{\delta}{l_{5,tot} * tg\alpha} + \frac{\delta}{l_{5,tot} * ctg\alpha}\right) * \frac{t_0^2 * f_{0.2}}{4}$$

$$* \rho_{0,HAZ} + 4 * \left(l_{5,tot} * \left(1 - \frac{2 * b_{HAZ}}{b_0 - b_1}\right)\right) * \left(\frac{\delta}{l_{5,tot} * tg\alpha} + \frac{\delta}{l_{5,tot} * ctg\alpha}\right)$$

$$* \frac{t_0^2 * f_{0.2}}{4}$$

$$W_{INT} = 2 * b_0 * \frac{t_0^2 * f_{0.2}}{4} * \frac{2 * \delta}{(b_0 - b_1) * ctg\alpha} + 2 * b_0 * \frac{t_0^2 * f_{0.2}}{4} * \rho_{0,HAZ}$$

$$* \frac{2 * \delta}{(b_0 - b_1) * ctg\alpha} + 4 * \left(\frac{\eta}{(1-\beta) * sin\theta} + ctg\alpha\right) * \frac{t_0^2 * f_{0.2}}{4} * \delta + 4$$

$$* \left(\frac{\eta}{(1-\beta) * sin\theta}\right) * \frac{t_0^2 * f_{0.2}}{4} * \rho_{0,HAZ} * \delta + 4 * \left(l_{5,tot} * \left(\frac{2 * b_{HAZ}}{b_0 - b_1}\right)\right)$$

$$* \left(\frac{\delta}{l_{5,tot} * tg\alpha} + \frac{\delta}{l_{5,tot} * ctg\alpha}\right) * \frac{t_0^2 * f_{0.2}}{4} * \rho_{0,HAZ} + 4$$

$$* \left(l_{5,tot} * \left(1 - \frac{2 * b_{HAZ}}{b_0 - b_1}\right)\right) * \left(\frac{\delta}{l_{5,tot} * tg\alpha} + \frac{\delta}{l_{5,tot} * ctg\alpha}\right) * \frac{t_0^2 * f_{0.2}}{4}$$

$$\boldsymbol{W_{EXT} = W_{INT}}$$

$$N_1 * \delta * sin\theta = \frac{\delta * t_0^2 * f_{0.2}}{(1-\beta)} * \left(\beta * \left(1 + \rho_{o,HAZ}\right) * tg\alpha + \frac{\eta * \left(1 + \rho_{o,HAZ}\right)}{sin\theta} + (ctg\alpha + tg\alpha) * \left(1 - \beta - 2\frac{b_{HAZ}}{b_0} * \left(1 - \rho_{o,HAZ}\right)\right)\right)$$

Minimal value of N_1 is derived from condition $\frac{dN_1}{d\alpha} = 0$

$$tg\alpha = \sqrt{\frac{2 * \left(1 - \beta - \frac{b_{HAZ}}{b_0} * \left(1 - \rho_{o,HAZ}\right)\right)}{\left(\beta * \left(1 + \rho_{o,HAZ}\right) + 2 * \left(1 - \beta - \frac{b_{HAZ}}{b_0} * \left(1 - \rho_{o,HAZ}\right)\right)\right)}}$$

Introducing new parameter k

$$k = \left(1 - \beta - \frac{b_{HAZ}}{b_0} * \left(1 - \rho_{o,HAZ}\right)\right)$$

Introducing new parameter Δ

$$\Delta = \sqrt{\frac{2 * k}{\left(\beta * \left(1 + \rho_{o,HAZ}\right) + 2 * k\right)}}$$

Expresion for N_1

$$N_1 = \frac{t_0^2 * f_{0.2} * \left(1 + \rho_{o,HAZ}\right)}{(1-\beta) * sin\theta} * \left(\frac{\eta}{sin\theta} + \beta * \Delta + \frac{2 * k}{\left(1 + \rho_{o,HAZ}\right)} * \left(\frac{1}{\Delta} + \Delta\right)\right)$$

Davies and Packer [83] proposed that, when considering the wall thickness t_0 and the weld size w, the plastic hinges around the brace can be assumed to form along the weld edge, while those at the corners of the main member are taken to lie along the centerlines

of the side walls. As a result, the geometric parameters, b_0, b_1 and h_1 in the original formulation should be replaced by their effective counterparts b'_0, b'_1 and h'_1, respectively, to better reflect the actual deformation behavior of the joint.

$$h'_1 = h_1 + 2w \quad b'_0 = b_0 - t_0 \quad b'_1 = b_1 + 2w$$

$$\beta' = \frac{b'_1}{b'_0} = \frac{b_1 + 2w}{b_0 - t_0}$$

Comparation of the theoretical results with the results from the numerical investigation, EN 1993 results, EN 1993 +EN 1999 results and experimental results

To validate the reliability and accuracy of the developed analytical expression, the theoretical results were compared against numerical simulations, experimental tests, and design capacities according to EN 1993 and EN 1993+EN 1999, see Tab. 34. The comparison considered three RHS X-joint configurations with a common chord member (SHS100) and varying brace widths (SHS40, SHS50, SHS60) at brace inclination angle θ_i=45^0. The effective width ratio was used as a key geometric parameter.

Tab. 34: Comparation of numerical, experimental, code-based (EN 1993 and EN1993+EN1999) and theoretical results of load-bearing capacity of SHS X-joints θ_i=45^0 with SHS 100 chord member.

Type	Chord member	Brace member	β'	P_{serv} (kN)	P_{ult} (kN)
Numerical results	SHS100	SHS 40	0.526	35.824	50.952
	SHS100	SHS 50	0.631	52.117	66.876
	SHS100	SHS 60	0.737	79.343	93.001
Experimental results	SHS100	SHS 40	0.526	31.715	43.306
	SHS100	SHS 50	0.631	43.827	63.597
	SHS100	SHS 60	0.737	86.080	99.487
EN1993	SHS100	SHS 40	0.526		77.487
	SHS100	SHS 50	0.631		98.905
	SHS100	SHS 60	0.737		136.054
EN1993 +EN 1999	SHS100	SHS 40	0.526		38.744
	SHS100	SHS 50	0.631		49.452
	SHS100	SHS 60	0.737		68.027
Theory	SHS100	SHS 40	0.526		55.971
	SHS100	SHS 50	0.631		67.680
	SHS100	SHS 60	0.737		104.352

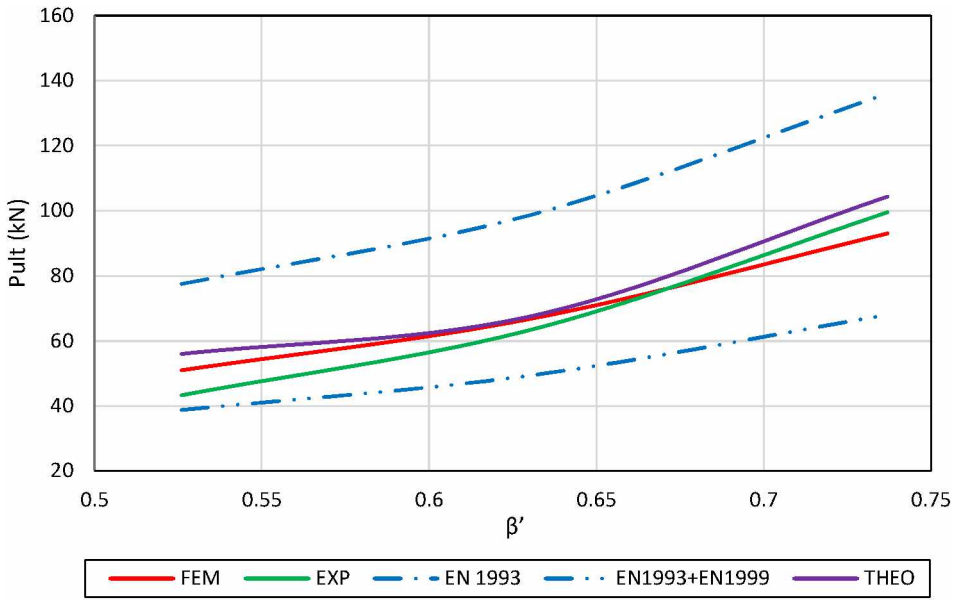

Fig. 104: Ultimate load P_{ult} versus β ratio for SHS X-joints for γ=10: comparison between numerical (FEM), experimental results (EXP) and predictions from EN 1993 (EN1993) and combined EN 1993 + EN 1999 design provisions (EN1993+EN1999).

The theoretical values show good agreement with numerical simulations, with deviations under 10% for all configurations, see Fig 104. This confirms the robustness of the derived expression in predicting plastification loads.

The theoretical predictions slightly overestimate the experimental results for SHS40 and SHS50 configurations but align more closely in the SHS60 case. This is expected due to simplifications in the yield line model, such as the assumption of rigid-plastic behavior and idealized hinge formation, see Fig 104.

The EN 1993-based predictions are significantly more conservative, especially for higher values. EN 1993+EN 1999 predictions are more in line with the experimental range, but tend to underestimate the capacity compared to both the theoretical and numerical results.

All methods show an increasing trend in joint capacity with increasing brace to chord width ratio. However, the rate of increase varies, with Eurocode predictions growing more rapidly than experimental and theoretical results, which could indicate conservative assumptions in the code at higher brace widths.

Second set of RHS X-joint configurations was analyzed. In this set, the chord member was SHS120, and the brace widths varied (SHS50, SHS60, SHS70). The same validation

methodology was used, comparing theoretical predictions to numerical simulations and code-based values from EN 1993 and EN 1993+EN 1999, as shown in Tab. 35.

Tab. 35: Comparation of numerical, experimental, code-based (EN 1993 and EN1993+EN1999) and theoretical results of load-bearing capacity of SHS X-joints $\theta_i=45^0$ with SHS 120 chord member.

Type	Chord member	Brace member	β'	P_{serv} (kN)	P_{ult} (kN)
Numerical results	SHS120	SHS50	0.522	34.774	49.629
	SHS120	SHS60	0.609	51.92	65.618
	SHS120	SHS70	0.696	67.34	84.063
EN1993	SHS120	SHS50	0.522		77.094
	SHS120	SHS60	0.609		93.833
	SHS120	SHS70	0.696		119.239
EN1993 +EN 1999	SHS120	SHS50	0.522		38.547
	SHS120	SHS60	0.609		46.917
	SHS120	SHS70	0.696		59.619
Theoretical results	SHS120	SHS50	0.522		48.379
	SHS120	SHS60	0.609		67.620
	SHS120	SHS70	0.696		82.540

The theoretical predictions are consistently close to the numerical results across all three configurations. This supports the applicability of the model beyond a single chord section.

As with the SHS100 series, EN 1993 predictions are significantly higher than both theoretical and numerical values, suggesting conservatism in code formulas. The combined EN 1993 + EN 1999 values are more conservative and align closer to theoretical values, especially for higher brace widths.

The pattern observed with increasing (higher brace width ratio) is consistent: all methods predict increasing resistance, but the theoretical values again offer a balanced estimate between conservative code predictions and detailed numerical models.

These additional results reinforce the robustness and generality of the derived analytical expression. It can reliably estimate ultimate resistance across a range of joint configurations and provides a practical alternative to both simplified design codes and computationally expensive simulations.

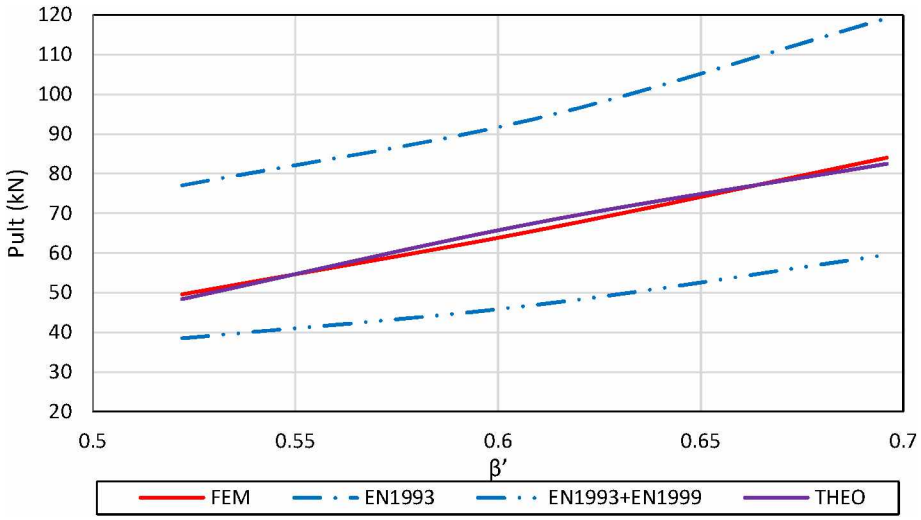

Fig. 105: Ultimate load P_{ult} versus β ratio for SHS X-joints for γ=12: comparison between numerical (FEM), experimental results (EXP) and predictions from EN 1993 (EN1993) and combined EN 1993 + EN 1999 design provisions (EN1993+EN1999).

To further extend the evaluation, the analytical expression was applied to a series of joints with a larger chord section (SHS150) and brace sizes ranging from SHS60 to SHS90. The comparison is shown below in the Tab. 35.

Tab. 35: Comparation of numerical, experimental, code-based (EN 1993 and EN1993+EN1999) and theoretical results of load-bearing capacity of SHS X-joints $\theta_i=45^0$ with SHS 120 chord member.

Type	Chord member	Brace member	β'	P_{serv}	P_{ult}
Numerical results	SHS150	SHS60	0.483	28.821	44.595
	SHS150	SHS70	0.5517	34.89	50.32
	SHS150	SHS80	0.621	52.843	68.263
	SHS 150	SHS90	0.69	65.045	84.531
EN1993	SHS150	SHS60	0.483		71.539
	SHS150	SHS70	0.5517		82.446
	SHS150	SHS80	0.621		97.041
	SHS 150	SHS90	0.69		117.489
EN1993 +EN 1999	SHS150	SHS60	0.483		35.770
	SHS150	SHS70	0.5517		41.223
	SHS150	SHS80	0.621		48.520
	SHS 150	SHS90	0.69		58.745
Theoretical results	SHS150	SHS60	0.483		55.754
	SHS150	SHS70	0.5517		62.887
	SHS150	SHS80	0.621		72.188
	SHS 150	SHS90	0.69		84.882

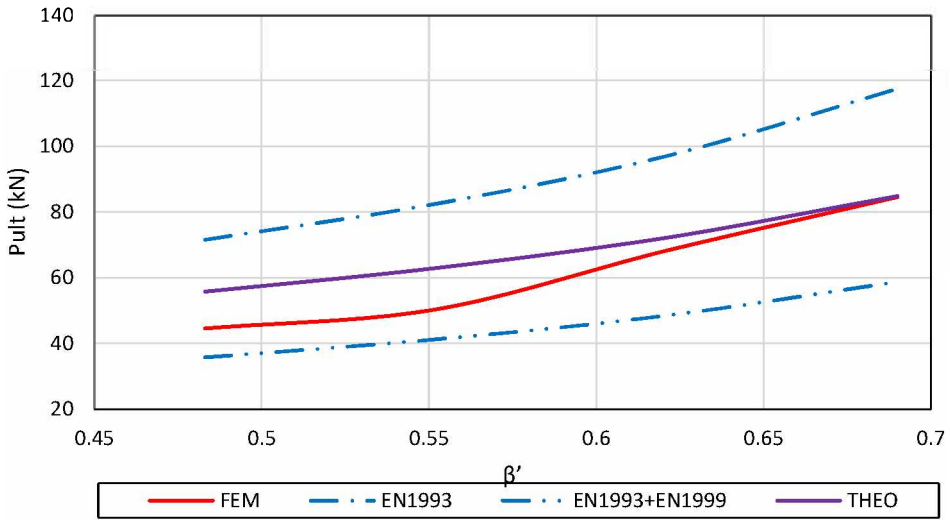

Fig. 106: Ultimate load P_{ult} versus β ratio for SHS X-joints for γ=15: comparison between numerical (FEM), experimental results (EXP) and predictions from EN 1993 (EN1993) and combined EN 1993 + EN 1999 design provisions (EN1993+EN1999).

The theoretical predictions continue to align closely with numerical results, maintaining consistency with previous comparisons. The Eurocode-based values (EN 1993) significantly overpredict capacity, especially at higher ratios. The EN 1993 + EN 1999 values are more conservative but underestimate capacity compared to both numerical and theoretical predictions.

The theoretical model provides a mid-range estimate that better captures actual behavior, reinforcing its practical applicability for design across a broad range of joint geometries. It can reliably estimate ultimate resistance across a range of joint configurations and provides a practical alternative to both simplified design codes and computationally expensive simulations.

Comparation of the theoretical results with the results from the numerical investigation, EN 1993 results, EN 1993 +EN 1999 results and experimental results

An additional evaluation was conducted for SHS-to-SHS 90-degree isolated X-joints using SHS100 as the chord member and varying brace widths. The results compare numerical, experimental, EN 1993, EN 1993+EN 1999, and theoretical results.

Tab. 36: Comparation of numerical, experimental, code-based (EN 1993 and EN1993+EN1999) and theoretical results of load-bearing capacity of SHS isolated X-joints $\theta_i=90^0$ with SHS 100 chord member.

Type	Chord member	Brace member	β'	P_{serv} (kN)	P_{ult} (kN)
Numerical results	SHS 100	SHS40	0.526	21.581	34.164
		SHS50	0.631	28.386	45.097
		SHS60	0.737	47.6	62.105
Experimental results	SHS 100	SHS40	0.526	18.51	32.02125
		SHS50	0.631	27.96	43.2235
		SHS60	0.737	39.271	56.42
EN 1993	SHS 100	SHS40	0.526		54.79113
		SHS50	0.631		69.93553
		SHS60	0.737		96.20357
EN 1993+EN 1999	SHS 100	SHS40	0.526		27.39556
		SHS50	0.631		34.96777
		SHS60	0.737		48.10179
Theoretical results	SHS 100	SHS40	0.526		35.394
		SHS50	0.631		41.774
		SHS60	0.737		51.252

The theoretical predictions continue to align closely with numerical results, maintaining consistency with previous comparisons.

The Eurocode-based values (EN 1993) significantly overpredict capacity, especially at higher ratios.

The EN 1993 + EN 1999 values are more conservative but underestimate capacity compared to both numerical and theoretical predictions.

The theoretical model provides a mid-range estimate that better captures actual behavior, reinforcing its practical applicability for design across a broad range of joint geometries, as shown in Fig. 107. It can reliably estimate ultimate resistance across a range of joint configurations and provides a practical alternative to both simplified design codes and computationally expensive simulations.

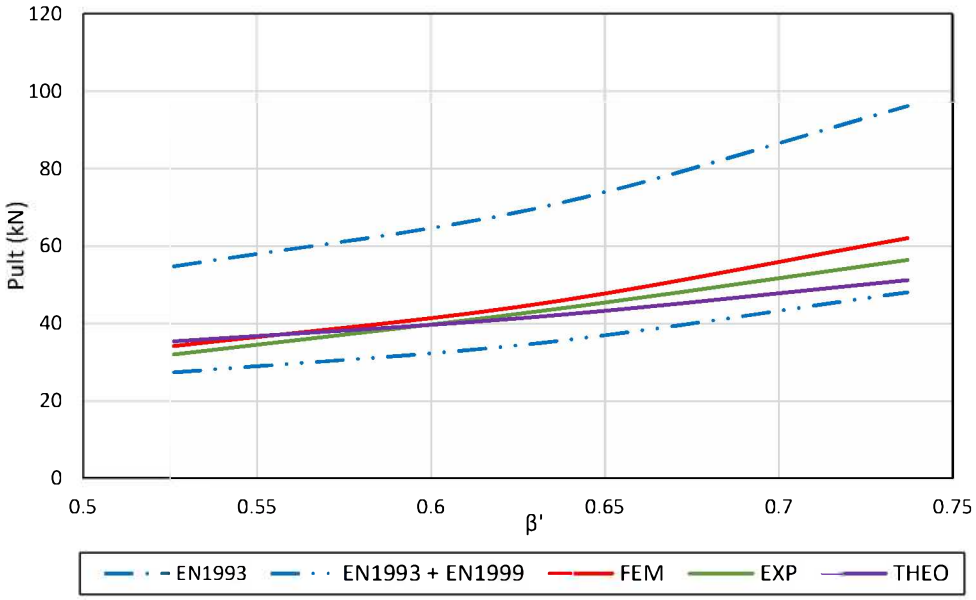

Fig. 107: Ultimate load P_{ult} versus β ratio for isolated SHS X-joints $\theta_i=90^0$ for $\gamma=10$: comparison between numerical (FEM), experimental results (EXP) and predictions from EN 1993 (EN1993) and combined EN 1993 + EN 1999 design provisions (EN1993+EN1999).

Further validation of the analytical model was conducted on SHS $\theta_i=90^0$ X-joints with a SHS120 chord member. The results are summarized below at the Tab. 37.

Tab. 37: Comparation of numerical, code-based (EN 1993 and EN1993+EN1999) and theoretical results of load-bearing capacity of SHS isolated X-joints $\theta_i=90^0$ $\gamma=12$ with SHS 120 chord member.

	Chord member	Brace member	β'	P_{serv} (kN)	P_{ult} (kN)
Numerical results	SHS 120	SHS50	0.522	17.826	32.022
		SHS60	0.609	26.651	42.384
		SHS70	0.696	33.737	55.285
EN 1993	SHS 120	SHS50	0.522		77.09408
		SHS60	0.609		93.83309
		SHS70	0.696		119.2386
EN 1993+EN 1999	SHS 120	SHS50	0.522		38.54704
		SHS60	0.609		46.91655
		SHS70	0.696		59.61928
Theoretical results	SHS 120	SHS40	0.522		36.713
		SHS50	0.609		42.24
		SHS60	0.696		50.082

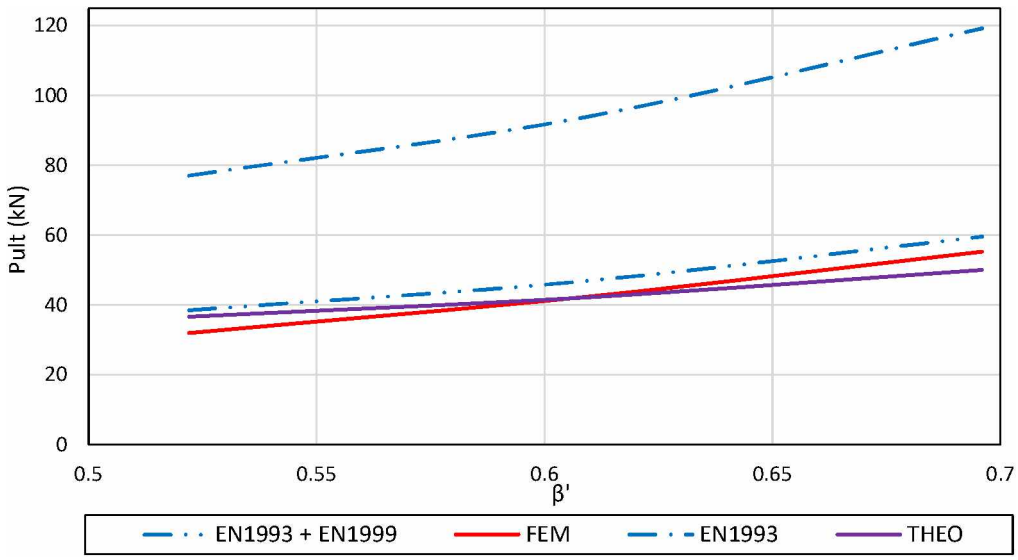

Fig. 107: Ultimate load P_{ult} versus β ratio for isolated SHS X-joints $\theta_i=90^0$ for γ=12: comparison between numerical (FEM), experimental results (EXP) and predictions from EN 1993 (EN1993) and combined EN 1993 + EN 1999 design provisions (EN1993+EN1999).

Agreement with numerical results is strong, particularly for SHS50 and SHS60 cases, as shown in Fig. 107. The EN 1993 values overestimate capacity by a wide margin.

The provided table presents a comparative analysis of SHS X-joints at 90 degrees, using SHS 150 as the chord member and varying brace sizes from SHS60 to SHS90. The joint geometry is defined by the β' ratio (brace width to chord width), and the table includes both numerical (NUM) and theoretical (THEO) results, as well as predictions from EN 1993, and the combined EN 1993 + EN 1999 design provisions. The parameters P1%bo and P3%bo represent the joint load capacities expressed as a percentage of the chord's outer width, indicating the load level at different joint deformation stages.

Tab. 37: Comparation of numerical, code-based (EN 1993 and EN1993+EN1999) and theoretical results of load-bearing capacity of SHS isolated X-joints $\theta_i=90^0$ γ=15 with SHS 150 chord member.

Type	Chord member	Brace member	β'	P_{serv} (kN)	P_{ult} (kN)
Numerical results	SHS 150	SHS60	0.483	14.191	27.486
		SHS70	0.5517	18.6	33.630
		SHS80	0.621	24.662	42.186
		SHS90	0.69	34.168	53.982
EN 1993	SHS 150	SHS60	0.483		71.539
		SHS70	0.5517		82.446

		SHS80	0.621		97.040
		SHS90	0.69		117.489
EN 1993+EN 1999	SHS 150	SHS60	0.483		35.769
		SHS70	0.5517		41.223
		SHS80	0.621		48.520
		SHS90	0.69		58.744
Numerical results	SHS 150	SHS60	0.483		26.867
		SHS70	0.5517		40.001
		SHS80	0.621		45.133
		SHS90	0.69		52.054

The comparison between the theoretical predictions and numerical results for SHS X-joints at 90 degrees, using SHS 150 as the chord member and brace sizes ranging from SHS60 to SHS90, reveals important insights into the accuracy and conservativeness of the theoretical model. In general, the theoretical values either slightly underestimate or modestly overestimate the joint resistance compared to the numerical simulations, depending on the β' ratio.

For the smallest brace size, SHS60 ($\beta' = 0.483$), the theoretical resistance (26.867 kN) is almost identical to the numerical result (27.486 kN), with only a 2.3% deviation. This indicates a strong agreement between theory and simulation for lower β' values. However, for SHS70 ($\beta' = 0.5517$), the theoretical prediction (40.001 kN) significantly overestimates the numerical result (33.63 kN) by nearly 19%. This suggests that the theoretical model may overpredict joint capacity at intermediate β' values, likely due to simplifications that do not fully capture localized yielding or stress concentrations in the joint region, as shown in Fig. 108.

For SHS80 ($\beta' = 0.621$), the theoretical value (45.133 kN) is about 7% higher than the numerical result (42.186 kN), showing better alignment but still indicating a modest overestimation. In contrast, for the largest brace size, SHS90 ($\beta' = 0.69$), the theoretical resistance (52.054 kN) is very close to the numerical outcome (53.982 kN), with only a 3.6% difference. This close match at high β' values confirms that the theoretical model performs well when brace members are relatively large compared to the chord, as shown in Fig. 108

Overall, the theoretical approach provides a reasonably conservative estimate of joint capacity, particularly for lower and higher β' values, while intermediate values may

require more refined analysis or calibration. The observed deviations emphasize the importance of validating theoretical models with numerical or experimental data, especially when designing critical connections in structural applications.

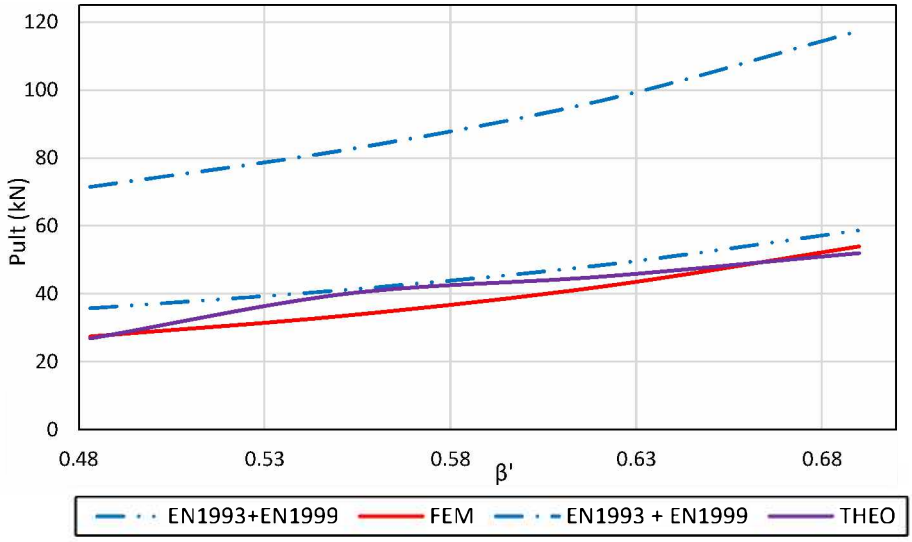

Fig. 108: Ultimate load P_{ult} versus β ratio for isolated SHS X-joints $\theta_i=90^0$ for $\gamma=15$: comparison between numerical (FEM), experimental results (EXP) and predictions from EN 1993 (EN1993) and combined EN 1993 + EN 1999 design provisions (EN1993+EN1999).

Conclusion

This doctoral dissertation presents a detailed investigation of the structural behavior of welded planar joints in aluminum truss systems, with a particular focus on the mechanical degradation occurring in the heat-affected zone (HAZ) as a result of welding. Through a multi-faceted methodology that combines experimental testing, numerical simulation, and analytical modeling, this research contributes both to fundamental scientific understanding and to practical advancements in the design of aluminum structures.

The experimental investigation included tensile testing, hardness mapping, and deformation tracking using Digital Image Correlation (DIC). Specimens were fabricated from the widely used EN AW-6082 T6 aluminum alloy and welded using conventional TIG welding procedure. Results demonstrated a notable reduction in mechanical properties within the HAZ, including:

A decrease in yield strength and ultimate tensile strength of up to 50% compared to the base material.

A localized drop in Vickers hardness measurements, especially within 10–30 mm of the weld seam.

Concentrated zones of plastic deformation and early failure initiation revealed via DIC, confirming the HAZ as the critical failure region.

Parallel to experimental work, numerical models were developed in ANSYS using the Finite Element Method (FEM). These models incorporated temperature-dependent material properties and spatially variable strength reductions in the HAZ. Numerical simulations closely mirrored the experimentally observed load-deformation behavior, accurately capturing the stiffness, yield point, and ultimate load. They were further used to analyze parametric influences such as joint geometry, weld configuration, and wall thickness.

The analytical component of the research focused on developing expressions for predicting joint load-bearing capacity using yield line theory and the principle of virtual work. These expressions were initially based on the yield mechanisms defined in EN 1993-1-8 for steel joints but were modified to account for aluminum-specific effects.

Reduction factors derived from experimental results were introduced to adjust the yield strength in the analytical expressions. A simplified formulation was developed for design use, with clear physical interpretation and consistency across a wide range of geometrical configurations. Validation of these models against experimental and numerical data showed deviations within ±10%, which confirms their high level of predictive accuracy and engineering applicability.

In summary, this research provides:

- A quantified assessment of HAZ softening in welded aluminum joints;
- Experimental data sets that characterize mechanical performance under axial loading;
- Calibrated FEM models for advanced joint simulation;
- Analytical expressions that can be directly implemented in engineering design.

These outcomes fill an important gap in current design standards, particularly in EN 1999-1-1, which lacks specific guidance for welded aluminum joints. The findings of this work support a more reliable and code-compliant use of aluminum in primary structural systems, particularly in lightweight, corrosion-resistant, and architecturally exposed applications.

Recommendations for Future Research

While this dissertation has made a significant contribution to the understanding and modeling of welded aluminum joints, several areas remain open for further exploration. The following recommendations are proposed for future research:

1. Fatigue Performance of Welded Joints

The present study addressed static loading; however, aluminum structures are frequently subjected to cyclic and fatigue loading (e.g., in bridges, offshore structures, and aircraft support systems). Further experimental research on high-cycle and low-cycle fatigue behavior of welded joints, with emphasis on crack initiation and propagation within the HAZ, is essential.

2. Friction Stir Welding and Alternative Joining Techniques

Conventional fusion welding introduces significant thermal gradients that cause HAZ softening. Investigating low-heat-input welding methods, such as Friction Stir Welding (FSW) or Laser Beam Welding, could yield improved mechanical performance and reduced property degradation. Comparative studies between these methods and TIG/MIG welding should be conducted.

3. Incorporation into Design Standards

The proposed analytical models and reduction factors should be further validated across different aluminum alloys and joint configurations, with the goal of contributing to the revision and expansion of EN 1999-1-1. Collaboration with standardization bodies is recommended to ensure practical impact.

References

[1] Mazzolani, Federico. (2006). Structural Applications of Aluminium in Civil Engineering. Structural Engineering International. 16. 280-285. 10.2749/101686606778995128.

[2] C. Vargel, Corrosion of aluminium, Oxford, Elsevier, 2004;

[3] Sharp, M.L. "Aluminum Structures" Structural Engineering Handbook Ed. Chen Wai-Fah Boca Raton: CRC Press LLC, 1999

[4]https://ingeniumcanada.org/channel/articles/on-the-bridge-of-arvida-a-national-historic-civil-engineering-site-they-are

[5] U. Muller, Introduction to structural aluminium design. Whittles Publishing, 2011.

[6] BSI Eurocode 9: Design of aluminium structures - part 1-1: General structural rules(2021) URL https://www.cys.org.cy/images/prEN_1999-1-1.pdf

[7] J. Randolph Kissell, Robert L. Ferry (2002.). Aluminum Structures. A guide to their specifications and design. New York: John Wiley & Sons, Inc;

[8] European Committee for Standardization, EN 573-1: Aluminium and aluminium alloys – Chemical composition and form of wrought products – Part 1: Numerical designation system, Brussels: CEN, 2004.

[9] F. Mazzolani, Aluminium alloy structures, 2nd ed. London: E & FN Spon;

[10] U. Stamenkovic, S. Ivanov, I. Markovic, N. Strbac and A. Mitovski, "The influence of the temperature of solution heat treatment on the properties of 6000 series aluminium alloys", Tehnika, vol. 72, no. 4, pp. 523-527, 2017. Available: 10.5937/tehnika1704523s;

[11] V. Macillo, "Special Joint Systems for Aluminium Structures: Experimental Tests and Numerical Models", Ph. D, Università degli Studi di Napoli Federico II, 2013;

[12] Comte, C. & Stebut, J. (2002). Microprobe-type measurement of Young's modulus and Poisson coefficient by means of depth sensing indentation and acoustic microscopy. Surface & Coatings Technology - SURF COAT TECH. 154. 42-48. 10.1016/S0257-8972(01)01706-6.

[13] Građevinski fakultet u Beogradu- lake metalne konstrukcije- online prezentacija;

[14] "Welded Aluminium Ship Structures", Journal of the American Society for Naval Engineers, vol. 69, no. 4, pp. 690-698, 2009;

[15] Đ. Đurić (2018.) Eksperimentalna i teorijska analiza graničnih stanja elemenata aluminijumskih rešetkastih konstrukcija, Doktorska desertacija, Univerzitet Crne Gore, Građevinski fakultet, Podgorica;

[16] Wardenier J., Kurobane Y., Packer J.A., Dutta D., Yeomans N.: Design Guide for Rectangular Hollow Sections (RHS) Joints Under Predominantly Static Loading, CIDECT, 1991;13;

[17] D. Buđevac, Z. Marković, D. Bogavac, D. Tošić, (1999.). Metalne konstrukcije. Osnove proračuna I konstruisanja. Beograd: Građevinski fakultet Univerziteta u Beogradu;

[18] D. Dujmović, B. Androić and D. Skejić, "Modeliranje priključaka čeličnih okvirnih konstrukcija", Građevinar, 2003;

[19] Eurocode 3: Design of steel structures - Part 1-8: Design of joints. Brussels, 2005;

[20] S. Živković, "Doprinos proračunu direktno zavarenih veza elemenata rešetkastih nosača od šupljih čeličnih profila pravougaonog i kvadratnog poprečnog ", Ph. D, Univerzitet u Nišu, 2014;

[21] J. Wardenier, J. Packer, X. Zhao and G. Van der Vegte, Hollow Sections in Structural Applications. Geneva, Switzerland, CIDECT, 2010;

[22] L. Lu, G. de Winkel, Y. Yu, J. Wardenier, Deformation limit for the ultimate strength of hollow section joints, in: Tubular Structures, Routledge, 1994, pp. 341–347.

[23] J. Dwight, Aluminium Design and Construction, 1st ed. London and New York: E & FN SPON, 1999;

[24] Y. Fai and W. Lai, "Buckling strength of welded and non-welded aluminium members", ph. D, University of Sheffield, 1988;

[25] Brungraber, R. J. & Clark, J. W., 1962. Strength of welded aluminum columns. *Transactions of the American Society of Civil Engineers*, 127 (Part II), pp. 687–701.

[26] M. P. Wong, Weld shrinkage in non-linear materials, Ph.D. dissertation, Univ. of Cambridge, Cambridge, U.K., 1982.

[27] I. Robertson, Strength loss in welded aluminium structures, Ph.D. dissertation, University of Cambridge, Cambridge, U.K., 1985.

[28] S. Baskutis, A. Žunda and R. Kreivaitis, "Mechanical properties and microstructure of aluminium alloy AW6082-T6 joints welded by double-sided MIG process before and after aging", Mechanics, vol. 25, no. 2, 2019;

[29] T. Wang, "Modelling of Welded Thin-Walled Aluminium Structures", Ph. D, Norwegian University of Science and Technology, 2006;

[30] G. E. Dieter, D. Bacon, Mechanical metallurgy, Vol. 3, McGraw-Hill New York, 1976;

[31] M. Matusiak, Strength and ductility of welded structures in aluminium alloys, Ph.D. thesis, Department of Structural Engineering, Norwegian University of Science and Technology (1999).

[32] M. D. Collette, "The Impact of Fusion Welds on the Ultimate Strength of Aluminum Structures," 10th International Symposium on Practical Design of Ships and Other Floating Structures Houston, Texas, United States of America, 2007;

[33] Y. Lai, D. Nethercot, Strength of aluminium members containing local transverse welds, Engineering Structures 14 (4) (1992) 241-254.

[34] T. Wang, Modelling of welded thin-walled aluminium structures, Phd thesis, Fakultet for ingeniorvitenskap og teknologi (2006).

[35] Y. Zhao, X. Zhai, Bending strength and design methods of the 6082- t6 aluminum alloy beams with circular hollow sections, in: Structures, Vol. 26, Elsevier, 2020, pp. 870-887.

[36] D. Yang, X. Sun, G. Zhou, H. Jiang, L. Sun, T. He, C. Yu, Y.Wei, P. Liu, Optimization of continuous drive friction welding process for aa6061-t6 circular pipe and conical head, in: Structures, Vol. 36, Elsevier, 2022, pp. 1068-1079.

[37] B. Li, F. Shen, J. Wang, X. Zhi, Y. Wang, S. Lin, Y. Ouyang, Experimental study on mechanical behaviour of friction stir welded aluminium alloy butt joints, in: Structures, Vol. 63, Elsevier, 2024, p. 106407.

[38] B. Li, P. He, J. Wang, X. Pan, Y. Wang, Z. Wang, C. C. Baniotopoulos, Mechanical characteristic and stress-strain modelling of friction stirwelded 6061-t6 aluminium alloy butt joints, Thin-Walled Structures 198 (2024) 111645.

[39] D. van Hove, F. Soetens, Numerical/experimental research on welded joints in aluminium truss girders, Key Engineering Materials 710 (2016) 295-300.

[40] Y. F. W. Lai and D. A. Nethercot, "Strenght of aluminium members containing local transverse welds," Construction and Building Materials, vol. 7, no. 1, pp. 27–39, 1993;

[41] J.-H. Zhu, B. Young, Experimental investigation of aluminum alloy circular hollow section columns, Engineering Structures 28 (2) (2006) 207-215.

[42] T. Schellekens, "Ductility analysis of aluminum alloy connections," MSc thesis, Technische Universiteit Eindhoven, 2020;

[43] M. D. Collette, The impact of fusion welds on the ultimate strength of aluminum structures, in: Proceedings of PRADS, Houston, TX, 2007.

[44] S. Meini, "Behaviour and Design of Aluminium Alloy Structural Elements," PhD dissertation, Imperial college London, 2014.

[45] U. Stamenkovic, S. Ivanov, I. Markovic, N. Strbac, and A. Mitovski, "The influence of the temperature of solution heat treatment on the properties of 6000 series aluminium alloys," Tehnika, vol. 72, no. 4, pp. 523–527, 2017.

[46] A. Astarita, A. Squillace, and L. Nele, "Mechanical characteristics of welded joints of aluminum alloy 6061 T6 formed by arc and Friction Stir Welding," Metal Science and Heat Treatment, vol. 57, no. 9-10, pp. 564–569, 2016

[47] K. A. Macdonald and P. J. Haagensen, "Fatigue of welded aluminium hollow section profiles," Engineering Failure Analysis, vol. 16, no. 1, pp. 254–261, Jan. 2009. https://doi.org/10.1016/j.engfailanal.2008.03.004

[48] H. Kos, "Zavarljivost aluminijske legure AW 6082," magistarska teza, Sveučilište u Zagrebu, Zagreb, 2014;

[49] S. Kalac, C. Radlbeck, M. Mensinger, D. Lucic Experimental and theoretical research on welded aluminium X-Joints Ce/ Pap., 6 (3–4) (2023), pp. 1434-1439

[50] Š. Kalač, M. Mensinger, C. Radlbeck, N. Zejnelagić, Đ. Đuričić, D. Lučić Experimental and theoretical research on welded aluminum K-joints Eng. Proc., 43 (1) (2023), p. 18

[51] S. Kalac, C. Radlbeck, M. Mensinger, N. Zejnelagic, and D. Lucic, "Research on the load-bearing capacity of welded aluminum K-joints," Journal of Constructional Steel Research, vol. 227, p. 109329, 2025, doi: 10.1016/j.jcsr.2025.109329.

[52] A. M. van Wingerde, J. A. Packer, and J. Wardenier, "Simplified SCF formulae and graphs for CHS and RHS K- and KK-connections," Journal of Constructional Steel Research, vol. 57, no. 3, pp. 221–252, 2001;

[53] R. Feng and B. Young, "Design of cold-formed stainless steel tubular T- and X-joints," Journal of Constructional Steel Research, vol. 67, no. 3, pp. 421–436, 2011;

[54] Y. Chen, R. Feng, and X. Ruan, "Behaviour of steel-concrete-steel SHS X-joints under Axial Compression," Journal of Constructional Steel Research, vol. 122, pp. 469–487, 2016;

[55] Y. Chen, J. Wan, K. Hu, J. Yang, and X. Chen, "Stress concentration factors of circular chord and square braces k-joints under axial loading," Thin-Walled Structures, vol. 113, pp. 287–298, 2017;

[56] Y. Chen, R. Feng, and L. Fu, "Investigation of grouted stainless steel SHS tubular X- and T-joints subjected to axial compression," Engineering Structures, vol. 150, pp. 318–333, 2017;

[57] Q. Zhu, Y. Chen, X. Zhang, X. Shen, and Y. Zhu, "Static behavior of X-joints with SHS Chord and CHS Braces," Journal of Constructional Steel Research, vol. 162, p. 105750, 2019.

[58] J. A. Packer, J. Wardenier, X.-L. Zhao, G. Van der Vegte, Y. Kurobane, Design guide for rectangular hollow section (RHS) joints under predominantly static loading, Cidect, 1991.

[59] G. Davies, C. Roper, Gap joints with tubular members–a yield line approach, Building Science 10 (3) (1975) 199–205.

[60] J. Packer, G. Davies, M. Coutie, Yield strength of gapped joints in rectangular hollow section trusses, Proceedings of the Institution of Civil Engineers 69 (4) (1980) 995–1013.

[61] Cao, J.J., Packer, J.A., Yang, G.J. (1998). Yield line analysis of RHS connections with axial loads. Journal of Constructional Steel Research, 48(1), 1–25.

[62] Johansen, K.W. (1972). Yield-Line Formulae for Slabs. Cement and Concrete Association, London.

[63] Wood, R.H. (1961). Plastic and Elastic Design of Slabs and Plates. Thames & Hudson, London.

[64] Zhao, X.L., Hancock, G.J. (1993). A theoretical analysis of the plastic-moment capacity of an inclined yield line under axial force. Thin-Walled Structures, 15(3), 185–207.

[65] I. Al Zamzami, V. Di Cocco, J. B. Davison, F. Iacoviello, and L. Susmel, "Static strength and design of aluminium-to-steel thin welded joints," Welding in the World, vol. 62, no. 6, pp. 1255–1272, 2018;

[66] G. Cornacchia and S. Cecchel, "Study and characterization of en aw 6181/6082-T6 and en AC 42100-T6 aluminum alloy welding of structural applications: Metal Inert Gas (mig), Cold Metal Transfer (CMT), and fiber laser-mig hybrid comparison," Metals, vol. 10, no. 4, p. 441, 2020

[67] S. Baskutis, A. Žunda and R. Kreivaitis, "Mechanical properties and microstructure of aluminium alloy AW6082-T6 joints welded by double-sided MIG process before and after aging", Mechanics, vol. 25, no. 2, 2019;

[68] Y. Lai, D. Nethercot, Strength of aluminium members containing local transverse welds, Engineering Structures 14 (4) (1992) 241–254.

[69] T. Wang, Modelling of welded thin-walled aluminium structures, Phd thesis, Fakultet for ingeniorvitenskap og teknologi (2006).

[70] Y. Zhao, X. Zhai, Bending strength and design methods of the 6082- t6 aluminum alloy beams with circular hollow sections, in: Structures, Vol. 26, Elsevier, 2020, pp. 870–887.

[71] D. Yang, X. Sun, G. Zhou, H. Jiang, L. Sun, T. He, C. Yu, Y.Wei, P. Liu, Optimization of continuous drive friction welding process for aa6061-t6 circular pipe and conical head, in: Structures, Vol. 36, Elsevier, 2022, pp. 1068–1079.

[72] B. Li, F. Shen, J. Wang, X. Zhi, Y. Wang, S. Lin, Y. Ouyang, Experimental study on mechanical behaviour of friction stir welded aluminium alloy butt joints, in: Structures, Vol. 63, Elsevier, 2024, p. 106407.

[73] B. Li, P. He, J. Wang, X. Pan, Y. Wang, Z. Wang, C. C. Baniotopoulos, Mechanical characteristic and stress-strain modelling of friction stirwelded 6061-t6 aluminium alloy butt joints, Thin-Walled Structures 198 (2024) 111645.

[74] D. van Hove, F. Soetens, Numerical/experimental research on welded joints in aluminium truss girders, Key Engineering Materials 710 (2016) 295–300.

[75] F. Soetens Welded connections in aluminium alloy structures Heron (Delft), 32 (1) (1987), pp. 1-48

[76] S. de Jongh, J.J. Maljaars, H.B. Snijder, S. Lundberg The resistance of welded X-joints of rectangular hollow sections in aluminum
(2016)

[77] W. Manders, J. Maljaars, B. Belin, M. Lukić Punching shear failure of welded rectangular hollow section joints in aluminium Constr. MÉ Tallique, 2019 (2) (2019), pp. 119-142

[78] H. Liu, J. Ying, Z. Chen, C. Ma, S. Qian, Y. Ouyang, X. Liu Research status of mechanical properties of aluminum alloy grid structure Structures, Vol. 61, Elsevier (2024), Article 105967

[79] C.W. Ziemian, R.D. Ziemian Numerical investigation of the influence of transverse welds on the strength of aluminum alloy I-shaped members–columns Structures, Vol. 60, Elsevier (2024), Article 105856

[80] M. Matusiak Strength and ductility of welded structures in aluminium alloys (Ph.D. thesis) Department of Structural Engineering, Norwegian University of Science and Technology (1999)

[81] EN ISO 6892-1:2019, *Metallic materials — Tensile testing — Part 1: Method of test at room temperature*, European Committee for Standardization, Brussels, Belgium, 2019.

[82] ASYS TUTORIALSURL https://www.ansys.com/academic/learning-resources

[83] Davies G, Packer JA. Predicting the strength of branch plate-RHS connections for punching shear. Canadian Journal of Civil Engineering 1982; 9:458–67.

Biography

Šemso Kalač was born on September 30, 1991, in Berane, Montenegro. He completed his primary education at *Pavle Rovinski* Elementary School and his secondary education at *Slobodan Škerović* Gymnasium in Podgorica, graduating with the *Luča* diploma for outstanding achievement.

He enrolled at the Faculty of Civil Engineering, University of Montenegro, in 2010, and completed his bachelor studies with a grade point average of 10.00. He finished his specialist studies in 2015 with a GPA of 9.91. During his undergraduate and specialist studies, he received several awards, including the University of Montenegro Award for the best student of the Faculty of Civil Engineering (2010), the Student Award of the Capital City Podgorica (2010), and multiple annual awards of the Faculty of Civil Engineering (2011, 2012, 2013). He was also a recipient of a Robert Bosch Foundation scholarship, as well as a scholarship from the Chamber of Engineers of Montenegro.

He enrolled in master's studies at the Faculty of Civil Engineering, University of Montenegro, in 2014. His master's thesis, entitled *Analysis of Strength and Stability of Shells According to Eurocode*, was defended on November 27, 2017. He completed his master's degree with a GPA of 10.00.

In 2019, he began doctoral studies at the Faculty of Civil Engineering, University of Montenegro. He passed all doctoral exams with the grade 10.00 and defended his initial research entitled *Experimental and Theoretical Investigation of Planar Connections in Aluminum Truss Structures*. During his doctoral studies, he was awarded a research grant by the Ministry of Science of Montenegro for the project *EKSTEORIS VAR*, followed by a research grant from the German Federal Environmental Foundation (*Deutsche Bundesstiftung Umwelt – DBU*) to continue his research on the application of aluminum as a sustainable material in civil engineering. This research was carried out at the Technical University of Munich, Chair of Metal Structures.

His professional career began in 2015 at the Faculty of Polytechnic Studies, University of Donja Gorica, where he worked as a teaching assistant and researcher in the ProDe Laboratory. He also gained professional experience through an internship in Beirut (Lebanon) in the field of structural design, followed by employment as a site engineer in the tunneling sector on the Bar–Boljare Highway project (2016–2018), and later on the Portonovi project (from 2018) in the fields of hydraulic engineering and building structures.

He is the author of several scientific papers published at international conferences and in peer-reviewed journals. He is the founder of the engineering firm *Dellkom Engineering doo* and the start-up company *ALCON doo*, specialized in the design and construction of lightweight modular aluminum bridges.

He is fluent in English (C1) and has working knowledge of German (A2) and Italian (A2). He is married and has a daughter, Maida.

Biografija

Šemso Kalač rođen je 30. septembra 1991. godine u Beranama. Osnovno obrazovanje stekao je u Osnovnoj školi „Pavle Rovinski“, a srednje u Gimnaziji „Slobodan Škerović“ u Podgorici, koju je završio sa diplomom Luča. Građevinski fakultet Univerziteta Crne Gore upisao je 2010. godine, bachelor studije završio sa prosječnom ocjenom 10.00. Specijalističke studije završio je 2015. godine sa prosječnom ocjenom 9.91. Tokom osnovnih i specijalističkih studija dobitnik je više nagrada, među kojima su: Nagrada Univerziteta Crne Gore za najboljeg studenta Građevinskog fakulteta (2010), Studentska nagrada Glavnog grada Podgorica (2010), te nagrade Građevinskog fakulteta u više navrata (2011, 2012, 2013), stipendija Robert Bosch Fondacije. Na specijalističkim studijama bio je i stipendista Inženjerske komore Crne Gore. Magistarske studije na Građevinskom fakultetu u Podgorici upisao je 2014. godine. Magistarski rad pod naslovom Analiza čvrstoće i stabilnosti ljuski prema Eurokodu odbranio je 27. novembra 2017. godine, a magistarske studije završio sa prosječnom ocjenom 10.00. Doktorske studije upisao je 2019. godine na Građevinskom fakultetu Univerziteta Crne Gore. Položio je sve ispite sa ocjenom 10.00 i odbranio polazna istraživanja pod naslovom Eksperimentalno i teorijsko ispitivanje ravanskih veza aluminijumskih rešetkastih konstrukcija. Tokom doktorskih studija bio je dobitnik istraživačkog granta Ministarstva nauke Crne Gore za projekat EKSTEORIS VAR, a potom i istraživačkog granta Njemačke savezne fondacije za održivi razvoj (Deutsche Bundesstiftung Umwelt – DBU) za nastavak istraživanja na temu primjene aluminijuma kao zelenog materijala u građevinarstvu. Istraživanja je realizovao na Tehničkom univerzitetu u Minhenu, na Katedri za metalne konstrukcije. Profesionalnu karijeru započeo je 2015. godine na Fakultetu za politehniku Univerziteta Donja Gorica kao saradnik u nastavi i istraživač u Laboratoriji ProDe. Stručno iskustvo sticao je i kroz praksu u Bejrutu (Liban) u oblasti projektovanja konstrukcija, zatim kao inženjer u sektoru tunelogradnje na projektu Autoputa Bar–Boljare (2016–2018), te na projektu Portonovi (od 2018) u oblasti hidrotehničkih konstrukcija i visokogradnje. Autor je više naučnoistraživačkih radova objavljenih na međunarodnim konferencijama i u stručnim časopisima. Osnivač je građevinskog biroa Dellkom Engineering doo i start-up kompanije ALCON doo, specijalizovane za projektovanje i izvođenje lakih montažnih aluminijumskih mostova. Tečno govori engleski jezik (C1), a služi se njemačkim (A2) i italijanskim jezikom (A2). Oženjen je i ima ćerku Maidu.

Bibliography

1. Kalač, S.; Radlbeck, C.; Mensinger, M.; Zejnelagić, N.; Lučić, D. Research on the Load-Bearing Capacity of Welded Aluminum K-Joints. *J. Constr. Steel Res.* 2025, *227*, 109329.

2.Kalač, Š.; Mensinger, M.; Radlbeck, C.; Zejnelagić, N.; Đuričić, Đ.; Lučić, D. Experimental and Theoretical Research on Welded Aluminum K-Joints. Eng. Proc. 2023, 43, 18. https://doi.org/10.3390/engproc2023043018

3.Kalač, Š.; Radlbeck, C.; Mensinger, M.; Lucic, D. (2023). Experimental and theoretical research on welded aluminium X joints. Ce/Papers, 6(3–4), 1434–1439. https://doi.org/10.1002/cepa.2260

4.Kalač Š., Zejnelagić N., Muhadinović M., Lučić D: "Overview of National Determined Parameters in EN 1993-1-6", DGKS 2022, Aranđelovac, 2022. god.;

5.Kalač Š., Zejnelagić N., Lučić D:"THE ALGORITHM OF ANALYSIS AND DESIGN OF STEEL WATER TANK ACCORDING TO EUROCODES", in MASE 19, Ohrid, 2022;

6. Kalač Š., Zejnelagić N., Đuričić Đ., Lučić D:" Proposal of an analytical expression for determination of load capacity for aluminum square hollow section (SHS) K joints under chord tension", GNP 2022, Kolašin, 2022. god. ISBN 978-86-82707-35-6;

7.Kalač Š., Zejnelagić N., Sterniša B.:" PATCH LOADING – numerička analiza stabilnosti I nosača sa i bez podužnog ukrućenja", 15 međunarodna naučna konferencija o planiranju, projektovanju, građenju i obnovi graditeljstva iNDiS 2021, Novi Sad, 2021. god., ISBN 978-86-6022-253-6; DOI: 10.13140/RG.2.2.21732.50565

8. Sterniša B., Kalač Š., Golubović V., Miljanić D.: "Real engineering problems rather than theory", Knowledge International Journal at Institute of management and knowledge, Skopje, Macedonia Volume: 43.3. 2020. god., ISSN:

2545-4439;

Prilog 2.

Izjava o autorstvu

Potpisani Šemso Kalač

Broj indeksa/upisa 19/1

Izjavljujem

da je doktorska disertacija pod naslovom:

EKSPERIMENTALNO I TEORIJSKO ISPITIVANJE RAVANSKIH VEZA ALUMINIJUMSKIH REŠETKASTIH KONSTRUKCIJA

- rezultat sopstvenog istraživačkog rada,
- da predloženi master rad ni u cjelini ni u djelovima nije bio predložen za dobijanje bilo koje diplome prema studijskim programima drugih ustanova visokog obrazovanja,
- da su rezultati korektno navedeni, i
- da nijesam povrijedio/la autorska i druga prava intelektualne svojine koja pripadaju trećim licima.

Potpis doktoranda

U

Podgorica, 04.09.2025. god.

Prilog 3.

Izjava o istovjetnosti štampane i elektronske verzije doktorskog rada

Ime i prezime autora Šemso Kalač

Broj indeksa/upisa 19/1

Studijski program građevinarstvo

Naslov rada EKSPERIMENTALNO I TEORIJSKO ISPITIVANJE RAVANSKIH VEZA ALUMINIJUMSKIH REŠETKASTIH KONSTRUKCIJA

Mentor prof. dr Duško Lučić

Potpisani/a

Izjavljujem da je štampana verzija moje doktorske disertacije istovjetna elektronskoj verziji koju sam predao/la za objavljivanje u Digitalni arhiv Univerziteta Crne Gore.

Istovremeno izjavljujem da dozvoljavam objavljivanje mojih ličnih podataka u vezi sa dobijanjem akademskog naziva doktora nauka, odnosno zvanja doktor umjetnosti, kao što su ime i prezime, godina i mjesto rođenja, naslov doktorskog rada i datum odbrane rada.

Potpis doktoranda

U Podgorici, 04.09.2025. god. _____

Prilog 4.

IZJAVA O KORIŠĆENJU

Ovlašćujem Univerzitetsku biblioteku da u Digitalnom arhivu Univerziteta Crne Gore pohrani moju doktorsku disertaciju pod nazivom:

EKSPERIMENTALNO I TEORIJSKO ISPITIVANJE RAVANSKIH VEZA ALUMINIJUMSKIH REŠETKASTIH KONSTRUKCIJA

koji je moje autorsko djelo.

Doktorska disertacija sa svim prilozima predao/la sam u elektronskom formatu pogodnom za trajno arhiviranje.

Moja doktorski disertacija pohranjena u Digitalnom arhivu Univerziteta Crne Gore mogu da koriste svi koji poštuju odredbe sadržane u odabranom tipu licence Kreativne zajednice (Creative Commons) za koju sam se odlučio/la.

1. Autorstvo
2. Autorstvo – nekomercijalno
3. Autorstvo – nekomercijalno – bez prerade
4. Autorstvo – nekomercijalno – dijeliti pod istim uslovima
5. Autorstvo – bez prerade
6. Autorstvo – dijeliti pod istim uslovima

(Molimo da zaokružite samo jednu od šest ponuđenih licenci, kratak opis licenci dat je na poleđini lista).

Potpis doktoranda

U Podgorici, 04.09.2025. god. _____

1. Autorstvo - Dozvoljavate umnožavanje, distribuciju i javno saopštavanje djela, i prerade, ako se navede ime autora na način određen od strane autora ili davaoca licence, čak i u komercijalne svrhe. Ovo je najslobodnija od svih licenci.

2. Autorstvo - nekomercijalno. Dozvoljavate umnožavanje, distribuciju i javno saopštavanje djela, i prerade, ako se navede ime autora na način određen od strane autora ili davaoca licence. Ova licenca ne dozvoljava komercijalnu upotrebu djela.

3. Autorstvo - nekomercijalno - bez prerade. Dozvoljavate umnožavanje, distribuciju i javno saopštavanje djela, bez promjena, preoblikovanja ili upotrebe djela u svom djelu, ako se navede ime autora na način određen od strane autora ili davaoca licence. Ova licenca ne dozvoljava komercijalnu upotrebu djela. U odnosu na sve ostale licence, ovom licencom se ograničava najveći obim prava korišćenja djela.

4. Autorstvo - nekomercijalno - dijeliti pod istim uslovima. Dozvoljavate umnožavanje, distribuciju i javno saopštavanje djela, i prerade, ako se navede ime autora na način određen od strane autora ili davaoca licence i ako se prerada distribuira pod istom ili sličnom licencom. Ova licenca ne dozvoljava komercijalnu upotrebu djela i prerade.

5. Autorstvo - bez prerade. Dozvoljavate umnožavanje, distribuciju i javno saopštavanje djela, bez promjena, preoblikovanja ili upotrebe djela u svom djelu, ako se navede ime autora na način određen od strane autora ili davaoca licence. Ova licenca dozvoljava komercijalnu upotrebu djela.

6. Autorstvo - dijeliti pod istim uslovima. Dozvoljavate umnožavanje, distribuciju i javno saopštavanje djela, i prerade, ako se navede ime autora na način određen od strane autora ili davaoca licence i ako se prerada distribuira pod istom ili sličnom licencom. Ova licenca dozvoljava komercijalnu upotrebu djela i prerada. Slična je softverskim licencama, odnosno licencama otvorenog koda.